8-2005

Analysis of Martian Parental Melts and Thermal Infrared Studies of Putative Paleolake Basins on Mars

Karen Renée Stockstill
University of Tennessee - Knoxville

To the Graduate Council:

I am submitting herewith a dissertation written by Karen Renée Stockstill entitled "Analysis of Martian Parental Melts and Thermal Infrared Studies of Putative Paleolake Basins on Mars." I have examined the final electronic copy of this dissertation for form and content and recommend that it be accepted in partial fulfillment of the requirements for the degree of Doctor of Philosophy, with a major in Geology.

Harry Y. McSween, Jr., Major Professor

We have read this dissertation and recommend its acceptance:

Kula Misra, Alexander Van Hook

Accepted for the Council:

Carolyn R. Hodges

Vice Provost and Dean of the Graduate School

(Original signatures are on file with official student records.)

To the Graduate Council:

I am submitting herewith a dissertation written by Karen Renée Stockstill entitled "Analysis of Martian Parental Melts and Thermal Infrared Studies of Putative Paleolake Basins on Mars." I have examined the final electronic copy of this dissertation for form and content and recommend that it be accepted in partial fulfillment of the requirements for the degree of Doctor of Philosophy, with a major in Geology.

Harry Y. McSween, Jr., Major Professor

Jeffrey E. Moersch, Major Professor

We have read this dissertation
and recommend its acceptance:

Kula Misra

Alexander Van Hook

Acceptance for the Council:

Anne Mayhew
Vice Chancellor and Dean of Graduate Studies

(Original signatures are on file with official student records.)

ANALYSIS OF MARTIAN PARENTAL MELTS AND THERMAL INFRARED STUDIES OF PUTATIVE PALEOLAKE BASINS ON MARS

A Dissertation
Presented for the
Doctor of Philosophy
Degree
The University of Tennessee, Knoxville

Karen Renée Stockstill
August 2005

Dedication

This dissertation is dedicated
To my Mom, who made this all possible over and over,
To my Dad, who always asked interesting questions,
To my brother Ray, who always shares without hesitation,
and
To Josh, who is always there when I come back from the Milky Way.

Acknowledgements

This adventure would not have been possible without the support and guidance of my co-advisors, Harry Y. McSween, Jr. and Jeffrey E. Moersch. If you want to learn how to do science in every way possible, these are your guys! My committee members, Kula C. Misra and Alexander Van Hook, asked questions along the way that helped us to avoid pitfalls and provided useful commentary on the chapters within. In addition, the encouragement of many in the UT Department of Earth & Planetary Sciences has been invaluable: Amitabha Ghosh, Bill Deane, the Britt family, the Lentz family, Jen Piatek, Mike Rampey, Linda Kah and Colin Sumrall – you guys are the greatest!! Last but not least, Penny King, who showed up in second overtime, but made up for lost time by cheering even harder!

Robert Bodnar welcomed me into his melt inclusion research group at Virginia Tech with open arms and I treasured my time spent in his lab. In addition, his students, post docs and lab techs provided invaluable assistance and advice regarding laboratory work: Jay Thomas, Charles Farley, Luca Fedele, Mercedes Gonzalez-Student and Jim Student. In addition, Gretchen Benedix provided priceless assistance in analyzing melt inclusions at the Virginia Tech microprobe facility. Additionally, the ASU/UH contingent of Steve Ruff, Mike Wyatt, Vicky Hamilton and Phil Christensen provided on-going support and expertise in the processing and appropriate interpretation of thermal infrared data of Mars. Without them, our pursuit of carbonates would have been much more obscure.

This adventure would not have been survivable without the support and laughter contributed by my fellow graduate students: Keith Milam, Valerie Reynolds, Rhiannon Mayne, Tasha Dunne, Livio Tornabene, Kathy Stone, Sandra Ciccole, and Tabbatha Cavendish. I did not realize that my grad school co-horts would teach me how to be the best kind of friend: one who never forgets all you've done for them, but does for you and forgets all about it. You also taught me a great deal about science and professionalism – I hope I returned the favor to each of you. I can't wait to tell your students our stories and how great you are. In addition, the friendship of Kerry Milam, Cari Corrigan, Ben

Bussey, Kevin Peterson, John Woodell, Michelle Prysby, David and Mary Gwynn, Julie Niekamp, Teresa Coffield and many others has been invaluable during this trial.

This adventure would not have been nearly as much fun without the Cahill/Saalfeld clan. They've been nice enough to distract me with Notre Dame football (GO IRISH!!!), eating lots of good food, betting on horses, yummy Graeters ice cream, swimming meets, Thanksgiving dinner, tours of Ireland, and more eating. I would probably be a rail-thin, miserable person without you!

The adventure would have meant nothing without my family to share it with. Mom, you always found a way to make my dreams possible on a shoe string budget and I will never forget all that you have done. Thanks for the truck! Dad, I wish you could have been at the defense, because I am sure you would have loved to see the pretty pictures and would have asked some great questions. And you would've grinned big! Ray, you are such a generous brother – you never hesitate to share what I need. I would not have finished this degree without your support and flight benefits. Thanks for laughs and please keep them coming!

This adventure was enhanced by the patience, encouragement, and Diamond-head view provided by Josh Cahill. You kept me swimming when the shoreline seemed too far away and the current too strong. You told me I could do it when I wasn't sure I could. You told me the dreams do return once you can see the sky again and you were right! I look forward to the rest of our adventure!

Abstract

Both martian meteorites and remote sensing data allow us to study the geologic history of Mars. Martian meteorites can reveal information regarding partial melting of the Mars mantle and the surface processes that affected the meteorite following eruption (weathering, impact ejection, etc.). Remote sensing data can be used to investigate the local-, regional- or global-scale surface of Mars in terms of composition and geomorphology. A well-rounded approach is necessary to address fundamental questions regarding the geologic history of Mars.

We studied melt inclusions in augite of the martian meteorite Nakhla to better understand the magma that produced this rock. This study used laboratory methods developed at the Virginia Tech Fluids Research Lab, electron microprobe analyses, and MELTS crystallization modeling. The result of this study was a new estimate of the Nakhla parent magma composition, which is basaltic in composition. Crystallization modeling of this composition provided the closest match to mineral abundances and composition observed within the nakhlites, suggesting an improved estimate.

In addition, we studied thermal infrared data of martian craters that some workers suggest display geomorphic evidence that they once contained lakes. If in fact these craters did hold water, they may still contain evaporite minerals deposited in this environment and detectable within the thermal infrared. We used data acquired by TES (Thermal Emission Spectrometer aboard the Mars Global Surveyor) and THEMIS (Thermal Emission Imaging System aboard Mars Odyssey). Because of its higher spatial resolution, THEMIS is best viewed as a spectral unit mapper, whereas TES is better at mineral identification because of its higher spectral resolution. Both studies employed a linear deconvolution routine developed at Arizona State University, spectral ratios and newly-developed carbonate indices to search for local-scale deposits of evaporites within craters. In these studies, we did not find mineralogic evidence supporting a paleolake origin for the surficial deposits within any crater.

Table of Contents

List of Tables

Part 2

Part 3

Part 4

Part 5

List of figures

Part 2

Part 3

Part 4

Part 5

Part I

Introduction

1. Overview

Understanding of the geologic history of Mars has been bolstered in the last decade by a rapid increase (>50% by mass) in recognized Martian meteorites [e.g., *Leroux et al.*, 2004; *Sautter et al.*, 2002; *Takashi et al.*, 2001; *Taylor et al.*, 2001] as well as a wealth of data from orbiting instruments [*Albee et al.*, 2001; *Saunders et al.*, 2004] and instruments aboard rovers on the surface [*Squyres et al.*, 2004*a*; *Squyres et al.*, 2004*b*]. In addition, new advances in technology and techniques [e.g., *Bandfield and Smith*, 2003; *Fagan et al.*, 2000; *Halter et al.*, 2002; *Milam et al, 2003*; *Ruff*, 2004; *Thomas and Bodnar*, 2002] allow us to re-examine samples and data in greater detail. This dissertation involved two different approaches for studying Mars, which resulted in three individual research papers submitted to peer-reviewed journals.

2. Martian meteorites

A number of meteorite types are now recognized to be martian igneous rocks [*Treiman et al.*, 2000]. These meteorites are grouped according to their petrography as Shergottites (both basaltic and lherzolitic), Nakhlites (clinopyroxenites/wehrlites), and Chassignites (dunites) and are often referred to as the SNC meteorites. The SNC meteorites were first proposed to be from Mars because of their relatively young crystallization age of <1.3Ga [*McSween et al*., 1979; *Walker et al*., 1979; *Wasson and Wetherill*, 1979]. Large planetary bodies have lower surface-to-volume ratios, thus losing heat more slowly than do small bodies; therefore, they might be expected to retain volcanic activity longer than a smaller body. Due to both its proximity to Earth and its size, Mars was a good potential source region for these young meteorites.

Chemical analyses of martian soils by Viking landers matched well to the composition of Shergotty meteorite [*Walker et al.*, 1979]. Furthermore, the isotopic compositions and relative abundances of gases trapped in impact-melted glasses of shergottites displayed an excellent match for the unique composition of the martian atmosphere [*Becker and Pepin*, 1984; *Swindle et al.*, 1986]. In addition, the SNC meteorites define an oxygen isotopic fractionation line that is displaced from the terrestrial-lunar line as well as trends defined by other meteorites [*Clayton and Mayeda*, 1983].

Our first approach involved studying melt inclusions trapped within augite of the Martian meteorite Nakhla (the type meteorite for the nakhlites) to improve our understanding of the parental magma that formed this rock. Melt inclusions are solidified pockets of melt trapped during crystal growth. They represent the liquids from which their host crystals grew [*Anderson*, 1979; *Danyushevsky et al.*, 2002; *Sobolev*, 1996], and inclusions encapsulated at different times can provide a record of evolving melt compositions. Melt inclusions may be used to determine major and trace element concentrations and abundances of volatiles (H_2O, CO_2, Cl, S, etc.) in the melt, as well as melt density [*Lowenstern*, 1995; *Newman et al.*, 1988; *Sisson and Layne*, 1993; *Wallace et al.*, 1999].

Melt inclusions are particularly useful in reconstructing the parent melts of cumulate rocks. Nakhla is a cumulate-rich rock, enriched in augite and olivine, so the bulk rock composition is not a good estimate of Nakhla's parent magma composition [e.g., *Harvey and McSween*, 1992*a*]. Various methods have been employed to estimate the parent magma composition for Nakhla [e.g., *Harvey and McSween*, 1992*b*; *Kaneda et al.*, 1998; *Longhi*, 1991; *Treiman*, 1993; *Treiman and Goodrich*, 2001; *Varela et al.*, 2001]. Most estimates

cluster within the basalt field on the total alkali silica (TAS) classification diagram; however, other estimates range into the andesite field.

Because the melt trapped in Nahkla augite continued to crystallize after entrapment, we cannot analyze the glass phase to determine the trapped melt composition. However, heating techniques [e.g., *Sobolev et al.*, 1990; *Varela et al.*, 2001] can be used to remelt any phases that formed after entrapment, followed by rapid quenching to produce a homogeneous glass that is representative of the melt composition. I performed heating experiments to rehomogenize melt inclusions trapped in Nakhla augite and obtained major element analyses via electron microprobe. The result of this study is a new estimate of the Nakhla parent magma composition, presented in the second part of this dissertation.

3. Evaporites on Mars

The second approach involved remote sensing studies of craters that were previously described as possible paleolakes based on photogeomorphic evidence, including alternating bands of light and dark material interpreted to be possible evaporite deposits [*Cabrol and Grin*, 1999]. If Mars' early atmosphere was warm enough and the atmospheric pressure high enough, standing water could have been stable at the surface for long periods. The stability of standing water at the surface is directly relevant to the question of whether life could have arisen and persisted on early Mars [*Farmer and Des Marais*, 1999].

This approach employed thermal emission spectra collected by the TES (Thermal Emission Spectrometer aboard the Mars Global Surveyor) and THEMIS (Thermal Emission Imaging System aboard Mars Odyssey) instruments. Within the thermal infrared spectral region (1670-200-cm^{-1} or 6-50 μm), various minerals have diagnostic absorption features that

result from vibrational modes within crystal lattices [*Christensen et al.*, 1992; *Lyon*, 1965; *Lyon and Lee*, 1970; *Salisbury et al.*, 1994]. If evaporite deposits are exposed to a sufficient extent within any of the proposed paleolake basins, these deposits might be detectable in orbital thermal infrared spectra.

TES data were acquired with a spatial resolution of 3 x 6 km and a spectral resolution of 10-cm^{-1} ranging from ~200-cm^{-1} to ~1655-cm^{-1} [*Christensen*, 1999]. THEMIS data were acquired with a spatial resolution of 100 m/pixel, but only contain ten spectral bands. These bands are centered at 9 different wavelengths ranging from ~1472-cm^{-1} to ~670-cm^{-1} (~6.8-14.9 μm) [*Christensen et al.*, 2004]. Because of its higher spatial resolution, THEMIS is best viewed as a spectral unit mapper, whereas TES is better at mineral identification because of its higher spectral resolution [*Christensen et al.*, 2003]. Combined, TES and THEMIS constitute a powerful tool for studying the surface of Mars. If potential small-scale outcrops are detected within the THEMIS image, a mean spectrum from the TES pixel (or pixels) covering the outcrop region can be analyzed to determine the mineralogy. By pinpointing a potential carbonate outcrop to a single TES observation, the spectral contribution from the carbonate would be increased.

In the thermal infrared, a rock's spectrum is simply a linear mixture of its component mineral spectra [*Gillespie*, 1992; *Thomson and Salisbury*, 1993; *Ramsey and Christensen*, 1998; *Feely and Christensen*, 1999]. A technique called factor analysis was developed to utilize this linear behavior to identify atmospheric and surface spectral components present in TES emissivity spectra [*Bandfield et al*., 2000*a*]. This technique fits measured TES apparent emissivity (i.e., emissivity containing spectral contributions from both the atmosphere and

the surface) spectrum in a linear least squares sense using both atmospheric spectral shapes and surface spectral shapes simultaneously [*Bandfield et al.*, 2000*a*; *Smith et al.*, 2000].

In the TES study, I used eight previously-defined TES spectral end member spectra to deconvolve the measured TES spectra. These end members include four surface types: Syrtis-type basalt, Acidalia-type, a hematite end member [*Bandfield et al.*, 2000*b*] and a surface dust end member [*Bandfield and Smith*, 2003]. Acidalia-type has been interpreted as either an andesite [*Bandfield et al*., 2000*b*; *Hamilton and Christensen*, 2000] or as partly weathered basalt [*Wyatt and McSween*, 2002; *Kraft et al.*, 2003; *Ruff*, 2004]. There are also four atmospheric end members referred to as 1) low CO_2 dust, 2) high CO_2 dust, 3) water ice $cloud_1$ and 4) water ice $cloud_2$ [*Bandfield et al.*, 2000*b*].

I also used spectral ratios to determine which end members provide the best model to measured spectra from large craters on the *Cabrol and Grin* [1999] list of possible paleolakes. In addition, I developed "carbonate indices" that are tuned to be sensitive to two carbonate absorptions and their relative band depths. This study, presented as the third and fourth part of this dissertation, did not find mineralogic evidence supporting a paleolake origin for surficial deposits within these craters.

In the THEMIS study, small scale spectral variations were identified using THEMIS images of basins within the Aeolis quadrangle of Mars. Where overlapping TES data existed, TES spectra were obtained and evaluated using linear deconvolution, spectral ratios and the carbonate indices. I evaluated both the TES and THEMIS spectra to assess what spectral end members best modeled the measured spectra. This study, presented as the fifth part of this dissertation, also did not find mineralogic evidence supporting a paleolake origin for the surficial deposits within craters of the Aeolis quadrangle.

4. Summary

Although these approaches are quite different, they address fundamental issues regarding the geologic history of Mars. First, by improving our estimates of parent magma compositions for Martian meteorites, we can enhance our understanding of the mantle which partially melted to produce the volcanic surface of Mars. A better understanding of magma compositions might even help clarify the evolutionary history of the early Martian atmosphere [Owen, 1992]. Second, by searching for evaporites and other water-derived minerals on the surface of Mars, we can provide additional constraints regarding the role of water in shaping and altering the planet's surface.

References cited

Albee, A.L., R.E. Arvidson, F. Palluconi, and T. Thorpe, Overview of the Mars Global Surveyor mission, *Journal of Geophysical Research*, 106 (E10), 23291-23316, 2001.

Anderson, A.T., Jr., Water in some hypersthenic magmas, *Journal of Geology*, 87 (5), 509-531, 1979.

Bandfield, J.L., and M.D. Smith, Multiple emission angle surface-atmosphere separations of Thermal Emission Spectrometer data, *Icarus*, *161*, 47-65, 2003.

Bandfield, J.L., P.R. Christensen, and M.D. Smith, Spectral data set factor analysis and end-member recovery: Application to analysis of Martian atmospheric particulates, *Journal of Geophysical Research*, *105* (E4), 9573-9587, 2000*a*.

Bandfield, J.L., V.E. Hamilton, and P.R. Christensen, A global view of Martian surface compositions from MGS-TES, *Science*, *287* (5458), 1626-1630, 2000*b*.

Becker, R.H., and R.O. Pepin, The case for a martian origin of the shegottites: Nitrogen and noble gases in EETA79001, *Earth and Planetary Science Letters*, *69*, 225-242, 1984.

Cabrol, N.A., and E.A. Grin, Distribution, Classification, and Ages of Martian Impact Crater Lakes, Icarus, 142, 160-172, 1999.

Christensen, P.R., Introduction to the special section: Mars Global Surveyor Thermal Emission Spectrometer, *Journal of Geophysical Research*, 105 (E4), 9507, 1999.

Christensen, P.R., D.L. Anderson, S.C. Chase, R.N. Clark, H.H. Kieffer, M.C. Malin, J.C. Pearl, J. Carpenter, N. Bandiera, F.G. Brown, and S. Silverman, Thermal Emission Spectrometer Experiment - Mars-Observer Mission, *Journal of Geophysical Research*, 97 (E5), 7719-7734, 1992.

Christensen, P.R., B.M. Jakosky, H.H. Kieffer, M.C. Malin, H.Y. McSween, Jr., K.H. Nealson, G.L. Mehall, S. Silverman, S. Ferry, M. Caplinger, and M. Ravine, The Thermal Emission Imaging System (THEMIS) for the Mars 2001 Odyssey Mission, *Space Science Reviews*, 110 (1-2), 85-130, 2004.

Christensen, P.R., J.L. Bandfield, J.F. Bell, III, N. Gorelick, V.E. Hamilton, A. Ivanov, B.M. Jakosky, H.H. Kieffer, M.D. Lane, M.C. Malin, T. McConnochie, A.S. McEwan, H.Y. McSween, Jr., G.L. Mehall, J.E. Moersch, K.H. Nealson, J. Rice, W., Jr., M.I. Richardson, S.W. Ruff, M.D. Smith, T.N. Titus, and M.B. Wyatt, Morphology and Composition of the Surface of Mars: Mars Odyssey THEMIS Results, *Science*, 300, 2056-2061, 2003.

Clayton, R.N., and T.K. Mayeda, Oxygen isotopes in eucrites, shergottites, nakhlites and chassignites, *Earth and Planetary Science Letters*, *62*, 1-6, 1983

Danyushevsky, L.V., A.W. McNeill, and A.V. Sobolev, Experimental and petrological studies of melt inclusions in phenocrysts from mantle-derived magmas: An overview of techniques, advantages and complications, *Chemical Geology*, 183 (1-4), 5-24, 2002.

Fagan, T.J., E.R.D. Scott, K. Keil, T.F. Cooney, and S.K. Sharma, Formation of feldspathic and metallic melts by shock in enstatite chondrite Reckling Peak A80259, *Meteoritics and Planetary Science*, 35 (2), 319-329, 2000.

Farmer, J.D., and D.J. Des Marais, Exploring for a record of ancient Martian life, *Journal of Geophysical Research*, 104 (E11), 26977-26995, 1999.

Feely, K.C., and P.R. Christensen, Quantitative compositional analysis using thermal emission spectroscopy: Application to igneous and metamorphic rocks, *Journal of Geophysical Research*, *104* (E10), 24195-24210, 1999.

Gillespie, A.R., Spectral mixture analysis of multispectral thermal infrared images, *Remote Sensing of Environment*, *42* (2), 137-145, 1992.

Halter, W.E., T. Pettke, C.A. Heinrich, and B. Rothen-Rutishauser, Major to trace element analysis of melt inclusions by laser-ablation ICP-MS; Methods of quantification, *Chemical Geology*, 183 (1-4), 63-86, 2002.

Hamilton, V.E., and P.R. Christensen, Determining the modal mineralogy of mafic and ultramafic igneous rocks using thermal emission spectroscopy, *Journal of Geophysical Research*, *105* (E4), 9717-9733, 2000.

Harvey, R.P., and H.Y. McSween, Jr., The petrogenesis of the nakhlites: Evidence from cumlate mineral zoning*, Geochimica et Cosmochimica Acta*, 56, 1655-1663, 1992a.

Harvey, R.P., and H.Y. McSween, Jr., The parent magma of the nakhlite meteorites: Clues from melt inclusions, *Earth and Planetary Science Letters*, 111 (2-4), 467-482, 1992b.

Kaneda, K., G.A. McKay, and L. Le, Synthetic and natural pyroxenes: A close match at last, in *Lunar Planet. Sci*., pp. #1620, Lunar and Planetary Institute, Houston, TX, USA, 1998.

Kraft, M.D., J.R. Michalski, and T.G. Sharp, Effects of pure silica coatings on thermal emission spectra of basaltic rocks: Considerations for Martian surface mineralogy, *Geophysical Research Letters*, *30* (24), 2288, doi: 10.1029/ 2003GL018848., 2003.

Leroux, H., B. Devouard, P. Cordier, and F. Guyot, Pyroxene microstructure in the Northwest Africa 856 Martian meteorite, *Meteoritics and Planetary Science*, 39 (5), 711-722, 2004.

Longhi, J., Comparative liquidus equilibria of hypersthene-normative basalts at low pressure, *American Mineralogist*, 76 (5-6), 785-800, 1991.

Lowenstern, J.B., Application of silicate-melt inclusions to the study of magmatic volatiles, in *Magmas, fluids and ore deposition*, edited by J.F.H. Thompson, pp. 71-98, Mineralogical Association of Canada, Short Course Series, Toronto, ON, Canada, 1995.

Lyon, R.J.P., Analysis of rocks by spectral infrared emission (8-25 μm), *Economic Geology*, 60 (4), 715-736, 1965.

Lyon, R.J.P., and K. Lee, Remote sensing in exploration for mineral deposits, *Economic Geology*, 65 (7), 785-800, 1970.

McSween, H.Y., Jr., E.M. Stolper, L.A. Taylor, R.A. Muntean, G. O'Kelley, J.S. Eldridge, S. Biswas, T. Ngo, and M.E. Lipschutz, Petrogenetic relationship between Allan Hills 77005 and other achondrites, *Earth and Planetary Science Letters*, *45*, 275-284, 1979.

Milam, K.A., K.R. Stockstill, J.E. Moersch, H.Y. McSween, Jr., L.L. Tornabene, A. Ghosh, M.B. Wyatt, and P.R. Christensen, THEMIS Characterization of the MER Gusev Crater Landing Site, *Journal of Geophysical Research*, 108 (E12), 19-1-19-24, 2003.

Newman, S., S. Epstein, and E. Stolper, Water, carbon dioxide, and hydrogen isotopes in glasses from the ca. 1340 eruption of Mono Craters, CA: Constraints on degassing phenomena and initial volatile content, *Journal of Volcanology and Geothermal Research*, 35 (1-2), 75-96, 1988.

Owen, T., The Composition and Early History of the Atmosphere of Mars, in *Mars*, edited by H.H. Kieffer, B.M. Jakosky, C.W. Snyder, and M.S. Matthews, pp. 818-834, The University of Arizona Press, Tucson, 1992.

Ramsey, M.S., and P.R. Christensen, Mineral abundance determination: Quantitative deconvolution of thermal emission spectra, *Journal of Geophysical Research*, *103* (B1), 577-596, 1998.

Ruff, S.W., Spectral evidence for zeolites in the dust on Mars, *Icarus*, *168*, 131-143, 2004.

Salisbury, J.W., A. Wald, and D.D. Aria, Thermal-infrared remote sensing and Kirchhoff's law; 1, Laboratory measurements, *Journal of Geophysical Research*, 99 (6), 11897-11911, 1994.

Saunders, R.S., R.E. Arvidson, G.D. Badhwar, W.V. Boynton, P.R. Christensen, F.A. Cucinotta, W.C. Feldman, R.G. Gibbs, C. Kloss, Jr., M.R. Landano, R.A. Mase, G.W. McSmith, M.A. Meyer, I.G. Mitrofanov, G.D. Pace, J.J. Plaut, W.P. Sidney, D.A. Spencer, T.W. Thompson, and C.J. Zeiten, 2001 Mars Odyssey Mission Summary, *Space Science Reviews*, 110 (1-2), 1-36, 2004.

Sautter, V., J.A. Barrat, A. Jambon, J.P. Lorand, P. Gillet, M. Javoy, J.L. Joron, and M. Lesourd, A new Martian meteorite from Morocco: The nakhlite North West Africa 817, *Earth and Planetary Science Letters*, 195 (3-4), 223-238, 2002.

Sisson, T.W., and G.D. Layne, H2O in basalt and basaltic andesite glass inclusions from four subduction-related volcanoes, *Earth and Planetary Science Letters*, 117 (3-4), 619-635, 1993.

Smith, M.D., J.L. Bandfield, and P.R. Christensen, Separation of atmospheric and surface spectral features in Mars Global Surveyor Thermal Emission Spectrometer (TES) spectra, *J. Geophys. Res.*, *105* (E4), 9589-9607, 2000.

Sobolev, A.V., Melt inclusions in minerals as a source of principal petrologic information, *Petrologiya*, 4 (3), 228-239, 1996.

Sobolev, A.V., V.S. Kamenetskiy, N. Metrich, R. Clocchiatti, N.N. Kononkova, A.L. Devirts, and V.I. Ustinov, Volatile regime and crystallization conditions in Etna hawaiite lavas, *Geokhimiya*, 9, 1277-1290, 1990.

Squyres, S.W., J.P. Grotzinger, R.E. Arvidson, J.F. Bell, III, W.M. Calvin, P.R. Christensen, B.C. Clark, J.A. Crisp, W.H. Farrand, K.E. Herkenhoff, J.R. Johnson, G. Klingelhöfer, A.H. Knoll, S.M. McLennan, H.Y. McSween, Jr., R.V. Morris, J. Rice, W., Jr., R. Rieder, and L.A. Soderblom, In Situ Evidence for an Ancient Aqueous Environment at Meridiani Planum, Mars, *Science*, 306 (5702), 1709-1714, 2004*a*.

Squyres, S.W., R.E. Arvidson, J.F. Bell, III, J. Brückner, N.A. Cabrol, W.M. Calvin, M.H. Carr, P.R. Christensen, B.C. Clark, L. Crumpler, D.J. Des Marais, C. d'Uston, T. Economou, J.D. Farmer, W. Farrand, W. Folkner, M. Golombek, S. Gorevan, J.A. Grant, R. Greeley, J. Grotzinger, L. Haskin, K.E. Herkenhoff, S. Hviid, J.R. Johnson, G. Klingelhöffer, A. Knoll, G. Landis, M. Lemmon, R. Li, M.B. Madsen, M.C. Malin, S. McLennan, H.Y. McSween, Jr., D.W. Ming, J.E. Moersch, R.V. Morris, T. Parker, J. Rice, W., Jr., L. Richter, R. Rieder, M. Sims, M.D. Smith, P. Smith, L.A. Soderblom, R. Sullivan, A. Wald, H. Wänke, T. Wdowiak, M.J. Wolff, and A. Yen, The Spirit Rover's Athena Science Investigation at Gusev crater, Mars,, *Science*, 305 (5685), 794-799, 2004*b*.

Swindle, T.D., M.W. Caffee, and C.M. Hohenberg, Xenon and other noble gases in shergottites, *Geochimica et Cosmochimica Acta*, *50*, 1001-1015, 1986.

Takashi, M., M. Miyamoto, and G.A. McKay, Mineralogy and petrology of the Dar al Gani 476 martian meteorite; implications for its cooling history and relationship to other shergottites, *Meteoritics and Planetary Science*, 36 (4), 531-548, 2001.

Taylor, L.A., M.A. Nazarov, C.K. Shearer, H.Y. McSween, Jr., J. Cahill, C.R. Neal, M.A. Ivanova, L.D. Barsukova, R.C. Lentz, R.N. Clayton, and T.K. Mayeda, Martian meteorite Dhofar 019; a new shergottite, *Meteoritics and Planetary Science*, 37 (8), 1107-1128, 2001.

Thomas, J.B., and R.J. Bodnar, A technique for mounting and polishing melt inclusions in small (<1mm) crystals, *American Mineralogist*, 87 (10), 1505-1508, 2002.

Thomson, J.L., and J.W. Salisbury, The mid-infrared reflectance of mineral mixtures (7–14 μm), *Remote Sensing of Environment*, *45* (1), 1-13, 1993.

Treiman, A.H., The parent magma of the Nakhla (SNC) meteorite, inferred from magmatic inclusions, Geochimica et Cosmochimica Acta, 57 (19), 4753-4767, 1993.

Treiman, A.H., and C.A. Goodrich, A parent magma for the Nakhla martian meteorite: Reconciliation of estimates from 1-bar experiments, magmatic inclusions in olivine, and magmatic inclusions in augite, in *Lunar Planet. Sci*., pp. #1107, Lunar and Planetary Institute, Houston, TX, 2001.

Treiman, A.H., J.D. Gleason, and D.D. Bogard, The SNC meteorites are from Mars, *Planetary and Space Science*, *48*, 1213-1230, 2000.

Varela, M.E., G. Kurat, and R. Clocchiatti, Glass-bearing inclusions in Nakhla (SNC meteorite) augite: Heterogeneously trapped phases, *Mineralogy and Petrology*, 71 (3-4), 155-172, 2001.

Walker, D., E.M. Stolper, and J.F. Hays, Basaltic volcanism: The importance of planet size, *Proceedings of the Lunar and Planetary Science Conference*, *10*, 1995-2015, 1979.

Wallace, P.J., A.T. Anderson, Jr., and A.M. Davis, Gradients in H2O, CO2, and exsolved gas in a large-volume silicic magma system: Interpreting the record preserved in melt inclusions from the Bishop Tuff, *Journal of Geophysical Research*, 104 (9), 20097-20122, 1999.

Wasson, J.T., and G.W. Wetherill, Dynamical, chemical and isotopic evidence regarding the formation locations of asteroids and meteorites, in *Asteroids*, edited by T. Gehrels, pp. 926-974, University of Arizona Press, Tucson, 1979.

Wyatt, M.B., and H.Y. McSween, Jr., Spectral evidence for weathered basalt as an alternative to andesite in the northern lowlands of Mars, *Nature*, *417* (6886), 263-266, 2002.

Part 2

Melt inclusions in augite of the Nakhla martian meteorite: Evidence for basaltic parental melt

This chapter is a reformatted version of a paper by the same name published in Meteoritics and Planetary Science in 2005 by Karen Renée Stockstill, Harry Y. McSween, Jr. and Robert J. Bodnar.

Stockstill, K.R., McSween, Jr., H.Y., and Bodnar, R.J., Melt inclusions in augite of the Nakhla martian meteorite: Evidence for basaltic parental melt, *Met. Planet. Sci.*, 40 (3), 377–396.

Abstract

Nakhla contains crystallized melt inclusions trapped in augite and olivine when these phases originally formed on Mars. Our study involved rehomogenization (slow- and fast-heating) experiments on multiphase melt inclusions in Nakhla augite. We studied melt inclusions trapped in augite because this phase re-equilibrated with the external melt to a lesser extent than olivine and results could be directly compared with previous Nakhla melt inclusion studies. Following heating and homogenization of encapsulated melt inclusions, single mineral grains were mounted and polished to expose inclusions. Major element chemistry was determined by electron microprobe. The most primitive melt inclusion analyzed in Nakhla, NA03, is basaltic and closely matches previously reported nakhlite parent melt compositions.

MELTS equilibrium and fractional crystallization models calculated for NA03 and previous Nakhla parent melt estimates at QFM and QFM-1 produced phase assemblages and compositions that can be compared to Nakhla. Of these models, equilibrium crystallization of NA03 at QFM-1 produced the best match to mineral phases and compositions in Nakhla. In all models, olivine and augite co-crystallize, consistent with the hypothesis that olivine is not xenocrystic but has undergone subsolidus re-equilibration. In addition, measured melt inclusion compositions plot along the MELTS-

calculated liquid line of descent and may represent pockets of melt trapped at various stages during crystallization. We attempt to resolve discrepancies between previous estimates of the Nakhla parental melt composition and to reinterpret the results of a previous study of rehomogenized melt inclusions in Nakhla. Melt inclusions demonstrate that Nakhla is an igneous rock whose parent melt composition and crystallization history reflect planetary igneous processes.

1. Introduction and background

Melt inclusions are solidified pockets (usually with diameters of a few hundred μm or less) of melt trapped during crystal growth. They represent the liquids from which their host crystals grew [*Anderson*, 1979; *Roedder*, 1979; *Sobolev*, 1996; *Frezzotti*, 2001; *Danyushevsky et al.*, 2002*a*], and inclusions encapsulated at different times can provide a record of evolving melt compositions. Melt inclusions may be used to determine major and trace element concentrations and abundances of volatiles (H_2O, CO_2, Cl, S, etc.) in the melt, as well as melt density [*Newman et al.*, 1988; *Sisson and Layne*, 1993; *Lowenstern*, 1995; *Wallace et al.*, 1999]. They are particularly useful in reconstructing the parent melts of cumulate rocks.

Unhomogenized melt inclusions in augite and olivine of nakhlite meteorites (thought to be martian igneous rocks, as reviewed by *Treiman et al.* [2000]) contain an assortment of daughter crystals (including the host phase that forms on the walls of the inclusion) that grew after the melt was trapped (Figure 1). (Note: All figures and tables within a chapter will follow that chapter in an appendix.) These are commonly referred to as multiphase or crystallized inclusions to distinguish them from glassy inclusions.

Multiphase melt inclusions in augite range from <10 to 75 μm; however, inclusions > 20 μm are rare. Their shapes vary from negative crystal morphologies to rounded. Multiphase melt inclusions commonly occur in clusters, rather than individually, and are ubiquitous in most augite grains (Figure 1a). The post-entrapment daughter mineral visible during petrographic examination of the inclusions is an Fe-Ti oxide (due to its reflectivity, this phase is visually distinct from the glass of the inclusion and the surrounding host mineral). In addition, augite precipitated on the inclusion walls following entrapment of the melt– material that is not visibly distinct via petrographic inspection. Bubble voids, either formed by shrinkage (due to volume change of glass during cooling) or representing volatiles exsolved from the melt during cooling, are also observable. The bubble voids represent only a few percent of the inclusion volume [*Lowenstern*, 1995]. To obtain a homogeneous glass for electron microprobe analysis, it is necessary to heat multiphase inclusions to redissolve the daughter phases. Once the melt inclusion is rehomogenized, the sample can be quenched to produce a glass, at which point it can be referred to as a *melt inclusion*.

Previous workers have estimated the composition of nakhlite parental melts by a variety of techniques. *Longhi and Pan* [1988] calculated major element oxide concentrations in the melt using augite-liquid partition coefficients from experiments that produced Nakhla-like augites, constraining the melt to lie on or near the olivine-augite liquidus, and using the composition of Nakhla augite cores to locate it along the liquidus. This composition plots within the basalt field on the total alkali-silica (TAS) diagram (Figure 2a) and within the augite field on the olivine (projection)-orthopyroxene-wollastonite-plagioclase phase diagram (Figure 2b). *Harvey and McSween* [1992*a*]

analyzed glass and daughter minerals in multiphase melt inclusions in olivine grains of Nakhla and Governador Valadares and employed mass-balance calculations to estimate the original melt inclusion composition. Like *Longhi and Pan* [1988], they considered only compositions that fell on or near the augite-olivine phase boundary to be representative of the parent liquid. Their favored composition for Nakhla falls in the TAS basalt field (Figure 2a), and within the augite field of the olivine projection (Figure 2b). *Treiman* [1993] studied multiphase melt inclusions from Nakhla olivine as well, but used rastered or defocused-beam electron microprobe analyses to determine the bulk composition of the largest melt inclusions. A weighted average of these compositions was calculated, followed by olivine subtraction to account for host olivine analyzed by the rastered beam, and finally addition of daughter olivine that plated out on the walls of the inclusion following entrapment. Then, this composition was adjusted to be in equilibrium with co-existing augite cores and thus to liquids co-saturated with augite and olivine. The final parental melt composition plots within the TAS basalt field (Figure 2a) and within the augite field of the olivine projection (Figure 2b). *Treiman* [1993] also recalculated the estimates of *Longhi and Pan* [1988] using a new average analysis of Nakhla core augite to produce a second composition, which plots within the TAS basalt field (Figure 2a) with low total alkali content (1.5%) and plots within the augite field on the olivine projection (Figure 2b). *Kaneda et al.* [1998] estimated the Nakhla parental melt composition from compositions used in their crystallization experiments. These experiments produced augites that exhibited the natural core compositions and the zoning patterns seen in Nakhla pyroxenes. The starting composition that produced the best match to Nakhla pyroxenes plots within the TAS basalt field near other estimates of

nakhlite parental melts (Figure 2a), but within the silica field on the olivine projection (Figure 2b). *Treiman and Goodrich* [2001] revised the Nakhla parent magma composition of *Treiman* [1993], principally by adjusting its (Fe, Mg)O content. Their preferred composition, NK01, plots in the TAS basalt field near other estimates (Figure 2a) and within the augite field on the phase diagram (Figure 2b). NK01 is the most recent and probably most accepted value of the Nakhla parent melt composition.

The only previous study of homogenized melt inclusions in Nakhla was preformed by *Varela et al.* [2001]. Their average composition of six heated melt inclusions in Nakhla augites (GH(6) in Figure 2a and b) was not in equilibrium with the host augite nor with co-existing olivine, and they questioned the accepted igneous origin of this meteorite. However, it is not clear that this average value can be representative of an actual trapped melt, as discussed below. Their study also showed heterogeneity in alkali contents among the melt inclusions. The experiments produced glasses with compositions ranging from basalt to andesite on the TAS diagram (Figure 2a) and plotting across several fields on the olivine projection (Figure 2b). Because of the lack of equilibrium and the variation in alkali contents, *Varela et al.* [2001] suggested that glass-bearing inclusions in Nakhla augite are most likely heterogeneously trapped liquids and solids formed through nebular (non-igneous) processes.

The estimates of nakhlite parental magma compositions described above show wide variation. Because these meteorites contain cumulus phases [*McSween*, 1994], their bulk compositions do not necessarily represent melt compositions [*Longhi and Pan*, 1988]. As part of this study, we reproduced the slow-heating homogenization experiments of Varela *et al.* (2001) on melt inclusions in Nakhla augite. However,

several workers [*Sobolev et al.*, 1990; *Qin et al.*, 1992; *Nielsen et al.*, 1998; *Danyushevsky et al.*, 2002*a*] have called attention to problems with host-inclusion mass exchange associated with slow heating rates, which will be discussed in detail below. Thus, we also performed fast-heating homogenization experiments on melt inclusions in Nakhla augite. The major objectives of this study were to use rehomogenized melt inclusions to 1) better constrain the parental melt compositions for Nakhla, and 2) resolve the question of whether Nakhla is an igneous rock, as believed by most previous workers, or a nebular conglomerate, as proposed in the melt inclusion study of Varela *et al.* (2001).

2. Sample preparation, experimental and analytical methods

An unweathered, pea-sized sample of Nakhla was obtained from the British Museum for melt inclusion studies. Doubly-polished "thick" sections (75 - 100 μm thick) were produced and then removed from glass slides by soaking in an acetone bath for several hours. Mineral grains were separated under a binocular microscope and examined at high power. Augite grains containing inclusions of sufficient size (i.e., electron microprobe analysis requires melt inclusions ≥ 10 μm) were isolated for heating experiments. Melt inclusions in these grains were completely enclosed by the host phase.

Melt inclusions in Nakhla are found within both augite and olivine. We chose to focus on melt inclusions in augite. The open-system behavior of olivine-hosted melt inclusions with respect to Fe/Mg exchange is well established [e.g., *Gaetani and Watson*, 2000; *Danyushevsky et al.*, 2002*b*], and nakhlite olivine appears to have re-equilibrated with the external melt to a greater degree than the co-existing augite [e.g., *Longhi and*

Pan, 1988; *Harvey and McSween*, 1992*a*]. The augites have nearly homogeneous cores ($Wo_{38-41}En_{37-40}Fs_{22-23}$ and Fe/Mg=0.55-0.62) and narrow rims that are zoned with increasing Fe/Mg ratios ($Wo_{33-41}En_{21-37}Fs_{26-44}$ and Fe/Mg=0.70-1.97) [*McSween and Treiman*, 1998; *Friedman Lentz et al.*, 1999; *Sautter et al.*, 2002]. Augite cores appear to have preserved their original magmatic composition [*Harvey and McSween*, 1992*b*], so augite-hosted inclusions should be closer to their original trapped composition. Furthermore, studying augite-hosted melt inclusions allows for direct comparison with the work of *Varela et al.* [2001].

The heating schedule is important during homogenization of multiphase melt inclusions. If the inclusions are heated too quickly, they may rupture or leak along fractures. If they are not held at high temperature for a sufficient length of time, the melt may not reach equilibrium with the host phase. Conversely, if the sample is heated too slowly or held at high temperature too long, the minerals may oxidize and become dark, precluding visual monitoring of the melting process, or excessive amounts of the host crystal may be incorporated into the melt. In addition, *Sobolev et al.* [1990] demonstrated that, with slow heating, mass exchange can occur between the inclusion and the host crystal. In particular, diffusion of hydrogen through the inclusion wall allows water to combine with FeO to produce titanomagnetite. Thus, even if the external atmosphere is reduced during heating, oxidation of the melt occurs. For experiments on Etna hawaiites, this process oxidized the enclosed melt inclusion and increased the homogenization temperature by 100° to 150°C [*Sobolev et al.*, 1990]. The net result is a change in the oxidation state of the trapped melt, thus affecting equilibrium between the host phase and the melt inclusion.

We first performed heating experiments similar to those of *Varela et al.* [2001] with slow heating rates (between 1° to 12° per minute, with slower rates at higher temperatures). The sample was held at the homogenization temperature (~1150ºC) for 20 minutes. Slow-heating experiments were performed in a Vernadsky high-temperature microscope heating stage at Virginia Tech. To avoid oxidation, the samples were heated in an atmosphere of He that had been de-oxygenated by passing over Ti metal at 600°C. The samples were placed on a mineral (olivine, pyroxene or sapphire) plate to facilitate their removal from the heating stage following each experiment. With this stage, the sample was visually monitored during the heating experiment.

Homogenization of the melt inclusion was considered complete when daughter crystals were resorbed and the shrinkage bubble was reduced significantly in size. The bubbles never completely disappeared, perhaps due to a difference in pressure conditions between the experiment and the original entrapment [*Lowenstern*, 1995]. Although this technically represents partial homogenization, *Fedele et al.* [2003] demonstrated that the melt inclusion composition is not affected by a remnant shrinkage bubble as long as all daughter phases are resorbed. Therefore, we will use the term homogenized to describe melt inclusions that have resorbed the daughter crystals leaving only a glassy phase and the remnants of a bubble. When the inclusion was homogenized completely, the temperature was recorded and the sample was quenched by switching off the power supply, allowing the temperature to drop rapidly. In a Vernadsky heating stage, the average cooling rate during quenching from a maximum temperature of 800ºC in a He atmosphere is up to 500º/sec [*Sobolev and Slutskiy*, 1984]. The samples were cooled to

several hundred degrees below the melting temperature in a few seconds, thus minimizing the possibility that compositional re-equilibration may have occurred.

In addition, fast-heating experiments were conducted in a 1-atmosphere tube furnace at Virginia Tech. Samples were placed within a platinum capsule with a drop of immersion oil covering the sample to prevent oxidation. The platinum capsule, suspended on a platinum wire, was lowered into a silica glass tube within the furnace. Samples were heated to the desired temperature in ~2 min and held at that temperature for 3 to 5 min, as suggested by *Sobolev et al.* [1990]. The capsule was then removed from the furnace and immediately quenched in water.

Homogenization temperatures were determined by step-heating the samples. The samples were heated to 1100°C, removed, and the melt inclusions were examined under a microscope. If a melt inclusion was not completely homogenized, the sample was heated to a temperature 10-20º higher than in the previous step and re-examined. This process was repeated until the melt inclusion was homogenized.

Following the heating experiments, the grains were mounted on the ends of silica glass rods and the (homogenized) melt inclusions were exposed at the surface by carefully polishing down to the level of the melt inclusion [*Thomas and Bodnar*, 2002]. The major and minor elemental (Na, K, Mg, Al, Cr, Si, P, K, Ca, Ti, Mn, and Fe) compositions of the melt inclusions and their hosts were measured on a Cameca SX-50 electron microprobe at Virginia Tech (Table 1). Previous work by *Fagan et al.* [2000] on glass analyses showed that using an accelerating voltage of 15 kV, a current of 2 nA and a defocused beam (5 to 10 μm) minimizes loss of Na, and so these instrumental conditions were employed in this study. In addition, Na was always analyzed first to

minimize its loss during exposure to the beam. Counting times range from 40 sec (for K, Na, and Ca) to 70 sec (for Mn and Cr), with all other elements being analyzed for 60 sec.

In this study, eight melt inclusions (each within a separate Nakhla augite grain) were successfully homogenized, remounted, exposed and analyzed by electron microprobe. Three melt inclusions were homogenized using the slow-heating method and five melt inclusions were homogenized using the fast-heating method. For melt inclusions of sufficient size, multiple analyses were obtained on different spots to assure homogeneity of the glass. Table 1 and related figures show representative compositions as measured using electron microprobe. In addition, Table 1 also presents information regarding the size, homogenization temperature and phases present in the final quenched inclusion. If a quenched inclusion contains an oxide, this phase probably represents an oxide that was melted during heating, but then re-precipitated during the quenching process.

3. Results

The composition of rehomogenized melt inclusions from our heating experiments (Table 1) are plotted on the TAS classification diagram (Figure 3a) and on the olivine projection (Figure 3b). Melt inclusion compositions range from basalt to dacite, spanning a range of SiO_2 similar to the melt inclusions of *Varela et al.* [2001]. In Figure 3b, the melt inclusion compositions plot within the augite, pigeonite and silica fields in both projections. The most primitive (i.e., lowest SiO_2) melt inclusion in Nakhla augite (NA03) plots within the basalt field on the TAS diagram (Figure 3a) and within the augite field on the olivine projection (Figure 3b). This melt inclusion plots close to some

previous estimates of Nakhla parental melt compositions, as well as the most primitive melt inclusion (GHa) of *Varela et al.* [2001] (compare Figures 2 and 3).

For a given silica content, inclusions homogenized by fast heating show lower abundances of alkalis than inclusions homogenized by slow heating. However, the low alkali contents of the two most evolved (highest silica) fast-heated inclusions may be due to loss of alkalis during heating and/or analyses. Omitting these most evolved inclusions, the remaining inclusions homogenized by both slow- and fast-heating form a distinct trend on the TAS diagram (Figure 3a). In addition, on an olivine projection diagram (Figure 3b), these two fast-heated inclusions project into the silica field suggesting that they should contain both olivine and silica and cannot represent equilibrium compositions.

Should these two high-silica compositions be disregarded? Figure 4 displays melt inclusion compositions from this study as well as those from *Varela et al.* [2001] on Harker variation diagrams. On these diagrams, these two compositions fall close to linear trends for fast-heated melt inclusions for some oxides (e.g., Al_2O_3, FeO and MnO) and behave as expected (increasing Al_2O_3, decreasing FeO and MgO) for crystallization of phases observed within Nakhla (e.g., augite, olivine, Fe-Ti oxide). However, for other oxides, the trends of rapidly heated melt inclusions appear flat (K_2O, CaO, and MgO) or do not co-vary as expected (Na_2O decreases while TiO_2 is erratic) (Figure 4). If we disregard the two high-silica melt inclusions from the fast heating experiments, the trends for the remaining (both fast- and slow-heated) inclusions improve. We conclude that these two points are affected by alkali loss during heating and we will disregard them in the remaining discussion.

The difference in the final homogenization temperature between the slow-heating vs. fast-heating experiments was small, with only 20°C higher homogenization temperatures for the fast-heating experiments (Table 1). In addition, the compositions of melt inclusions that were rapidly heated extend to more primitive compositions compared to those that were heated more slowly (Figure 4). However, we must also examine whether each melt inclusion was in equilibrium with co-existing minerals at solidus temperatures. Equilibrium temperatures between each melt inclusion and co-existing mineral phases (clinopyroxene, olivine and plagioclase) were calculated using the PETROLOG software (A. Sobolev, *pers. comm*., 2004; http://www.geol.utas.edu.au/~leonid/Petrolog.html). The melt inclusions that were homogenized by the slow-heating technique are in equilibrium with host augite at subsolidus temperatures (<1100ºC), while inclusions that were heated by the fast-heating technique are in equilibrium with host augite at higher temperatures (~1140-1160ºC) (A. Sobolev, *pers. comm.*, 2004). This suggests that the slow heating inclusions did not remain in equilibrium with the host augite during the heating experiment, while the fast-heating inclusions did remain in equilibrium. Furthermore, only our most primitive melt inclusion, NA03, is saturated with both augite and olivine at high temperatures (A. Sobolev, *pers. comm*., 2004).

4. Discussion

4.1. MELTS modeling of melt inclusion compositions

Compositions of melt inclusions within Nakhla augite extend into the andesite and trachydacite fields (Figure 3a). These more evolved compositions may represent

pockets of melt that were trapped later in the crystallization history of the rock. Several questions arise when considering this possibility: (1) Did augite continue to crystallize long enough to trap such highly evolved melts? (2) If so, what composition of augite was in equilibrium with the most evolved melt inclusion and how does this match the observed range of augite compositions in Nakhla? (3) Do these melt inclusions fall along a reasonable liquid line of descent? In an attempt to answer these questions, results from the melt inclusion study were compared with those predicted by crystallization modeling using MELTS [*Ghiorso and Sack*, 1995]. In addition, measured phase abundances and compositions in Nakhla can be directly compared to those predicted by MELTS to determine which starting composition best matches the Nakhla parent melt composition. We compared the most primitive melt inclusion from this study (NA03) with the currently accepted Nakhla parent magma composition (NK01) of *Treiman and Goodrich* [2001]. These starting compositions were input into MELTS to obtain crystallization sequences for both fractional and equilibrium crystallization (Table 2).

The oxidation state under which Nakhla crystallized is not well constrained. The intrinsic oxygen fugacity measurements of *Delano and Arculus* [1980] suggest Nakhla crystallized under reducing conditions near the iron-wüstite buffer, but this interpretation is not generally accepted for nakhlites. Moreover, MELTS crystallization modeling at the iron-wüstite buffer does not produce a mineral assemblage that matches the Nakhla mineral assemblage [*Slater et al.*, 2003]. Compositions of coexisting Fe-Ti oxides (magnetite and ilmenite) in Nakhla are consistent with an oxidation state of $fO_2 = 10^{-17}$ at 740ºC, just below the quartz-fayalite-magnetite buffer, at QFM-0.4 log units [*Reid and Bunch*, 1975]. More recently, *Szymanski et al*. [2003] constrained the oxygen fugacity of

nakhlites using 1) activities of magnetite in spinel and of hematite in ilmenite after *Ghiorso and Sack* [1991] and 2) the Ca-QUILF model [*Andersen et al.*, 1993]. The temperature and log fO_2 determined by these two methods were 1) T=824ºC and QFM-0.20 log units and 2) T=795ºC and QFM+0.14 log units, with the absolute error of the oxygen fugacity estimates of ±0.5 log units.

We ran MELTS at both QFM and QFM-1 as bounding conditions for the modeling. We first obtained the liquidus temperature for an individual run and then began crystallization runs 10ºC above the liquidus. Equilibrium crystallization was modeled in 10º temperature steps, stopping at 900ºC. Fractional crystallization was also modeled in 10º intervals; however, it was not always possible to continue fractional crystallization down to 900ºC, possibly due to problems when applying the MELTS program outside its calibrated compositional range (i.e., for Fe-rich melts, as noted by *Hale et al.* [1999]). In these cases, modeling was terminated at higher temperatures.

4.1.1. Duration of augite crystallization

The crystallizing phases and corresponding temperature ranges for models using NA03 from this study are shown in Figure 5a. In equilibrium crystallization models, augite crystallized through all time steps, whereas for fractional crystallization models augite stopped crystallizing when 50%-25% liquid remained. All average augite compositions fall within the measured range of Nakhla augites and the model compositional ranges for augites are similar to those observed in nakhlites (Table 2 and Figure 6a).

For models using NK01 from the study of *Treiman and Goodrich* [2001], the phases that crystallized and the temperature ranges over which they crystallized are

summarized in Figure 5b. Note that augite continued to crystallize until the last temperature step for all models. The average augite compositions from both equilibrium and fractional crystallization fall within the measured range of augite compositions (Table 2 and Figure 6a).

An important result of these models is that augite (similar in composition to that found in nakhlites) continues to crystallize from a liquid as evolved as rhyolite, suggesting that it is possible for the Nakhla augite to been in equilibrium with the more evolved melt inclusions. In addition, augite in equilibrium with evolved liquids (65 wt. % SiO_2) is similar in composition to augite from the unannealed nakhlite. Therefore, the more evolved melt inclusions may represent pockets of liquid that were trapped as melt inclusions within augite at various times during the crystallization history.

4.1.2. Model augite composition compared to nakhlite augites

The augite composition in equilibrium with evolved liquids in these calculations (e.g., ~65 wt. % SiO_2, similar to the most evolved melt inclusion) matches the measured augite compositions in some nakhlites. The augite composition in equilibrium with this liquid is plotted as an open star on the pyroxene quadrilateral for equilibrium crystallization of NA03 at QFM and at QFM-1 (Figure 6a). This augite composition plots within the field of augite composition in the unannealed nakhlite, North West Africa (NWA 817) [*Sautter et al.*, 2002] for both oxidation states (Figure 6a). Other nakhlites have experienced various degrees of subsolidus annealing [*Harvey and McSween*, 1992*b*]. The model pyroxenes have Fe/Mg ratios ranging from 0.48-2.10 (QFM) and 0.51-2.16 (QFM-1), similar to the observed Fe/Mg range for annealed nakhlites (core to rim ranges: 0.55 to 1.97 [*McSween and Treiman*, 1998; *Friedman-Lentz et al.*, 1999]) and roughly within the

Fe/Mg ratio range for the unannealed nakhlite NWA 817 (core to rim range: 0.61 to 7.42 [*Sautter et al.*, 2002]).

4.1.3. Model liquid lines of descent versus measured melt inclusion compositions

The calculated liquid lines of descent from MELTS crystallization modeling of NA03 and NK01 are shown in Figure 7a-d. Each plot shows the evolution of the liquid path at both QFM and QFM-1 on TAS diagram. We use these two paths to define a zone of predicted compositions for liquids at various degrees of crystallization. Thus, if representative pockets of this liquid were trapped as melt inclusions during crystallization of the melt, these inclusions should be distributed along this zone.

The liquid paths for both starting compositions straddle the sub-alkaline/alkaline border on the TAS diagram (Figures 7a-d). In general, for low silica contents (e.g., in the basalt to basaltic andesite range), the alkali abundances of these paths are higher than measured in Nakhla melt inclusions having the same SiO_2 composition. However, at higher silica contents, the Nakhla melt inclusions match more closely the predicted alkali abundances. In general, these liquid paths define the regions where measured melt inclusion compositions plot (c.f. Figures 2 and 3), suggesting that the melt inclusions could represent pockets of liquid that were trapped during progressive crystallization of the nakhlite parent melt. An alternative interpretation is that all inclusions, other than NA03, were modified after trapping by necking down and that the similarity between inclusion compositions and the modeled liquid lines of descent is fortuitous. This interpretation may be supported by the range in incompatible elements (Ti, K, P) present in the melt inclusion data. However, no petrographic evidence for necking down was observed.

4.1.4. Comparison of model phase abundances and compositions with the nakhlites

Finally, let us see how well the MELTS crystallization models for the two starting compositions (NA03 and NK01) match the crystallization sequence inferred for the nakhlites. Both augite and olivine are inferred to have been early crystallizing phases, although there is disagreement as to which began to crystallize first [*Treiman*, 1986; *Harvey and McSween*, 1992*a*; *Treiman*, 1993; *Wadhwa and Crozaz*, 1995; *Mikouchi et al.*, 2003]. Low-Ca pyroxene occurs as overgrowths on augite and as a replacement of olivine and augite [*Treiman*, 1990; *Harvey and McSween*, 1992*a*]. Feldspars, oxides (titanomagnetite and ilmenite) and sulfides occur within the mesostasis and represent late-stage crystallization products [*Berkley et al.*, 1980].

All crystallizing phases and corresponding temperature ranges for models using NA03 are shown in Figure 5a. Differences in oxidation state and type of crystallization (equilibrium vs. fractional) had a greater effect on the appearance of phases than for NK01 models (Figure 5b). Equilibrium crystallization produced augite, olivine, spinel, plagioclase, and whitlockite. Under more oxidizing conditions orthopyroxene crystallized, whereas ilmenite crystallized under more reducing conditions. Plagioclase appeared before olivine and spinel during equilibrium crystallization at QFM. Fractional crystallization modeling produced augite, plagioclase, olivine and spinel. Oxidation state affected the temperature stability range of the phases and their order of appearance, but did not change the phase assemblage.

As mentioned above, the NA03 models produce average augite compositions that fall within the measured range of nakhlite augites. Furthermore, the model compositional ranges are similar to those observed in nakhlites (Table 2 and Figure 6a). The average

orthopyroxene composition is more Fe-rich than the range of measured orthopyroxene compositions (Table 2 and Figure 6a). In fact, the model compositional ranges are very narrow and extend to more Fe-rich compositions when compared to the observed ranges. All average olivine compositions fall within the measured range, but model olivine compositional ranges tend to exceed the observed compositional range, especially for fractional crystallization models (Table 2 and Figure 6a). Average plagioclase compositions (Figure 6b) fall within the measured range in nakhlites, with the exception of the average plagioclase composition for fractional crystallization at QFM-1. All models have plagioclases that extend to more calcic compositions than the measured compositional range. Model plagioclase compositions for fractional crystallization at QFM-1 are not consistent with the measured compositional range (Table 2 and Figure 6b).

All models of NK01 predict spinel, augite, olivine, whitlockite, plagioclase and K-feldspar (Figure 5b). However, spinel crystallizes before both augite and olivine in all models. Orthopyroxene only formed (late) during equilibrium crystallization. Oxidation state affected the temperature at which the phases appeared, but not their presence in the system. The appearance of a phase at a higher temperature resulted in production of a greater quantity of that phase. In fractional crystallization models, olivine crystallization ceased at elevated temperatures (980°C to 1010°C), but did not necessarily decrease the amount of olivine produced (e.g., at QFM-1, 15.1 g of olivine crystallized).

As mentioned above, NK01 models produced average augite compositions from both equilibrium and fractional crystallization that fall within the measured range of augite compositions in nakhlites (Table 2 and Figure 6a). The average orthopyroxene

compositions are too Fe-rich and display very narrow compositional ranges relative to measured compositions in the nakhlites (Table 2 and Figure 6a). All average olivine compositions fall within the measured range (Table 2 and Figure 6a). However, model olivine compositional ranges tend to exceed the measured range, especially for fractional crystallization at QFM-1. All model plagioclase compositions for NK01 models are significantly more calcic than the measured compositional range (Table 2 and Figure 6b).

MELTS crystallization modeling provides insight into the Nakhla parent melt composition and the conditions under which it crystallized. Perhaps most telling is that, regardless of the type of crystallization within a plausible range of oxidation state, both NA03 and NK01 co-crystallize augite and olivine from a single parent melt. Disequilibrium between augite and olivine in Nakhla has been documented previously [*Treiman*, 1986; *Harvey and McSween*, 1992*a*] and explained as either the olivines being xenocrysts [*Treiman*, 1986] or as a result of varying degrees of re-equilibration of both olivine and augite grains near solidus temperatures [*Harvey and McSween*, 1992*a*]. According to MELTS crystallization modeling, the disequilibrium observed between augite and olivine Fe/Mg ratio must then indicate subsequent re-equilibration of olivine [*Harvey and McSween*, 1992*a*] and lesser re-equilibration of augite. This is consistent with the findings from NWA 817, an unannealed nakhlite. The olivine in NWA 817 exhibits strong zoning from core to rim (e.g., Fo_{56} to Fo_{86} in one grain) and extend to more fosteritic compositions relative to other nakhlites (Figure 6a) [*Sautter et al.*, 2002]. Olivine zoning indicates that this sample spent a shorter time near the solidus temperature, and underwent less re-equilibration than other nakhlites. Clinopyroxene

core compositions are very similar to those measured in other nakhlites, suggesting that the cores of augite in all nakhlites are relatively unaltered [*Sautter et al.*, 2002].

Equilibrium crystallization models produce augite and olivine compositions that match the measured compositions more closely (Table 2 and Figure 6a-b). Both starting compositions produced reasonable pyroxene and olivine compositions; however, the NK01 models failed to produce plagioclase compositions that match any measured nakhlite composition, and they predict very early crystallization of spinel, which has not been seen in nakhlites. The NA03 model plagioclase compositions agree with measured plagioclase, so we suggest that NA03 may be more representative of the Nakhla parental melt composition.

In the crystallization models of NA03, plagioclase appears before olivine in both equilibrium and fractional crystallization models at QFM. However, in the crystallization models at QFM-1, olivine appears before plagioclase, providing a better match to the inferred order of appearance (Figure 5a). Between the two models at QFM-1, equilibrium crystallization provides a better match to the phases present in nakhlites (Figure 5a) as well as predicts model plagioclase that correspond more closely to the measured plagioclase compositions in nakhlites (Figure 6b). Therefore, we suggest that equilibrium crystallization of NA03 at QFM-1 best represents the conditions of crystallization and parental melt composition of the nakhlites.

4.2. Water content of the Nakhla parent magma

In the study of *Sobolev et al.* [1990], melt inclusions in Etna hawaiites showed a large variation in homogenization temperatures (150°C) as a function of heating rate due to high water contents (estimated to be ~1 wt. %). The relatively small variation in the

homogenization temperature between the fast- and slow-heating experiments on Nakhla melt inclusions is consistent with a low water content of the nakhlite parental melt. The higher homogenization temperatures for more primitive melt inclusions that were heated rapidly suggest that these are the earliest melts that were trapped. A low water content for the Nakhla parent melt is consistent with the absence of hydrous minerals (e.g., hydrous amphiboles, mica) in melt inclusions. Such phases have been found in other types of Martian meteorites [*Treiman*, 1985; *Johnson et al.*, 1991], and have been used to infer higher magmatic water contents [*Johnson et al.*, 1991; *McSween and Harvey*, 1993].

4.3 Apparent disequilibria between melt inclusions and Nakhla augite and olivine

In melt inclusion studies, the most primitive inclusion composition is normally chosen to represent the parental melt composition. In contrast, *Varela et al.* [2001] regarded their most primitive melt inclusion composition (GHa) as anomalous, because it did not cluster with the other measured melt inclusions. Based on its composition, shape and bubble size, this basaltic melt inclusion was interpreted to be a product of necking, whereby an inclusion becomes divided into two inclusions, each of which may no longer represent the original trapped melt composition. However, Figures 2, 3 and 4 show that GHa plots close to both the previous estimates for the parental melt of Nakhla and our most primitive melt inclusion (NA03).

Instead, *Varela et al.* [2001] presented their average melt inclusion composition GH(6) as a representative composition and suggested that it was not in equilibrium with the host augite or co-existing olivine. However, their melt inclusion data show a large standard deviation for this average composition (Figure 2) and no individual melt

inclusion compositions from that study were evaluated to determine if they were in equilibrium with host augite or the co-existing olivine.

Table 3 displays calculated $K_D(Fe\text{-}Mg)_{augite\text{-}liquid}$ for several parental melt compositions discussed in this paper. *Longhi and Pan* [1988] calculated a range of $K_D(Fe\text{-}Mg)$ from augite-glass pairs in crystallization experiments, ranging from 0.293 to 0.179. The average composition GH(6) of *Varela et al.* [2001] has the largest $K_D(Fe\text{-}Mg)$ value, but the $K_D(Fe\text{-}Mg)$ for inclusion GHa from *Varela et al.* [2001] is much closer to the acceptable range. In fact, by subtracting only 3% of their average augite composition from the melt inclusion GHa, the melt composition is brought into equilibrium with its host. This suggests that more augite has been dissolved into the melt than was originally precipitated onto the walls of the melt inclusion.

The $K_D(Fe\text{-}Mg)$ of augite-liquid for NA03 falls within the range of $K_D(Fe\text{-}Mg)$ values indicated by the crystallization experiments of *Longhi and Pan* [1988]. This is consistent with an interpretation in which the correct amount of augite (i.e., the amount plated out on the walls of the inclusion following entrapment) was resorbed back into the melt inclusion. NA03 is the most primitive (i.e., earliest trapped) melt inclusion among the inclusions from both melt inclusion studies and is in equilibrium with both host augite and olivine at high temperature (~1150ºC). Therefore, NA03 is considered to be the melt inclusion most representative of Nakhla's parental melt composition.

In discussion of the results of *Varela et al.* [2001], *Treiman* [2003] suggested the disequilibrium between melt inclusions and host augite might be due to a boundary layer effect. This occurs when the melt adjacent to the growing crystal becomes enriched in components that diffuse slowly towards the growing crystal or that are incompatible with

respect to the growing phase [*Anderson*, 1974; *Bacon*, 1989]. *Treiman* [2003] reasoned that excess SiO_2, Al_2O_3, TiO_2 and Na_2O in small melt inclusions would be expected due to boundary layer problems. However, more recent work has shown that, with the exception of the smallest inclusions and the fastest crystal growth rates, the compositions of melt inclusions are not affected by boundary layers [*Thomas et al.*, 2002].

Our calculations of boundary layer effects (after Lu *et al.*, 1995; using constants from Donaldson, 1975 and Friedman-Lentz *et al.*, 1995) reveal that gradients would exist for Ca, Fe and Mg at the crystal-melt boundary, but would extend only 1 μm into the melt (Table 4). Gradients would exist out to 2 μm for Ti and out to 3 μm for Al. The effect of this gradient on the bulk composition of the melt inclusion can also be calculated [*Lu et al.*, 1995]. The smallest inclusion that can be analyzed by our technique is 10 μm, so we will discuss compositional changes due to a boundary layer effect for a 10 μm inclusion as a worst-case scenario; it should be noted that all homogenized inclusions from this study with the exception of one (~15 μm) were >20 μm.

For a 10 μm melt inclusion, the boundary layer effect would not produce measurable differences in the concentration of CaO, FeO or MgO, but might produce measurable changes in Al_2O_3 (+0.20 wt. %) and TiO_2 (+0.02 wt. %). For major elements, the precision of electron microprobe analyses is generally ±2% relative; for minor elements, the precision is ±5-10 % relative. In this study, the average Nakhla melt inclusion contained 9.9 wt. % Al_2O_3, so the precision of that analysis would ±0.20 wt. %. Therefore, only the enrichment in Al_2O_3 in a 10 μm melt inclusion would be near measurable levels. As can be seen in Figure 8, the increase in Al_2O_3 abundance in a melt

inclusion due to an Al_2O_3-enriched boundary layer quickly decreases as melt inclusion size increases. Compositional errors for Al_2O_3 resulting from boundary layer processes would be undetectable in all melt inclusions 16 μm and larger.

Finally, the lack of equilibrium between augite-hosted melt inclusions and co-existing olivine is expected. Olivines in Nakhla are no longer in equilibrium with co-existing augite, probably due to variable degrees of subsolidus equilibration of these two phases [*Harvey and McSween*, 1992*a*]. Therefore, the Nakhla olivine composition should not be in equilibrium with the melt inclusions located within co-existing augite cores.

4.4 Igneous origin for nakhlites

MELTS modeling demonstrates that equilibrium crystallization of a basaltic parental melt similar in composition to NA03 or NK01 predicts extended crystallization of augite and olivine, so that these phases might trap highly evolved melt inclusions. In addition, the melt inclusion compositions match well with liquid paths predicted by MELTS crystallization modeling for a parent melt similar in composition to NA03 or NK01.

There is no reason to argue, as did *Varela et al.* [2001], that the melt inclusions in nakhlites require a non-igneous origin for these meteorites. The apparent disequilibrium between Nakhla augite, olivine and the augite-hosted melt inclusions and the erratic behavior of the alkalis do not rule out an igneous origin for Nakhla. The apparent disequilibrium is relatively small for the most primitive melt inclusion from the study of *Varela et al.* [2001] and is easily corrected by subtracting small amounts of the host augite. This suggests that the previous study dissolved too much augite (more than that

crystallized on the walls of the inclusion following entrapment), which would create the appearance of disequilibrium between the melt inclusion and the host augite. In addition, since olivines in Nakhla are no longer in equilibrium with co-existing augite [e.g., *Treiman*, 1986; *Harvey and McSween*, 1992*a*], the Nakhla olivine composition should not be in equilibrium with the augite-hosted melt inclusions (although the inclusions should be in equilibrium with an appropriate olivine composition). Finally, the variability of alkalis in Nakhla melt inclusions reported by *Varela et al.* [2001] may result from experimental or analytical problems. In particular, the validity of an augite-hosted melt inclusion that contains less than 1 wt. % alkalis (Figure 2a) may need to be re-examined. According to distribution coefficients calculated from the experimental work of *Longhi and Pan* [1988], a liquid in equilibrium with Nakhla augite must contain more than 1 wt. % alkalis. We did not observe as much scatter in the alkali contents of Nakhla melt inclusions in our study.

5. Summary

Partly crystallized melt inclusions in the Nakhla meteorite have been studied in an attempt to reconcile differences among estimated compositions of the Nakhla parental melt. We selected inclusions hosted in augite rather than olivine, because Nakhla olivines re-equilibrated during annealing and because olivine-hosted inclusions are known to re-equilibrate easily during heating, both in nature and in the laboratory. We experimentally homogenized melt inclusions using both slow- and fast-heating techniques. The compositions of melt inclusions generally agree with the results of Varela *et al.* (2001). From this study, we have learned:

1. Melt inclusion compositions are consistent with Nakhla being an igneous rock whose parent melt composition and crystallization history clearly reflect planetary (Martian) igneous processes.
    a. Calculations of the Fe-Mg equilibrium distribution coefficient ($K_D(Fe\text{-}Mg)_{augite\text{-}liquid}$) values for measured melt inclusion compositions are consistent with the range determined by crystallization experiments of [*Longhi and Pan*, 1988].
    b. The hypothesis of *Varela et al.* [2001] that Nakhla melt inclusions represent heterogeneously trapped liquids and solids not formed through igneous processes is unwarranted. Their conclusion was based on an assumption that Nakhla's parent melt could be represented by an average of all their melt inclusions. We argue instead that the parent melt is approximated by their most primitive melt inclusion, GHa.
    c. Calculations of the effect of boundary layer diffusion on small melt inclusions for the Nakhla parent melt [as suggested by *Treiman*, 2003] demonstrate that any compositional effect would not be detectable by electron microprobe analyses.
2. Melt inclusions are distributed along MELTS-calculated liquid lines of descent for proposed Nakhla parental melts (NA03 or NK01), suggesting the inclusions may represent liquids trapped at various points along a fractionation sequence.
    a. In MELTS models at QFM-1, the calculated equilibrium crystallization sequence for NA03 was augite, olivine, plagioclase, spinel, whitlockite and

ilmenite, consistent with the crystallization sequence inferred from Nakhla petrography.

b. The composition of host augite predicted by MELTS does not change significantly during the crystallization interval corresponding to the melt inclusions and is consistent with measured augite composition.

c. Co-crystallization of augite and olivine in these crystallization models supports the hypothesis that olivines in Nakhla re-equilibrated during subsolidus annealing [*Harvey and McSween*, 1992*a*] rather than the olivine being xenocrystic [*Treiman*, 1986].

3. Melt inclusion NA03 most closely represents the composition of the original parental melt from Nakhla.

   a. Our most primitive melt inclusion composition (NA03) has the lowest SiO_2 and a high Mg# and relatively high homogenization temperature (1170ºC). We infer that this basaltic composition most closely represents the Nakhla parent melt. This composition is very similar to NK01, derived by *Treiman and Goodrich* [2001], and to GHa, the most primitive melt inclusion of *Varela et al.* [2001].

   b. Compositions of augite and olivine for both NA03 and NK01 crystallization models match compositions observed in nakhlites. However, NK01 models crystallize spinel very early (not observed in Nakhla) and plagioclase that is more calcic than measured in nakhlites. Thus, we suggest that NA03 may be a better parental melt composition.

c. The small variation in homogenization temperatures between slow- and fast-heated melt inclusions suggests that the Nakhla parental melt had a low water content.

Acknowledgements We are grateful to The British Museum of Natural History, through the Meteorite Working Group, for providing samples, and to Jay Thomas, Charles Farley, Luca Fedele, Mercedes Gonzalez-Student and Jim Student for their assistance and advice regarding laboratory work. This work benefited from discussions with or reviews by Rachel Lentz, Mark Ghiorso, Cyrena Goodrich, Leonid Danyushevsky, Allan Treiman, Richard Sacks, Ralph Harvey, Steve Singletary, and Alex Sobolev; Gretchen Benedix and Bob Tracy provided support in acquiring glass analyses. This study was supported by NASA Cosmochemistry grants NAG5-11744 to HYM and NAG5-10733 to RJB, and awards from the UT Scholarly Activities Research Incentive Fund and the Southeast Section of the Geological Society America to KRS.

References cited

Andersen, D.J., D.H. Lindsley, and P.M. Davidson, QUILF: a Pascal program to assess equilibria among Fe-Mg-Mn-Ti oxides, pyroxenes, olivine, and quartz, *Comput. Geosci.*, *19* (9), 1333-1350, 1993.

Anderson, A.T., Jr., Evidence for a picritic, volatile-rich magma beneath Mt. Shasta, California., *J. Petrol.*, *15* (2), 243-267, 1974.

Anderson, A.T., Jr., Water in some hypersthenic magmas, *J. Geol.*, *87* (5), 509-531, 1979.

Bacon, C.R., Crystallization of accessory phases in magmas by local saturation adjacent to phenocrysts, *Geochim. Cosmochim. Acta*, *53* (5), 1055-1066, 1989.

Berkley, J.L., K. Keil, and M. Prinz, Comparative petrology and origin of Governador Valadares and other nakhlites, in *Proc. Lunar Planet. Sci. Conf.*, edited by P.R. Criswell, and R.B. Merrill, pp. 1089-1102, Lunar and Planetary Institute, Houston, TX, 1980.

Danyushevsky, L.V., A.W. McNeill, and A.V. Sobolev, Experimental and petrological studies of melt inclusions in phenocrysts from mantle-derived magmas: An overview of techniques, advantages and complications, *Chem. Geol.*, *183* (1-4), 5-24, 2002*a*.

Danyushevsky, L.V., S. Sokolev, and T.J. Falloon, Melt inclusions in olivine phenocrysts: Using diffusive re-equilibration to determine the cooling history of a crystal, with implications for the origin of olivine-phyric volcanic rocks, *J. Petrol.*, *43* (9), 1651-1671, 2002*b*.

Delano, J., and R. Arculus, Nakhla: Oxidation state and other constraints, in *Proc. Lunar Planet. Sci. Conf.*, pp. 219-221, Lunar and Planetary Institute, Houston, TX, USA, 1980.

Donaldson, C.H., Calculated diffusion coefficients and the growth rate of olivine in a basalt magma, *Lithos*, *8* (2), 163-174, 1975.

Fagan, T.J., E.R.D. Scott, K. Keil, T.F. Cooney, and S.K. Sharma, Formation of feldspathic and metallic melts by shock in enstatite chondrite Reckling Peak A80259, *Meteorit. Planet. Sci.*, *35* (2), 319-329, 2000.

Fedele, L., R.J. Bodnar, B. DeVivo, and R. Tracy, Melt inclusion geochemistry and computer modeling of trachyte petrogenesis at Ponza, Italy, *Chem. Geol.*, *194* (1-3), 81-104, 2003.

Frezzotti, M.L., Silicate-melt inclusions in magmatic rocks: Applications to petrology, *Lithos*, *55* (1-4), 273-299, 2001.

Friedman Lentz, R.C., G.J. Taylor, and A.H. Treiman, Formation of a martian pyroxenite: A comparative study of the nakhlite meteorites and Theo's Flow, *Meteorit. Planet. Sci.*, *34*, 919-932, 1999.

Gaetani, G.A., and E.B. Watson, Open system behavior of olivine-hosted melt inclusions, *Earth Planet. Sci. Lett.*, *183* (1-2), 27-41, 2000.

Ghiorso, M.S., and R.O. Sack, Fe-Ti oxide geothermometry; thermodynamic formulation and the estimation of intensive variables in silicic magmas, *Contrib. Mineral. Petrol.*, *108* (4), 485-510, 1991.

Ghiorso, M.S., and R.O. Sack, Chemical mass transfer in magmatic processes, IV. A revised and internally consistent thermodynamic model for the interpolation and extrapolation of liquid-solid equilibria in magmatic systems at elevated temperatures and pressures, *Contrib. Mineral. Petrol.*, *119* (2-3), 197-212, 1995.

Hale, V.P., H.Y. McSween, Jr. , and G.A. McKay, Re-evaluation of intercumulus liquid composition and oxidation state for the Shergotty meteorite, *Geochim. Cosmochim. Acta*, *63* (9), 1459-1470, 1999.

Harvey, R.P., and H.Y. McSween, Jr., The parent magma of the nakhlite meteorites: Clues from melt inclusions, *Earth Planet. Sci. Lett.*, *111* (2-4), 467-482, 1992*a*.

Harvey, R.P., and H.Y. McSween, Jr., The petrogenesis of the nakhlites: Evidence from cumlate mineral zoning, *Geochim. Cosmochim. Acta*, *56*, 1655-1663, 1992*b*.

Johnson, M.C., M.J. Rutherford, and P.C. Hess, Chassigny petrogenesis: Melt compositions, intensive parameters, and water contents of Martian (?) magmas, *Geochim. Cosmochim. Acta*, *55* (1), 349-366, 1991.

Kaneda, K., G.A. McKay, and L. Le, Synthetic and natural pyroxenes: A close match at last, in *Lunar Planet. Sci.*, pp. #1620, Lunar and Planetary Institute, Houston, TX, USA, 1998.

Longhi, J., and V. Pan, The parent magmas of the SNC meteorites, in *Proc. Lunar Planet. Sci. Conf.*, edited by G. Ryder, and V.L. Sharpton, pp. 451-464, Lunar and Planetary Institute, Houston, TX, 1988.

Lowenstern, J.B., Application of silicate-melt inclusions to the study of magmatic volatiles, in *Magmas, fluids and ore deposition*, edited by J.F.H. Thompson, pp. 71-98, Mineralogical Association of Canada, Short Course Series, Toronto, ON, Canada, 1995.

Lu, F., A.T. Anderson, Jr., and A.M. Davis, Diffusional gradients at the crystal/melt interface and their effect on the composition of melt inclusions, *J. Geol.*, *103* (5), 591-597, 1995.

McSween, H.Y., Jr., What we have learned about Mars from SNC meteorites, *Meteoritics*, *29* (6), 757-779, 1994.

McSween, H.Y., Jr., and R.P. Harvey, Outgassed Water on Mars: Constraints from Melt Inclusions in SNC Meteorites, *Science*, *259* (5103), 1890-1892, 1993.

McSween, H.Y., Jr., and A.H. Treiman, Martian Meteorites, in *Planetary Materials*, edited by J.J. Papike, pp. 1-53, Mineralogical Society of America, Washington, D.C., 1998.

Mikouchi, T., E. Koizumu, A. Monkawa, Y. Ueda, and M. Miyamoto, Mineralogy and petrology of Yamato 000593: Comparison with other Martian nakhlite meteorites, *Antarctic Meteorite Res.*, *16*, 34-57, 2003.

Newman, S., S. Epstein, and E. Stolper, Water, carbon dioxide, and hydrogen isotopes in glasses from the ca. 1340 eruption of Mono Craters, CA: Constraints on degassing phenomena and initial volatile content, *J. Volc. Geotherm. Res.*, *35* (1-2), 75-96, 1988.

Nielsen, R.L., P.J. Michael, and R. Sours-Page, Chemical and physical indicators of compromised melt inclusions, *Geochim. Cosmochim. Acta*, *62* (5), 831-838, 1998.

Qin, Z., F. Lu, and A.T. Anderson, Jr., Diffusive reequilibration of melt and fluid inclusions, *Am. Mineral.*, *77* (5-6), 565-576, 1992.

Reid, A.M., and T.E. Bunch, The Nakhlites, Part II: Where, when, and how, *Meteoritics*, *10* (4), 317-324, 1975.

Roedder, E., Origin and significance of magmatic inclusions, *Bull. Mineral.*, *102* (5-6), 487-510, 1979.

Sautter, V., J.A. Barrat, A. Jambon, J.P. Lorand, P. Gillet, M. Javoy, J.L. Joron, and M. Lesourd, A new Martian meteorite from Morocco: The nakhlite North West Africa 817, *Earth Planet. Sci. Lett.*, *195* (3-4), 223-238, 2002.

Sisson, T.W., and G.D. Layne, H_2O in basalt and basaltic andesite glass inclusions from four subduction-related volcanoes, *Earth Planet. Sci. Lett.*, *117* (3-4), 619-635, 1993.

Slater, V.P., C.K. Thompson, J. Nettles, K. Milam, K.R. Stockstill, J.T. Cahill, M. Anand, and L.A. Taylor, An evaluation of the igneous crystallization programs -- MELTS, MAGPOX, and COMAGMAT Part II: importance of magmatic fO_2, in *Lunar Planet. Sci.*, pp. #1896, Lunar and Planetary Institute, Houston, TX, USA, 2003.

Sobolev, A.V., Melt inclusions in minerals as a source of principal petrologic information, *Petrologiya*, *4* (3), 228-239, 1996.

Sobolev, A.V., and A.B. Slutskiy, Composition and crystallization conditions of the initial melt of the Siberian meimechites in relation to the general problem of ultrabasic magmas, *Soviet Geol. Geophys.*, *25* (12), 97-110, 1984.

Sobolev, A.V., V.S. Kamenetskiy, N. Metrich, R. Clocchiatti, N.N. Kononkova, A.L. Devirts, and V.I. Ustinov, Volatile regime and crystallization conditions in Etna hawaiite lavas, *Geokhimiya*, *9*, 1277-1290, 1990.

Szymanksi, A., A. El Goresy, F.E. Brenker, and H. Palme, Application of the Fe-, Ti-Thermometer/OxyBarometer to Nakhla and Y000593, in *Evolution of Solar System Materials: A New Perspective from Antarctic Meteorites*, pp. 132-133, National Institute of Polar Research, Tokyo, Japan, 2003.

Thomas, J.B., and R.J. Bodnar, A technique for mounting and polishing melt inclusions in small (<1mm) crystals, *Am. Mineral.*, *87* (10), 1505-1508, 2002.

Thomas, J.B., R.J. Bodnar, N. Shimizu, and C. Chesner, The boundary layer problem and the reliability of melt inclusions as petrogenetic monitors: Evidence from melt inclusions in zircon, allanite, plagioclase and quartz, in *Workshop-Short Course on Volcanic Systems; Geochemical and Geophysical Monitoring. Melt Inclusions: Methods, Applications and Problems*, edited by B. DeVivo, and R.J. Bodnar, pp. 205-209, De Frede Editore, Naples, Italy, 2002.

Treiman, A.H., Amphibole and hercynite spinel in Shergotty and Zagami; magmatic water, depth of crystallization, and metasomatism, *Meteoritics*, *20* (2), 229-243, 1985.

Treiman, A.H., The parental magma of the Nakhla achondrite: Ultrabasic volcanism on the shergottite parent body, *Geochim. Cosmochim. Acta*, *50* (6), 1061-1070, 1986.

Treiman, A.H., Complex petrogenesis of the Nakhla (SNC) meteorite: Evidence from petrography and mineral chemistry, in *Proc. Lunar Planet. Sci. Conf.*, pp. 273-280, Lunar and Planetary Science Institute, Houston, TX, USA, 1990.

Treiman, A.H., The parent magma of the Nakhla (SNC) meteorite, inferred from magmatic inclusions, *Geochim. Cosmochim. Acta*, *57* (19), 4753-4767, 1993.

Treiman, A.H., The Nakhla Martian meteorite is a cumulate igneous rock. Comment on "Glass-bearing inclusions in Nakhla (SNC meteorite) augite: heterogeneously trapped phases" (2001) by M. E. Varela, G. Kurat, and R. Clocchiatti, *Mineral. Petrol.*, *76* (3-4), 271-277, 2003.

Treiman, A.H., and C.A. Goodrich, A parent magma for the Nakhla martian meteorite: Reconciliation of estimates from 1-bar experiments, magmatic inclusions in olivine, and magmatic inclusions in augite, in *Lunar Planet. Sci.*, pp. #1107, Lunar and Planetary Institute, Houston, TX, 2001.

Treiman, A.H., J.D. Gleason, and D.D. Bogard, The SNC meteorites are from Mars, *Planet. Space. Sci.*, *48*, 1213-1230, 2000.

Varela, M.E., G. Kurat, and R. Clocchiatti, Glass-bearing inclusions in Nakhla (SNC meteorite) augite: Heterogeneously trapped phases, *Mineral. Petrol.*, *71* (3-4), 155-172, 2001.

Wadhwa, M., and G. Crozaz, Trace and minor elements in minerals of nakhlites and Chassigny; clues to their petrogenesis, *Geochim. Cosmochim. Acta*, *59* (17), 3629-3645, 1995.

Wallace, P.J., A.T. Anderson, Jr., and A.M. Davis, Gradients in H_2O, CO_2, and exsolved gas in a large-volume silicic magma system: Interpreting the record preserved in melt inclusions from the Bishop Tuff, *J. Geophys. Res.*, *104* (9), 20097-20122, 1999.

Appendix

Table 1: Representative electron microprobe analyses of melt inclusions in Nakhla augite (NA##) from this study and the nakhlite parental magma composition derived by *Treiman and Goodrich* (2001), NK01. Size and homogenization temperature (T_h) are also listed for Nakhla melt inclusions.

	Rehomogenized – slow-heating experiments			**Rehomogenized – fast-heating experiments**					**T&G 2001**
	NA01a	**NA01b**	**NA02**	**NA03**	**NA04**	**NA05**	**NA06**	**NA07**	**NK01**
Size	15 μm	20 μm	45 μm	20 μm	20 μm	30 μm	20 μm	20 μm	-
T_h	1150	1150	1150	1170	1170	1170	1170	1170	-
SiO_2	56.0	64.4	62.5	47.2	51.2	63.1	54.9	59.2	49.8
TiO_2	1.3	0.62	0.27	0.88	0.84	2.1	0.63	0.34	0.80
Al_2O_3	10.7	13.4	11.0	5.9	7.1	12.3	9.4	9.2	7.5
Cr_2O_3	0.02	0.06	-	-	-	-	-	-	0.10
FeO	14.5	7.5	11.1	26.9	19.6	3.4	15.0	12.3	22.3
MnO	0.39	0.37	0.25	0.71	0.53	0.32	0.43	0.32	0.50
MgO	2.1	0.74	2.5	4.6	4.6	4.0	4.8	4.4	4.6
CaO	8.2	3.5	5.1	10.1	11.2	11.1	9.3	10.1	10.4
NiO	-	-	-	0.07	-	0.0	0.0	-	-
Na_2O	3.4	4.1	3.7	2.3	2.1	1.0	3.6	1.2	1.1
K_2O	2.0	3.6	2.7	0.39	0.70	0.63	0.33	0.66	2.4
P_2O_5	0.65	0.30	0.04	0.09	0.97	0.47	0.42	1.1	0.60
Total	99.2	98.6	99.3	99.1	98.8	98.3	98.8	99.0	100.1
Phases present	Glass	Glass	Glass + oxide	Glass	Glass	Glass + oxide	Glass	Glass	-

Table 2: Mineral compositions measured in nakhlites and produced by MELTS equilibrium and fractional crystallization modeling of NK01 and NA03. Measured compositional ranges include core and rim compositions from the nakhlites.

Nakhlites measured		Clinopyroxene			Orthopyroxene			Olivine		Plagioclase		
		Wo	En	Fs	Wo	En	Fs	Fo	Fa	An	Ab	Or
	Range	22-41	9-40	22-66	2-24	16-38	24-44	14-41	57-86	10-26	60-74	3-30
NA03		**Clinopyroxene**			**Orthopyroxene**			**Olivine**		**Plagioclase**		
		Wo	**En**	**Fs**	**Wo**	**En**	**Fs**	**Fo**	**Fa**	**An**	**Ab**	**Or**
QFM Equilibrium	**Range**	37-43	20-39	19-42	9-10	25-26	64-66	15-34	66-85	15-47	50-76	3-9
	Average	40	26	34	10	25	65	21	79	27	67	6
QFM -1 Equilibrium	**Range**	39-42	20-39	20-42	-	-	-	14-34	66-86	14-48	50-77	2-10
	Average	41	25	35	-	-	-	19	82	25	68	7
QFM Fractional	**Range**	39-43	8-39	19-50	-	-	-	6-29	71-94	26-48	50-70	3-7
	Average	41	27	32	-	-	-	17	83	34	62	4
QFM-1 Fractional	**Range**	41-44	4-39	20-53	-	-	-	2-34	66-98	37-50	48-59	2-4
	Average	42	25	33	-	-	-	18	82	42	54	3
NK01		**Clinopyroxene**			**Orthopyroxene**			**Olivine**		**Plagioclase**		
		Wo	**En**	**Fs**	**Wo**	**En**	**Fs**	**Fo**	**Fa**	**An**	**Ab**	**Or**
QFM Equilibrium	**Range**	35-41	21-39	20-42	9-10	26	64-65	17-36	64-84	41-45	47-50	6-10
	Average	39	28	34	9	26	65	25	76	43	49	8
QFM -1 Equilibrium	**Range**	34-42	20-40	20-45	10	23-24	66-67	14-45	56-86	45-51	42-47	6-9
	Average	39	26	35	10	24	67	22	78	46	46	8
QFM Fractional	**Range**	39-43	0-39	19-58	-	-	-	9-29	71-92	39-49	44-53	7-9
	Average	41	19	40	-	-	-	18	82	43	49	8
QFM-1 Fractional	**Range**	40-44	0-40	20-59	-	-	-	3-43	57-97	49-62	33-44	5-7
	Average	42	19	39	-	-	-	21	79	55	39	6

Table 3: $K_D(Fe\text{-}Mg)_{augite\text{-}glass}$ values* for several proposed parental magma compositions.

	NA03[1]	**GH(6)**[2]	**Gha**[3]	**Gha**[3] **– 3% augite**	**NK01**[4]
FeO/MgO_{glass}	5.79	2.73	3.56	3.75	4.85
FeO/MgO_{augite}	1.47	1.09	1.09	1.09	1.09
$K_D(Fe\text{-}Mg)_{augite\text{-}glass}$	0.254	0.399	0.307	0.291	0.226

* Note: $K_D(Fe\text{-}Mg)_{augite\text{-}glass}$ was determined experimentally by Longhi and Pan (1988) to range from 0.293 to 0.179. The FeO/MgO_{augite} for melt inclusions studies come from host pyroxene compositions of the respective studies, whereas FeO/MgO_{augite} for the other estimates comes from a representative augite core composition from Treiman (1990).

[1] The most primitive melt inclusion from this study.

[2] Average composition of 6 melt inclusion from the study of Varela et al. (2001).

[3] The most primitive melt inclusion from the study of Varela et al. (2001).

[4] Most recent nakhlite parent magma composition from the study of Treiman and Goodrich (2001).

Table 4: Calculations of potential boundary layer problems for a basaltic liquid after *Lu et al*. (1995).[1]

Parameters used in calculations:			
Growth rate[2]	**V (cm/s)**	2.05 e -08	
Diffusivity[3] **(cm^2/s)**		**1100°C**	**1200°C**
	D (Ca^{2+})	1.41 e -09	4.37 e -09
	D (Mg^{2+})	2.14 e -09	6.76 e -09
	D (Fe^{2+})	1.91 e -09	5.62 e -09
	D (Al^{3+})	2.75 e -09	8.91 e -09
	D (Ti^{4-})	2.14 e -09	6.76 e -09
Augite/liquid partition coefficients[4]	**$k(CaO)_{aug\text{-}liq}$**	1.41 ± 0.1	
	$k(MgO)_{aug\text{-}liq}$	1.9 ± 0.1	
	$k(FeO)_{aug\text{-}liq}$	0.43 ± 0.08	
	$k(Al_2O_3)_{aug\text{-}liq}$	0.13 ± 0.01	
	$k(TiO_2)_{aug\text{-}liq}$	0.17 ± 0.03	

Growth at 1100°C :						**Growth at 1200°C :**					
x (μm)	**C_x (Ca)**	**C_x (Mg)**	**C_x (Fe)**	**C_x (Al)**	**C_x (Ti)**	**x (μm)**	**C_x (Ca)**	**C_x (Mg)**	**C_x (Fe)**	**C_x (Al)**	**C_x (Ti)**
0	0.7	0.5	2.3	7.7	5.9	**0**	0.7	0.5	2.3	7.7	5.9
1	1.0	1.0	1.0	1.0	1.0	**1**	1.0	1.0	1.0	1.7	1.2
2	1.0	1.0	1.0	1.0	1.0	**2**	1.0	1.0	1.0	1.1	1.0
3	1.0	1.0	1.0	1.0	1.0	**3**	1.0	1.0	1.0	1.0	1.0
4	1.0	1.0	1.0	1.0	1.0	**4**	1.0	1.0	1.0	1.0	1.0
5	1.0	1.0	1.0	1.0	1.0	**5**	1.0	1.0	1.0	1.0	1.0
10	1.0	1.0	1.0	1.0	1.0	**10**	1.0	1.0	1.0	1.0	1.0
15	1.0	1.0	1.0	1.0	1.0	**15**	1.0	1.0	1.0	1.0	1.0
20	1.0	1.0	1.0	1.0	1.0	**20**	1.0	1.0	1.0	1.0	1.0
25	1.0	1.0	1.0	1.0	1.0	**25**	1.0	1.0	1.0	1.0	1.0

[1]Note: The calculated concentration is the concentra-tion of component i ($C_x(i)$) at distance x from the crystal-melt interface equal to some multiple (n) of the original concentration of component i. ($C_o(i)$) [$C_x(i) = n * C_o(i)$]

[2]*Friedman Lentz et al.* (1999)

[3]Calculated after *Donaldson* (1975)

[4]k-values calculated from the experiments of *Longhi and Pan* (1988)

Figure 1: Photomicrographs of melt inclusions in Nakhla augite. (a) Low magnification view (40x) of Nakhla augite containing several unhomogenized melt inclusions at variable depths within the crystal. The field of view is 4 mm. Fields of view for all other photomicrographs are 2 mm across. (b) Transmitted light photomicrograph of an unhomogenized 10 μm melt inclusion in a Nakhla augite. A shrinkage bubble and daughter opaque phase are visible in this view. (c) Transmitted light photomicrograph of a homogenized 20 μm melt inclusion in Nakhla that has been exposed at the surface following homogenization. (d) Same melt inclusion in reflected light. In both views, the bubble void is visible. Notice that the full melt inclusion diameter has not been exposed at the surface.

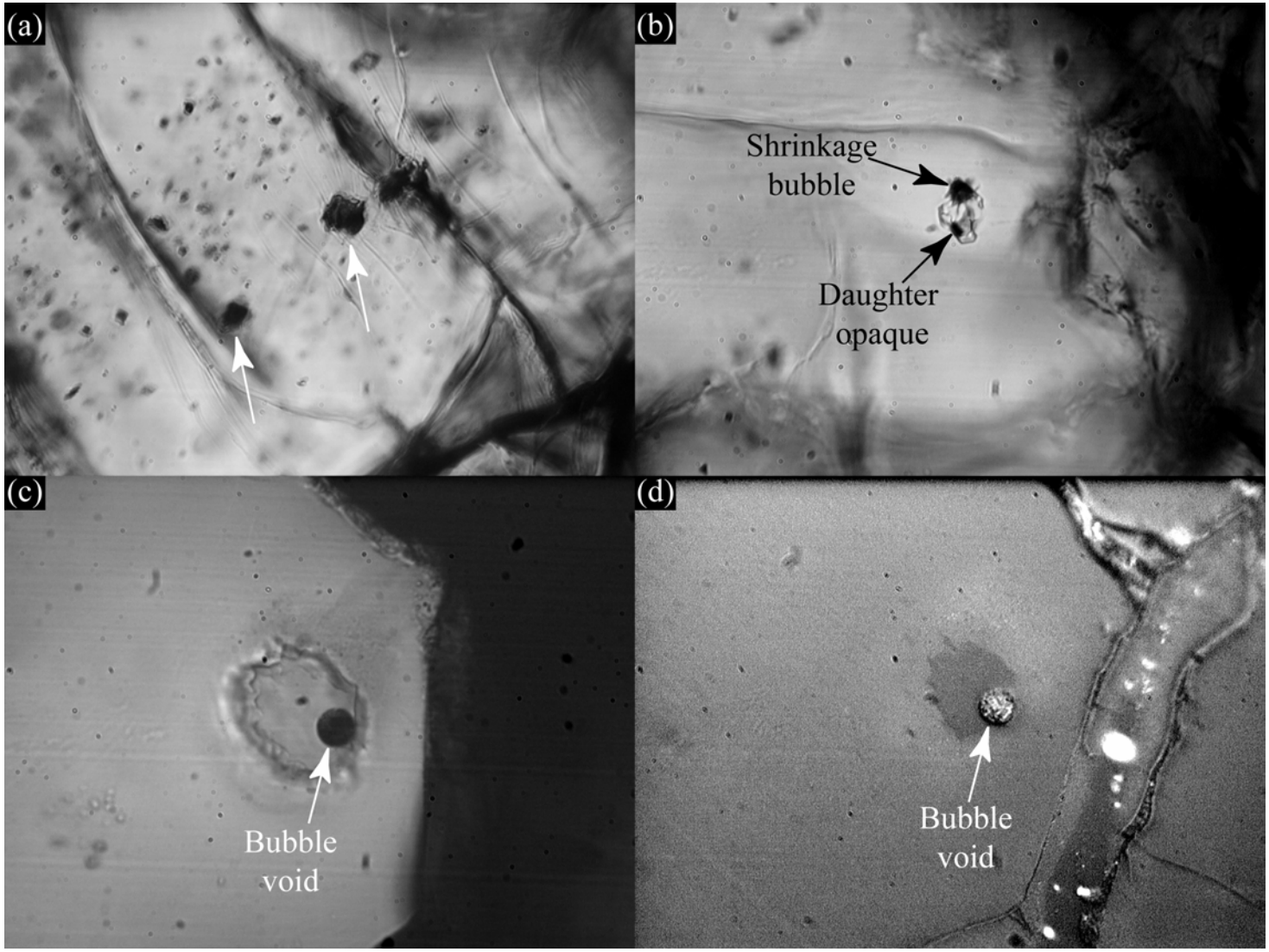
(a)
(b)
Shrinkage
bubble
Daughter
opaque
(c)
Bubble
void
(d)
Bubble
void

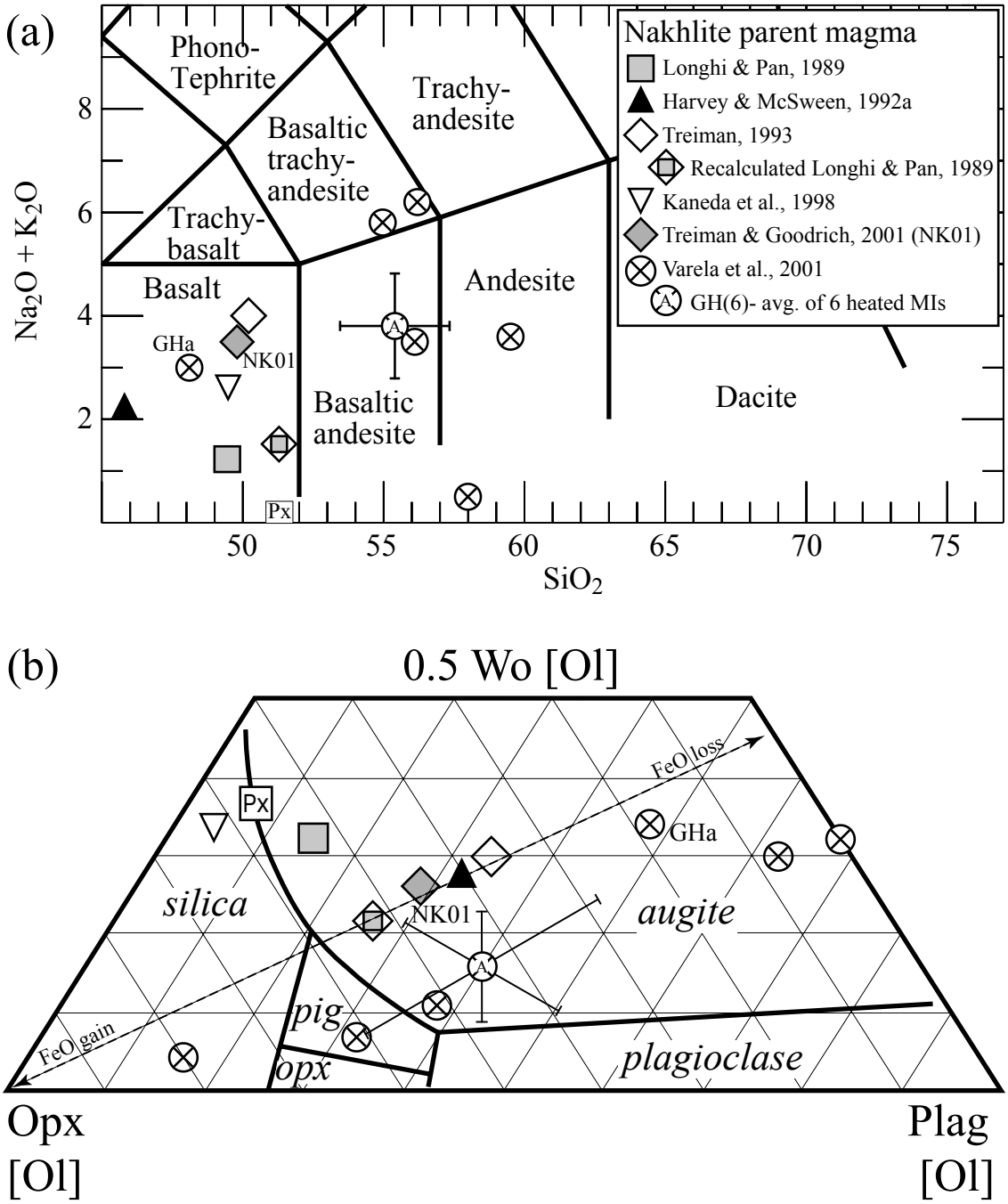

Figure 2: Published estimates of SNC parental magma compositions and previously heated melt inclusion compositions. Plotted on (a) the total alkalis-silica (TAS) diagram and (b) an orthopyroxene-wollastonite-plagioclase phase diagram projected from olivine (after Longhi, 1991). Most previous estimates of SNC parental magma compositions plot within the basalt field on the TAS and within the augite field of the olivine projection. The host pyroxene phase for melt inclusions is represented by "Px" within a square. FeO loss and gain is represented by a double-arrow dashed line and is important when considering re-equilibration of olivine.

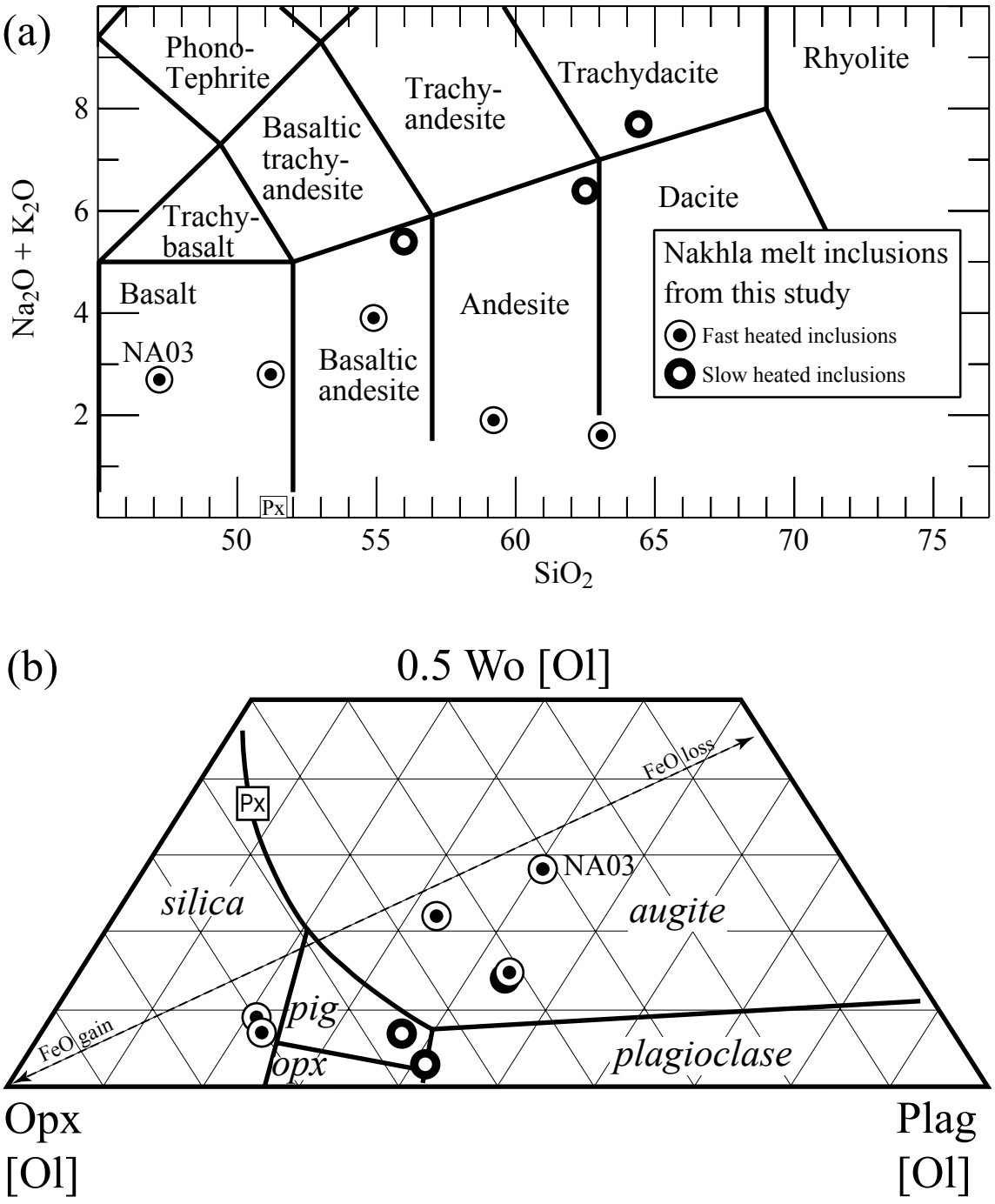

Figure 3: Melt inclusion compositions from this study. Plotted on the same diagrams as in Figure 2. The trend of the homogenized Nakhla inclusion data on the TAS diagram does not point towards the host augite (Px) composition. Incorporating too much host augite would simply move Nakhla melt inclusion compositions towards the host pyroxene composition, suggesting that the most primitive melt inclusions have not re-incorporated excessive amounts of the host phase.

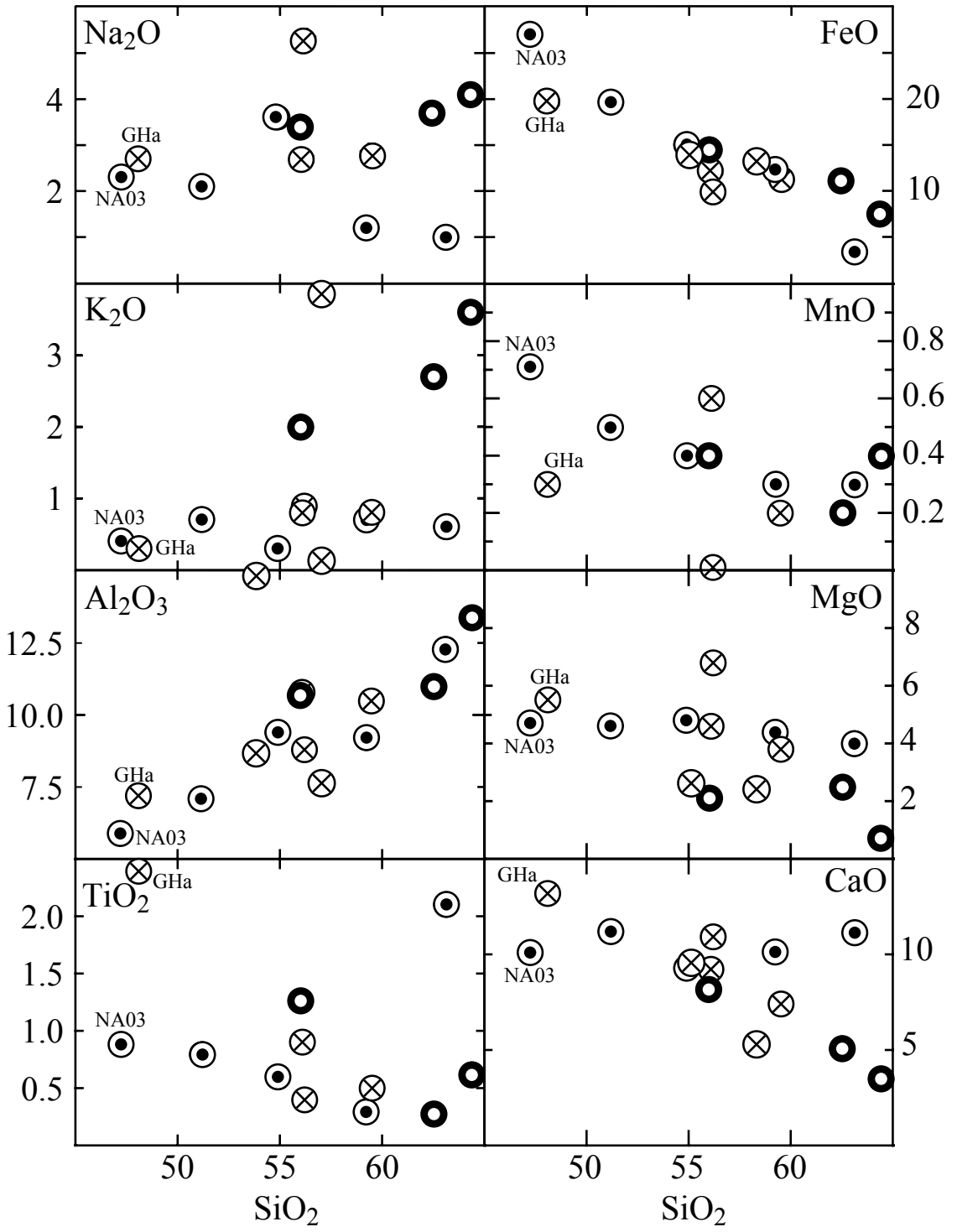

Figure 4: Harker (wt. % oxide) diagrams of melt inclusion data. Diagrams display trends of slowly and rapidly heated melt inclusions in Nakhla pyroxenes from this study and the study of Varela *et al.* (2001). Symbols for Nakhla melt inclusions as in Figures 2 and 3 and the most primitive melt inclusions for both studies are labeled. Several oxides show consistent trends regardless of heating rate, whereas others, especially the alkalis and oxides present in lower abundances, show more erratic behavior.

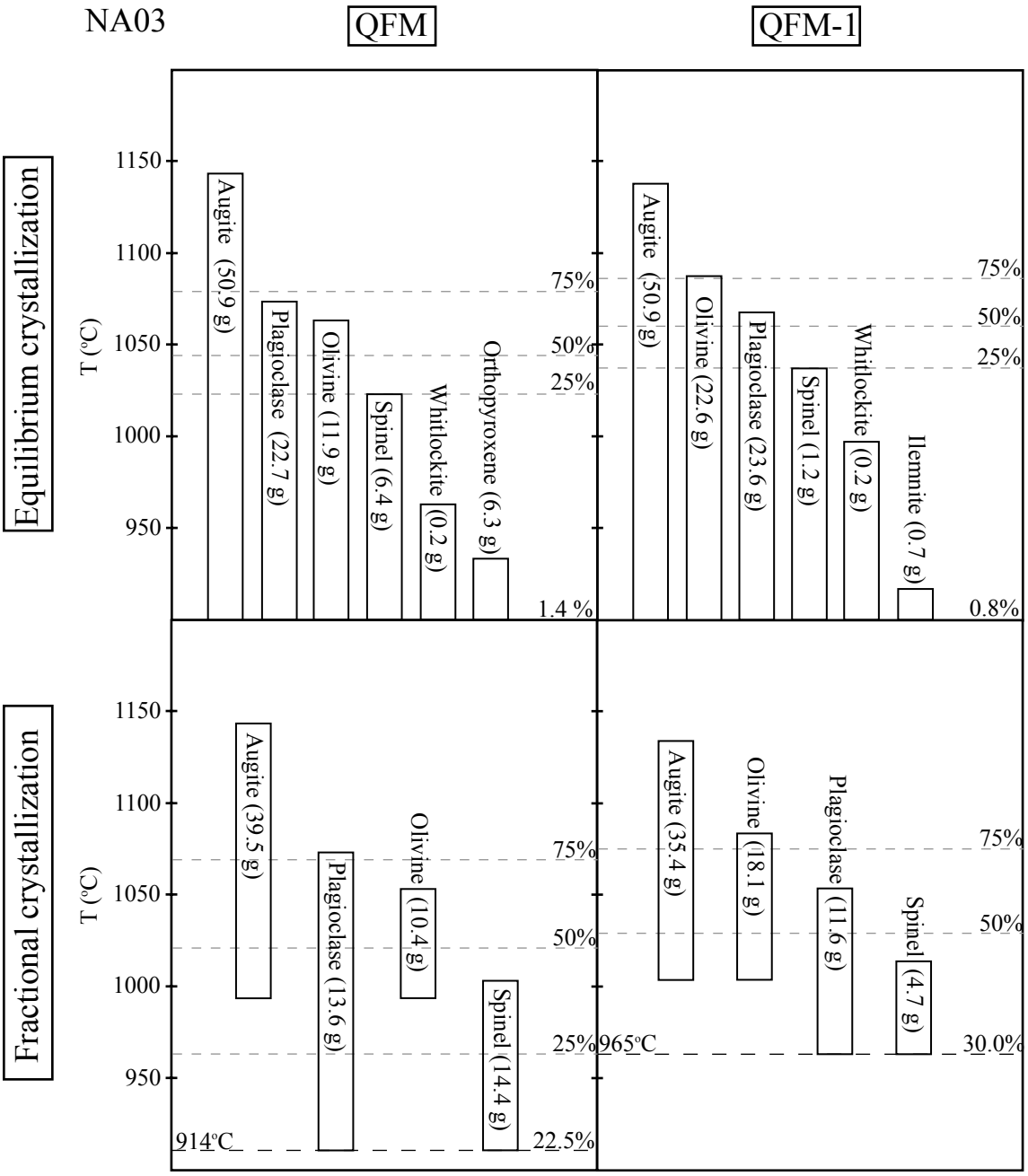

Figure 5: Results of MELTS modeling for NA03 and NK01. (a) NA03: Dashed lines (top to bottom) represent temperatures at which there was 75%, 50% and 25% liquid remaining and the final amount of liquid remaining (at the end of the run) is displayed at the final temperature step for that model. Runs were performed from the liquidus temperature to 900°C for all conditions except for fractional crystallization, where modeling could only be run to ~914°C for QFM and ~965°C for QFM-1 (see discussion section for details). Cumulative amounts of the phases are listed in parentheses after the phase names.

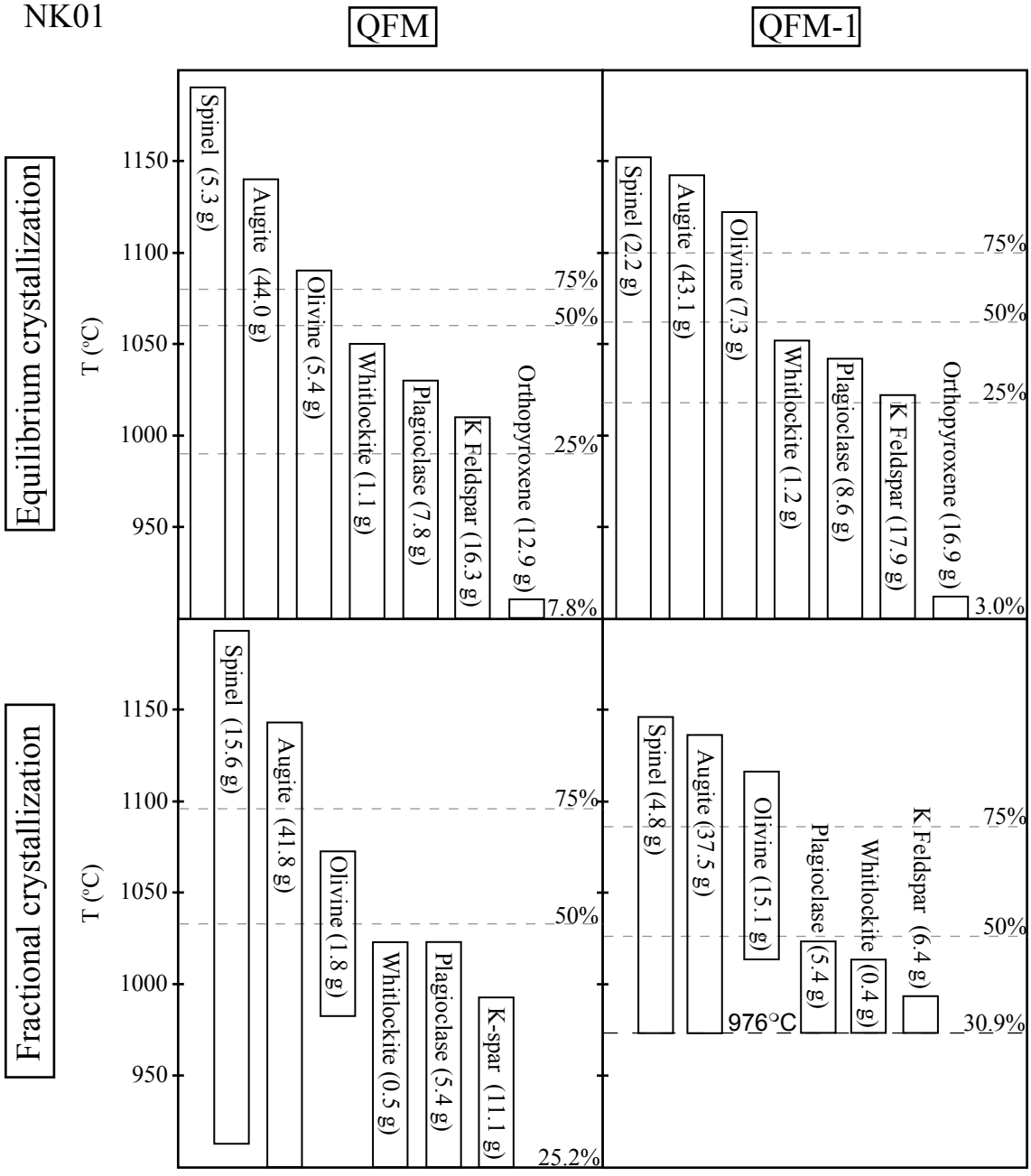

Figure 5 (con't): (b) NK01: Runs were performed from the liquidus to 900°C except for fractional crystallization at QFM-1, where modeling could only be run to 976°C (see discussion section for details). Fractional crystallization modeling results have greater amounts of liquid remaining at the end of runs. Dashed lines represent the temperature at which there was 75%, 50% and 25% liquid remaining and the final amount of liquid remaining is displayed at the final temperature step.

Figure 6: Mineral compositions produced by MELTS crystallization modeling for NA03 and NK01. (a) Pyroxene and olivine resulting from MELTS crystallization models for NA03 and NK01. On the pyxroxene quadrilateral, open squares represent augite and filled circles are orthopyroxene. The average augite is shown by a black diamond. Gray areas enclose pyroxene compositions measured in most nakhlites (*Harvey and McSween*, 1992*b*), whereas the outlined area encloses pyroxene compositions analyzed in the unannealed nakhlite NWA 817 (*Sautter et al*., 2002). On the olivine bar, the upper black box displays the range of olivine produced by the model, with the average olivine represented by the polygon. The gray box displays the range of measured olivine in most nakhlites (*Harvey and McSween*, 1992*b*), whereas the open box displays the large range of olivine in NWA 817 (*Sautter et al*., 2002). On the NA03 equilibrium crystallization at QFM and at QFM-1 quadrilaterals, the open stars represent the augite produced by the MELTS model for liquids similar in composition to our most evolved melt inclusion.

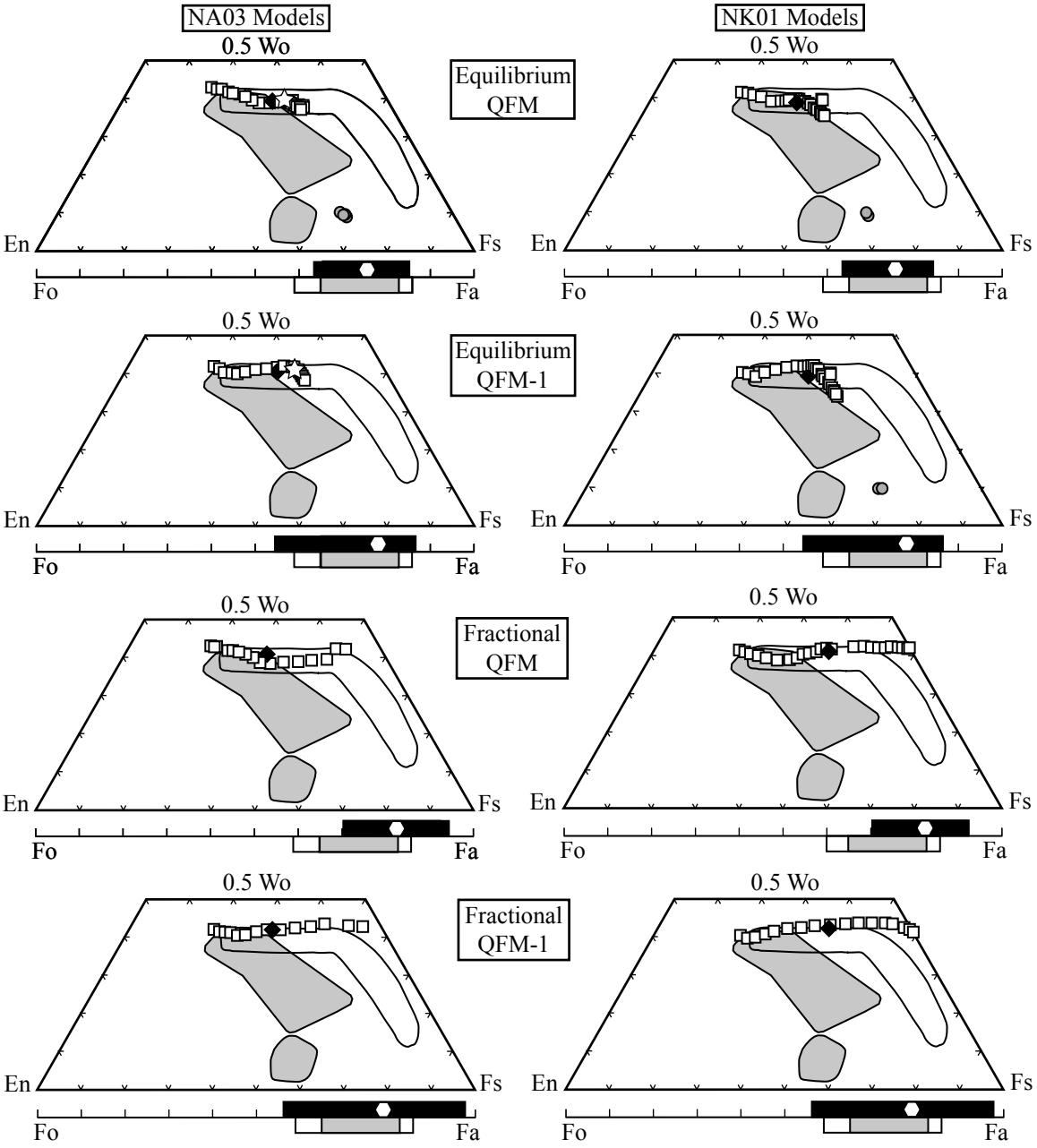
NA03 Models
NK01 Models
0.5 Wo
Equilibrium
QFM
Equilibrium
QFM-1
Fractional
QFM
Fractional
QFM-1
En
Fs
Fo
Fa

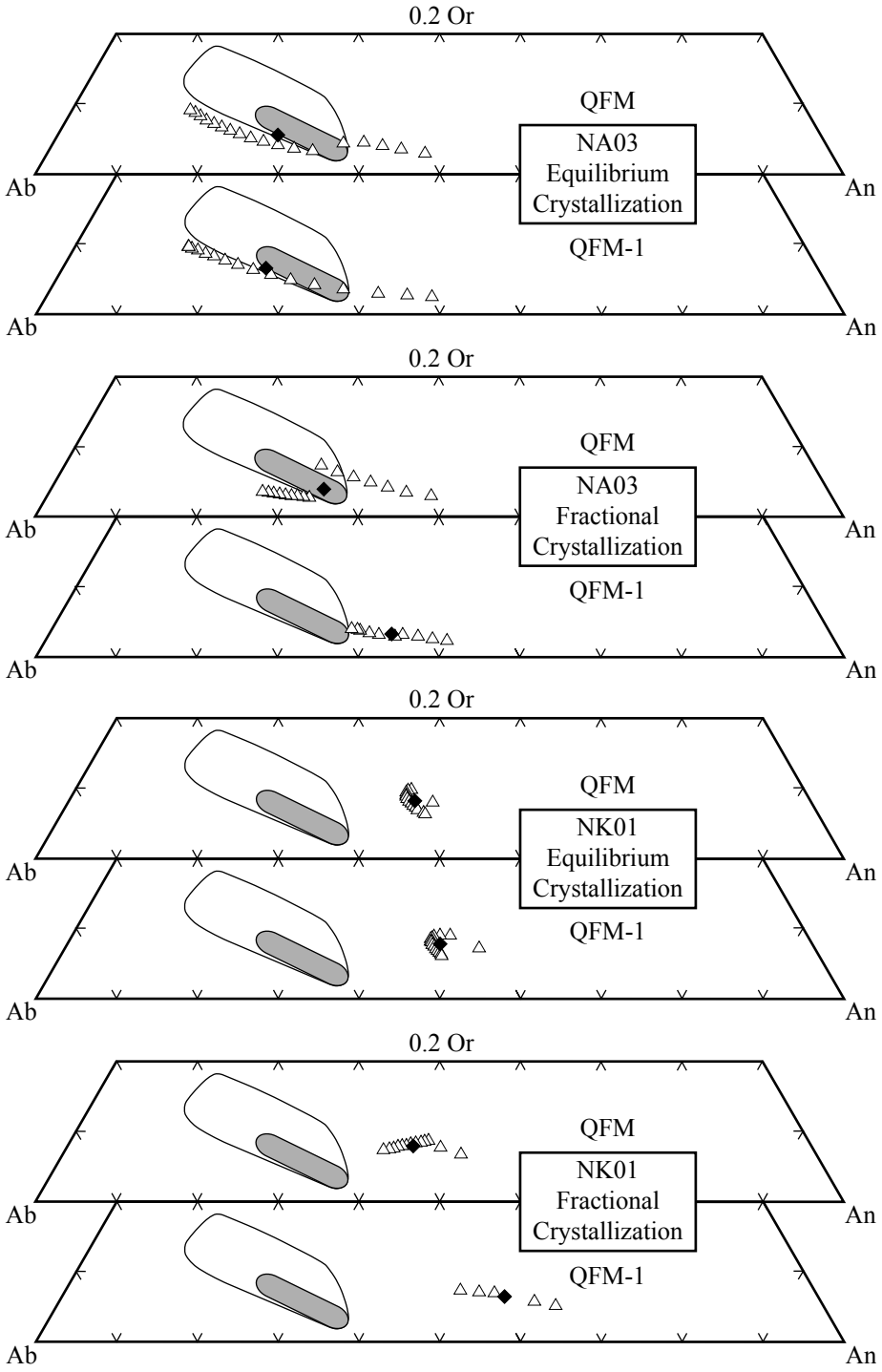

Figure 6 (con't): (b) Plagioclase compositions from MELTS crystallization models for NA03 and NK01. Triangles represent plagioclase compositions from the model and the black diamond represents the average of these plagioclases. Gray area outlines measured plagioclase compositions in most nakhlites (*Berkley et al.*, 1980), whereas the outlined area includes plagioclase compositions measured in NWA 817 (*Sautter et al*., 2002).

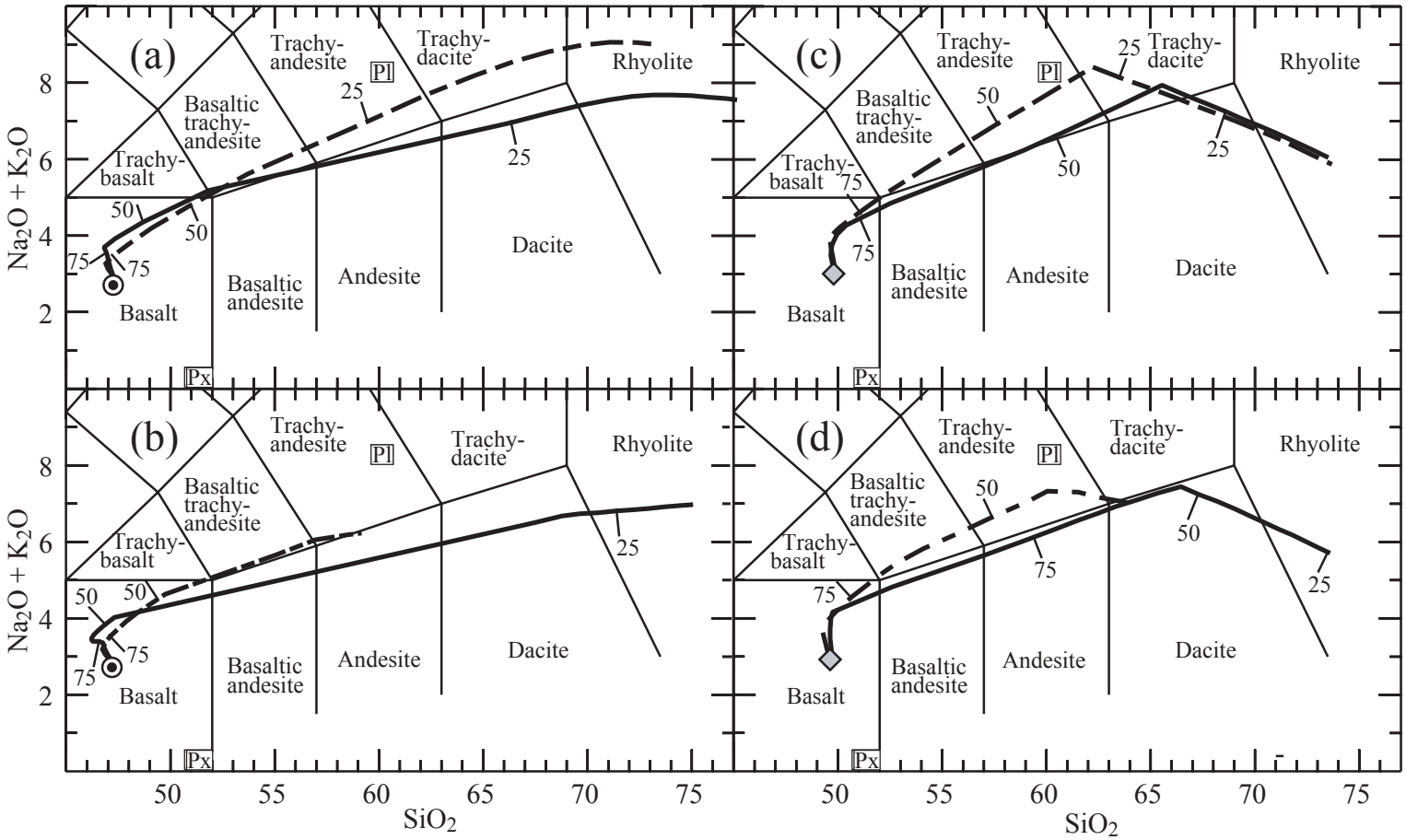

Figure 7: Calculated evolutionary paths of liquid compositions produced from crystallization modeling in MELTS. Plotted on the TAS diagram. Hatch marks along paths indicate 75%, 50% and 25% liquid remaining, unless otherwise indicated. Solid lines represent crystallization at QFM, whereas dashed lines represent crystallization at QFM-1. Starting composition symbols as in Figs. 2 and 3. (a) Equilibrium crystallization of NA03; (b) Fractional crystallization of NA03 (QFM-1 path stops at 30% liquid remaining); (c) Equilibrium crystallization of NK01; (d) Fractional crystallization of NK01 (QFM-1 path stops at 31% liquid remaining).

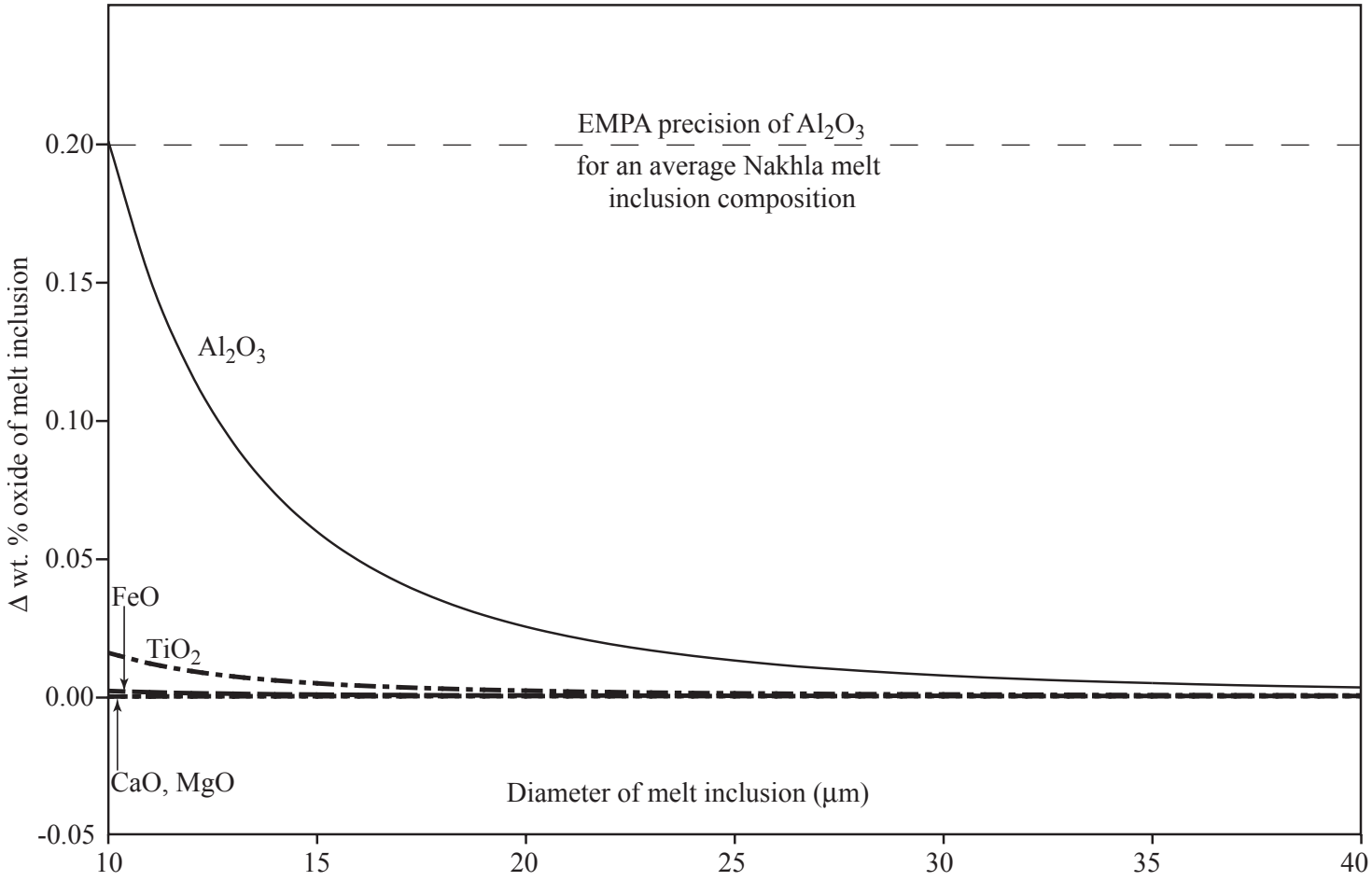

Figure 8: Evaluation of the magnitude of the boundary layer effect on the composition of melt inclusions of variable sizes, as suggested by *Treiman* (2003). The difference in oxide abundance caused by the boundary layer is below the detection limits of this method for all oxides, except Al_2O_3. For melt inclusions with a diameter of ~16 μm and larger, no compositional effect is detectable by electron microprobe analysis.

Part 3

TES Hyperspectral Analyses of Proposed Paleolake Basins on Mars: No Evidence for In-Place Carbonates

This chapter is a reformatted version of a paper by the same name published in Journal of Geophysical Research - Planets in 2005 by Karen Renée Stockstill, Jeffrey E. Moersch, Steve Ruff, Alice Baldridge and Jack Farmer

Stockstill, K.R., Moersch, J.E., Ruff, S. W., Bladridge, A., and Farmer, J., TES Hyperspectral Analyses of Proposed Paleolake Basins on Mars: No Evidence for In-Place Carbonates, JGR-Planets*, in press*, 2005.

Abstract

Several studies have described photogeologic evidence for paleolacustrine basins on Mars, mostly within impact craters. If these basins contained persistent standing water in the past, they could still contain deposits of evaporite minerals (e.g., carbonates, sulfates). Many such deposits, if exposed at the surface to a sufficient extent, would be detectable in thermal infrared spectra taken from orbit. Using data from the Mars Global Surveyor Thermal Emission Spectrometer (TES), we have conducted a hyperspectral investigation of 43 putative paleolake basins to search for the spectral signatures of evaporite minerals exposed at a scale comparable to the spatial resolution of a single TES pixel (~3 x 5 km). Seven basins displaying sufficient surface-related spectral variation were identified using a principal component analysis on the TES spectral image cube covering the basin and its surroundings and spectral regions of interest (ROIs) were defined. Averaged spectra from ROIs were evaluated using previously developed dust cover index. Those spectra determined to be "dust-free" were analyzed for composition using linear spectral deconvolution. The same spectra were also analyzed using a spectral ratio and a set of carbonate indices developed in the present work. Most TES spectra in this study were well-modeled using only previously-defined TES spectral end members. In addition, the spectral ratios and the carbonate index analyses of these basins

indicated that carbonates are not present in abundances greater than the detection limits of these methods. Therefore, this study did not find any spectral evidence for evaporite deposits in the basins studied.

1. Introduction and background

Drastically different views exist regarding the early Martian surface environment. One view is that present temperature and pressure conditions have prevailed from the earliest of times, in which water could only exist within the ground as permafrost or groundwater and in the ice caps [e.g., *Baker*, 1978; *Carr*, 1983; *Gulick and Baker*, 1989; *Hoffman*, 2000; *Peale et al.*, 1975; *Squyres*, 1984; *Wallace and Sagan*, 1979]. Another view is that of an early, warm, wet Mars [e.g., *Baker*, 2001; *Cabrol and Grin*, 1997; *Forsythe and Zimbelman*, 1995; *Pollack et al.*, 1987; *Schneeberger*, 1989]. Still others suggest that Mars has always been cold, with transient episodes of H_2O cycling [*Baker*, 2001; *Christensen*, 2003; *Lee and McKay*, 2003]. If the atmosphere was indeed warm enough and the atmospheric pressure high enough, standing water could have been stable at the surface for long periods on early Mars. The stability of standing water at the surface is directly relevant to the question of whether life could have arisen and persisted on early Mars [e.g., *Farmer and Des Marais*, 1999].

Many geomorphic features on Mars provide compelling evidence for an early period of hydrologic activity, requiring abundant and persistent liquid water at the surface [e.g., *Carr*, 1996]. The small valley networks, as well as the high degree of erosion of large impact craters, suggest that early Mars was indeed warmer and wetter than at present. Several studies have argued that photogeologic evidence supports the existence

of paleolake basins on Mars [*Cabrol and Grin*, 1999; *Forsythe and Zimbelman*, 1995; *Malin and Edgett*, 2000]. The sedimentary layers described by *Malin and Edgett* [2000] are also found within some of the proposed paleolake basins.

Cabrol and Grin [1999] presented a survey of 179 possible paleolake basins in Martian impact craters. They identified different types of paleolake basins, depending on their relationship to neighboring basins. The three types of basins identified include closed, open and lake-chain systems. In addition, these basins were categorized according to the types of channels associated with them as "fluvial valley network", "outflow", or "fretted". These authors also identified possible sedimentary structures within each basin that might support the existence of paleolake deposits. The features proposed include lacustrine deltas, sedimentary terraces, layering, shorelines, mounds, and alternating bands of light and dark albedo materials.

Some of the putative basins display alternating bands of light and dark albedo materials that are conformable to basin margins, or bright materials exposed in the central portion of basins [*Cabrol and Grin*, 1999]. These authors suggested that bright material, such as that which forms the "White Rock" deposit in Pollack Crater, might be evaporite deposits; however, this idea is controversial [*Ruff et al.*, 2001]. On Earth, playa basin evaporites often display a characteristic spatial pattern resulting from their order of deposition [e.g., *Eugster*, 1980; *Eugster and Hardie*, 1978; *Jones*, 1965]. Carbonates, being the least soluble of the salts, are deposited in marginal basin areas. Sulfates have an intermediate solubility and precipitate at more basinward locations. Chlorides precipitate last in the central portions of the basins. In plan view, this depositional

sequence appears as a bulls-eye pattern (e.g., Deep Springs Basin, Inyo County, California, as described by *Jones* [1965].)

Geochemical and thermodynamic models predict a similar sequence of evaporite deposits within Martian paleolake basins [e.g., *Catling*, 1999; *Clark and Van Hart*, 1981]. In addition, these studies assessed which varieties of these evaporite minerals were mostly likely deposited within the Martian lacustrine environments. *Clark and Van Hart* [1981] showed that Fe-bearing carbonates would be most stable under current Martian conditions. *Catling* [1999] agreed that siderite ($FeCO_3$) would be the first carbonate to precipitate, followed by calcite ($CaCO_3$) and then hydromagnesite ($Mg_5(CO_3)_4(OH)_2 \bullet 4H_2O$). The most abundant sulfate mineral would be magnesium sulfate ($MgSO_4 \bullet nH_2O$), which could exist in multiple stable forms, dependent on the number of water molecules present [*Clark and Van Hart*, 1981]. Another cation expected to be in solution is calcium, which *Catling* [1999] noted would be deposited primarily as gypsum ($CaSO_4 \bullet 2(H_2O)$) beds rather than calcite. Finally, the most stable chloride would be halite (NaCl) [*Clark and Van Hart*, 1981].

The presence of carbonates, sulfates, and chlorides has been noted in martian SNC meteorites. *Carr et al.* [1985] demonstrated the presence of carbonate in Nakhla through stepped combustion analyses. These workers attributed the presence of carbonates to hydrothermal alteration of the rock while on Mars. *Chatzitheodoridis and Turner* [1990] were the first to identify siderite in Nakhla. *Gooding et al.* [1991] showed that carbonate and sulfate minerals had been deposited along cracks by low-temperature, hydrous alteration. *Grady et al.* [1995] demonstrated with carbon isotopes that the carbonate underwent isotopic exchange with fluids that were in contact with the Martian

atmosphere. In addition, *Bridges and Grady* [2000] identified anhydrite, chlorapatite, halite and siderite in Nakhla, which they proposed represented crustal materials that were incorporated by Nakhla's parent lava flow.

Another martian meteorite that apparently contains evaporite minerals is ALH84001. This sample is more pertinent to the investigation of Martian paleoenvironments because its radioisotopic age (4.5 ± 1.3 Ga) is significantly older than other SNC meteorites [*Nyquist et al.*, 1995]. How and when the carbonates formed are somewhat controversial, although the isotopic compositions of the carbonate minerals retain an extraterrestrial (martian) signature [*Jull et al*., 1997; *Jull et al.*, 1995]. The carbonates formed early in Martian history, with ages ranging from 3.83 ± 0.15 Ga [*Turner et al.*, 1997] to 4.04 ± 0.01 Ga [*Borg et al.*, 1999], and include several distinct generations of carbonate formation [*Corrigan and Harvey*, 2004]. *Warren* [1998] argued that the carbonates formed as evaporite deposits from floodwaters that percolated through fractures of ALH84001, but noted that this exposure must have been brief to avoid aqueous alteration of the rock. *McSween and Harvey* [1999] suggested that the isotopically heavy composition and oxygen isotope zonation observed in the carbonates are consistent with direct precipitation from a ponded evaporating brine that had infiltrated into fractures in the floor of the crater from which the meteorite was later ejected.

Hydrated sulfates in light-toned layered deposits in and around Valles Marineris, Margaritifer Terra, and Terra Meridiani have been remotely detected by the Observatoire pour la Minéralogie, l'Eau, les Glaces, et l'Activité (OMEGA) instrument aboard the European Space Agency Mars Express [*Gendrin et al.*, 2005]. These deposits correlate

with layers at a variety of elevations and range in extent of aerial exposure from sub-km to 100s of km on a side [*Gendrin et al.*, 2005]. In addition, OMEGA has identified a large deposit (i.e., 60 km by 200 km) of calcium-rich sulfates, most likely gypsum, in a region corresponding to dark longitudinal dunes of Olympia Planitia near the north pole of Mars [*Langevin et al*., 2005]. It should be noted, however, that OMEGA has not detected carbonates above the detection limit of a few percent [*Bibring et al*., 2005].

Within the thermal infrared spectral region (1670-200-cm^{-1} or 6-50 μm), minerals have diagnostic absorption features that result from vibrational modes within crystal lattices [e.g., *Christensen et al.*, 1992; *Lyon*, 1965; *Lyon and Lee*, 1970; *Salisbury et al.*, 1994]. Carbonates display absorption features at approximately 1540, 890, 730 and 330 cm^{-1} (6.5, 11.2, 13.7 and 30.3 μm, respectively) as a result of vibrations within the CO_3 structure [e.g., *Adler and Kerr*, 1962; *Adler and Kerr*, 1963*a*; *Adler and Kerr*, 1963*b*; *Huang and Kerr*, 1960; *Keller et al.*, 1952; *Lane and Christensen*, 1997]. Sulfate minerals display absorption features at approximately 1160, 680, and 600 cm^{-1} (8.6, 14.7, and 16.7 μm, respectively) as a result of vibrations in the sulfate anion [*Adler and Kerr*, 1965; *Lane and Christensen*, 1998]. The strong ionic bonding of chlorides prevents individual bond vibrations; instead, the entire crystal lattice vibrates. The resulting spectral signature of chlorides includes an absorption feature much broader than the relatively discrete bands seen in the emissivity spectra of carbonates and sulfates [e.g., *Lane and Christensen*, 1998]. However, this broad absorption feature may be indiscernible in the thermal infrared spectrum of a rock, so this wavelength region is not ideal for the detection of chlorides. Additional mineral groups (such as oxides, phosphates, and clays) show diagnostic spectral features within the thermal infrared

spectral region [e.g., *Christensen et al.*, 1992; *Lyon*, 1965; *Lyon and Lee*, 1970; *Salisbury et al.*, 1994].

Global-scale searches using TES data so far have detected only two mineral signatures of possible aqueous origin: coarse-grained crystalline hematite [*Christensen et al.*, 2000*c*] and a minor (~2 to 5 weight %) component of carbonate in fine-grained surface dust deposits [*Bandfield et al.*, 2003]. Although carbonates may be a minor component of the surface dust deposits, a global search by *Bandfield* [2002] did not reveal any large-scale occurrences of evaporite minerals on Mars. Even an intensive study of "White Rock", a feature suggested as a candidate evaporite deposit since the days of the Mariner 9 mission [*McCauley*, 1974; *Ward*, 1979; *Williams and Zimbelman*, 1994; *Zimbelman and Kieffer*, 1979], has not revealed evaporite minerals [*Ruff et al.*, 2001]. However, minor, spatially-confined exposures of evaporite mineral deposits may have been missed in global-scale searches. The importance of these minerals to our understanding the history of Martian surface environments is the motivation for the current study.

In the global mineral maps generated from TES data, the spectra were spatially binned to increase the signal-to-noise ratio as well as to reduce the data volume being processed [*Bandfield*, 2002]. This practice "dilutes" the spectral contribution of surface components that are smaller than the bin size of the map. For example, the most detailed global surface emissivity map produced to date [*Bandfield*, 2002] averages TES spectra into a map of 0.25 x 0.25º bin pixels, which corresponds to the area of approximately 15 individual TES footprints at the equator. The individual TES footprints within a given

bin do not necessarily cover the area of the bin evenly, and for many bins, there is only sparse, partial TES coverage of the area within a bin.

We have conducted a detailed TES hyperspectral analysis of proposed Martian paleolake basins using the list of sites presented by *Cabrol and Grin* [1999]. The objective of this work was to search for exposures of evaporite minerals, especially carbonates, within these basins at a spatial scale of a few TES pixels (a few 10s of km^2). The approach of this study differs from previous searches for *in situ* evaporites in several ways. First, all spectra were assembled into a hyperspectral cube without binning multiple TES spectra, which could preserve potential spatial relationships otherwise lost if data are binned. Second, no atmospheric removal was performed before mapping to preserve subtle surface spectral signatures that might otherwise be removed in the process of atmospheric correction. Third, we use a spectral ratio of the measured spectrum to the modeled spectrum to ascertain how well the TES atmospheric and surface end members model the region of interest (ROI) spectrum. Finally, we have developed carbonate indices that can be applied to spectra that still contain atmospheric components in order to search for spectral evidence of these minerals.

This approach allowed us to look for spatial patterns characteristic of playa deposits (i.e., the previously-described "bulls-eye" distribution pattern). In addition, we can examine how well previously-known TES atmospheric and surface end members can be combined to model the observed spectra from ROIs (i.e., whether or not additional end members are needed to better the fit). Finally, we can apply the carbonate indices as an additional test for spectral signatures of calcite, siderite and magnesite.

2. Methods

TES emissivity spectra were assembled into hyperspectral data cubes for the 80 largest putative paleolake basins identified by *Cabrol and Grin* [1999]. These data cubes were composites of TES data acquired during separate orbital passes. Spectral variation in the scene was enhanced using principal component analysis (PCA). This allowed the identification of those orbits whose major variation was due to atmospheric dust and ice. For example, the atmospheric components of a given orbit may differ in both amount and/or type (e.g., dust vs. water ice clouds) from the atmospheric components of other orbits in the scene. In a 3-color band PCA image, the orbit(s) with the most anomalous atmospheric component abundances would have a different color than the orbits with more typical atmospheric component abundances.

Because we were interested in surface spectral variation, spectra from orbits whose atmospheric component differed substantially from the scene's average atmospheric component were removed from the data cube. This process was repeated until most spectral variation within the scene was related to spectral variation of the surface spanning observations from multiple orbits. At that point, each potential surface spectral end member was defined as an ROI and their mean spectra were collected. Mean ROI spectra could then be unmixed using the linear deconvolution technique of *Smith et al.* [2000*a*] and evaluated using the spectral ratio technique and the carbonate indices. A more detailed discussion of these methods follows and is diagrammed in Figure 1.

2.1. Data compilation and processing

Spectra for this study include only those from nadir-pointing, daytime observations with TES orbit numbers (OCK) 1683-7000 and are further constrained to

exclude data at risk for increased noise due to motion of the spacecraft's solar panel and high-gain antenna (HGA) and errors resulting from major phase inversions. The spectra for a given target area were assembled into a hyperspectral image cube using custom software we have written for ITT Industries' ENVI remote sensing software package. For each hyperspectral image cube, an ancillary data cube was also constructed, which contains data planes for the latitudes, longitudes, TES temperatures, and TES albedos of every pixel, as well as observational data such as the TES OCK and ICK numbers. Steps involved with the assembly of the TES hyperspectral and ancillary data cubes are diagrammed in Figure 1 (Step 1).

On Mars, the occurrence of water-ice clouds is highly variable in space and time [*Pearl et al.*, 2001]. In addition, there is variability in dust opacity of the Martian atmosphere due to both the regional and global-scale dust storms and seasonal trends [*Smith et al.*, 2000*b*]. As a result, if no atmospheric correction is applied, averaging spectra from multiple orbits also has the effect of complicating the atmospheric component. For this project, we chose to not bin individual TES spectra when making our hyperspectral image cubes. Where orbital tracks overlap, our custom software allows the user to choose to overlay the orbits with the highest brightness temperature or lowest corresponding TES albedo; data with the lowest TES albedo should correspond to the highest brightness temperature. For this project, geographic locations with overlapping TES footprints were assembled so that only the spectrum with the lowest corresponding TES albedo was used for a given location. We also tried an algorithm that chose the spectrum with the highest brightness temperature, but found that this approach did not work as well in minimizing atmospheric variability in a hyperspectral scene. This

approach helps to avoid displaying orbit tracks where excessive atmospheric dust opacity raises the apparent albedo of the scene. Such spectra should have the highest spectral contribution from surface.

In order to distill the enormous amount of data contained within the hyperspectral cubes, a type of principal component analysis (PCA) was used. In a given hyperspectral cube, emissivity values are typically highly correlated from one spectral band to the next. Each spectrum in the cube can be treated as a point in n-dimensional space, where n is the number of spectral bands. Spectral data plotted in this space forms a cloud of points. The original coordinate system can be translated and rotated to maximize the variance of the data cloud along a new set of orthogonal axes, and then the data cloud is rescaled to fit the full available dynamic range along each of the new axes. The axes in the new coordinate system are the principal components of the data. PCA axes are ordered according to the degree of variance of the data cloud along each axis and each axis has an associated eigenvalue from the operation. Principal component bands with the highest eigenvalues are usually associated with true spectral end members.

TES data contains very subtle spectral differences, which are often not detected by automated routines available in ENVI. However, when the PCA bands with the highest eigenvalues are displayed as a 3-band color image, these subtle spectral differences are enhanced and pixels of similar spectral character appear as the same color. The human eye is adept at recognizing spatial clustering of color in these images, allowing the user to observe contiguous areas of color. Therefore, this technique has two advantages over automated methods available in ENVI. First, it is very sensitive to

subtle spectral differences present in TES data and, second, it allows for the spatial relationship of pixels with similar spectral character to be considered.

The PCA application used for this study was the Minimum Noise Fraction (MNF) in ENVI [*Green et al.*, 1988]. A forward MNF rotation was performed, estimating the noise statistics from the data. A data mask was applied so that areas lacking data were not included in the MNF statistics. The MNF used 106 of the 143 TES bands, from 232 to 1651 cm^{-1}, excluding bands within the CO_2 absorption band from 518 and 815 cm^{-1}. Most previous studies discard bands higher than ~1300 cm^{-1}, due to decreased signal-to-noise at higher wavenumbers [e.g., *Smith et al.*, 2000]. In this study, additional bands were used for the MNF rotation because there is a prominent carbonate band centered near 1550-cm^{-1}. If carbonates were present, we would expect to see large spectral variability at these higher wavenumbers. The MNF transform segregates noisy spectral channels into higher order MNF bands, which are not used in subsequent analysis. If the prominent band (1550-cm^{-1}) appears at a level stronger than the noise, it will be segregated into a lower order MNF band. This rotation produced a 106-band MNF file, which could then be displayed, three bands at a time, as RGB composite images. This step is diagrammed in Figure 1 (Step 2).

The first three MNF bands, which represent the most significant spectral variation in the scene, were displayed as an RGB color composite image. (Additional RGB combinations using higher order MNF bands did not display independent spectral components and were therefore not used in this study. However, they were often displayed to confirm consistency.) This was done to identify spatially correlated spectral units in the scene, which showed up as regions of contiguous color in the RGB composite

image. This technique proved very effective in identifying orbits with anomalously high or low atmospheric contributions or other problems (Figure 2a). The underlying assumption is that areas of contiguous color that span multiple orbits in the MNF color composite image are related to the spectral character of the surface, whereas areas of contiguous color that are confined to particular orbit tracks are related to variations in spectral contributions from atmospheric dust and ice. The orbital tracks covering a scene are not necessarily acquired contemporaneously by TES; therefore, the spectral contributions of atmospheric components can sometimes vary greatly from one orbital track to the next.

The hyperspectral cube was re-assembled, omitting qualifying problematic orbits from the previous iteration(s). This process was repeated until most spectral variation in the MNF composite scene was related to surface spectral units. (We define a surface spectral unit as an area of the martian surface that displays distinct spectral properties in TES data. In a 3-band MNF color composite image, a surface spectral unit stands out as contiguous areas of a particular color.) Note that this removal of problematic orbits is not the same as a correction or removal of atmospheric spectral features. Rather, the process described acts to eliminate spectra with anomalously high or low atmospheric contributions. The result is a hyperspectral image cube in which the atmospheric contributions are relatively constant across the scene. More precisely, the degree of spectral variance caused by atmospheric components in the resulting scene is less than that caused by surface-related spectral variations. This makes our TES hyperspectral image cubes comparable to typical hyperspectral cubes from terrestrial remote sensing instruments, where an entire scene is usually acquired in a very short span of time and the

atmospheric component is essentially constant (neglecting elevation variations and discrete clouds). The main drawback to this strategy is a reduction in spatial coverage. An example of a final TES MNF image, in which most of the spectral variation related to atmospheric variation has been removed, is shown in Figure 2b.

After reconstructing the hyperspectral cube without problematic orbits, the first three (most significant) MNF bands were displayed as a RGB color composite image. On this color composite image, possible surface spectral end members were identified within the scene (Figure 1, Step 3). These surface spectral end members appeared as areas of similar MNF values (i.e., areas of contiguous color on the RGB composite image) and were outlined using ENVI's Region of Interest tool (Figure 2c).

The ROIs were overlain on the original emissivity data and the mean emissivity spectra for each region were collected. This method of spectral averaging provides the same type of SNR-enhancing benefit that simple geographic binning [e.g., *Bandfield*, 2002] affords. However, our technique also avoids the problem of spatially "diluting" minor spectral components because only pixels of similar spectral nature are averaged together in custom-tailored regions of interest.

Mean ROI spectra were evaluated using the dust cover index (DCI) of *Ruff and Christensen* [2002] (Figure 1, Step 4). The DCI exploits the short wavelength absorption feature resulting from particle size effects of silicate particles $<<100\mu m$ in size and can be used to identify surfaces that range from "dust-free" to "dust-covered". The DCI value is calculated by averaging the apparent emissivity from 1350- to 1400-cm^{-1}. The DCI values for dust-covered surfaces are ≤ 0.940, whereas dust-free surfaces have values ≥ 0.962. The spectra of dust-covered surfaces so-defined contain nothing but the same

spectral signature of dust seen in all dusty regions of the planet. Because these spectra revealed nothing about the underlying surface composition, they were of no value to this study and were discarded. DCI values were also found to correlate with the amount of "high albedo surface" spectral end member indicated in the initial spectral deconvolution step (see below).

2.2. Linear deconvolution of TES spectra

The mean emissivity spectrum from each region of interest was deconvolved using the linear deconvolution technique of *Smith et al.* [2000] and *Bandfield et al.* [2000*b*]. The deconvolution technique fits the measured TES apparent emissivity spectrum in a linear least squares sense using both atmospheric spectral shapes and surface spectral shapes simultaneously. This strategy is based on the empirical finding that atmospheric spectral components may be treated as linearly-mixed end members in emissivity-space [*Feely and Christensen*, 1999; *Gillespie*, 1992; *Ramsey and Christensen*, 1998; *Smith et al.*, 2000; *Thomson and Salisbury*, 1993].

Mean ROI spectra were modeled by deconvolution multiple times using different spectral end member sets. One set of spectral end members consisted of the TES Acidalia-type end member, the Syrtis-type end member, the hematite end member [*Bandfield et al.*, 2000*a*] and an average high albedo surface end member [*Bandfield and Smith*, 2003]. Atmospheric spectral end members included a high CO_2 dust end member, a low CO_2 dust end member, and two water-ice cloud end members [*Bandfield et al.*, 2000*a*]. These comprise the eight previously-identified global TES end members (Figure 1, Step 5a).

Next, another deconvolution of the mean ROI spectra was performed using the four TES atmospheric end members, the average high albedo surface end member, and thirty-one laboratory spectra of igneous minerals that have been used to model the TES surface end members [*Christensen et al.*, 2000*b*] (Figure 1, Step 5b).

Finally, yet another deconvolution of the mean ROI spectra was performed using the four TES atmospheric end members, the average high albedo surface, the same thirty-one igneous minerals and twenty-four candidate evaporite minerals (e.g., carbonates, sulfates and chlorides) [*Lane and Christensen*, 1997] (Figure 1, Step 5c). Spectral end members used for each type of deconvolution are listed in Table 1. The results of these deconvolution runs show that sulfate end members were never used in significant amounts. In fact, the maximum amount of sulfate used in any spectral deconvolution was 4.2%, well below their lower detection limit of 15% [*Christensen et al.*, 2001*b*]. However, carbonates were commonly included in the 5-10% range, approaching their lower detection limit, which has been estimated to be from 5% [*Christensen et al.*, 2000*a*; *Hamilton and Christensen*, 2000] to 10% [*Bandfield*, 2002; *Christensen et al.*, 2001*b*]. Consequently, it was necessary to determine whether such small amounts of carbonate end members used by the deconvolution were "real" or due to other factors. Two separate strategies, described below, were developed to address this uncertainty: a spectral ratio technique and a spectral-feature index technique.

2.3. Carbonate detection strategies

2.3.1. Spectral ratio technique

The spectral ratio technique uses the ratio of the measured ROI spectrum to the deconvolution modeled spectrum in an effort to highlight residual surface spectral

features that are not well modeled by the eight TES end member spectra (Figure 1, Step 6). This ratio uses the modeled spectrum produced by linear deconvolution using the previously-known TES end members (Figure 1, Step 5a); no additional mineral spectra were provided as spectral end members, because we intended to test how well the measured spectra were modeled using only the TES end members. This technique relies on the fact that the eight TES end members are dominated by relatively broad and deep features that would not mask the narrower features of carbonates or other minerals.

To demonstrate this, we mathematically mixed a non-atmospherically-corrected average spectrum from Syrtis Major with three representative carbonate spectra at the 10% level (reduced by 40% spectral contrast, as described below), then deconvolved them using the TES end members and examined the resulting spectra. Ideally, these mixtures would use TES-derived carbonate spectra; however, TES-derived carbonate end members (other than the fine-grained dust spectrum, which we are not searching for) do not exist. Therefore, we are forced to use laboratory carbonate spectra in these mixtures to test the spectra ratio technique or carbonate indices for sensitivity to carbonate end members. Additional confidence in our technique is derived from using multiple approaches to search for carbonates.

The measured and modeled spectra from the Syrtis end member and Syrtis-carbonate mixtures are shown in Figure 3a. For the Syrtis end member spectrum, the boxes located near 890-cm^{-1} and 350-cm^{-1} define the spectral region of two carbonate absorption features. One additional absorption feature of carbonates exists at ~1540-cm^{-1} and is the deepest absorption feature for carbonates. However, *Christensen et al.* [2001*b*] demonstrated that there is significant spectral structure in the 1200- to 1650-cm^{-1} region

in TES data due to atmospheric CO_2 and H_2O, which complicates the use of this region for carbonate studies of Mars.

For each mixture, the vertical lines mark the spectral locations of the deepest part of the 890-cm^{-1} and 350-cm^{-1} absorption features for the appropriate carbonate. For comparison, these lines have the same vertical scale as the boxes on the Syrtis-only plot. The input spectra of these mixtures have a small, sharp absorption feature near 890-cm^{-1} and a broader feature near 350-cm^{-1} due to carbonates (compare Figure 4a). A ratio of the measured to modeled spectra emphasizes the location and shape of features that are present in the former but absent in the latter (Figure 3b). Where the ratio deviates from unity, there may be an absorption not well modeled by the deconvolution routine, or a residual absorption feature. When a residual absorption feature was identified within a spectral ratio, both the location and the width of the deviation were considered when trying to identify the mineral causing the absorption.

In Figure 3b, the distinctive carbonate features are evident in the ratio spectrum of each of the three mixtures. Notice that, although the 890-cm^{-1} feature for the siderite mixture is quite distinct, the 350-cm^{-1} feature is less obvious. This is due to the relatively broad, shallow 350-cm^{-1} absorption feature of siderite (Figure 4a). It should be noted that the sensitivity of this technique depends upon the depth and width of a mineral absorption feature (also related to the grain size present). Deeper, sharper absorption features will be more easily recognized by this technique. Regardless, Figure 3b demonstrates that a ratio of a measured spectrum to a spectrum modeled using deconvolution with only the eight TES end members can be sensitive to residual components, specifically carbonates.

The carbonate spectra used in the above mixtures and as end members in the deconvolution of ROI spectra were obtained from single crystal hand samples [*Lane and Christensen*, 1997]. However, carbonates found in terrestrial dry lakes are precipitated as mm-thick carbonate lamina, micritic carbonate mud, intra-sediment coatings, or hard surface crusts [*Eugster*, 1980; *Eugster and Hardie*, 1978]. In the thermal-IR, spectral contrast is muted in particulate samples compared to their solid, crystalline counterparts due to an increase in porosity (specifically, an increased number of grain/air interfaces and the decreased optical thickness of individual particles) and subsequent incoherent scattering of light from multiple surface reflections [*Hunt and Vincent*, 1968; *Kirkland et al.*, 2002; *Lane*, 1999; *Lyon*, 1965; *Moersch and Christensen*, 1995]. Therefore, the crystalline sample spectra were reduced in spectral contrast, to approximate that of particulate samples. Previous comparisons of rock and particle spectra of the same composition showed typical contrast reductions of ~40% [*Lane*, 1999; *Ruff*, 1998]. Comparison between carbonate spectra of hand samples and 710-1000 micron particles are also consistent with a 40% reduction in spectral contrast. Therefore, the carbonate end member spectra used in this study have artificially-reduced spectral contrast representative of a 710-1000 micron particle size. This assumption of reduced spectral contrast is reasonable in the context of this study, considering that natural surfaces on Mars are likely to be rough or particulate. However, features resulting from a non-contrast-reduced carbonate component would be even easier to see at the 10% mixing level in ratio spectra (e.g., those in Figure 3b).

2.3.2. Carbonate spectral indices technique

To further address the identification of carbonates in the Mean ROI spectra, we created spectral indices sensitive to carbonates, to look for the presence of calcite, magnesite and siderite features (Figure 1, Step 7). Similar in concept to the hematite index of *Christensen et al.* [2000*a*], the dust cover index of *Ruff and Christensen* [2002] and the bound water index of *Ruff* [2004], our carbonate indices were tuned to be sensitive to the carbonate absorption features near 890-cm^{-1} and 350-cm^{-1} (Figure 4a).

The exact positions of the minima of carbonate spectral absorptions vary with composition and this variation is sufficient to distinguish between them at TES (10-cm^{-1}) spectral resolution [*Lane and Christensen*, 1997]. Although spectra of other minerals (e.g., silicates) may also have absorptions near these same wavenumbers, carbonate spectra are unique in that the absorption feature near 350-cm^{-1} is between 1.75 and 2.63 times deeper than the 890-cm^{-1} absorption feature (Figure 4a). Therefore, the depths of these two absorptions relative to each other may be used to distinguish carbonate spectra from the spectra of other mineral classes. As will be shown, this band depth relationship persists in mineral mixtures and would still be present in non-atmospherically-corrected TES spectra.

Our carbonate indexing procedure works as follows: First, we test the ROI spectra to see if either of the carbonate spectral features is present. Windows of TES channels are defined on both sides of the absorption and an average local continuum value is calculated for both windows. These two average values are used to calculate an interpolated continuum value at the same wavenumber as the minimum of the absorption feature (Figure 4b). This predicted continuum emissivity is divided by the measured

apparent emissivity at the same wavenumber to give an "absorption index". If the absorption is present, the absorption index ($I_{Abs,\ x,\ A}$ or $I_{Abs,\ x,\ B}$, where *x* is the carbonate mineral of interest, *A* is the absorption feature in the 350-cm^{-1} region and *B* is the absorption feature in the 890-cm^{-1} region) will be greater than one.

Once the absorption index is calculated for both absorption features, the relative band depth (RBD) for each feature is calculated as follows:

$$RBD_{x,\ A} = 1 - (I_{Abs,\ x,\ A})^{-1}$$

and

$$RBD_{x,\ B} = 1 - (I_{Abs,\ x,\ B})^{-1}.$$

Next, if the calculated relative band depth indicates that both absorption features are present in the measured spectrum, we check to see if these features are present in the proportions expected based on lab spectra. The relative band depth ratio (RBDR) of the two band depths is calculated by dividing the RBD of the deeper absorption in the 360-cm^{-1} region by the RBD of the relatively shallow absorption in the 890-cm^{-1} region.

$$RBDR(x) = RBD_{x,\ A} / RBD_{x,\ B}.$$

We then compare the RBDR value for the unknown spectrum to the RBDR value calculated using the lab spectrum of the specific carbonate mineral sought to see if the bands are present in approximately the right proportions. For all carbonate mineral spectra, the RBDR values range from 1.75 (siderite) to 2.63 (calcite).

Because carbonate features are relatively narrow and RBD values are calculated using local continuum values in the immediate vicinity of the absorptions, the RBDR value in spectra of mixtures is not strongly affected by other non-carbonate spectral components with broad features that might affect the overall shape of the spectrum. However, spectral mixing may lead to some small departures from the ideal RBDR values derived from monomineralic lab spectra. Therefore, for application to ROI spectra, a range of acceptable RBDR values was defined for each mineral index. As we have defined it, the carbonate indices method is only successful if an index only detects the carbonate for which it was designed (i.e., does not detect other minerals, including other carbonates). Therefore, the range of acceptable RBDR values was constrained to ensure detection of only the mineral of interest. The absorption index, relative band depth and relative band depth ratio for representative mineral spectra calculated by this method are shown in Table 2. Notice that the carbonate indices are insensitive to the carbonate that has been detected in the surface dust component (average high albedo surface in Table 2), as detected by *Bandfield et al.* [2003].

To determine the sensitivity of the carbonate indices method, we applied each index to synthetic spectra created by numerically mixing TES emissivity spectra of bright and dark surfaces from *Ruff and Christensen* [2002] with varying amounts of contrast-reduced carbonate spectra. The mix with the smallest amount of a particular carbonate to give a positive detection with our index method was defined as the lower detection limit for the mineral in that surface type. Lower detection limits for the indices are shown in Table 3.

In addition, we applied the calcite index to spectra of a suite of calcite samples with a range of particle sizes [*Lane*, 1999]. This suite includes spectra for the following particle sizes: 710-1000 μm, 500-710 μm, 355-500 μm, 250-355 μm, 180-250 μm, 125-180 μm, 90-125 μm, and <63 μm. As particle sizes get smaller, the two absorption features shallow out, but not at the same rate. Specifically, the shallower 890-cm^{-1} feature shallows out faster than the deeper 360-cm^{-1} feature. As a result, the relative band depth ratio is higher than seen for the single crystal calcite spectra (2.53), ranging from 3.54 to 4.68 for the particulate samples (Table 4). Despite this, the calcite index works for the pure particulate calcite samples down to the 125-180 μm group. The 90-125 μm size fraction has a relative band depth ratio outside the acceptable range, but displays the two absorptions features of interest. However, the ≤63 μm size fraction lacks the absorption feature near 890-cm^{-1} and thus has a negative relative band depth ratio (Table 4). Overall, decreasing particle size does not have a significant effect on the carbonate indices, except for the smallest particle sizes (i.e., the 90-125 μm size fraction and smaller).

3. Results

For this study, 80 putative paleolake basins from the survey of *Cabrol and Grin* [1999] were examined. Fifty of these basins were greater than 50 km in diameter; the remaining 30 basins were less than 50 km. No basins below 50 km in diameter displayed evidence of more than one surface spectral unit, possibly indicating a lower size limit for the application of this technique with TES-resolution data. Three of the craters studied were described by *Cabrol and Grin* [1999] as containing photogeologic evidence for

evaporites, whereas six other craters were reported to possibly contain evaporites. Of these nine basins, only Gusev displayed more than one spectral unit.

Of the 80 basins studied in the present work, seven basins have shown evidence of one or more surface spectral units that are distinct from the spectral nature of the surrounding terrain. Of the remaining 73 basins, six did not show spectral differences between the basin and the surrounding terrain, thirty basins contained too much atmospheric variability for successful processing, and there was insufficient TES data coverage within thirty-seven craters. These will not be presented.

3.1. Craters well-modeled by TES spectral end members only

Six of the seven basins displaying more than one spectral end member were well-modeled using TES spectral end members only. These basins include Schiaparelli Crater, Aram Chaos, Gusev Crater, Becquerel Crater, Gale Crater, and one crater located in Terra Sabaeus (crater number 107 from the *Cabrol and Grin* [1999] list). Two of these basins, Aram Chaos and Gale Crater, will be presented below as examples of basins that did not require additional spectral end members to explain the variation present in ROI spectra.

3.1.1. Aram Chaos (2.8N, 21.2W)

Aram Chaos is a 260 km-diameter basin in the Oxia Palus quadrangle that has previously been noted to contain hematite, suggested to be an *in situ* sedimentary layer composed primarily of basaltic sediments [*Christensen et al.*, 2001*a*]. *Cabrol and Grin* [1999] classified this basin as a closed paleolake basin with an associated outflow channel and as containing a delta, sedimentary terraces, layering, shorelines and a central

mound. The hematite contained within this basin is thought to have formed during basin infilling and has more recently been exposed by erosion [*Christensen et al.*, 2001*a*].

Figure 5a displays the final MNF color composite image overlain on a MOLA-derived shaded-relief image, with the manually-defined ROIs outlined in white. DCI values demonstrate that no mean ROI spectra for Aram Chaos classify as completely dust-covered surfaces (Table 5). Raw mean ROI spectra for Aram Chaos are displayed in Figure 6a. The northwest crater floor and the northwest and east external terrain appear to have intermediate dust cover, whereas all other regions fall within the range of values for dust-free surfaces (Table 5).

The linear deconvolution results confirm that this region consists of relatively dust-free surfaces, because the surface dust end member was not used for deconvolution of any mean ROI spectra for this basin (Table 5). The mesa tops, shown in aqua in Figure 5a, have a spectrum that was fairly well-modeled using just TES atmospheric end members with Syrtis-type and hematite surface end members (Table 5). Spectra of crater floor units were also well-modeled using atmospheric end members and only the Syrtis-type surface end member (Table 5). The spectra of external terrain units also mapped well using only Syrtis-type surface end member, with no other surface end members above lower detection limits (Table 5). Again, models of the ROIs with intermediate DCI values modeled using more Low CO_2 dust atmospheric end member than did other ROIs. When carbonate end members were provided for linear deconvolution, carbonates were used in amounts ranging from 3% to 8%. Some of these abundances were close to the detection limits of carbonates, so we could not say with certainty, based on deconvolution alone, that their signature is not present in the spectra. Therefore, although

linear unmixing of these regions of interest did not require additional end members to explain the spectral variation observed, we did apply additional spectral analyses to confirm this.

For Aram Chaos, the modeled spectra provide good matches to absorption features observed in all of the measured mean ROI spectra (Figure 6b and c). In addition, the measured-to-modeled spectral ratios for these ROIs display little variation from unity (Figure 6d and e). Therefore, measured mean ROI spectra do not contain any residual absorption features that are not present in their modeled spectra.

The results of the carbonate index analysis for Aram Chaos are displayed in Table 6. No spectral signatures of carbonates were detected in any of the mean ROI spectra from Aram Chaos by this method. Because the linear deconvolution method, the spectral ratio technique and the carbonate spectral indices technique gave no positive indications for carbonates, we conclude that carbonates are not exposed in Aram Chaos in abundances above the detection limits of these methods.

3.1.2. Gale Crater (5.5S, 222.2W)

Gale Crater is a 142 km-diameter crater located near the boundary of cratered uplands and lowlands in Elysium Planitia in the Aeolis Quadrangle. The boundary between the flat-lying cratered uplands and smooth lowlands has a regional slope of 1-2º. Gale appears to have been emplaced on a pre-existing regional slope of ~1º, therefore post-dating the elevation difference between the uplands and lowlands, which occurred in the mid- to late-Noachian [*Frey et al.*, 1998]. Because of the regional slope, the northern rim of Gale Crater is 2 km lower than its southern rim [*Frey et al.*, 1998].

Cabrol and Grin [1997] proposed that the supply of water to create a lake in Gale Crater came from floods in the Elysium Basin overtopping this lower northern rim. These workers also identified 21 layers on the 1000-m central mound in Gale, terracing and drainage systems that they interpreted as evidence for a pre-existing ice-covered lake [*Cabrol and Grin*, 1997]. In addition, crater age dating for proposed lacustrine deposits suggested an early Amazonian age [*Cabrol*, 1997]. More recently, *Cabrol and Grin* [1999] classified Gale as an open basin with an associated outflow channel. It was reported to show evidence for sedimentary layering, sedimentary deposits, shoreline terraces and a central mound.

Pelkey and Jakosky [2002] studied Gale Crater using MOLA, TES and MOC data and found that the crater floor is generally dust free relative to the central mound. The central mound was found to have a thermally thick layer of dust atop a lightly indurated soil. The northern crater floor has a smooth floor interpreted to be a cemented mantle with a thermally thin layer of dust that decreases to the east and west. The crater floor to the east, west and south of the central mound has a smooth floor and crater ejecta material, with the southern floor likely being dust free [*Pelkey and Jakosky*, 2002].

Figure 2c displays the final MNF color composite image overlain on a MOLA-derived shaded relief image, with the manually-defined ROIs outlined in white. The central mound in Gale Crater, shown by the red region in Figure 2c, and the terrain north of the crater, had DCI values indicating a dusty surface (Table 7), consistent with the study of *Pelkey and Jakosky* [2002]. In addition, the results of the deconvolution for these spectra used the surface dust end member (Table 7). These spectra represent

typical dusty surfaces and were not processed further. Raw mean ROI spectra for Gale Crater are displayed in Figure 7a.

The western portion of the basin floor, shown by greens in Figure 2c, has a DCI value just below the threshold for dust-free surface, consistent with the findings of *Pelkey and Jakosky* [2002]. Likewise, linear deconvolution modeling did not use the surface dust end member. The western basin floor ROI is well-modeled using TES atmospheric end members and a Syrtis-type surface (Table 7). The southern and eastern portion of the basin floor, shown by blues and teals in Figure 2c, as well as the terrain south of the crater had a DCI value above the threshold for a dust-free surface and are also consistent with the interpretations of *Pelkey and Jakosky* [2002]. In addition, deconvolution using the standard TES spectral end members did not choose the surface dust end member for these ROIs (Table 7). When carbonate end members were provided for linear deconvolution, carbonates were only used in amounts ranging from 5 to 8%. Because these abundances were close to the detection limits of carbonates, we could not say with certainty that a carbonate spectral signature was not present in the spectra based on deconvolution results alone. Therefore, although linear unmixing of these regions of interest did not require additional end members to explain the spectral variation observed, we did apply additional spectral analyses to confirm this.

The modeled spectra provide good matches to the measured mean ROI spectra for these region of interest mean spectra (Figure 7b). In addition, the measured-to-modeled spectral ratios for these ROIs show very little variation from unity (Figure 7c). Therefore, measured mean ROI spectra do not contain any residual absorption features that are not present in their modeled spectra.

Additionally, the carbonate index analysis for Gale Crater did not detect a contribution from carbonates in either mean ROI spectra (Table 8). This implies that carbonates are not present in abundances greater than the lower detection limit for this technique. Because the linear deconvolution method, the spectral ratio technique and the carbonate spectral indices technique gave no positive indications for carbonates, we conclude that carbonates are not exposed in Gale Crater in abundances above the detection limits of these methods.

3.2. Crater not well-modeled by only TES spectral end members

One basin required additional spectral end members to explain the variation present in ROI spectra and is presented below.

3.2.1. Crater 117 near Ganges Chasm (9.5S, 51.4W)

The crater we informally call C117 is a 68 km-diameter basin within the Coprates quadrangle and is the smallest basin for which surface spectral units could be distinguished, perhaps defining a lower size limit for which this technique can be successfully performed with TES data. This crater was crater number 117 from the *Cabrol and Grin* [1999] survey and was classified as an open paleolake basin fed by a fluvial valley network. Sedimentary structures reported within this basin include sedimentary terraces and deposits, as well as shorelines [*Cabrol and Grin*, 1999]. In addition, recent work by *Hamilton et al.* [2003] identified local-scale (100s-1000s km^2) concentrations of olivine- and orthopyroxene-bearing materials, similar in composition to the martian meteorite ALHA77005, in and near Ganges Chasma.

Figure 5b displays the final MNF band color composite image overlain on MOLA-derived shaded relief. All of the regions of interest have a dust index of 0.964 or

above, indicating dust-free surfaces (Table 9). Raw mean ROI spectra for the C107 area are displayed in Figure 8a.

The floor of the crater was modeled using Syrtis-type surface material with TES atmospheric end members (Table 9). The east-southeast external terrain also models using Syrtis-type material with slightly more TES atmospheric end members (Table 9). However, the terrain southwest of the crater was modeled using a combination of both Acidalia- and Syrtis-type materials combined with TES atmospheric materials (Table 9). The distinct surface spectral unit north of the basin is Ganges Chasma and clearly reflects the additional influence of a greater atmospheric path, due to a large topographic difference between the chasma and surrounding regions (Table 9). When carbonate end members were provided for linear deconvolution, carbonates were used in amounts ranging from 6 to 10%. The deconvolution results of the crater floor ROI spectra used 10.2% carbonates, just above the detection limit of carbonates. Since all model carbonate abundances were close to the detection limits, we could not say with certainty that their signature is not present in the spectra based on deconvolution results alone. Therefore, although linear unmixing of these regions of interest did not require additional end members to explain the spectral variation observed, we did apply additional spectral analyses to confirm this.

The modeled spectra provide fairly good matches to the measured mean ROI spectra of all regions of interest for this crater, with a possible mismatch near 900-cm^{-1} in the north external terrain and the crater floor (Figure 8b). In addition, the measured-to-modeled spectral ratios for the ROIs show some variation from unity in the north external terrain and the regions of interest within the crater (Figure 8c). Both forsterite and

fayalite have deep, broad absorption features in this region (Figure 8c). In fact, the location of the fayalite absorption matches very well to the residual absorption feature present in the spectral ratios of the north external terrain and the crater floor. Furthermore, forsterite and fayalite were used by subsequent deconvolution of these regions. Nevertheless, measured mean ROI spectra do not contain any residual carbonate absorption features that are not present in their modeled spectra.

Application of the carbonate indices method was in agreement with the linear deconvolution method (Table 10). The indices did not detect the signature of carbonates for any region defined for this basin. Because the linear deconvolution method, the spectral ratio technique and the carbonate spectral indices technique gave no positive indications for carbonates, we conclude that carbonates are not exposed in crater C117 in abundances above the detection limits of these methods.

4. Discussion

4.1. Linear deconvolution and detection limits of carbonates

Recent work by *Bandfield and Smith* [2003] used TES multiple emission phase angle observations of the Martian surface to better separate the surface and atmospheric spectral contributions. This technique yielded the first emissivity spectrum of surface dust. The analysis of this spectrum by *Bandfield et al.* [2003] identified a small concentration (~2-5 weight %) of carbonate, dominated by magnesite, present in the surface dust. This carbonate is widely distributed, with no concentrated source indicated. Our rejection of spectra indicating dust-covered surfaces intentionally avoided the dust-borne carbonate component – the point of the present study was to look for outcrops of *in*

situ aqueous minerals associated with possible ancient lake deposits. Ideally, one would want to use EPF observations of the crater basins discussed in this work because they could provide for much lower thresholds of detectability for carbonates. Unfortunately, such observations are very sparse in the TES database.

Only the linear deconvolution results for runs using TES atmospheric and surface spectral end members have been reported here. Although all of the mean ROI spectra were also deconvolved using lab-measured spectra of carbonates and other evaporite minerals, these components were rarely identified in significant amounts (i.e., >10%). However, when we deconvolved TES surface spectral end members (e.g., Syrtis, Acidalia, etc.) using the mineral library, carbonates were even used in slightly greater amounts (14-17%). Examination of these models revealed that when carbonates were used in the deconvolution, correspondingly less blackbody component was included. In addition, comparison of the measured and modeled spectra from these models revealed that the carbonate absorption feature near 890-cm^{-1} was only present in the modeled spectra.

Except for the two relatively narrow absorption features previously noted, carbonate spectra are otherwise featureless in the range of wavenumbers used in the deconvolution. In deconvolution runs where carbonate end members were chosen, the carbonate spectra may have served to reduce spectral contrast in the modeled spectra (instead of blackbody) to better fit the measured spectra. In addition, carbonate spectra may serve to better fit spectra with a negatively-sloped continuum. With their much deeper feature at low wavenumbers, carbonate spectra in low abundances (low contrast)

can partially mimic such a slope. In fact, this may be the reason why carbonates are chosen over blackbody by the deconvolution routine.

For these reasons, the detection limit of carbonates may be somewhat higher than for other mineral types (e.g., igneous minerals, etc.). However, a complete study of the sensitivity of the linear deconvolution method to the presence of carbonates is beyond the scope of the present work. Instead, the use of the ratio technique and carbonate index method previously described are intended to determine whether small amounts of carbonate end members used in deconvolution modeling are credible.

Previous studies have demonstrated that detection limits of sulfates are estimated to be 15% [*Christensen et al.*, 2001], also higher than other mineral end members. In this study, one deconvolution result for an ROI mean spectrum included carbonates at the 10% level and ten mean ROI spectra exceeded 8% total carbonates. Therefore, if we assume a detection limit for carbonates is similar to the detection limit of sulfates, the linear deconvolution results do not indicate the presence of carbonates in abundances above the threshold of detectability within any ROI mean spectrum from this study.

4.2. Carbonate detection strategies

4.2.1. Spectral ratio technique

For most basins, the TES atmospheric and surface spectral end members are sufficient to model the non-dusty ROI spectra well. However, for crater C117, careful examination of spectra produced by the linear deconvolution routine and their spectral ratios revealed that two mean ROI spectra were not well-modeled using only the TES end members. The crater floor and the north external terrain have residual absorption features that are not modeled by deconvolution with the eight TES end members. The spectral

location of the residual absorption feature matches well to absorption features found in olivine spectra, as demonstrated in Figure 8c. This is consistent with the results of *Hamilton et al.* [2003] who identified local-scale (100s-1000s km^2) concentrations of olivine- and orthopyroxene-bearing materials within this crater and Ganges Chasma. All other basins were well-modeled using the eight TES atmospheric and surface spectral end members and do not require additional end members to model the observed variation.

4.2.2. Carbonate spectral indices technique

When applied to mean ROI spectra (whose surface composition is not obscured by surface dust) defined in this study, the carbonate indices did not detect spectral signatures of carbonates in any mean ROI spectrum. Therefore, carbonates are not present in any ROI spectra above the detection limits for this method. This is consistent with results of linear deconvolution of the same mean ROI spectra, which never used carbonates at credible levels (>15%).

5. Summary

A hyperspectral study of TES data was conducted on 80 putative paleolake basins to search for the spectral signatures of evaporite minerals exposed at a scale comparable to the spatial resolution of a single TES pixel (~3 x 5 km). Principal component analysis on TES spectral image cubes covering each basin and its surroundings was used to reveal distinct spectral surface units. Of the 80 basins, 7 basins displayed more than one distinct surface spectral unit. Averaged spectra from regions of interest containing the different spectral units were evaluated using a previously developed dust cover index. Those spectra determined to be "dust-free" were analyzed for composition using linear spectral

deconvolution, a spectral ratioing technique, and a compound spectral index technique tailored for the detection of carbonates.

In this study, carbonates were usually used by linear deconvolution modeling at the 8% and below level and only once used at the 10% level, while sulfates were never used in excess of 5%. These carbonate abundances approach the TES deconvolution detectability limit of 10% [*Bandfield*, 2002; *Christensen et al.*, 2001*b*], but evidence suggest that they are used in place of blackbody and that their detectability limit may be higher than 10%. The sulfate abundances fall well below the stated TES deconvolution detectability limit of ~15% [*Christensen et al.*, 2001*a*]. This means that the deconvolution algorithm's use of these small amounts of carbonates and sulfates should not be considered significant.

Furthermore, the spectral ratio technique demonstrates that most ROI spectra from this study are well-modeled using only the eight TES atmospheric and surface end members. The exceptions are within a crater dubbed "C117" and its northern external terrain (Ganges Chasm), where residual absorption features are present in the measured-to-modeled spectral ratio plots. These residual absorption features are consistent in both location and width with olivine and are consistent with the findings of *Hamilton et al.* [2003]. However, no ROI spectra contain residual absorption features due to carbonates or other evaporite minerals. Finally, the carbonate indices technique, with detection limits as low as 12%, do not detect the presence of carbonates in any ROI spectra.

Therefore, this study did not find any spectral evidence of evaporite minerals by linear deconvolution or by the carbonate detection strategies developed in this paper. The absence of evaporite minerals within these basins, including Gusev Crater, where the

possible presence of evaporite deposits was reported previously on geomorphic arguments [*Cabrol et al.*, 1998], does not provide mineralogical support for the previously proposed paleolake origin [*Cabrol and Grin*, 1999]. It must be said, however, that the present study cannot refute the paleolake basin hypothesis. For example, evaporites may be present in some or all of these basins, but buried under dust or other deposits or exposed in abundances below the detection limits of the methods used. It is also possible that the paleolake environment was dominated by clastic sedimentation instead of chemical precipitation of carbonates.

The Thermal Emission Imaging System (THEMIS) aboard the Odyssey spacecraft is acquiring images at 100 m/pixel resolution, 320 pixels across, in nine spectral bands between 6.6 μm and 15.0 μm with global coverage. Due to its higher spatial resolution, THEMIS is best viewed as a spectral unit mapper whereas, due to its higher spectral resolution, TES is better at mineral identification [e.g., *Christensen et al.*, 2003]. Therefore, the high spatial resolution data from THEMIS will provide a way to search for potential carbonate outcrops of a smaller scale than is discernible using TES data. If potential outcrops are detected, a TES spectrum covering the outcrop region could be analyzed by itself to determine the mineralogy. By pinpointing a potential carbonate outcrop to a single TES observation, the spectral contribution from the carbonate would be increased, perhaps above the detection limits of our carbonate index technique.

Acknowledgements. This work benefited from discussions with Phil Christensen, Vicky Hamilton, Mike Wyatt and Keith Milam. This study was supported by NASA Grant NAG5-11201.

References cited

Adler, H.H., and P.F. Kerr (1962), Infrared study of aragonite and calcite, *Am. Mineral.*, *47*, 700-717.

Adler, H.H., and P.F. Kerr (1963*a*), Infrared absorption frequency trends for anhydrous normal carbonates, *Am. Mineral*., *48*, 124-137.

Adler, H.H., and P.F. Kerr (1963*b*), Infrared spectra, symmetry and structure relations of some carbonate minerals, *Am. Mineral*., *48*, 839-853.

Adler, H.H., and P.F. Kerr (1965), Variations in infrared spectra, molecular symmetry and site symmetry of sulfate minerals, *Am. Mineral*., *50*, 132-147.

Baker, V.R. (1978), The Spokane flood controversy and the Martian outflow channels, *Science*, *202*, 1249-1256.

Baker, V.R. (2001), Water and the martian landscape, *Nature*, *412*(6843), 228-236.

Bandfield, J.L. (2002), Global mineral distributions on Mars, *J. Geophys. Res*., *107*(6), 5042, doi:10.1029/2001JE001510.

Bandfield, J.L., and M.D. Smith (2003), Multiple emission angle surface-atmosphere separations of Thermal Emission Spectrometer data, *Icarus*, *161*, 47-65.

Bandfield, J.L., V.E. Hamilton, and P.R. Christensen (2000*a*), A global view of Martian surface compositions from MGS-TES, *Science*, *287*(5458), 1626-1630.

Bandfield, J.L., P.R. Christensen, and M.D. Smith (2000*b*), Spectral data set factor analysis and end-member recovery: Application to analysis of Martian atmospheric particulates, *J. Geophys. Res.*, *105*(E4), 9573-9587.

Bandfield, J.L., T.D. Glotch, and P.R. Christensen (2003), Spectroscopic Identification of Carbonate Mineral in the Martian Dust, *Science*, *301*, 1084-1087.

Bibring, J.-P., Y. Langevin, A. Gendrin, B. Gondet, F. Poulet, M. Berthé, A. Soufflot, R. Arvidson, N. Mangold, J.F. Mustard, P. Drossart, and O. team, Mars Surface Diversity as Revealed by the OMEGA/Mars Express Observations, Science, 307 (5715), 1576-1581, 2005.

Borg, L.E., J.N. Connely, L.E. Nyquist, C.Y. Shih, H. Wiesmann, and Y. Reese (1999), The age of the carbonates in Martian meteorite ALH84001, *Science*, *286*(5437), 90-94.

Bridges, J.C., and M.M. Grady (2000), A halite-siderite-anhydrite-chlorapatite assemblage in Nakhla: Mineralogical evidence for evaporites on Mars, *Met. Planet. Sci*., *34*(3), 407-415.

Cabrol, N.A. (1997), Early Amazonian lake in Gale Crater (Mars), paper presented at the Lunar and Planetary Science Conference XXVIII, Lunar and Planetary Institute, Houston, TX.

Cabrol, N.A., and E.A. Grin (1997), Hydrogeology and exobiology significance of Martian large crater lakes, in *Conference on early Mars; geologic and hydrologic evolution, physical and chemical environments, and the implications for life*, edited by S.M. Clifford, A.H. Treiman, H.E. Newsom, and J.D. Farmer, pp. 14-15, Lunar and Planetary Institute, Houston, TX.

Cabrol, N.A., and E.A. Grin (1999), Distribution, Classification, and Ages of Martian Impact Crater Lakes, *Icarus*, *142*, 160-172.

Cabrol, N.A., E.A. Grin, R. Landheim, R.O. Kuzmin, and R. Greeley (1998), Duration of the Ma'adim Vallis/Gusev Crater hydrogeologic system, *Icarus*, *133*(1), 98-108.

Carr, M.H. (1983), Stability of streams and lakes on Mars, *Icarus*, *56*, 476-495.

Carr, M.H. (1996), Formation of the Martian drainage system; redistribution of groundwater in response to global topography and cold climates, in *Workshop on Evolution of Martian volatiles LPI Technical report*, edited by B.M. Jakosky, and A. Treiman, pp. 7-9, Lunar and Planetary Institute, Houston, TX.

Carr, R.H., M.M. Grady, I.P. Wright, and C.T. Pillinger (1985), Martian atmospheric carbon dioxide and weathering-products in SNC meteorites, *Nature*, *314*(6008), 248-250.

Catling, D.C. (1999), A chemical model for evaporites on early Mars: Possible sedimentary tracers of the early climate and implications for exploration, *J. Geophys. Res.*, *104*(E7), 16453-16469.

Chatzitheodoridis, E., and G. Turner (1990), Secondary minerals in the Nakhla meteorite, *Met. Planet. Sci.*, *25*(4), 354.

Christensen, P.R. (2003), Formation of recent Martian gullies through melting of extensive water-rich snow deposits, *Nature*, *422*(6927), 45-48.

Christensen, P.R., D.L. Anderson, S.C. Chase, R.N. Clark, H.H. Kieffer, M.C. Malin, J.C. Pearl, J. Carpenter, N. Bandiera, F.G. Brown, and S. Silverman (1992), Thermal Emission Spectrometer Experiment - Mars-Observer Mission, *J. Geophys. Res.*, *97*(E5), 7719-7734.

Christensen, P.R., J.L. Bandfield, M.D. Smith, V.E. Hamilton, and R.N. Clark (2000*a*), Identification of a basaltic component on the Martian surface from Thermal Emission Spectrometer data, *J. Geophys. Res.*, *105*(E4), 9609-9621.

Christensen, P.R., J.L. Bandfield, V.E. Hamilton, D.A. Howard, M.D. Lane, J.L. Piatek, S.W. Ruff, and W.L. Stefanov (2000*b*), A thermal emission spectral library of rock-forming minerals., *J. Geophys. Res.*, *105*(E4), 9735-9739.

Christensen, P.R., J.L. Bandfield, R.N. Clark, K.S. Edgett, V.E. Hamilton, T. Hoefen, H.H. Kieffer, R.O. Kuzmin, M.D. Lane, M.C. Malin, R.V. Morris, J.C. Pearl, R. Pearson, T.L. Roush, S.W. Ruff, and M.D. Smith (2000*c*), Detection of crystalline hematite mineralization on Mars by the Thermal Emission Spectrometer: Evidence for near-surface water, *J. Geophys. Res.*, *105*(E4), 9623-9642.

Christensen, P.R., R.V. Morris, M.D. Lane, J.L. Bandfield, and M.C. Malin (2001*a*), Global mapping of Martian hematite mineral deposits: Remnants of water-driven processes on early Mars, *J. Geophys. Res.*, *106*(E10), 23875-23855.

Christensen, P.R., J.L. Bandfield, V.E. Hamilton, S.W. Ruff, H.H. Kieffer, T.N. Titus, M.C. Malin, R.V. Morris, M.D. Lane, R.L. Clark, B.M. Jakosky, M.T. Mellon, J.C. Pearl, B.J. Conrath, M.D. Smith, R.T. Clancy, R.O. Kuzmin, T.L. Roush, G.L. Mehall, N. Gorelick, K. Bender, K. Murray, S. Dason, E. Greene, S. Silverman, and M. Greenfield (2001*b*), Mars Global Surveyor Thermal Emission Spectrometer experiment: Investigation description and surface science results, *J. Geophys. Res*., *106*(E10), 23823–23871.

Christensen, P.R., J.L. Bandfield, J.F. Bell, III, N. Gorelick, V.E. Hamilton, A. Ivanov, B.M. Jakosky, H.H. Kieffer, M.D. Lane, M.C. Malin, T. McConnochie, A.S. McEwan, H.Y. McSween, Jr., G.L. Mehall, J.E. Moersch, K.H. Nealson, J. Rice,

W., Jr., M.I. Richardson, S.W. Ruff, M.D. Smith, T.N. Titus, and M.B. Wyatt (2003), Morphology and Composition of the Surface of Mars: Mars Odyssey THEMIS Results, *Science*, *300*, 2056-2061.

Clark, B.C., and D.C. Van Hart (1981) The Salts of Mars, *Icarus*, *45*, 370-378.

Corrigan, C.M., and R.P. Harvey (2004), Multi-generational carbonate assemblages in Martian meteorite Allan Hills 84001; implications for nucleation, growth, and alteration, *Met. Planet. Sci.*, *39*(1), 17-30.

Eugster, H.P. (1980), Geochemistry of Evaporitic Lacustrine Deposits, *Ann. Rev. Earth Planet. Sci.*, *8*, 35-63.

Eugster, H.P., and L.A. Hardie (1978), Saline lakes, in *Lakes; chemistry, geology, physics*, edited by A. Lernam, pp. 237-293, Springer-Verlag, New York.

Farmer, J.D., and D.J. Des Marais (1999), Exploring for a record of ancient Martian life, *J. Geophys. Res.*, *104*(E11), 26977-26995.

Feely, K.C., and P.R. Christensen (1999), Quantitative compositional analysis using thermal emission spectroscopy: Application to igneous and metamorphic rocks, *J. Geophys. Res.*, *104*(E10), 24195-24210.

Forsythe, R.D., and J.R. Zimbelman (1995), A case for ancient evaporite basins on Mars, *J. Geophys. Res.*, *100*(E3), 5553-5563.

Frey, H.V., S.E.H. Sakimoto, and J.H. Roark (1998), MOLA topography of the crustal dichotomy boundary zone, Mars, *Geol. Soc. Am. Abstr. Programs*, *30*(7), 404.

Gendrin, A., N. Mangold, J.-P. Bibring, Y. Langevin, B. Gondet, F. Poulet, G. Bonello, C. Quantin, J.F. Mustard, R. Arvidson, and S. LeMouélic, Sulfates in Martian Layered Terrains: The OMEGA/Mars Express View, Science, 307 (5715), 1587-1591, 2005.

Gillespie, A.R. (1992), Spectral mixture analysis of multispectral thermal infrared images, *Remote Sens. Environ.*, *42*(2), 137-145.

Gooding, J.L., S.J. Wentworth, and M.E. Zolensky (1991), Aqueous alteration of the Nakhla parent meteorite, *Met. Planet. Sci.*, *26*(2), 135-143.

Grady, M.M., I.P. Wright, C. Douglas, and C.T. Pillinger (1995), Carbonates in Martian meteorites - a reappraisal, *Met. Planet. Sci.*, *30*(5), 511-512.

Green, A.A., M. Berman, P. Switzer, and M.D. Craig (1988), A transformation for ordering multispectral data in terms of image quality with implications for noise removal, *IEEE Trans. Geosci. Remote Sens.*, *26*(1), 65-74.

Gulick, V.C., and V.R. Baker (1989), Fluvial valleys and Martian paleoclimates, *Nature*, *341*, 514-516.

Hamilton, V.E., and P.R. Christensen (2000), Determining the modal mineralogy of mafic and ultramafic igneous rocks using thermal emission spectroscopy, *J. Geophys. Res.*, *105*(E4), 9717-9733.

Hamilton, V.E., P.R. Christensen, H.Y. McSween, Jr., and J.L. Bandfield (2003), Searching for the source regions of martian meteorites using MGS TES: Integrating martian meteorites into the global distribution of igneous materials on Mars, *Met. Planet. Sci.*, *38*(6), 871-885.

Hoffman, N. (2000), White Mars: A New Model for Mars' Surface and Atmosphere Based on CO_2, *Icarus*, *146*(2), 326-342.

Huang, C.K., and P.F. Kerr (1960), Infrared study of the carbonate minerals, *Am. Mineral.*, *45*(3-4), 311-324.

Hunt, G.R., and R.K. Vincent (1968), The behavior of spectral features in the infrared emission from particulate surfaces of various grain sizes, *J. Geophys. Res.*, *73*(18), 6039-6046.

Jones, B.F. (1965), The hydrology and mineralogy of Deep Springs Lake, Inyo County, California, *USGS Professional Paper 502-A*, pp. A1-A56, U. S. Geological Survey, Reston, VA, United States.

Jull, A.J.T., C.J. Eastoe, and S. Cloudt (1997), Isotopic composition of carbonates in the SNC meteorites, Allan Hills 84001 and Zagami, *J. Geophys. Res.*, *102*(E1), 1633-1669.

Jull, A.J.T., C.J. Eastoe, S. Xue, and G.F. Herzog (1995), Isotopic composition of carbonates in the SNC meteorites Allan Hills 84001 and Nakhla, *Met. Planet. Sci.*, *30*(3), 311-318.

Keller, W.D., J.H. Spotts, and D.L. Biggs (1952), Infrared spectra of some rock forming minerals, *Am. J. Science*, *250*(6), 453-471.

Kirkland, L.E., K.C. Herr, E.R. Keim, P.M. Adams, J.W. Salisbury, J.A. Hackwell, and A. Treiman (2002), First Use of an Airborne Thermal Infrared Hyperspectral Scanner for Compositional Mapping, *Remote Sens. Environ.*, *80*, 447-459.

Lane, M.D. (1999), Midinfrared optical constants of calcite and their relationship to particle size effects in thermal emission spectra of granular calcite, *J. Geophys. Res.*, *104*(E6), 14099-14108.

Lane, M.D., and P.R. Christensen (1997), Thermal infrared emission spectroscopy of anhydrous carbonates, *J. Geophys. Res.*, *102*(E11), 25581-25592.

Lane, M.D., and P.R. Christensen (1998), Salt Minerals Predicted for Mars and Their Thermal Infrared Emission Spectra, Lunar and Planetary Science XXIX, Lunar and Planetary Institute, Houston, TX.

Langevin, Y., F. Poulet, J.-P. Bibring, and B. Gondet, Sulfates in the North Polar Region of Mars Detected by OMEGA/Mars Express, Science, 307 (5715), 1584-1586, 2005

Lee, P., and C.P. McKay (2003), Mars: Always Cold, Sometimes Wet?, Lunar and Planetary Science XXXIV, Lunar and Planetary Institute, Houston, TX.

Lyon, R.J.P. (1965), Analysis of rocks by spectral infrared emission (8-25 μm), *Econ. Geol.*, *60*(4), 715-736.

Lyon, R.J.P., and K. Lee (1970), Remote sensing in exploration for mineral deposits, *Econ. Geol.*, *65*(7), 785-800.

Malin, M.C., and K.S. Edgett (2000), Sedimentary rocks of early Mars, *Science*, *290*(5498), 1927-1937.

McCauley, J.F. (1974), White Rock: A Martian enigma, *NASA Spec. Publ.*, *329*, 170-171.

McSween, H.Y., Jr., and R.P. Harvey (1999), An evaporation model for formation of carbonates in the ALH 84001 Martian meteorite, in *Planetary petrology and geochemistry*, edited by G.A. Snyder, C.R. Neal, and W.G. Ernst, pp. 252-261, Bellwether Publishing, Columbia, MD.

Moersch, J.E., and P.R. Christensen (1995), Thermal emission from particulate surfaces: A comparison of scattering models with measured spectra, *J. Geophys. Res.*, *100*, 7465-7477.

Nyquist, L.E., B.M. Bansal, H. Wiesmann, and C.Y. Shih (1995), "Martians" young and old: Zagami and ALH84001, Lunar and Planetary Science XXVI, Lunar and Planetary Institute, Houston, TX.

Peale, S.J., G. Schubert, and R.E. Lingenfelter (1975), Origin of Martian channels: Clathrates and water, *Science*, *187*, 273-274.

Pearl, J.C., M.D. Smith, B.J. Conrath, J.L. Bandfield, and P.R. Christensen (2001), Observations of Martian ice clouds by the Mars Global Surveyor thermal emission spectrometer; the first Martian year, *J. Geophys. Res.*, *106*(6), 12325-12338.

Pelkey, S.M., and B.M. Jakosky (2002), Surficial geologic surveys of Gale Crater and Melas Chasma, Mars: Integration of remote-sensing data, *Icarus*, *160*(2), 228-257.

Pollack, J.B., J.F. Kasting, S.M. Richardson, and K. Poliakoff (1987), The case for a wet, warm climate on Mars, *Icarus*, *71*(2), 203-224.

Ramsey, M.S., and P.R. Christensen (1998), Mineral abundance determination: Quantitative deconvolution of thermal emission spectra, *J. Geophys. Res.*, *103*(B1), 577-596.

Ruff, S.W. (1998), Quantitative Thermal Infrared Emission Spectroscopy Applied to Granitoid Petrology, PhD dissertation, Arizona State University, Tempe, AZ.

Ruff, S.W. (2004), Spectral evidence for zeolites in the dust on Mars, *Icarus*, *168*, 131-143.

Ruff, S.W., and P.R. Christensen (2002), Bright and dark regions on Mars: Particle size and mineralogical characteristics based on Thermal Emission Spectrometer data, *J. Geophys. Res.*, *107*(E12), 5127-5148.

Ruff, S.W., P.R. Christensen, R.N. Clark, H.H. Kieffer, M.C. Malin, J.L. Bandfield, B.M. Jakosky, M.D. Lane, M.T. Mellon, and M.A. Presley (2001), Mars' "White Rock" feature lacks evidence of an aqueous origin: Result from Mars Global Surveyor, *J. Geophys. Res.*, *106*(E10), 23921-23927.

Salisbury, J.W., A. Wald, and D.D. Aria (1994), Thermal-infrared remote sensing and Kirchhoff's law; 1, Laboratory measurements, *J. Geophys. Res.*, *99*(6), 11897-11911.

Schneeberger, D.M. (1989), Episodic channel activity at Ma'adim Vallis, Mars, Lunar and Planetary Science XX, Lunar and Planetary Institute, Houston, TX.

Smith, M.D., J.L. Bandfield, and P.R. Christensen (2000*a*), Separation of atmospheric and surface spectral features in Mars Global Surveyor Thermal Emission Spectrometer (TES) spectra, *J. Geophys. Res.*, *105*(E4), 9589-9607.

Smith, M.D., J.C. Pearl, B.J. Conrath, and P.R. Christensen (2000*b*), Mars Global Surveyor Thermal Emission Spectrometer (TES) observations of dust opacity during aerobraking and science phasing, *J. Geophys. Res.*, *105*(E4), 9539-9552.

Squyres, S.W. (1984), The history of water on Mars, *Ann. Rev. Earth Planet. Sci.*, *12*, 83-106.

Thomson, J.L., and J.W. Salisbury (1993), The mid-infrared reflectance of mineral mixtures (7–14 mm), *Remote Sens. Environ.*, *45*(1), 1-13.

Turner, G., S.F. Knott, R.D. Ash, and J.D. Gilmour (1997), Ar-Ar chronology of the Martian meteorite ALH84001; evidence for the timing of the early bombardment of Mars, *Geochimica et Cosmochimica Acta*, *61*(18), 3835-3850.

Wallace, D., and C. Sagan (1979), Evaporation of ice in planetary atmospheres: Ice-covered rivers on Mars, *Icarus*, *39*, 385-400.

Ward, A.W. (1979), Yardangs on Mars: Evidence of Recent Wind Erosion, *J. Geophys. Res.*, *84*(B14), 8147-8166.

Warren, P.H. (1998), Petrologic evidence for low-temperature, possibly flood evaporitic origin of carbonates in the ALH84001 meteorite, *J. Geophys. Res.*, *103*(E7), 16759-16773.

Williams, S.H., and J.R. Zimbelman (1994), "White Rock": An eroded Martian lacustrine deposit(?), *Geology*, *22*(2), 107-110.

Zimbelman, J.R., and H.H. Kieffer (1979), Thermal Mapping of the Northern Equatorial and Temperate Latitudes of Mars, *J. Geophys. Res.*, *84*(B14), 8239-8251.

Appendix

Table 1: TES end member and mineral end member spectra used in linear deconvolution routines.

TES Spectral end members	Igneous spectral end members
Acidalia-type surface	Oligoclase WAR-0234 22
Syrtis-type surface	Oligoclase WAR-5804 70
Hematite (TT-derived)	Andesine BUR-240 1
Average high albedo surface (surface dust)	Labradorite WAR-4524 63
	Labradorite WAR-RGAD01 222
Dust Low CO_2	Bytownite WAR-5859
Dust High CO_2	Anorthite BUR-340 178
Water Ice $Cloud_1$	Anorthite WAR-5759 221
Water Ice $Cloud_2$	Quartz BUR-4120 55
	K-rich glass
Evaporite spectral end members	Silica glass
Calcite C22 116*	Enstatite HS-9.4B 30
Magnesite C60 139*	Bronzite NMNH-93527 168
Siderite C50 130*	Diopside WAR-5780 165
Dolomite C17 111*	Augite HS-119.4B 56
Anhydrite ML-S9 81	Hedenbergite, manganoan DSM-HED01 145
Gypsum ML-S5 80	Diopside WAR-6476 54
Hematite BUR-2600	Augite BUR-620 71
Bloedite - $Na_2Mg(SO_4)_2 \cdot 4H_2O$	Augite NMNH-9780 157
Glauberite - $Na_2Ca(SO_4)_2$	Pigeonite
Mirabilite – $Na_2SO_4 \cdot 10H_2O$	Forsterite AZ-01 38
Thenardite - Na_2SO_4	Fayalite WAR-RGFAY01 167
	Magnesiohastingsite HS-115.4B 3
*Carbonate spectra are 40% contrast reduced	Magnesiohornblende WAR-0354 44
	Serpentine HS-8.4B 14
	Maskelynite (chunk) ASU-7591
	Ca-montmorillonite STx-1 solid 197
	Nontronite WAR-5108 granular 203
	Saponite ASU-SAP01 granular 194
	Illite Imt-2 granular 211

Table 2: Absorption index, relative band depths and relative band depth ratios (RBDR). Rpresentative mineral spectra and TES surface spectral end members.

	Calcite C22 116	**Magnesite C60139**	**Siderite C50 130**	**Dolomite C17 111**	**Avg. high albedo surface**	**Acidalia-type surface**	**Syrtis-type surface**	**Hematite BUR-2600 50**	**Gypsum ML-S5 80**
I_{Abs} (Cal, 884)	1.064	1.029	1.048	1.049	0.999	1.002	1.006	1.002	1.000
I_{Abs} (Cal, 317)	1.181	0.955	1.068	1.026	1.003	1.001	1.017	1.123	0.986
RBD (Cal, 884)	0.061	0.028	0.046	0.047	-0.001	0.002	0.006	0.002	0.000
RBD (Cal, 317)	0.153	-0.048	0.063	0.025	0.003	0.001	0.017	0.109	-0.014
RBDR (Cal)	2.532	-1.677	1.380	0.536	-4.856	0.664	2.785	59.435	-79.284
I_{Abs} (Cal, 884) > 1.01?	TRUE	TRUE	TRUE	TRUE	FALSE	FALSE	FALSE	TRUE	TRUE
I_{Abs} (Cal, 317) > 1.03?	TRUE	FALSE	TRUE	TRUE	TRUE	FALSE	FALSE	TRUE	FALSE
2.0 < RBDR(Cal) < 4.0?	TRUE	FALSE	FALSE	FALSE	FALSE	FALSE	TRUE	FALSE	FALSE
Calcite?	**TRUE**	**FALSE**	**FALSE**	**FALSE**	**FALSE**	**FALSE**	**FALSE**	**FALSE**	**FALSE**
I_{Abs}(Mag, 894)	1.026	1.085	1.007	1.075	0.998	1.002	1.005	1.001	1.000
I_{Abs}(Mag, 381)	0.991	1.224	1.052	1.145	1.003	1.002	1.002	0.898	0.992
RBD (Mag, 894)	0.026	0.078	0.007	0.070	-0.002	0.002	0.005	0.001	0.000
RBD (Mag, 381)	-0.009	0.183	0.049	0.126	0.003	0.002	0.002	-0.113	-0.008
RBDR(Mag)	-0.336	2.339	7.281	1.809	-1.467	1.326	0.422	-82.839	-24.315
I_{Abs}(Mag, 381) > 1.0?	TRUE	TRUE	TRUE	TRUE	FALSE	TRUE	TRUE	TRUE	TRUE
I_{Abs}(Mag, 894) > 1.02?	FALSE	TRUE	TRUE	TRUE	FALSE	FALSE	FALSE	FALSE	FALSE
1.82 < RBDR(Mag) < 2.35?	FALSE	TRUE	FALSE	FALSE	FALSE	FALSE	FALSE	FALSE	FALSE
Magnesite?	**FALSE**	**TRUE**	**FALSE**	**FALSE**	**FALSE**	**FALSE**	**FALSE**	**FALSE**	**FALSE**
I_{Abs}(Sid, 360)	1.046	1.014	1.047	1.032	1.000	1.002	1.008	1.002	1.001
I_{Abs}(Sid, 878)	1.118	1.052	1.086	1.111	1.004	1.003	1.016	1.000	0.989
RBD (Cal, 884)	0.044	0.014	0.045	0.031	0.000	0.002	0.008	0.002	0.001
RBD (Cal, 317)	0.106	0.049	0.079	0.100	0.004	0.003	0.015	0.000	-0.011
RBDR(Sid)	2.382	3.462	1.750	3.182	34.510	1.654	2.023	-0.072	-14.406
I_{Abs}(Sid, 360) > 1.024?	TRUE	FALSE	TRUE	TRUE	FALSE	TRUE	TRUE	FALSE	FALSE
I_{Abs}(Sid, 878) > 1.014?	TRUE	TRUE	TRUE	TRUE	FALSE	TRUE	TRUE	FALSE	FALSE
0.85 < RBDR(Sid) < 1.05?	FALSE	FALSE	TRUE	FALSE	FALSE	FALSE	FALSE	FALSE	FALSE
Siderite?	**FALSE**	**FALSE**	**TRUE**	**FALSE**	**FALSE**	**FALSE**	**FALSE**	**FALSE**	**FALSE**

Table 2 (con't): Representative mineral spectra and TES surface spectral end members.

	Anorthite BUR-340 178	Quartz BUR-4120 55	K-rich glass	Augite HS-119.4B 56	Pigeonite	ForsteriteA Z-01 38	Mask. (chunk) ASU-7591	Fe-smec. Swa-1 solid 207
I_{Abs} (Cal, 884)	0.993	1.000	0.999	1.009	1.017	1.039	1.000	0.999
I_{Abs} (Cal, 317)	1.003	1.012	0.988	0.975	0.998	0.916	1.000	0.984
RBD (Cal, 884)	-0.007	0.000	-0.001	0.008	0.017	0.037	0.000	-0.001
RBD (Cal, 317)	0.003	0.011	-0.012	-0.025	-0.002	-0.091	0.000	-0.017
RBDR (Cal)	-0.458	-544.317	9.408	-3.005	-0.148	-2.448	1.853	18.077
I_{Abs} (Cal, 884) > 1.01?	FALSE	FALSE	FALSE	TRUE	TRUE	TRUE	TRUE	FALSE
I_{Abs} (Cal, 317) > 1.03?	TRUE	TRUE	FALSE	FALSE	FALSE	FALSE	TRUE	FALSE
2.0 < RBDR(Cal) < 4.0?	FALSE	FALSE	FALSE	FALSE	FALSE	FALSE	FALSE	FALSE
Calcite?	FALSE	FALSE	FALSE	FALSE	FALSE	FALSE	FALSE	FALSE
I_{Abs}(Mag, 894)	1.002	1.000	0.998	1.018	1.012	1.046	1.003	0.997
I_{Abs}(Mag, 381)	1.042	1.007	1.026	0.977	0.985	1.030	1.046	0.995
RBD (Mag, 894)	0.002	0.000	-0.002	0.018	0.012	0.044	0.003	-0.003
RBD (Mag, 381)	0.040	0.007	0.025	-0.024	-0.015	0.029	0.044	-0.005
RBDR(Mag)	24.925	31.153	-15.853	-1.305	-1.250	0.658	12.648	2.047
I_{Abs}(Mag, 381) > 1.0?	TRUE	TRUE	FALSE	TRUE	TRUE	TRUE	TRUE	FALSE
I_{Abs}(Mag, 894) > 1.02?	TRUE	FALSE	TRUE	FALSE	FALSE	TRUE	TRUE	FALSE
1.82 < RBDR(Mag) < 2.35?	FALSE	FALSE	FALSE	FALSE	FALSE	FALSE	FALSE	TRUE
Magnesite?	FALSE	FALSE	FALSE	FALSE	FALSE	FALSE	FALSE	FALSE
I_{Abs}(Sid, 360)	0.991	1.001	0.999	1.017	1.016	1.018	0.999	1.000
I_{Abs}(Sid, 878)	1.027	1.008	0.970	0.976	0.998	0.987	1.007	0.982
RBD (Cal, 884)	-0.009	0.001	-0.001	0.017	0.016	0.018	-0.001	0.000
RBD (Cal, 317)	0.026	0.008	-0.031	-0.025	-0.002	-0.013	0.007	-0.018
RBDR(Sid)	-2.995	12.124	28.685	-1.453	-0.118	-0.748	-6.812	170.351
I_{Abs}(Sid, 360) > 1.024?	FALSE	FALSE	FALSE	TRUE	TRUE	TRUE	FALSE	FALSE
I_{Abs}(Sid, 878) > 1.014?	TRUE	FALSE	FALSE	FALSE	FALSE	FALSE	FALSE	FALSE
0.85 < RBDR(Sid) < 1.05?	FALSE	FALSE	FALSE	FALSE	FALSE	FALSE	FALSE	FALSE
Siderite?	FALSE	FALSE	FALSE	FALSE	FALSE	FALSE	FALSE	FALSE

Table 3: Amount of carbonate minerals required in mixtures with bright and dark spectra of Mars (*Ruff and Christensen*, 2001) in order to be detected by the carbonate indices method.

Surface Type	Calcite Index	Magnesite Index	Siderite Index
Syrtis	29% Cc	30% Mag	20% Sid
Sinus Meridiani	18% Cc	45% Mag	53% Sid
Acidalia	33% Cc	20% Mag	43% Sid
Tharsis	28% Cc	12% Mag	33% Sid
Arabia	36% Cc	12% Mag	40% Sid
Elysium	43% Cc	26% Mag	48% Sid

Table 4: Absorption index, relative band depths and relative band depth ratios (RBDR) for calcite spectra of various grain sizes.

	Calcite Suite								
	Crystalline sample	**710-1000 microns**	**500-710 microns**	**355-500 microns**	**250-355 microns**	**180-250 microns**	**125-180 microns**	**90-125 microns**	**0-63 microns**
I_{Abs} (Cal, 884)	1.064	1.117	1.117	1.119	1.129	1.102	1.091	1.073	0.891
I_{Abs} (Cal, 317)	1.181	1.593	1.588	1.585	1.578	1.480	1.477	1.469	1.061
RBD (Cal, 884)	0.061	0.105	0.105	0.107	0.114	0.092	0.083	0.068	-0.123
RBD (Cal, 317)	0.153	0.372	0.370	0.369	0.366	0.324	0.323	0.319	0.058
RBDR (Cal)	2.532	3.543	3.530	3.459	3.206	3.516	3.871	4.680	-0.471
I_{Abs} (Cal, 884) > 1.01?	TRUE	TRUE	TRUE	TRUE	TRUE	TRUE	TRUE	TRUE	FALSE
I_{Abs} (Cal, 317) > 1.03?	TRUE	TRUE	TRUE	TRUE	TRUE	TRUE	TRUE	TRUE	TRUE
2.0 < RBDR(Cal) < 4.0?	TRUE	TRUE	TRUE	TRUE	TRUE	TRUE	TRUE	FALSE	FALSE
Calcite?	**TRUE**	**TRUE**	**TRUE**	**TRUE**	**TRUE**	**TRUE**	**TRUE**	**FALSE**	**FALSE**

Table 5: Results of linear deconvolution and dust cover index (DCI) calculations for Aram Chaos mean ROI spectra.

	NE mesa tops	SW crater floor	NE crater floor	SE crater floor	NW crater floor	NW external terrain	SE external terrain1	SE external terrain2	E external terrain	SW external terrain	NE external terrain
Acidalia type	0.0	0.0	0.0	0.0	0.0	0.0	0.0	0.0	0.0	0.0	0.0
Syrtis type	22.9	23.6	29.2	20.2	1.6	5.7	20.3	26.1	3.6	25.0	28.2
Hematite	14.2	0.0	0.0	0.0	0.0	0.0	4.1	0.0	0.0	0.0	0.9
Dust Low CO_2	57.1	65.5	62.2	70.7	90.4	81.8	63.2	66.3	87.8	66.7	60.7
Dust High CO_2	0.0	0.0	0.0	0.0	0.0	0.0	0.8	0.0	0.0	0.0	0.0
Water Ice $Cloud_1$	0.5	3.9	2.6	7.6	7.1	6.2	3.7	5.9	4.7	2.9	3.5
Water Ice $Cloud_2$	4.1	5.6	4.3	0.0	0.0	6.2	7.6	0.0	3.1	4.1	5.4
Surface dust	0.0	0.0	0.0	0.0	0.0	0.0	0.0	0.0	0.0	0.0	0.0
Total	98.9	98.5	98.3	98.5	99.1	100.0	99.7	98.4	99.2	98.7	98.7
Spectral RMS	0.00446	0.00444	0.00337	0.00377	0.00524	0.00376	0.00289	0.00389	0.00492	0.00408	0.00386
DCI	0.967	0.968	0.969	0.967	0.952	0.949	0.962	0.969	0.956	0.966	0.969
DCI value interpretation?	dust free	dust free	dust free	dust free	inter-mediate	inter-mediate	dust free	dust free	inter-mediate	dust free	dust free

Table 6: Results of carbonate indices calculations for Aram Chaos ROI mean spectra. Excludes regions which appear dust covered according to the DCI and linear deconvolutions.

	NE mesa tops	**SW crater floor**	**NE crater floor**	**SE crater floor**	**NW crater floor**	**NW external terrain**	**SE external terrain1**	**SE external terrain2**	**E external terrain**	**SW external terrain**	**NE external terrain**
I_{Abs} (Cal, 884)	1.011	1.011	1.011	1.010	1.009	1.007	1.007	1.011	1.009	1.011	1.010
I_{Abs} (Cal, 317)	1.001	0.997	1.000	0.998	0.997	0.994	0.997	1.000	0.996	1.001	1.000
RBD (Cal, 884)	0.011	0.011	0.011	0.010	0.008	0.007	0.007	0.011	0.009	0.010	0.010
RBD (Cal, 317)	0.001	-0.003	0.000	-0.002	-0.003	-0.006	-0.003	0.000	-0.004	0.001	0.000
RBDR (Cal)	0.127	-0.228	-0.016	-0.158	-0.336	-0.876	-0.391	0.026	-0.463	0.110	-0.022
I_{Abs} (Cal, 884) > 1.01?	TRUE	TRUE	TRUE	FALSE	FALSE	FALSE	FALSE	TRUE	FALSE	TRUE	TRUE
I_{Abs} (Cal, 317) > 1.03?	FALSE	FALSE	FALSE	FALSE	FALSE	FALSE	FALSE	FALSE	FALSE	FALSE	FALSE
2.0 < RBDR(Cal) < 4.0?	FALSE	FALSE	FALSE	FALSE	FALSE	FALSE	FALSE	FALSE	FALSE	FALSE	FALSE
Calcite?	**FALSE**	**FALSE**	**FALSE**	**FALSE**	**FALSE**	**FALSE**	**FALSE**	**FALSE**	**FALSE**	**FALSE**	**FALSE**
I_{Abs}(Mag, 894)	1.008	1.009	1.007	1.007	1.005	1.004	1.004	1.007	1.005	1.007	1.007
I_{Abs}(Mag, 381)	0.980	0.996	0.997	0.997	0.998	0.997	0.996	0.998	0.997	0.997	0.996
RBD (Mag, 894)	0.008	0.009	0.007	0.007	0.005	0.004	0.004	0.007	0.005	0.007	0.007
RBD (Mag, 381)	-0.021	-0.004	-0.003	-0.003	-0.002	-0.003	-0.004	-0.002	-0.003	-0.003	-0.004
RBDR(Mag)	-2.604	-0.406	-0.429	-0.418	-0.406	-0.755	-1.024	-0.216	-0.577	-0.474	-0.492
I_{Abs}(Mag, 381) > 1.0?	TRUE	TRUE	TRUE	TRUE	TRUE	TRUE	TRUE	TRUE	TRUE	TRUE	TRUE
I_{Abs}(Mag, 894) > 1.02?	FALSE	FALSE	FALSE	FALSE	FALSE	FALSE	FALSE	FALSE	FALSE	FALSE	FALSE
1.82 < RBDR(Mag) < 2.35?	FALSE	FALSE	FALSE	FALSE	FALSE	FALSE	FALSE	FALSE	FALSE	FALSE	FALSE
Magnesite?	**FALSE**	**FALSE**	**FALSE**	**FALSE**	**FALSE**	**FALSE**	**FALSE**	**FALSE**	**FALSE**	**FALSE**	**FALSE**
I_{Abs}(Sid, 360)	1.010	1.011	1.011	1.009	1.007	1.006	1.006	1.010	1.008	1.010	1.010
I_{Abs}(Sid, 878)	0.987	0.996	0.998	0.997	0.995	0.994	0.996	0.999	0.994	0.998	0.998
RBD (Cal, 884)	0.010	0.011	0.011	0.009	0.007	0.006	0.006	0.010	0.008	0.010	0.010
RBD (Cal, 317)	-0.013	-0.004	-0.002	-0.003	-0.005	-0.006	-0.004	-0.001	-0.006	-0.002	-0.002
RBDR(Sid)	-1.363	-0.314	-0.213	-0.360	-0.629	-1.125	-0.689	-0.115	-0.781	-0.197	-0.193
I_{Abs}(Sid, 360) > 1.024?	FALSE	FALSE	FALSE	FALSE	FALSE	FALSE	FALSE	FALSE	FALSE	FALSE	FALSE
I_{Abs}(Sid, 878) > 1.014?	FALSE	FALSE	FALSE	FALSE	FALSE	FALSE	FALSE	FALSE	FALSE	FALSE	FALSE
0.85 < RBDR(Sid) < 1.05?	FALSE	FALSE	FALSE	FALSE	FALSE	FALSE	FALSE	FALSE	FALSE	FALSE	FALSE
Siderite?	**FALSE**	**FALSE**	**FALSE**	**FALSE**	**FALSE**	**FALSE**	**FALSE**	**FALSE**	**FALSE**	**FALSE**	**FALSE**

Table 7: Results of linear deconvolution and dust cover index (DCI) calculations for Gale Crater mean ROI spectra.

	Central mound	W crater floor	E crater floor	S crater floor	S external terrain	N external terrain
Acidalia type	10.1	0.0	0.0	34.6	21.2	5.6
Syrtis type	0.0	22.7	31.7	15.6	25.7	0.0
Hematite	0.0	0.0	0.0	0.0	1.9	0.0
Dust Low CO_2	35.5	74.7	61.2	39.4	46.2	55.5
Dust High CO_2	16.4	0.0	1.4	7.4	0.9	7.3
Water Ice Cloud$_1$	0.0	0.0	0.3	0.0	0.0	0.0
Water Ice Cloud$_2$	8.0	1.2	4.4	2.5	3.3	7.1
Surface dust	31.0	0.0	0.0	0.0	0.0	25.3
Total	101.0	98.6	99.1	99.4	99.3	100.8
Spectral RMS	0.00237	0.00355	0.00276	0.00242	0.00208	0.00295
DCI	0.936	0.961	0.964	0.968	0.969	0.936
DCI value interpretation?	dust covered	intermediate	dust free	dust free	dust free	dust covered

Table 8: Results of carbonate indices calculations for Gale Crater ROI mean spectra. Excludes regions which appear dust covered according to the DCI and linear deconvolutions.

	W crater floor	E crater floor	S crater floor	S external terrain
I_{Abs} (Cal, 884)	1.008	1.008	1.007	1.007
I_{Abs} (Cal, 317)	1.000	1.002	1.001	1.002
RBD (Cal, 884)	0.008	0.008	0.007	0.007
RBD (Cal, 317)	0.000	0.002	0.001	0.002
RBDR (Cal)	-0.010	0.217	0.114	0.239
I_{Abs} (Cal, 884) > 1.01?	FALSE	FALSE	FALSE	FALSE
I_{Abs} (Cal, 317) > 1.03?	FALSE	FALSE	FALSE	FALSE
2.0 < RBDR(Cal) < 4.0?	FALSE	FALSE	FALSE	FALSE
Calcite?	**FALSE**	**FALSE**	**FALSE**	**FALSE**
I_{Abs}(Mag, 894)	1.004	1.005	1.004	1.004
I_{Abs}(Mag, 381)	0.998	0.999	0.998	0.998
RBD (Mag, 894)	0.004	0.005	0.004	0.004
RBD (Mag, 381)	-0.002	-0.001	-0.002	-0.002
RBDR(Mag)	-0.577	-0.275	-0.511	-0.463
I_{Abs}(Mag, 381) > 1.0?	TRUE	TRUE	TRUE	TRUE
I_{Abs}(Mag, 894) > 1.02?	FALSE	FALSE	FALSE	FALSE
1.82 < RBDR(Mag) < 2.35?	FALSE	FALSE	FALSE	FALSE
Magnesite?	**FALSE**	**FALSE**	**FALSE**	**FALSE**
I_{Abs}(Sid, 360)	1.007	1.007	1.006	1.007
I_{Abs}(Sid, 878)	0.997	1.000	0.999	0.999
RBD (Cal, 884)	0.007	0.007	0.006	0.006
RBD (Cal, 317)	-0.003	0.000	-0.001	-0.001
RBDR(Sid)	-0.395	-0.070	-0.175	-0.110
I_{Abs}(Sid, 360) > 1.024?	FALSE	FALSE	FALSE	FALSE
I_{Abs}(Sid, 878) > 1.014?	FALSE	FALSE	FALSE	FALSE
0.85 < RBDR(Sid) < 1.05?	FALSE	FALSE	FALSE	FALSE
Siderite?	**FALSE**	**FALSE**	**FALSE**	**FALSE**

Table 9: Results of linear deconvolution and dust cover index (DCI) calculations for Crater C117 mean ROI spectra.

	Crater floor	Small crater within crater	ESE external terrain	N external terrain (Ganges Chasma)	SW external terrain
Acidalia type	0.0	0.0	0.0	0.0	0.0
Syrtis type	43.4	32.1	37.1	19.4	43.4
Hematite	0.0	0.0	0.0	0.0	0.0
Dust Low CO_2	46.2	59.5	55.5	73.5	46.2
Dust High CO_2	0.0	0.0	0.0	0.0	0.0
Water Ice $Cloud_1$	9.6	7.3	4.0	5.4	9.6
Water Ice $Cloud_2$	0.0	0.0	2.4	0.0	0.0
Surface dust	0.0	0.0	0.0	0.0	0.0
Total	99.2	99.0	99.1	98.3	99.2
Spectral RMS	0.00407	0.00381	0.00356	0.00554	0.00407
DCI	0.973	0.971	0.970	0.964	0.973
DCI value interpretation?	dust free	dust free	dust free	dust free	dust free

Table 10: Results of carbonate indices calculations for Crater 117 ROI mean spectra. Excludes regions which appear dust covered according to the DCI and linear deconvolutions.

	Crater floor	**Small crater within crater**	**ESE external terrain**	**N external terrain (Ganges Chasma)**	**SW external terrain**
I_{Abs} (Cal, 884)	1.012	1.010	1.010	1.012	1.010
I_{Abs} (Cal, 317)	1.003	1.005	1.001	1.001	1.000
RBD (Cal, 884)	0.012	0.010	0.009	0.012	0.009
RBD (Cal, 317)	0.003	0.005	0.001	0.001	0.000
RBDR (Cal)	0.225	0.506	0.151	0.074	-0.015
I_{Abs} (Cal, 884) > 1.01?	TRUE	TRUE	FALSE	TRUE	FALSE
I_{Abs} (Cal, 317) > 1.03?	FALSE	FALSE	FALSE	FALSE	FALSE
2.0 < RBDR(Cal) < 4.0?	FALSE	FALSE	FALSE	FALSE	FALSE
Calcite?	**FALSE**	**FALSE**	**FALSE**	**FALSE**	**FALSE**
I_{Abs}(Mag, 894)	1.012	1.007	1.008	1.009	1.008
I_{Abs}(Mag, 381)	1.001	1.000	1.000	1.000	0.999
RBD (Mag, 894)	0.012	0.007	0.008	0.009	0.008
RBD (Mag, 381)	0.001	0.000	0.000	0.000	-0.001
RBDR(Mag)	0.052	0.042	-0.064	-0.039	-0.157
I_{Abs}(Mag, 381) > 1.0?	TRUE	TRUE	TRUE	TRUE	TRUE
I_{Abs}(Mag, 894) > 1.02?	FALSE	FALSE	FALSE	FALSE	FALSE
1.82 < RBDR(Mag) < 2.35?	FALSE	FALSE	FALSE	FALSE	FALSE
Magnesite?	**FALSE**	**FALSE**	**FALSE**	**FALSE**	**FALSE**
I_{Abs}(Sid, 360)	1.012	1.010	1.009	1.010	1.010
I_{Abs}(Sid, 878)	1.004	1.002	1.000	0.999	1.001
RBD (Cal, 884)	0.012	0.010	0.009	0.010	0.010
RBD (Cal, 317)	0.004	0.002	0.000	-0.001	0.001
RBDR(Sid)	0.332	0.223	0.036	-0.132	0.057
I_{Abs}(Sid, 360) > 1.024?	FALSE	FALSE	FALSE	FALSE	FALSE
I_{Abs}(Sid, 878) > 1.014?	FALSE	FALSE	FALSE	FALSE	FALSE
0.85 < RBDR(Sid) < 1.05?	FALSE	FALSE	FALSE	FALSE	FALSE
Siderite?	**FALSE**	**FALSE**	**FALSE**	**FALSE**	**FALSE**

Step 1: Assembly of TES hyperspectral and data cube for target area

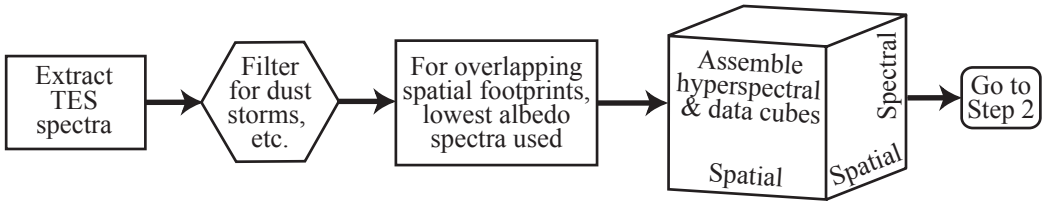

Step 2: Identification/removal of problematic orbits via Principal Component Analysis

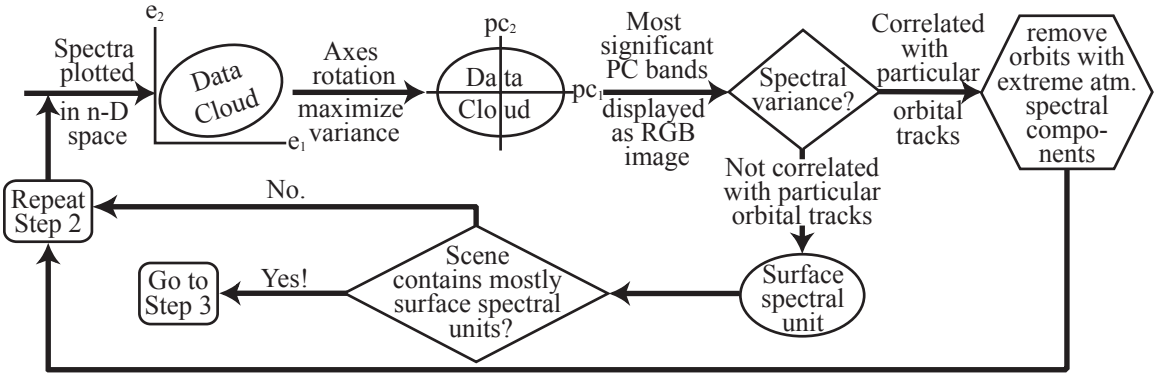

Step 3: Defining Regions of Interest (ROIs) and collecting spectra

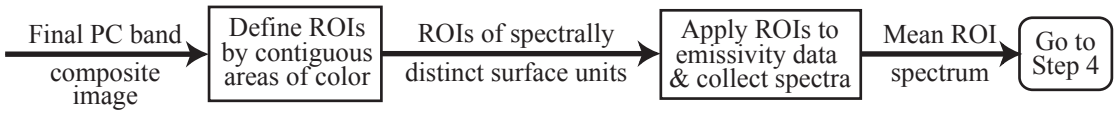

Step 4: Evaluate mean ROI spectra using the dust cover index (DCI):

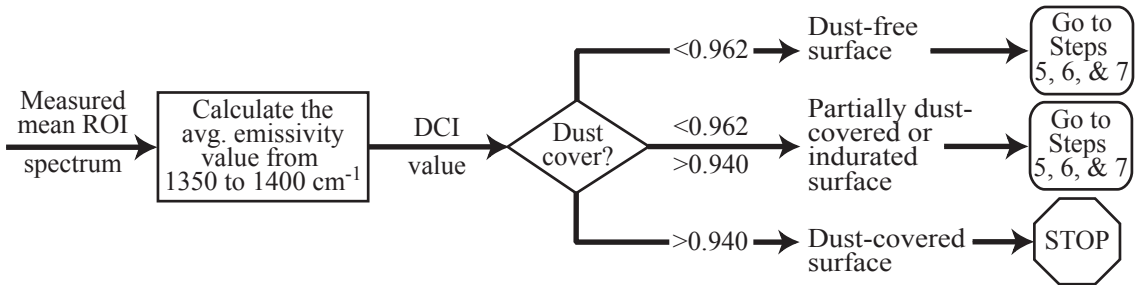

Figure 1: Flow chart illustrating assembly and processing of the TES data cubes for this study. Assembly of the data cube, identification and removal of orbits with the most extreme atmospheric spectral component abundances, ROI definition and evaluation of mean ROI spectra using the DCI index.

Step 5: Deconvolve the mean emissivity spectra of the ROIs

Step 5a: Previously-known TES endmembers only

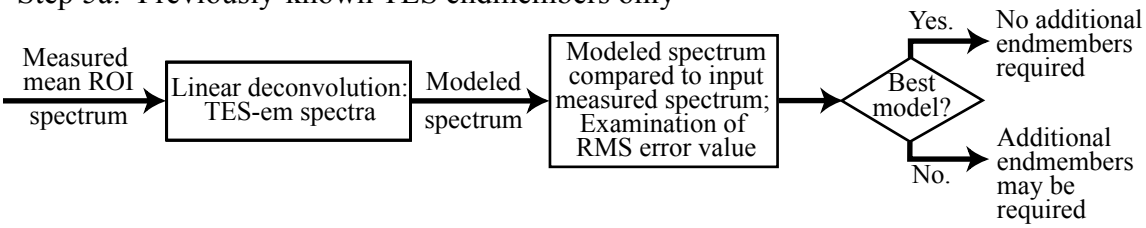

Step 5b: TES atmospheric endmembers plus igneous minerals

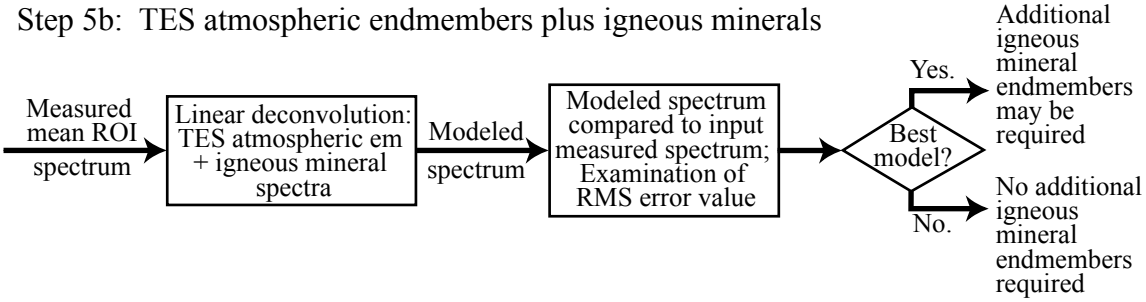

Step 5c: TES atmospheric endmembers plus igneous and evaporite minerals

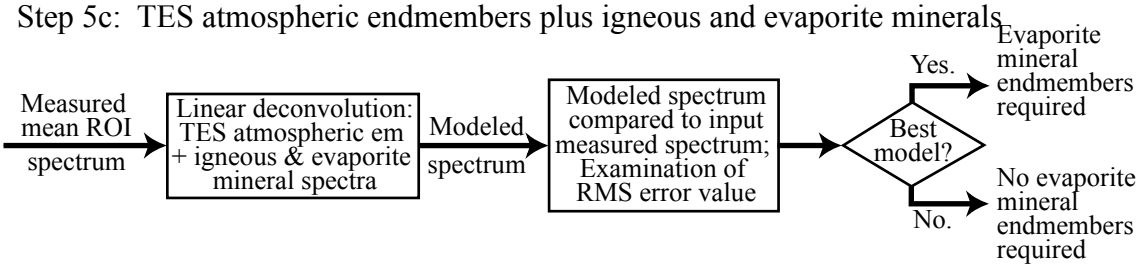

Step 6: Evaluate non-dusty mean ROI spectra using spectral ratio technique:

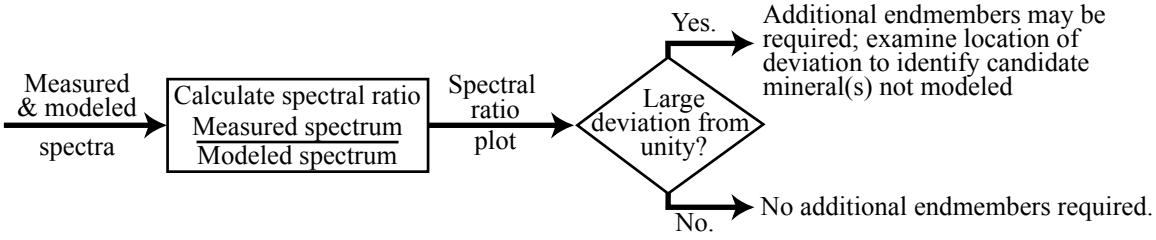

Figure 1 (con't): Deconvolution of the mean ROI spectra using three spectral sets (TES end members only, TES atmospheric end members plus igneous minerals, TES atmospheric end members plus igneous and evaporate minerals) and evaluation of mean ROI spectra using the spectral ratio technique.

Step 7: Evaluate non-dusty mean ROI spectra using the carbonate indices technique to detect carbonate of interest (calcite, magnesite or siderite):

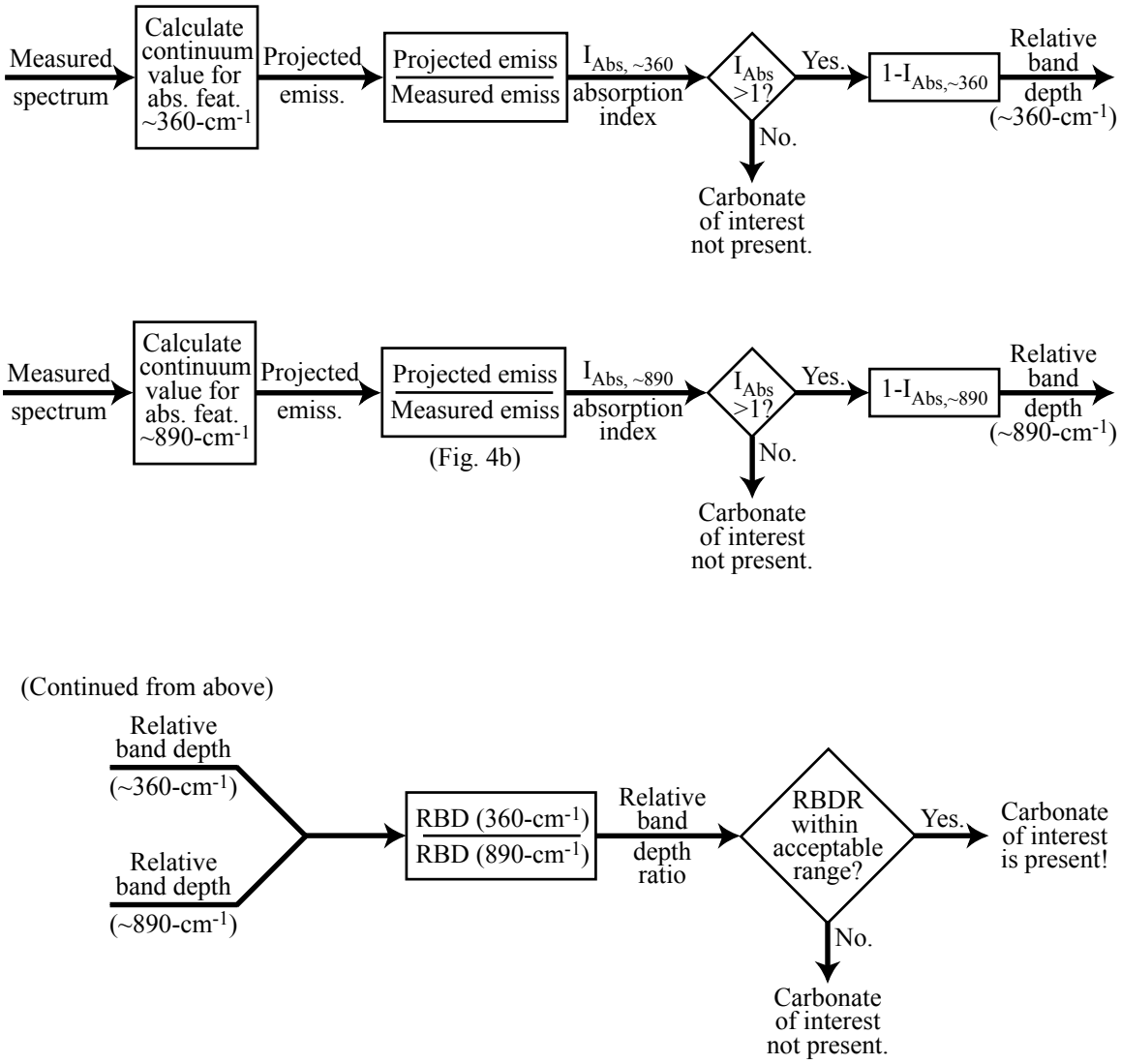

Figure 1 (con't): Evaluation of mean ROI spectra using the carbonate indices.

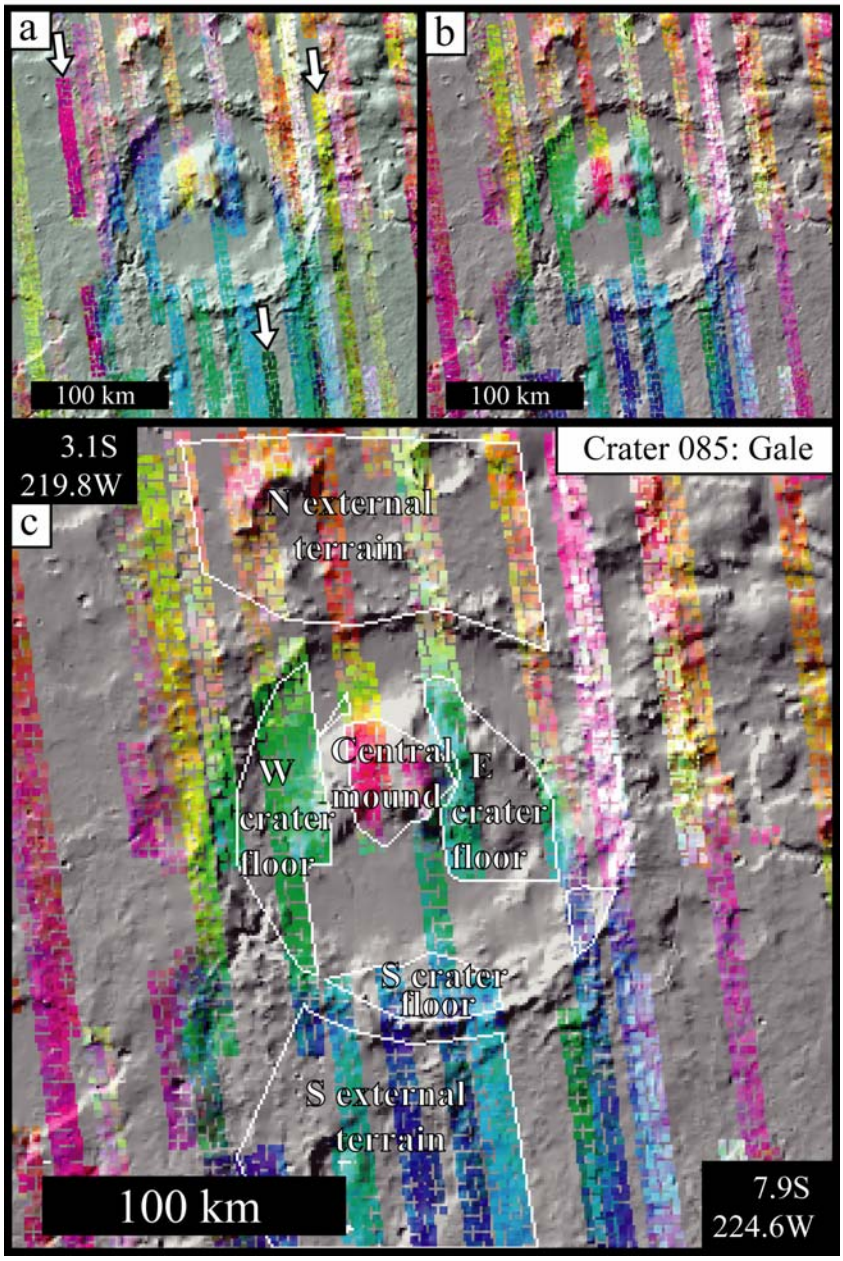

Figure 2: MNF color composite images overlain on MOLA-derived shaded relief image of Gale Crater. (a) The initial MNF color composite image for Gale Crater, which still contain "problematic" orbits (i.e., orbits with excessive atmospheric contamination or other problems). Arrows point to several potentially problematic orbits that might be removed from this TES data cube. Note that these orbits have colors that stand out as different from other orbits in this representation. (b) Final MNF color composite image of Gale Crater, in which most of the atmospheric variation has been removed. In this image, units seen as different colors span multiple orbits, indicating that they represent a surface spectral unit. (c) Final MNF color composite image of Gale Crater with manually-defined ROIs outline in white. Mean ROI spectra are obtained from these regions and used in subsequent deconvolution and carbonate index analysis.

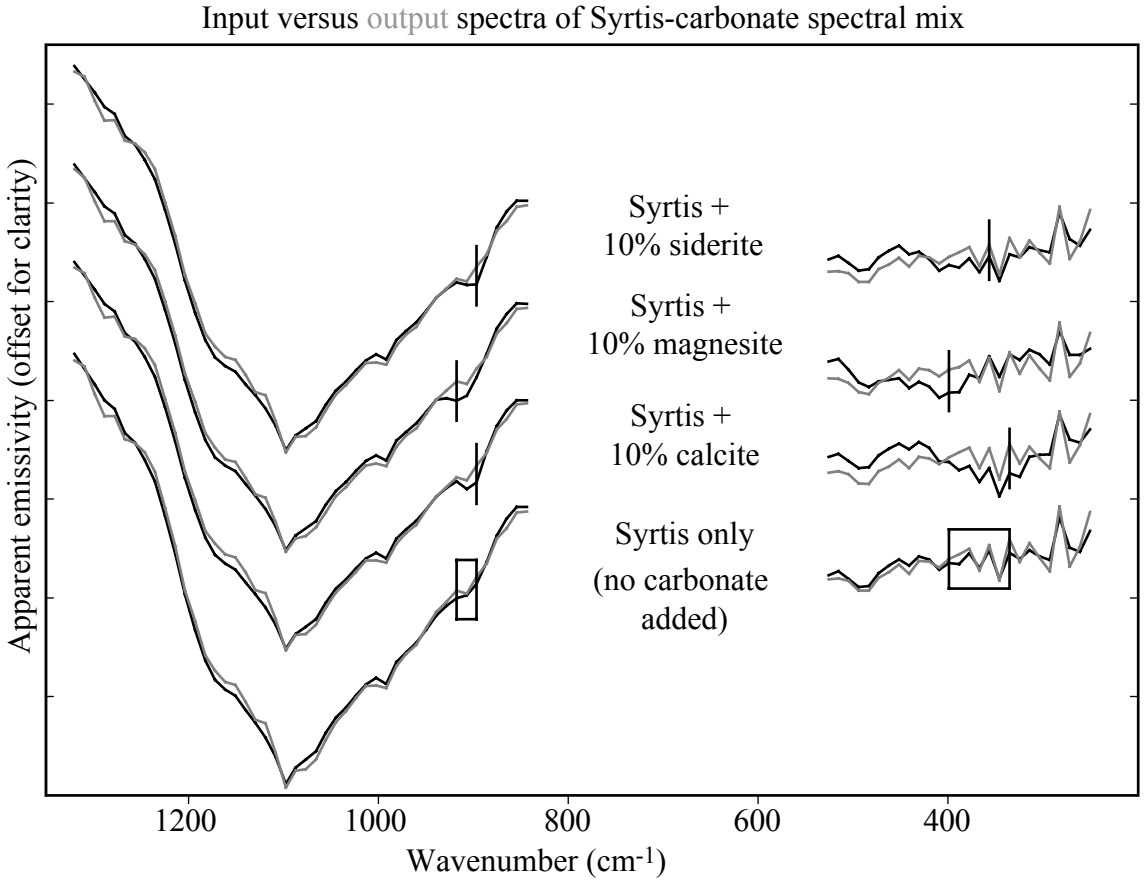

Figure 3: Plots for Syrtis and Syrtis-carbonate mixtures (a) Plot of input spectra (black) versus modeled spectra (gray) for Syrtis and Syrtis-carbonate mixtures, offset for clarity. On the Syrtis spectra, the boxes located near 890-cm^{-1} and 350-cm^{-1} define spectral regions of carbonate absorption features. For each mixture, vertical lines mark the location of the deepest part of the absorption features for the appropriate carbonate. These lines have the same vertical scale as the boxes on the Syrtis spectra.

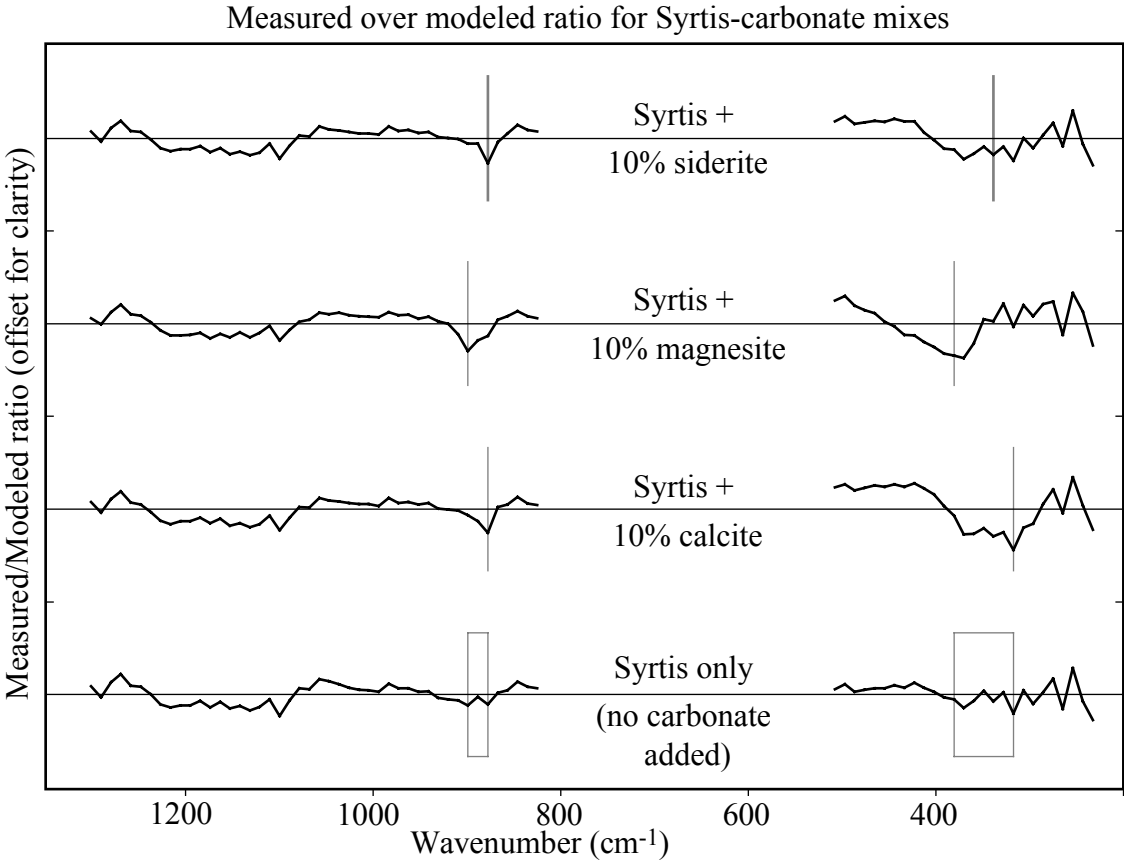

Figure 3 (con't): (b) Plot of the input-to-modeled spectral ratios for Syrtis and Syrtis-carbonate mixtures, offset for clarity. On the Syrtis spectral ratio, the boxes located near 890-cm^{-1} and 350-cm^{-1} define the spectral regions of carbonate absorption features. For each mixture, the vertical lines mark the locations of the deepest part of the absorption features for the appropriate carbonate. These lines have the same vertical scale as the boxes on the Syrtis ratio. Spectral ratio plots for all ROIs will have the same vertical scale to allow direct comparison.

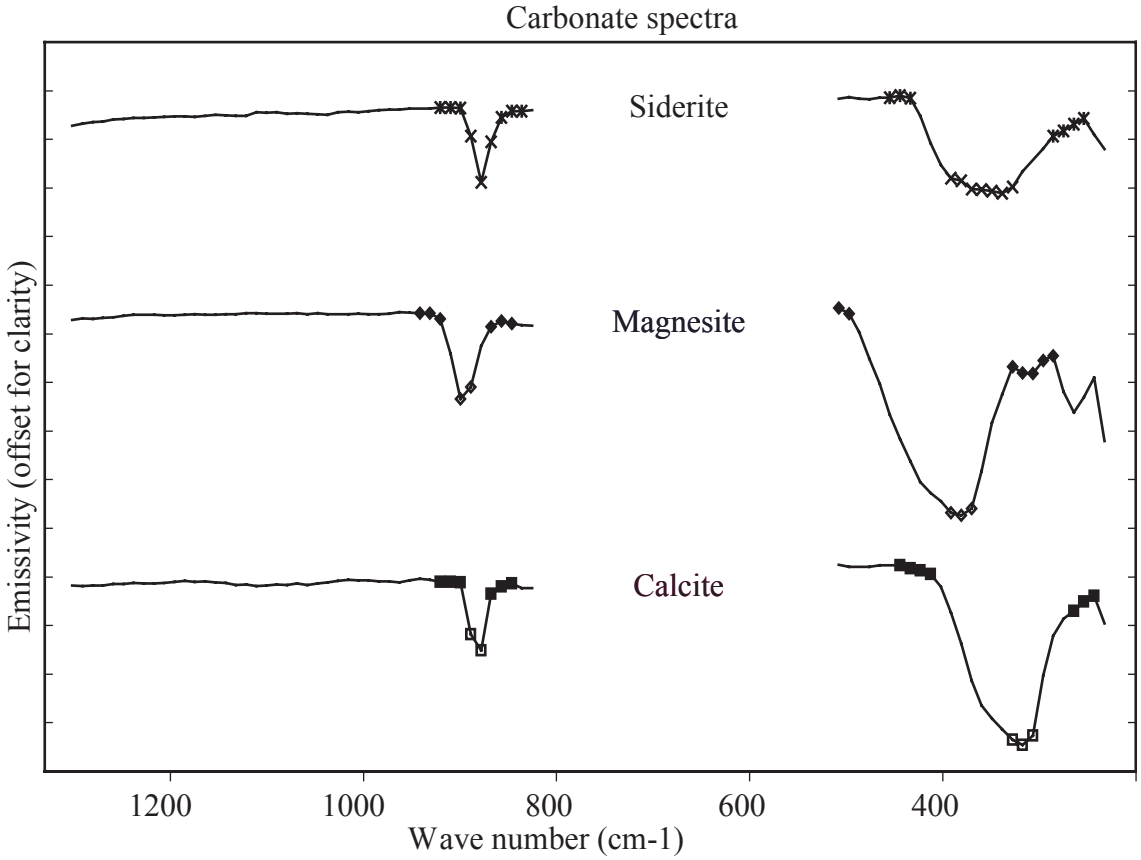

Figure 4: Carbonate spectra within the spectral range of linear deconvolution. (a) Carbonate spectra within the wavenumber range used by the linear deconvolution routine. Carbonate spectra are relatively flat except for two absorptions centered near 890-cm^{-1} and 350-cm^{-1}. In addition, examination of these spectra reveals that the 350-cm^{-1} feature is approximately twice as deep as the 890-cm^{-1} feature for calcite and magnesite. This spectral characteristic is useful in separating spectral contributions of carbonates from the spectral contribution of other minerals with absorptions near the two carbonate features.

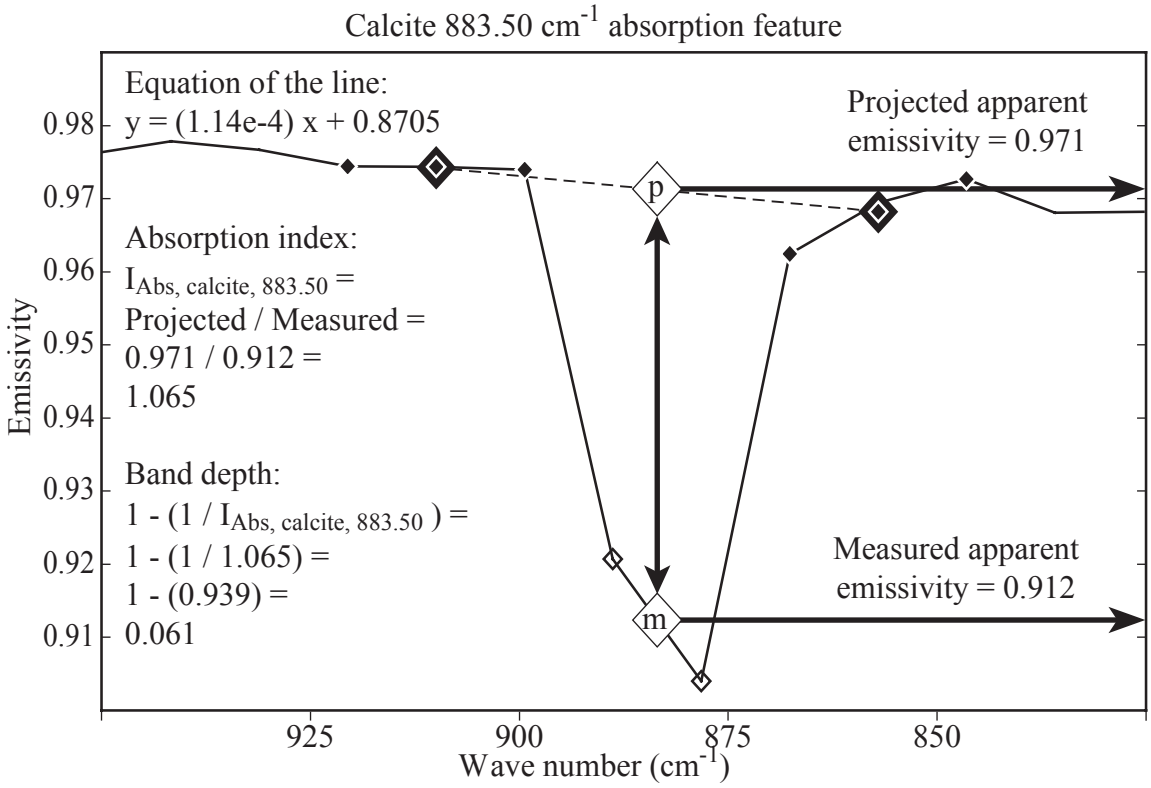

Figure 4 (con't): (b) Illustration of the calcite index calculation for the 884-cm^{-1} calcite absorption feature. Average continuum values (large filled diamonds) are calculated from several points (small filled diamonds) on either side of the absorption feature. An equation of line is calculated from these two average continuum values, which then yields the projected emissivity (open diamond labeled "p"). This is then compared to the measured emissivity (open diamond labeled "m") to calculate the absorption index. If an absorption feature is present, this index value will be greater than 1. Finally, a band depth is calculated for the absorption feature and compared to the band depth of the 317-cm^{-1} feature, as explained in the text.

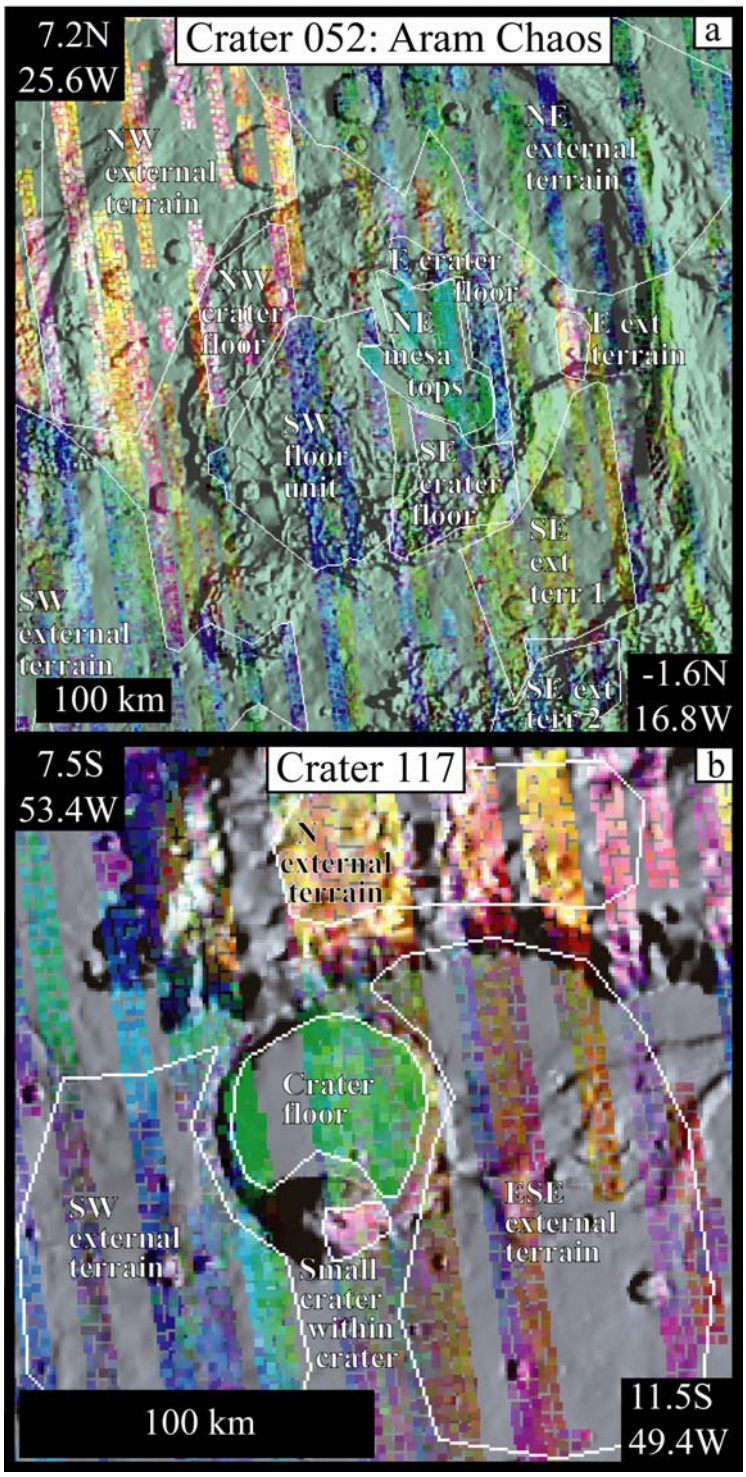

Figure 5: Final MNF color composite images overlain on MOLA-derived shaded relief images for two additional craters. (a) Aram Chaos, with manually-defined ROIs outline in white. (b) Crater C117 south of Ganges Chasm, with manually-defined ROIs outline in white.

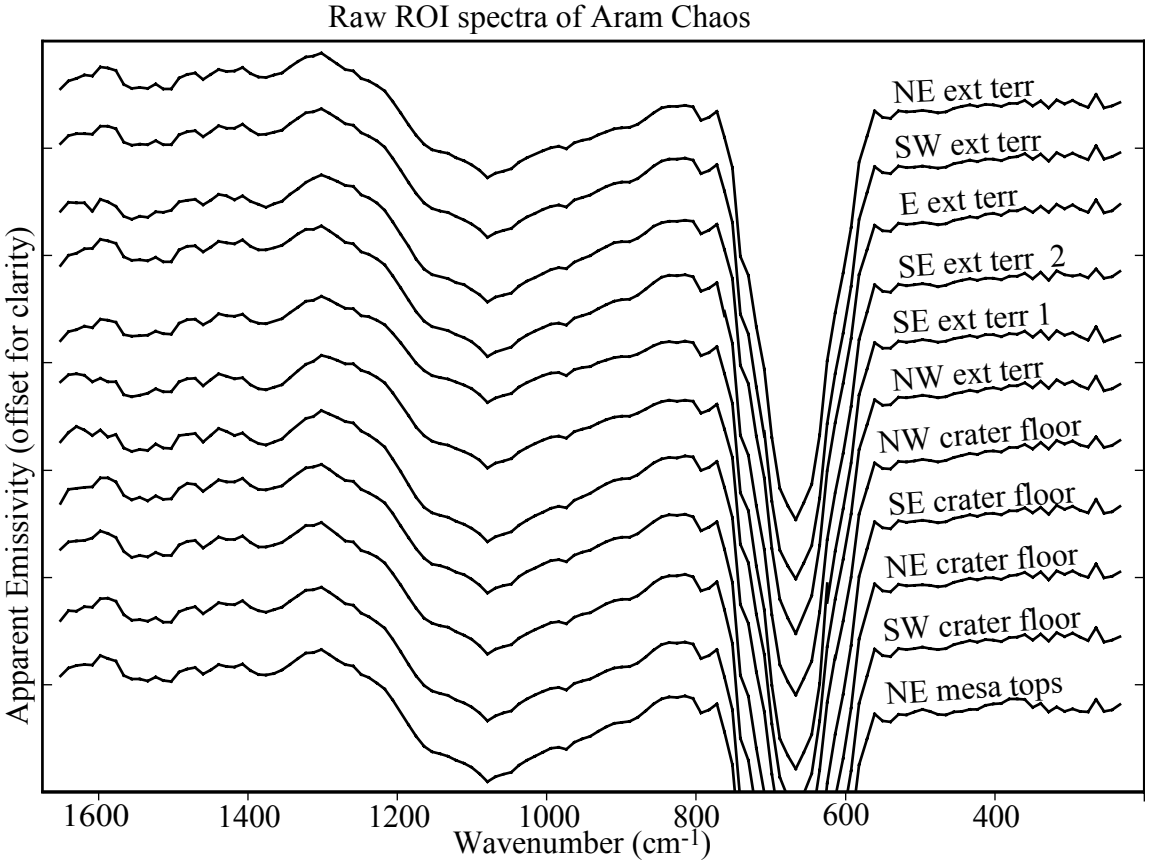

Figure 6: Spectra and spectral ratios for Aram Chaos. (a) Raw mean ROI spectra from Aram Chaos input into linear deconvolution routine, including the deep CO_2 feature near 670-cm^{-1}. Spectra have been offset for clarity.

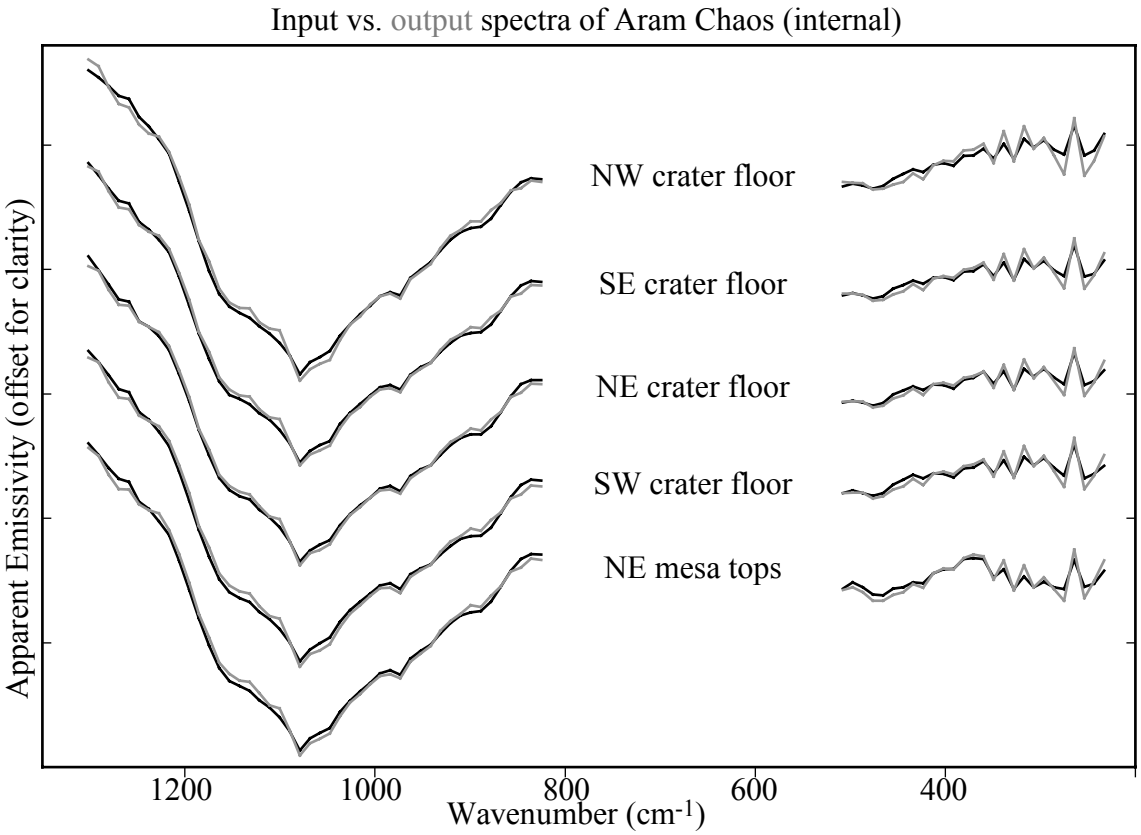

Figure 6 (con't): (b) Measured mean ROI spectra (black) and model spectra (gray) produced by linear deconvolution for Aram Chaos internal ROIs. Spectra of have been offset for clarity and do not include the deep CO_2 feature.

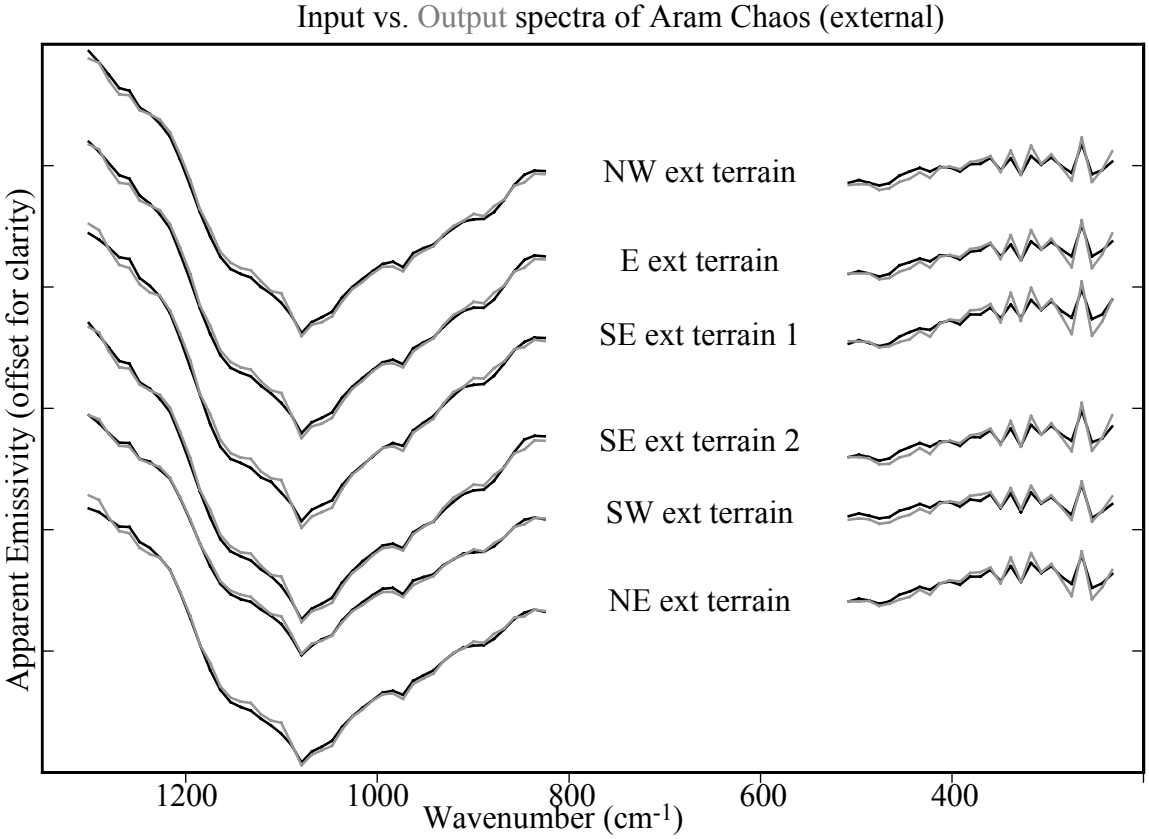

Figure 6 (con't): (c) Measured mean ROI spectra (black) and modeled spectra (gray) produced by linear deconvolution for Aram Chaos external ROIs. Spectra of have been offset for clarity and do not include the deep CO_2 feature.

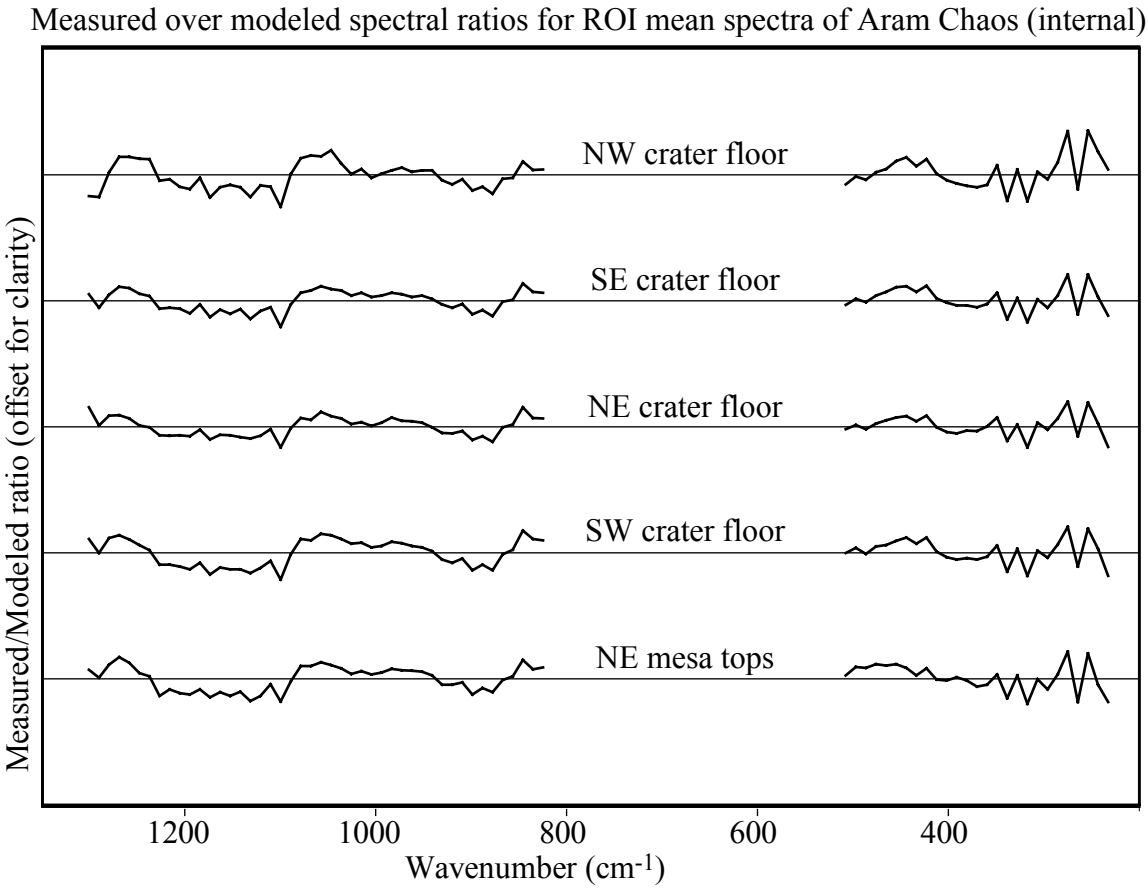

Figure 6 (con't): (d) Measured-to-modeled spectral ratios for Aram Chaos internal ROIs, offset for clarity.

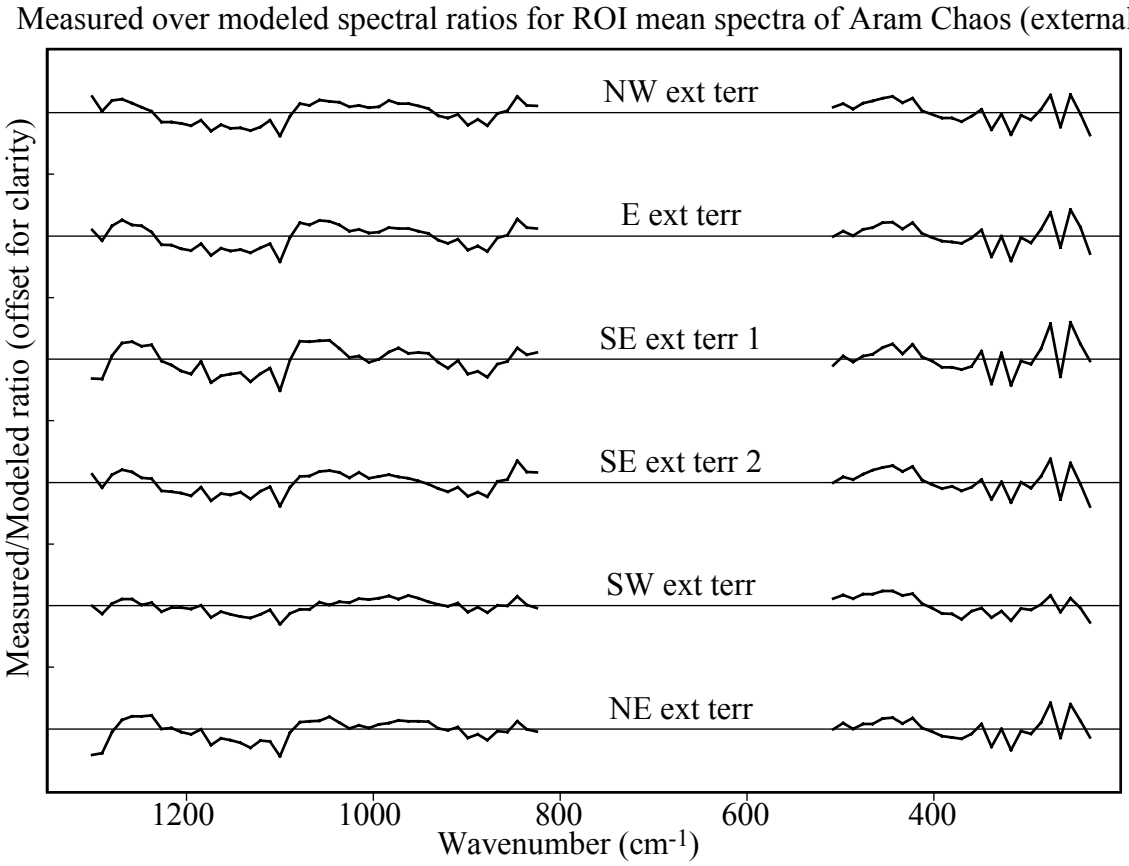

Figure 6 (con't): (e) Measured-to-modeled spectral ratios for Aram Chaos external ROIs, offset for clarity.

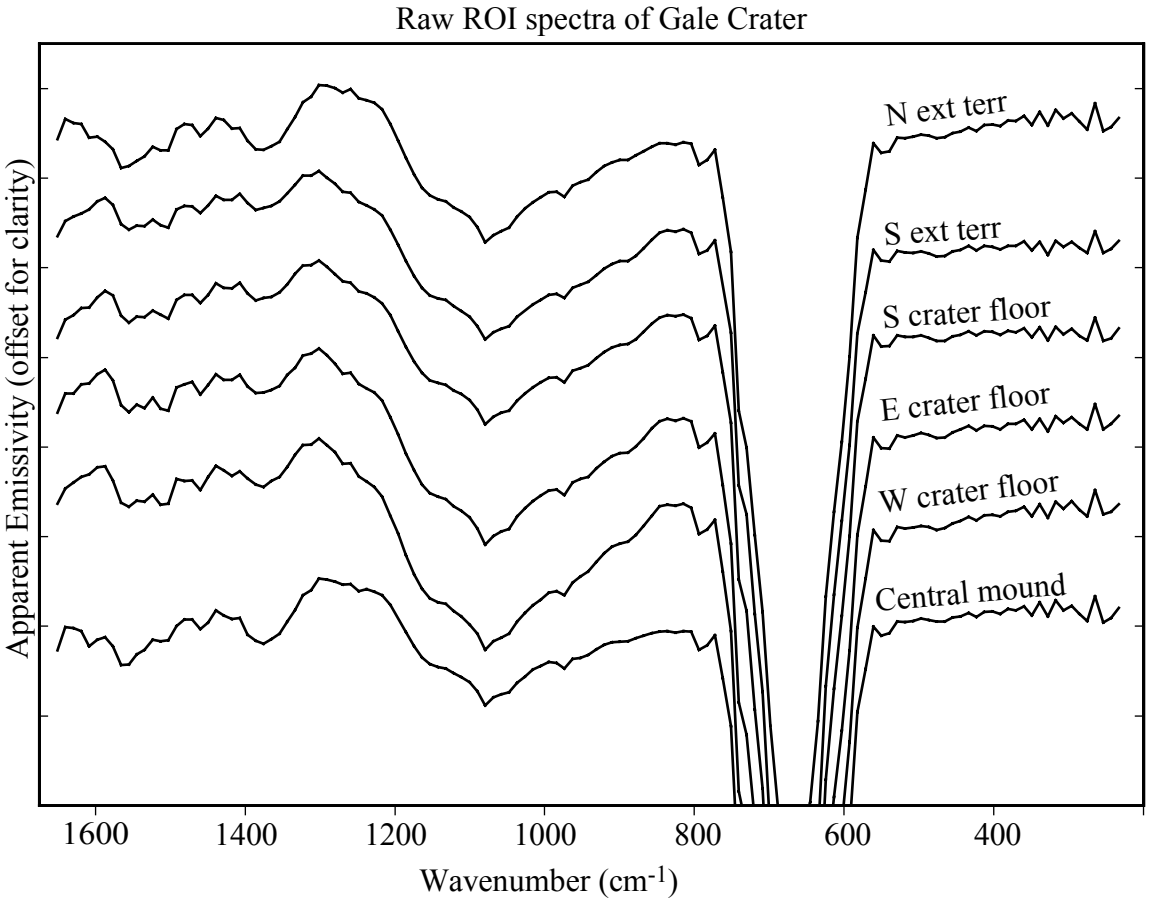

Figure 7: Spectra and spectral ratios for Gale Crater (a) Raw mean ROI spectra from Gale Crater input into linear deconvolution routine, including the deep CO_2 feature near 670-cm^{-1}. Spectra have been offset for clarity.

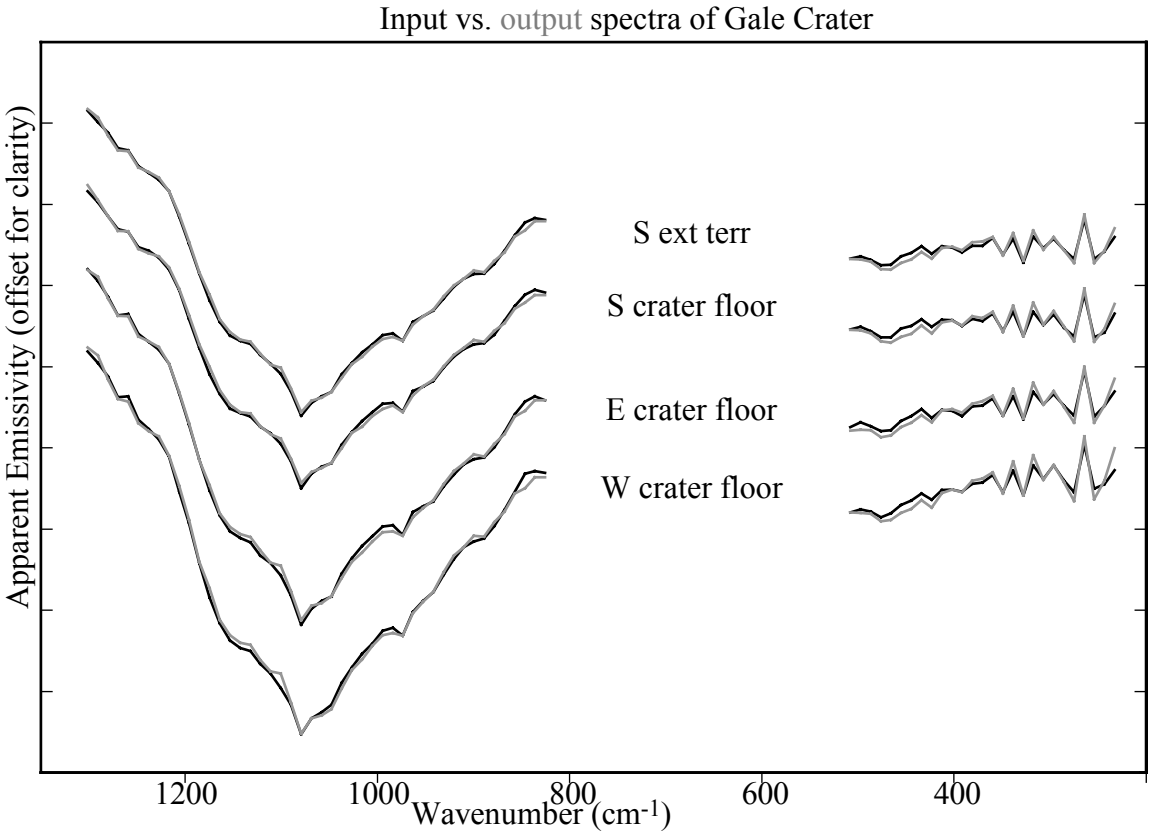

Figure 7 (con't): (b) Measured mean ROI spectra (black) and modeled spectra (gray) produced by linear deconvolution for Gale Crater. Spectra of have been offset for clarity and do not include the deep CO_2 feature.

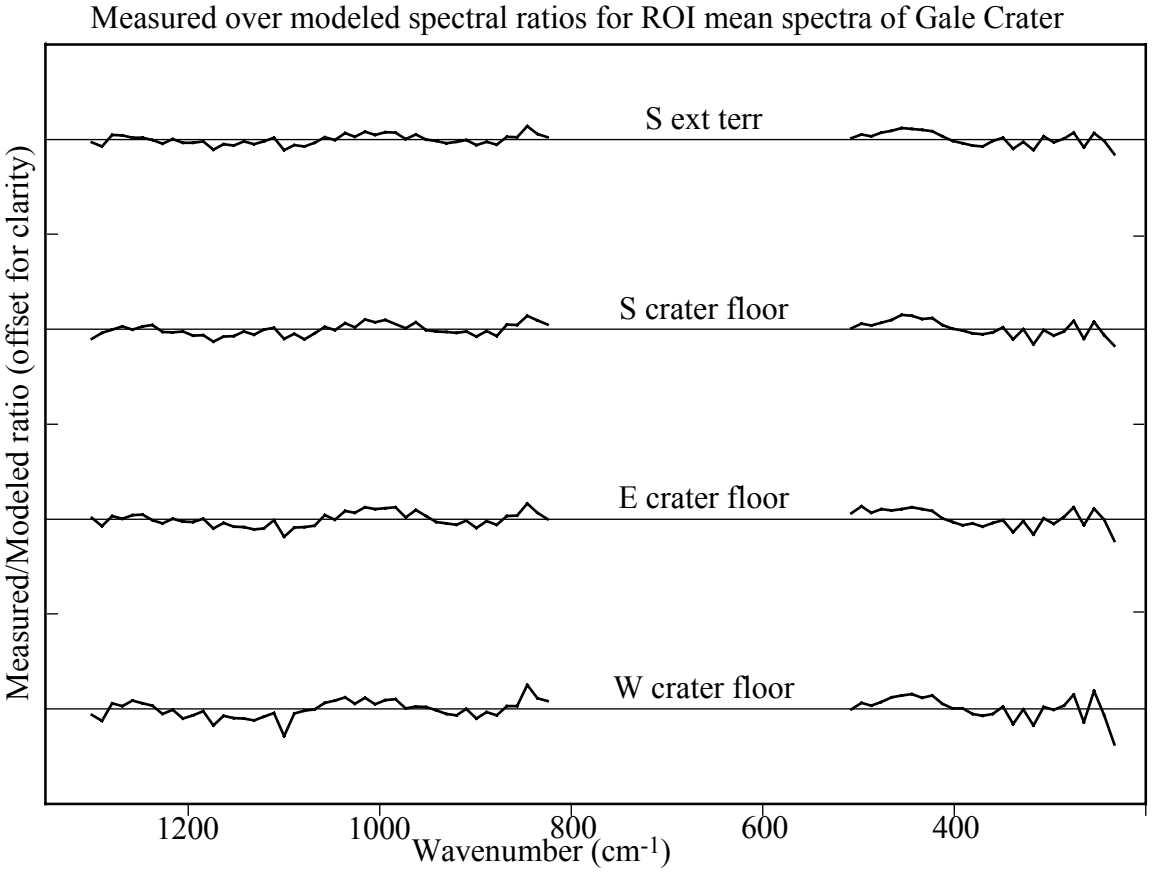

Figure 7 (con't): (c) Measured-to-modeled spectral ratios for Gale Crater ROIs, offset for clarity.

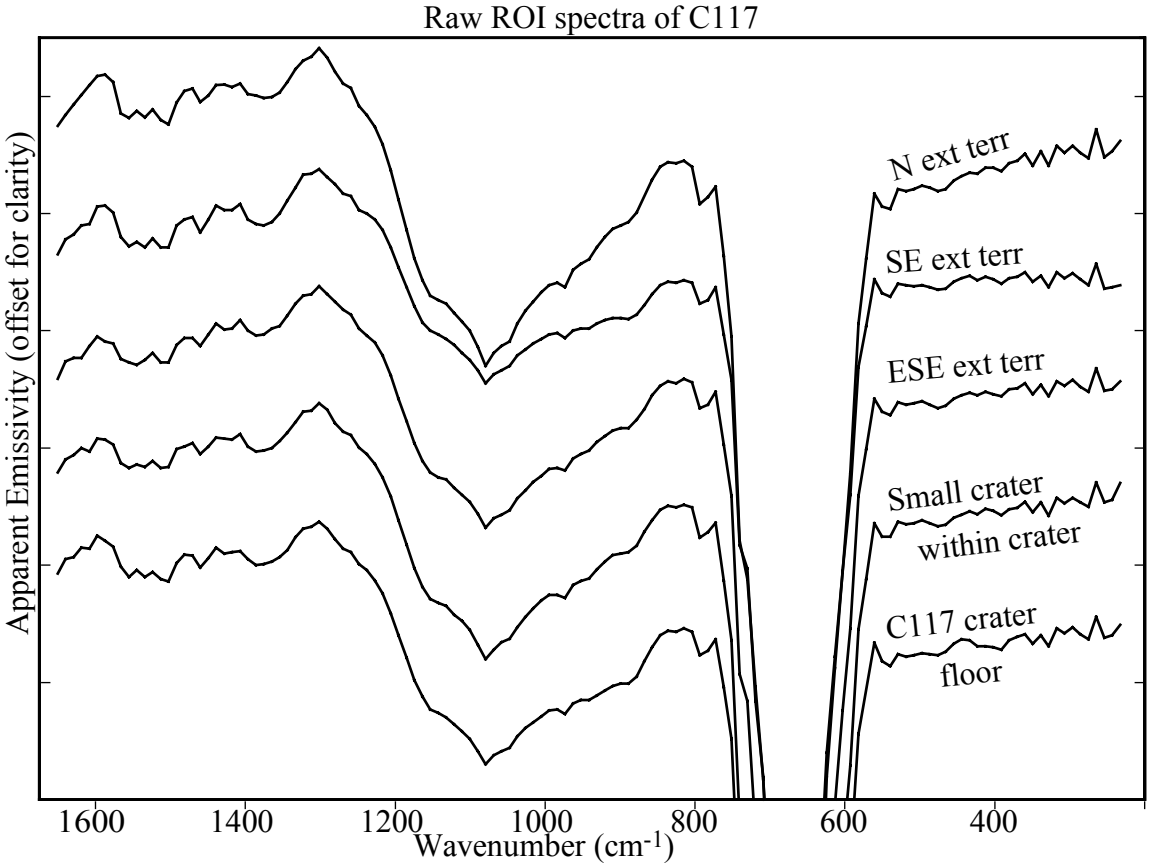

Figure 8: Spectra and spectral ratios for crater C117 (a) Raw mean ROI spectra from crater C117 input into linear deconvolution routine, including the deep CO_2 feature near 670-cm^{-1}. Spectra have been offset for clarity.

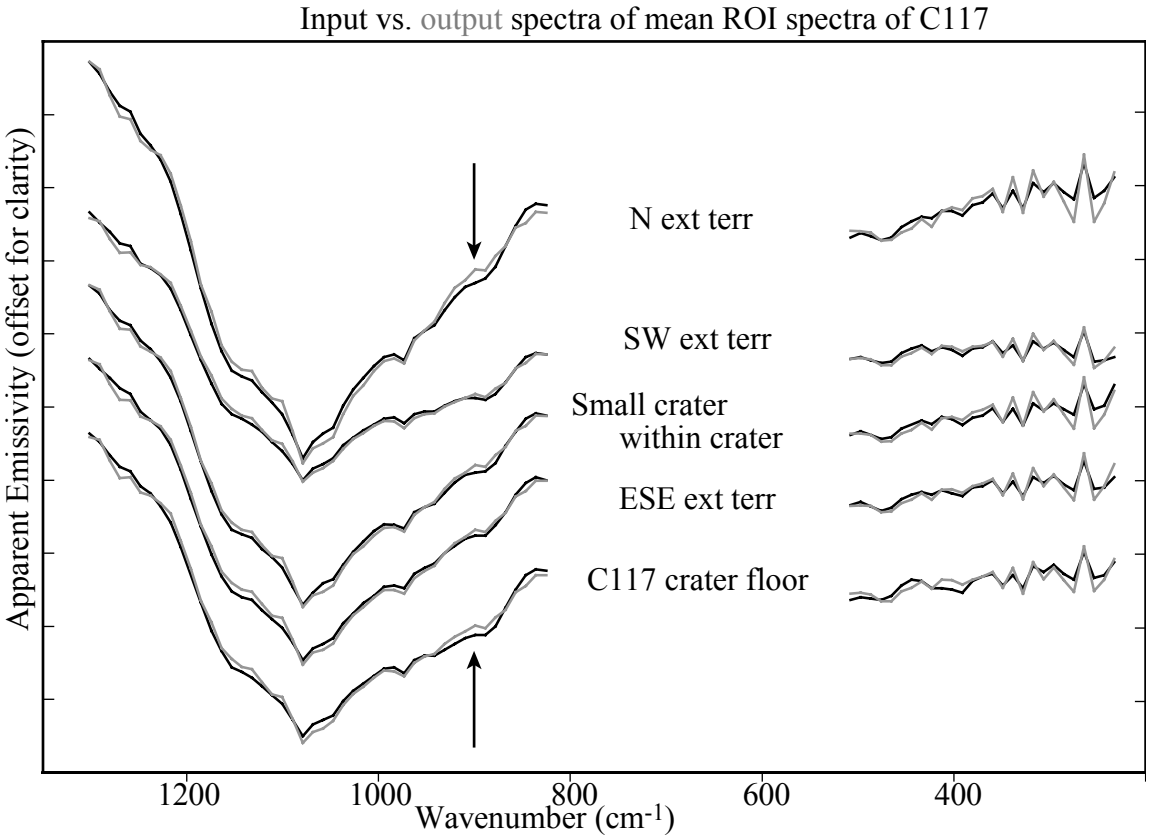

Figure 8 (con't): (b) Measured mean ROI spectra (black) and modeled spectra (gray) produced by linear deconvolution for crater C117. Spectra of have been offset for clarity and do not include the deep CO_2 feature. The arrows indicate possible mismatches between the measured and modeled spectra near 900-cm^{-1} in the north external terrain and the crater floor spectra. Specifically, an absorption feature may be present in the measured spectra, which is not present in the modeled spectra.

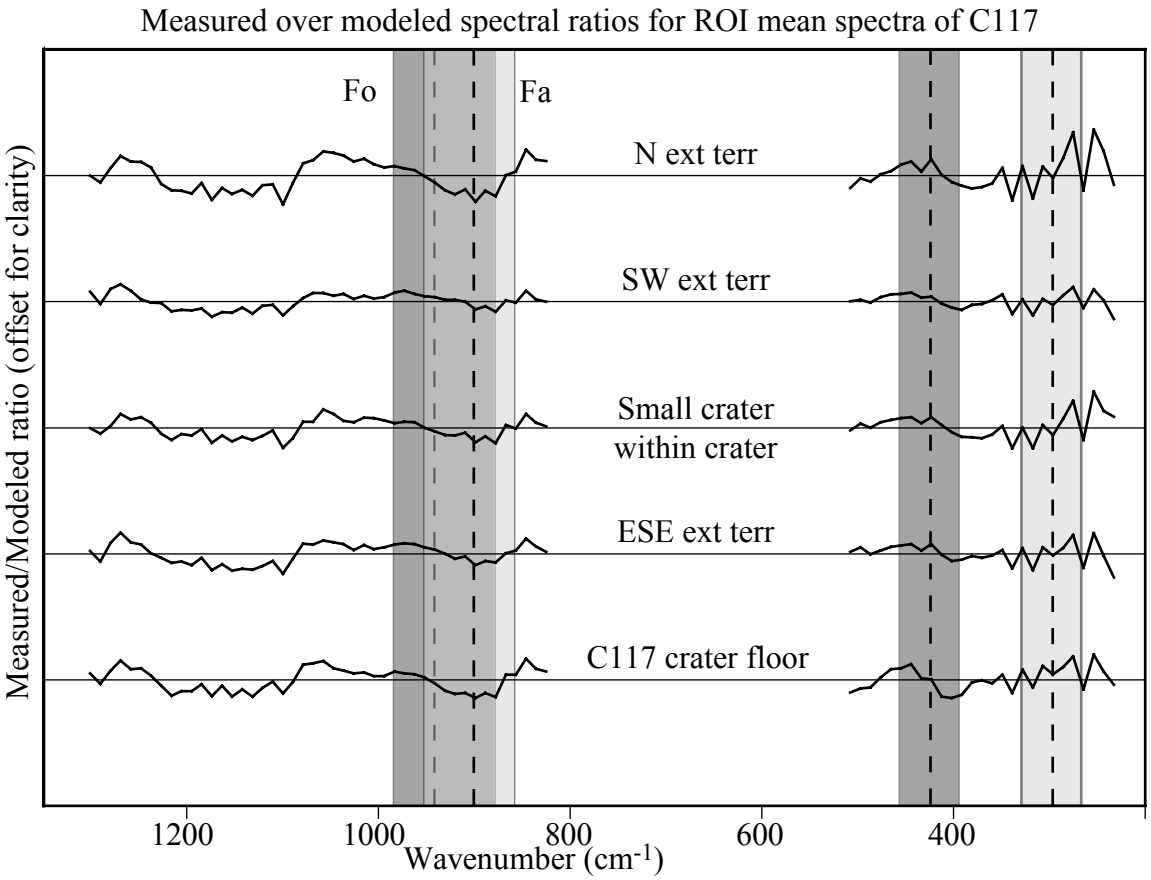

Figure 8 (con't): (c) Measured-to-modeled spectral ratios for crater C117 ROIs, offset for clarity. The crater floor and northern terrain ROI spectral ratios depart from unity near 900-cm^{-1}. Also shown are the spectral locations (dashed vertical lines) and halfwidths (gray boxes) of forsterite (dark gray box) and fayalite (light gray boxes) absorption features.

Part 4

TES Hyperspectral Analyses of Proposed Paleolake Basins on Mars: No Evidence for In-Place Carbonates (Part II)

This chapter contains the results of our TES study for the remaining four basins that were not presented within Chapter 2 or the associated JGR-Planets paper. It is meant to accompany chapter 2 and represents the results and discussion section for these four basins. You will note that there is no introduction, methods or summary section within this chapter, as these sections would be the same as in Chapter 2.

1. Additional craters well-modeled by TES spectral end members only

This appendix contains the results of our TES study for the remaining four basins that were not presented within the paper. These basins include Schiaparelli Crater (Figure 1a), Gusev Crater (Figure 1b), Becquerel Crater (Figure 2a), and one crater located in Terra Sabaeus (crater number 107 from the *Cabrol and Grin* [1999] list and displayed in Figure 2b).

1.1. Schiaparelli Crater (2.5S, 343.3W)

Schiaparelli Crater is a 404 km-diameter basin in the Sinus Sabaeus quadrangle, which has been classified as a closed paleolake basin with an associated fluvial valley network feeder. This basin was reported to contain structures associated with sedimentary deposits and shorelines [*Cabrol and Grin*, 1999].

The final MNF color composite image overlain on a MOLA-derived shaded relief image is displayed in Figure 1a, with the manually-defined ROIs outlined in white. Six surface spectral units were distinguished within the basin. The most obvious units appear in pink tones (Figure 1a) in the northwest and southeast portions of the basin. A third unit appears orange in Figure 1a in the eastern portion of the basin. The remaining floor in the basin ranges from shades of blue to shades of green and has been divided into three units, a southern crater floor unit (purples), a central floor unit (blues) and a northern

crater floor unit (green). Raw mean ROI spectra for Schiaparelli Crater are displayed in Figure 2a.

Table 1 displays the DCI values and spectral deconvolution results for the mean ROI spectra of Schiaparelli Crater. The DCI values for the mean ROI spectra indicate that only the southeast crater floor is a completely dust-free surface. The DCI values for all other mean ROI spectra are intermediate values, indicating that these surfaces are either partially dust covered (i.e., the surface unit composition is not entirely obscured) or is an indurated surface [*Ruff and Christensen*, 2002].

Linear deconvolution results for the mean spectra from each of the six identified ROIs are relatively consistent with the DCI values (Table 1). The northwest and southeast crater floor spectra, which have the two highest DCI values (least dust cover), contain higher proportions of non-dust spectral components than the spectra from other ROIs. Both of these mean ROI spectra are well-modeled using a combination of Acidalia- and Syrtis-type materials (Table 1). The east crater floor is well-modeled by Acidalia- and Syrtis-type materials and small amounts of surface dust (Table 1). The north, south and central crater floor mean ROI spectra are well-modeled by Syrtis-type material, with only the north crater floor model including small amounts of the surface dust endmember (Table 1). When carbonate end members were provided for linear deconvolution, carbonates were used in amounts ranging from 6% to 8%. Some of these abundances were close to the detection limits of carbonates, so we could not say with certainty, based on deconvolution alone, that their signature is not present in the spectra. Therefore, although linear unmixing of these regions of interest did not require additional

end members to explain the spectral variation observed, we did apply additional spectral analyses to confirm this.

The modeled spectra provide good matches to absorption features observed in all of the measured mean ROI spectra (Figure 2b). In addition, the measured-to-modeled spectral ratios for these ROIs display little variation from unity (Figure 2c). Therefore, measured mean ROI spectra do not contain any residual absorption features that are not present in their modeled spectra.

The results of the carbonate index analysis for Schiaparelli Crater mean ROI spectra are shown in Table 2. Using the indices, no spectral signatures of carbonates were detected in any of the mean ROI spectra from Schiaparelli Crater. Because the linear deconvolution method, the spectral ratio technique and the carbonate spectral indices technique gave no positive indications for carbonates, we conclude that carbonates are not exposed in Schiaparelli Crater in abundances above the detection limits of these methods.

1.2. Gusev Crater (14.5S, 184.5W)

Gusev Crater is a 160 km-diameter basin within the Aeolis Quadrangle and is located at the terminus of the 900 km-long Ma'adim Vallis, leading several researchers to propose Gusev was a lacustrine depocenter for the Ma'adim drainage system [*Schneeberger*, 1989; *Cabrol et al.*, 1998]. *Cabrol and Grin* [1999] classified Gusev as having been a lake chain basin with a fluvial valley network. Associated proposed sedimentary structures include delta deposits, sedimentary terraces, shorelines, mounds and possible indicators of evaporite deposits [*Cabrol and Grin*, 1999]. The typically high rates of chemical sedimentation and high biological productivity in similar terminal lake

basin settings on Earth are very favorable for the preservation of biomarkers [*Farmer and Des Marais*, 1999]; if life existed on Mars in the past, Martian fluvio-lacustrine environments would be a favored setting for exploring for evidence of past Martian life. The volume of sediments filling Gusev Crater has been estimated to be 500-m thick and 7,300 km^3 [*Cabrol et al.*, 1998] up to 3200-m thick and 15,100 km^3 [*Carter et al.*, 2001].

A recent investigation by *Milam et al.* [2003] using orbit-based visible wavelength images and day/night thermal infrared brightness temperature images provided a detailed map of the surface units within Gusev. This study revealed that the various surface units present within Gusev are consistent with fluvio-lacustrine, aeolian and/or volcanic deposition. However, the spatial resolution of the data did not allow for the distinction of textures associated with any one type of deposition, nor did it provide unambiguous evidence for a fluvio-lacustrine depocenter.

Figure 1b displays the final MNF color composite image overlain on a MOLA-derived shaded relief image, with the manually-defined ROIs outlined in white. These regions include the low albedo features, which appear in pinks in the MNF image, and the northeast crater floor, which appears in blue. Raw mean ROI input spectra for Gusev Crater are displayed in Figure 3a. The DCI values for these regions reveal that the northeast crater floor of Gusev is a dust-covered surface, so no surface compositional information can be derived from this spectrum (Table 3). The low albedo features have an intermediate DCI value indicating a surface that is partially dust-covered.

It is clear that the use of the surface dust endmember in the linear deconvolution correlates well with the DCI values (Table 3). The deconvolution routine used nearly one-third surface dust component to model the northeast crater floor (Table 3). The low

albedo deposit spectrum was modeled with significantly less surface dust. The low albedo features were well-modeled using TES atmospheric endmembers and Acidalia- and Syrtis-type materials (Table 3). When carbonate end members were provided for linear deconvolution, carbonates were used in amounts ranging from 2% to 9%. Some of these abundances were close to the detection limits of carbonates, so we could not say with certainty that their signature is not present in the spectra based solely on the deconvolution results. As a result, although linear unmixing of these regions of interest did not require additional end members to explain the spectral variation observed, we did apply additional spectral analyses to confirm this.

The low albedo deposit modeled spectrum matches well with the measured mean ROI spectrum (Figure 3b). In addition, the measured-to-modeled spectral ratio for the low albedo features shows very little variation from unity (Figure 3c). Therefore, measured mean ROI spectra do not contain any residual absorption features that are not present in their modeled spectra.

The carbonate indices method was applied to the low albedo deposit mean ROI spectrum and is shown in Table 4. This method did not detect any carbonates within the low albedo deposit mean ROI spectrum. Because the linear deconvolution method, the spectral ratio technique and the carbonate spectral indices technique gave no positive indications for carbonates, we conclude that carbonates are not exposed in Gusev Crater in abundances above the detection limits of these methods. This finding is consistent with results from the Mars Exploration Rover Spirit, which has not found any evidence for carbonates on the surface in its traverses within the low albedo features of Gusev,

with the possible exception of minor amounts in fine-grained dust deposits [*Christensen et al.*, 2004; *Squyres et al.*, 2004].

1.3. Becquerel Crater (21.9N, 7.0W)

Becquerel Crater is a 152 km-diameter basin within the Oxia Palus quadrangle that was classified as a closed paleolake basin with an associated fluvial valley network [*Cabrol and Grin*, 1999]. Putative sedimentary structures associated with this basin include delta deposits, sedimentary terraces, sedimentary deposits, shorelines and mounds [*Cabrol and Grin*, 1999]. *Malin and Edgett* [2000] noted a relatively small, isolated mound within Becquerel Crater composed of layered outcrop material, which is visible in Mars Orbiter Camera (MOC) images. They suggested that these types of intra-crater deposits were either lacustrine in origin or were deposited in a subaerial setting in which atmospheric density imitated a subaqueous depositional environment.

Figure 1c displays the final MNF color composite image overlain on a MOLA-derived shaded relief image, with the manually-defined ROIs outlined in white. ROIs were defined for the southwest crater floor and the east crater floor of Becquerel. In addition, a small impact crater southwest of Becquerel also displays a distinct surface spectral unit and was defined as an ROI as well. Raw mean ROI input spectra for Becquerel Crater are displayed in Figure 4a. DCI values for these ROIs demonstrate that the southwest portion of Becquerel is a fairly dust-free surface, while the east portion of Becquerel crater is fully dust-covered and the small crater to the southwest probably is partially dust-covered (Table 5).

Deconvolution results for the crater floor of Becquerel use TES atmospheric endmembers and Syrtis-type materials, but no surface dust component, consistent with its

DCI value (Table 5). The east crater floor of Becquerel and the small crater southwest of Becquerel both use surface dust with Acidalia-type and TES atmospheric endmembers at levels consistent with their DCI values. When carbonate end members were provided for linear deconvolution, carbonates were used in amounts ranging from 3% to 8%. Since ome of these abundances were close to the detection limits of carbonates, we could not say with certainty that their signature is not present in the spectra based on the deconvolution resuts. Therefore, although deconvolution of these regions of interest did not require additional end members to explain the spectral variation observed, we did apply additional spectral analyses to confirm this.

The modeled spectra provide good matches to the measured mean ROI spectra for these two ROIs (Figure 4b). In addition, the measured-to-modeled spectral ratios for these regions show very little variation from unity (Figure 4c). Therefore, measured mean ROI spectra do not contain any residual absorption features that are not present in their modeled spectra.

Additionally, the carbonate index analysis for Becquerel Crater did not detect a contribution from carbonates in the southwest crater floor ROI spectrum (Table 6). This implies that carbonates are not present in abundances greater than the lower detection limit for the carbonate indices technique. The other two ROI are covered by a spectrally thick layer of dust and therefore the carbonate indices were not applied to these spectra. Because the linear deconvolution method, the spectral ratio technique and the carbonate spectral indices technique gave no positive indications for carbonates, we conclude that carbonates are not exposed in Becquerel Crater in abundances above the detection limits of these methods.

1.4. Crater 107 and 107S in Terra Sabaeus (9.5S, 328W)

Two craters we informally call "C107" and "C107S" located within Terra Sabaeus, are 80 km- and 70 km-diameter basins, respectively (Figure 1d). Crater "C107" is basin number 107 in the *Cabrol and Grin* [1999] survey. This basin was classified as an open paleolake basin with an associated fluvial valley network. Sedimentary deposits are the only type of sedimentary structure identified within this basin [*Cabrol and Grin*, 1999].

Figure 1d displays the final MNF image overlain on MOLA-derived topography with the regions of interest defined for these two putative crater paleolakes and the surrounding plains. Raw mean ROI input spectra for the C107 area are displayed in Figure 5a. All ROIs defined for this region had a DCI values consistent with dust free surfaces (Table 7). The southern floor portion of C107 is well-modeled by TES atmospheric endmembers and both Acidalia- and Syrtis-type materials. However, the northern portion of that same basin appears to be dominated by Syrtis-type surface endmember only (Table 7). The smaller, southern crater (C107S) also models well using atmospheric endmembers with Acidalia- and Syrtis-type materials (Table 7). The spectrum of terrain external to the craters appears to be a combination of TES atmospheric endmembers and both Acidalia- and Syrtis-type materials (Table 7). When carbonate end members were provided for linear deconvolution, carbonates were used in amounts ranging from 7% to 8%. Because some of these abundances were close to the detection limits of carbonates, we could not say with certainty, based on deconvolution alone, that their signature is not present in the spectra. Therefore, although linear

unmixing of these regions of interest did not require additional end members to explain the spectral variation observed, we did apply additional spectral analyses to confirm this.

The output spectra provide good matches to the measured mean spectra for these region of interest mean spectra (Figure 5b). In addition, the measured-to-modeled spectral ratios for the ROIs show very little variation from unity (Figures 5c and d). Therefore, measured mean ROI spectra do not contain any residual absorption features that are not present in their modeled spectra.

The results of the carbonate index analysis for C107 mean ROI spectra are shown in Table 8. The carbonate index analysis for these basins demonstrates that carbonates are not present in this region in abundances greater than the lower detection limits of this method. Because the linear deconvolution method, the spectral ratio technique and the carbonate spectral indices technique gave no positive indications for carbonates, we conclude that carbonates are not exposed in crater C107 in abundances above the detection limits of these methods.

References cited

Cabrol, N.A., and E.A. Grin (1999), Distribution, Classification, and Ages of Martian Impact Crater Lakes, *Icarus*, *142*, 160-172.

Cabrol, N.A., E.A. Grin, R. Landheim, R.O. Kuzmin, and R. Greeley (1998), Duration of the Ma'adim Vallis/Gusev Crater hydrogeologic system, *Icarus*, *133*(1), 98-108.

Carter, B.L., H.V. Frey, S.E.H. Sakimoto, and J.H. Roark (2001), Constraints on Gusev Basin Infill from the Mars Orbiter Laser Altimeter (MOLA) Topography, in *Lunar and Planetary Science Conference*, Lunar and Planetary Institute, Houston, TX.

Christensen, P.R., S.W. Ruff, R.L. Fergason, A.T. Knudson, S. Anwar, R.E. Arvidson, J.L. Bandfield, D.L. Blaney, C. Budney, W.M. Calvin, T.D. Glotch, M.P. Golombek, N. Gorelick, T.G. Graff, V.E. Hamilton, A. Hayes, J.R. Johnson, H.Y. McSween, Jr., G.L. Mehall, L. Mehall, J.E. Moersch, R.V. Morris, A.D. Rogers, M.D. Smith, S.W. Squyres, M.J. Wolff, and M.B. Wyatt (2004), Initial results from the Miniature Thermal Emission Spectrometer Experiment at the Spirit Landing Site in Gusev Crater, *Science*, *305*(5685), 837-842.

Farmer, J.D., and D.J. Des Marais (1999), Exploring for a record of ancient Martian life, *J. Geophys. Res.*, *104*(E11), 26977-26995.

Malin, M.C., and K.S. Edgett (2000), Sedimentary rocks of early Mars, *Science*, *290*(5498), 1927-1937.

Milam, K.A., K.R. Stockstill, J.E. Moersch, H.Y. McSween, Jr., L.L. Tornabene, A. Ghosh, M.B. Wyatt, and P.R. Christensen (2003), THEMIS Characterization of the MER Gusev Crater Landing Site, *Journal of Geophysical Research*, *108*(E12), 8078, 10.1029/2002JE002023.

Ruff, S.W., and P.R. Christensen (2002), Bright and dark regions on Mars: Particle size and mineralogical characteristics based on Thermal Emission Spectrometer data, *J. Geophys. Res.*, *107*(E12), 5127-5148.

Schneeberger, D.M. (1989), Episodic channel activity at Ma'adim Vallis, Mars, Lunar and Planetary Science XX, Lunar and Planetary Institute, Houston, TX.

Squyres, S.W., R.E. Arvidson, J.F. Bell, III, J. Brückner, N.A. Cabrol, W.M. Calvin, M.H. Carr, P.R. Christensen, B.C. Clark, L. Crumpler, D.J. Des Marais, C. d'Uston, T. Economou, J.D. Farmer, W. Farrand, W. Folkner, M. Golombek, S. Gorevan, J.A. Grant, R. Greeley, J. Grotzinger, L. Haskin, K.E. Herkenhoff, S. Hviid, J.R. Johnson, G. Klingelhöffer, A. Knoll, G. Landis, M. Lemmon, R. Li, M.B. Madsen, M.C. Malin, S. McLennan, H.Y. McSween, Jr., D.W. Ming, J.E. Moersch, R.V. Morris, T. Parker, J. Rice, W., Jr., L. Richter, R. Rieder, M. Sims, M.D. Smith, P. Smith, L.A. Soderblom, R. Sullivan, A. Wald, H. Wänke, T. Wdowiak, M.J. Wolff, and A. Yen (2004), The Spirit Rover's Athena Science Investigation at Gusev crater, Mars, *Science*, *305*(5685), 794-799.

Appendix

Table 1: Results of linear deconvolution and dust cover index (DCI) calculations for Schiaparelli Crater mean ROI spectra.

	N crater floor	NW crater floor	SE crater floor	S crater floor	Central floor	E crater floor
Acidalia type	0.0	12.8	11.0	0.0	0.0	11.7
Syrtis type	7.1	10.1	18.0	13.8	8.9	2.1
Hematite	0.0	2.1	1.1	0.2	0.0	0.9
Dust Low CO_2	66.6	60.7	59.9	73.2	78.5	41.9
Dust High CO_2	1.3	0.0	0.0	0.7	0.0	12.6
Water Ice Cloud$_1$	7.8	5.1	1.8	3.7	5.3	16.0
Water Ice Cloud$_2$	8.2	9.4	7.9	8.6	7.4	8.1
Surface dust	9.8	0.0	0.0	0.0	0.0	8.1
Total	100.7	100.2	99.8	100.2	100.1	101.4
Spectral RMS	0.00262	0.00243	0.00262	0.00251	0.00287	0.00251
DCI	0.943	0.960	0.962	0.948	0.944	0.949
DCI value interpretation	intermediate	intermediate	dust free	intermediate	intermediate	intermediate

Table 2: Results of carbonate indices calculations for Schiaparelli Crater ROI mean spectra. Excludes regions which appear dust covered according to the DCI and linear deconvolutions.

	N crater floor	NW crater floor	SE crater floor	S crater floor	Central floor	E crater floor
I_{Abs} (Cal, 884)	1.004	1.006	1.008	1.005	1.005	1.003
I_{Abs} (Cal, 317)	0.994	0.994	0.996	0.996	0.995	0.994
RBD (Cal, 884)	0.004	0.006	0.008	0.005	0.005	0.003
RBD (Cal, 317)	-0.006	-0.006	-0.004	-0.004	-0.005	-0.006
RBDR (Cal)	-1.504	-1.025	-0.539	-0.921	-1.072	-2.209
I_{Abs} (Cal, 884) > 1.0?	FALSE	FALSE	FALSE	FALSE	FALSE	FALSE
I_{Abs} (Cal, 317) > 1.0?	FALSE	FALSE	FALSE	FALSE	FALSE	FALSE
2.0 < RBDR(Cal) < 4.0?	FALSE	FALSE	FALSE	FALSE	FALSE	FALSE
Calcite?	**FALSE**	**FALSE**	**FALSE**	**FALSE**	**FALSE**	**FALSE**
I_{Abs}(Mag, 894)	1.001	1.003	1.005	1.002	1.002	1.001
I_{Abs}(Mag, 381)	0.997	0.996	0.997	0.997	0.997	0.996
RBD (Mag, 894)	0.001	0.003	0.005	0.002	0.002	0.001
RBD (Mag, 381)	-0.003	-0.004	-0.003	-0.003	-0.003	-0.005
RBDR(Mag)	-1.849	-1.179	-0.591	-1.291	-1.391	-3.296
I_{Abs}(Mag, 381) > 1.0?	TRUE	TRUE	TRUE	TRUE	TRUE	TRUE
I_{Abs}(Mag, 894) > 1.02?	FALSE	FALSE	FALSE	FALSE	FALSE	FALSE
1.82 < RBDR(Mag) < 2.35?	FALSE	FALSE	FALSE	FALSE	FALSE	FALSE
Magnesite?	**FALSE**	**FALSE**	**FALSE**	**FALSE**	**FALSE**	**FALSE**
I_{Abs}(Sid, 360)	1.003	1.005	1.007	1.003	1.004	1.003
I_{Abs}(Sid, 878)	0.995	0.994	0.996	0.995	0.994	0.994
RBD (Cal, 884)	0.003	0.005	0.007	0.003	0.004	0.003
RBD (Cal, 317)	-0.005	-0.006	-0.005	-0.005	-0.006	-0.006
RBDR(Sid)	-1.647	-1.089	-0.668	-1.425	-1.508	-1.857
I_{Abs}(Sid, 360) > 1.024?	FALSE	FALSE	FALSE	FALSE	FALSE	FALSE
I_{Abs}(Sid, 878) > 1.014?	FALSE	FALSE	FALSE	FALSE	FALSE	FALSE
0.85 < RBDR(Sid) < 1.05?	FALSE	FALSE	FALSE	FALSE	FALSE	FALSE
Siderite?	**FALSE**	**FALSE**	**FALSE**	**FALSE**	**FALSE**	**FALSE**

Table 3: Results of linear deconvolution and dust cover index (DCI) calculations for Gusev Crater ROI mean spectra.

	NE crater floor	Low albedo features
Acidalia type	0.0	21.3
Syrtis type	2.6	10.5
Hematite	0.0	0.0
Dust Low CO_2	55.8	34.2
Dust High CO_2	8.0	21.4
Water Ice $Cloud_1$	0.0	0.0
Water Ice $Cloud_2$	4.6	6.3
Surface dust	29.5	6.4
Total	100.5	100.3
Spectral RMS	0.00275	0.00214
DCI	0.935	0.958
DCI value interpretation	dust covered	intermediate

Table 4: Results of carbonate indices calculations for Gusev Crater ROI mean spectra. Excludes regions which appear dust covered according to the DCI and linear deconvolutions.

	Low albedo features
I_{Abs} (Cal, 884)	1.002
I_{Abs} (Cal, 317)	1.001
RBD (Cal, 884)	0.002
RBD (Cal, 317)	0.001
RBDR (Cal)	0.330
I_{Abs} (Cal, 884) > 1.0?	FALSE
I_{Abs} (Cal, 317) > 1.0?	FALSE
2.0 < RBDR(Cal) < 4.0?	FALSE
Calcite?	**FALSE**
I_{Abs}(Mag, 894)	0.999
I_{Abs}(Mag, 381)	0.997
RBD (Mag, 894)	-0.001
RBD (Mag, 381)	-0.003
RBDR(Mag)	2.841
I_{Abs}(Mag, 381) > 1.0?	FALSE
I_{Abs}(Mag, 894) > 1.02?	FALSE
1.82 < RBDR(Mag) < 2.35?	FALSE
Magnesite?	**FALSE**
I_{Abs}(Sid, 360)	1.001
I_{Abs}(Sid, 878)	0.999
RBD (Cal, 884)	0.001
RBD (Cal, 317)	-0.001
RBDR(Sid)	-1.440
I_{Abs}(Sid, 360) > 1.024?	FALSE
I_{Abs}(Sid, 878) > 1.014?	FALSE
0.85 < RBDR(Sid) < 1.05?	FALSE
Siderite?	**FALSE**

Table 5: Results of linear deconvolution and dust cover index (DCI) calculations for Becquerel Crater ROI mean spectra.

	SW crater floor	E crater floor	Small crater to SW
Acidalia type	0.0	9.7	25.8
Syrtis type	20.1	0.0	0.0
Hematite	0.3	0.0	0.0
Dust Low CO_2	71.3	21.5	32.2
Dust High CO_2	0.0	25.7	24.4
Water Ice $Cloud_1$	6.8	1.7	0.0
Water Ice $Cloud_2$	0.0	6.4	9.9
Surface dust	0.0	36.2	8.7
Total	98.5	101.2	101.0
Spectral RMS	0.00321	0.00315	0.00284
DCI	0.968	0.925	0.942
DCI value interpretation	dust free	dust covered	intermediate

Table 6: Results of carbonate indices calculations for Becquerel Crater ROI mean spectra. Excludes regions which appear dust covered according to the DCI and linear deconvolution.

	SW crater floor	**Small crater to SW**
I_{Abs} (Cal, 884)	1.006	1.002
I_{Abs} (Cal, 317)	0.999	0.998
RBD (Cal, 884)	0.006	0.002
RBD (Cal, 317)	-0.001	-0.002
RBDR (Cal)	-0.114	-0.964
I_{Abs} (Cal, 884) > 1.0?	TRUE	TRUE
I_{Abs} (Cal, 317) > 1.0?	FALSE	FALSE
2.0 < RBDR(Cal) < 4.0?	FALSE	FALSE
Calcite?	**FALSE**	**FALSE**
I_{Abs}(Mag, 894)	1.003	0.999
I_{Abs}(Mag, 381)	0.997	0.996
RBD (Mag, 894)	0.003	-0.001
RBD (Mag, 381)	-0.003	-0.004
RBDR(Mag)	-0.764	6.453
I_{Abs}(Mag, 381) > 1.0?	TRUE	FALSE
I_{Abs}(Mag, 894) > 1.02?	FALSE	FALSE
1.82 < RBDR(Mag) < 2.35?	FALSE	FALSE
Magnesite?	**FALSE**	**FALSE**
I_{Abs}(Sid, 360)	1.006	1.001
I_{Abs}(Sid, 878)	0.997	0.996
RBD (Cal, 884)	0.006	0.001
RBD (Cal, 317)	-0.003	-0.004
RBDR(Sid)	-0.564	-3.887
I_{Abs}(Sid, 360) > 1.024?	FALSE	FALSE
I_{Abs}(Sid, 878) > 1.014?	FALSE	FALSE
0.85 < RBDR(Sid) < 1.05?	FALSE	FALSE
Siderite?	**FALSE**	**FALSE**

Table 7: Results of linear deconvolution and dust cover index (DCI) calculations for Crater 107 (in Terra Sabaea) ROI mean spectra.

	C107S S crater floor	**C107N S crater floor**	**C107N N crater floor**	**C107 NN ext terr**	**C107 N ext terr**	**C107 W ext terr**	**C107 Small crater to NE**
Acidalia type	24.1	41.1	25.6	11.1	22.3	17.0	28.4
Syrtis type	30.4	0.3	35.0	27.6	25.0	20.6	25.1
Hematite	1.4	3.4	0.9	2.1	2.3	1.6	3.0
Dust Low CO_2	38.0	23.2	34.1	55.6	43.8	50.3	31.4
Dust High CO_2	0.0	14.7	0.0	0.0	0.0	0.7	6.3
Water Ice $Cloud_1$	1.0	5.7	0.0	0.0	2.1	1.8	1.5
Water Ice $Cloud_2$	4.7	12.7	3.8	2.7	4.3	8.3	4.1
Surface dust	0.0	0.0	0.0	0.0	0.0	0.0	0.0
Total	99.7	101.1	99.5	99.0	99.8	100.2	99.8
Spectral RMS	0.00225	0.00247	0.00199	0.00307	0.00200	0.00200	0.00205
DCI	0.973	0.966	0.974	0.969	0.970	0.962	0.975
DCI value interpretation	dust free	dust free	dust free	dust free	dust free	dust free	dust free

Table 8: Results of carbonate indices calculations for Crater 107 ROI mean spectra. Excludes regions which appear dust covered according to the DCI and linear deconvolution.

	C107S S crater floor	C107N S crater floor	C107N N crater floor	C107 NN ext terr	C107 N ext terr	C107 W ext terr	C107 Small crater to NE
I_{Abs} (Cal, 884)	1.007	1.008	1.003	1.006	1.007	1.005	1.007
I_{Abs} (Cal, 317)	1.006	1.003	0.995	0.998	1.000	1.003	1.003
RBD (Cal, 884)	0.007	0.007	0.003	0.006	0.007	0.005	0.007
RBD (Cal, 317)	0.005	0.003	-0.005	-0.002	0.000	0.002	0.003
RBDR (Cal)	0.741	0.447	-1.652	-0.369	0.017	0.527	0.359
I_{Abs} (Cal, 884) > 1.0?	FALSE	FALSE	FALSE	FALSE	FALSE	FALSE	FALSE
I_{Abs} (Cal, 317) > 1.0?	FALSE	FALSE	FALSE	FALSE	FALSE	FALSE	FALSE
2.0 < RBDR(Cal) < 4.0?	FALSE	FALSE	FALSE	FALSE	FALSE	FALSE	FALSE
Calcite?	**FALSE**	**FALSE**	**FALSE**	**FALSE**	**FALSE**	**FALSE**	**FALSE**
I_{Abs}(Mag, 894)	1.005	1.005	1.002	1.004	1.005	1.003	1.005
I_{Abs}(Mag, 381)	1.000	0.999	0.993	0.997	0.998	0.998	0.998
RBD (Mag, 894)	0.005	0.005	0.002	0.004	0.005	0.003	0.005
RBD (Mag, 381)	0.000	-0.001	-0.007	-0.003	-0.002	-0.002	-0.002
RBDR(Mag)	-0.096	-0.238	-2.950	-0.750	-0.351	-0.555	-0.433
I_{Abs}(Mag, 381) > 1.0?	TRUE	TRUE	TRUE	TRUE	TRUE	TRUE	TRUE
I_{Abs}(Mag, 894) > 1.02?	FALSE	FALSE	FALSE	FALSE	FALSE	FALSE	FALSE
1.82 < RBDR(Mag) < 2.35?	FALSE	FALSE	FALSE	FALSE	FALSE	FALSE	FALSE
Magnesite?	**FALSE**	**FALSE**	**FALSE**	**FALSE**	**FALSE**	**FALSE**	**FALSE**
I_{Abs}(Sid, 360)	1.008	1.008	1.002	1.005	1.006	1.005	1.006
I_{Abs}(Sid, 878)	1.003	1.001	0.996	0.997	0.998	1.001	0.999
RBD (Cal, 884)	0.008	0.008	0.002	0.005	0.006	0.005	0.006
RBD (Cal, 317)	0.003	0.001	-0.004	-0.003	-0.002	0.001	-0.001
RBDR(Sid)	0.322	0.124	-1.670	-0.555	-0.335	0.112	-0.110
I_{Abs}(Sid, 360) > 1.024?	FALSE	FALSE	FALSE	FALSE	FALSE	FALSE	FALSE
I_{Abs}(Sid, 878) > 1.014?	FALSE	FALSE	FALSE	FALSE	FALSE	FALSE	FALSE
0.85 < RBDR(Sid) < 1.05?	FALSE	FALSE	FALSE	FALSE	FALSE	FALSE	FALSE
Siderite?	**FALSE**	**FALSE**	**FALSE**	**FALSE**	**FALSE**	**FALSE**	**FALSE**

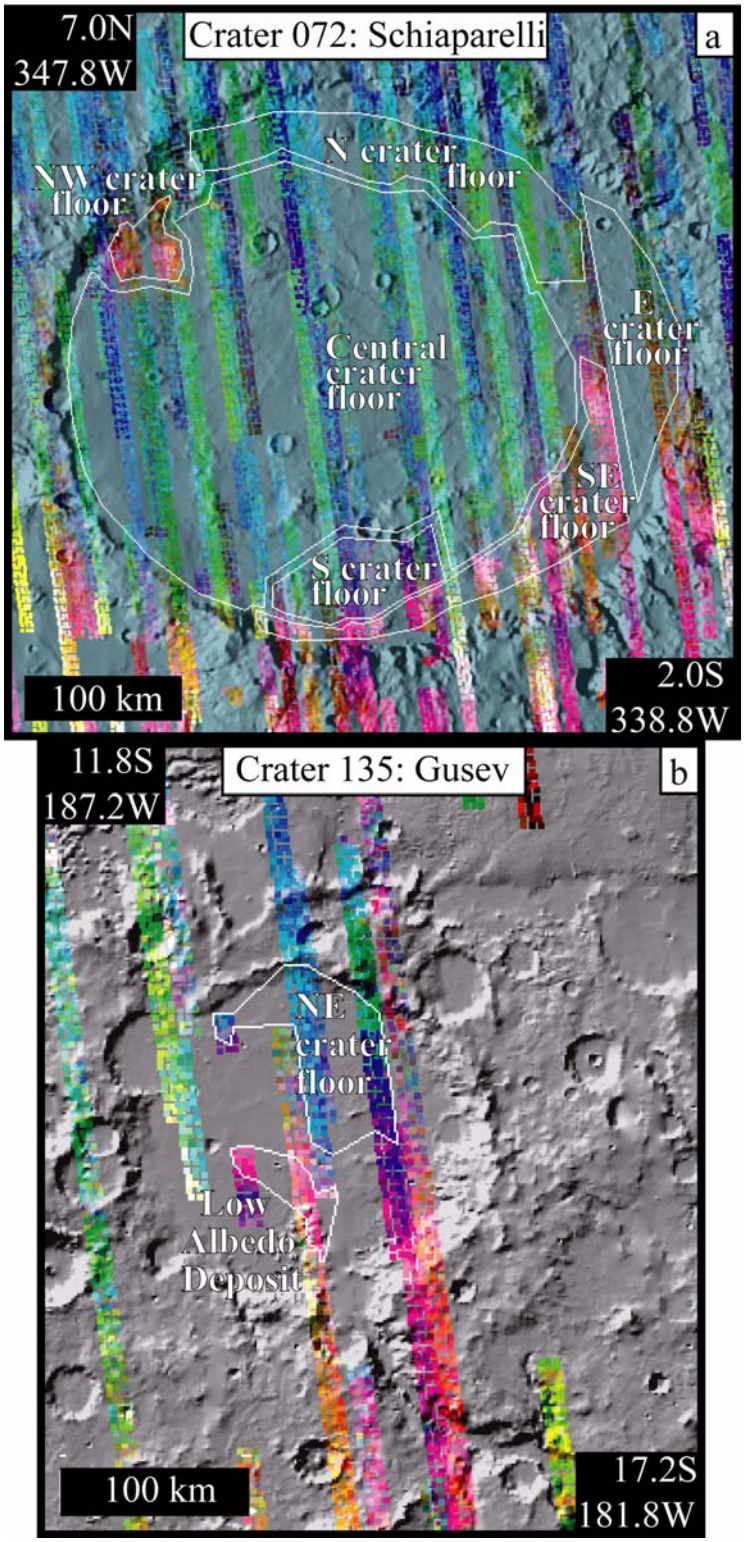

Figure 1: Final MNF color composite images overlain on MOLA-derived shaded relief image of additional craters, with manually-defined ROIs outlined in white. (a) Schiaparelli Crater and (b) Gusev Crater.

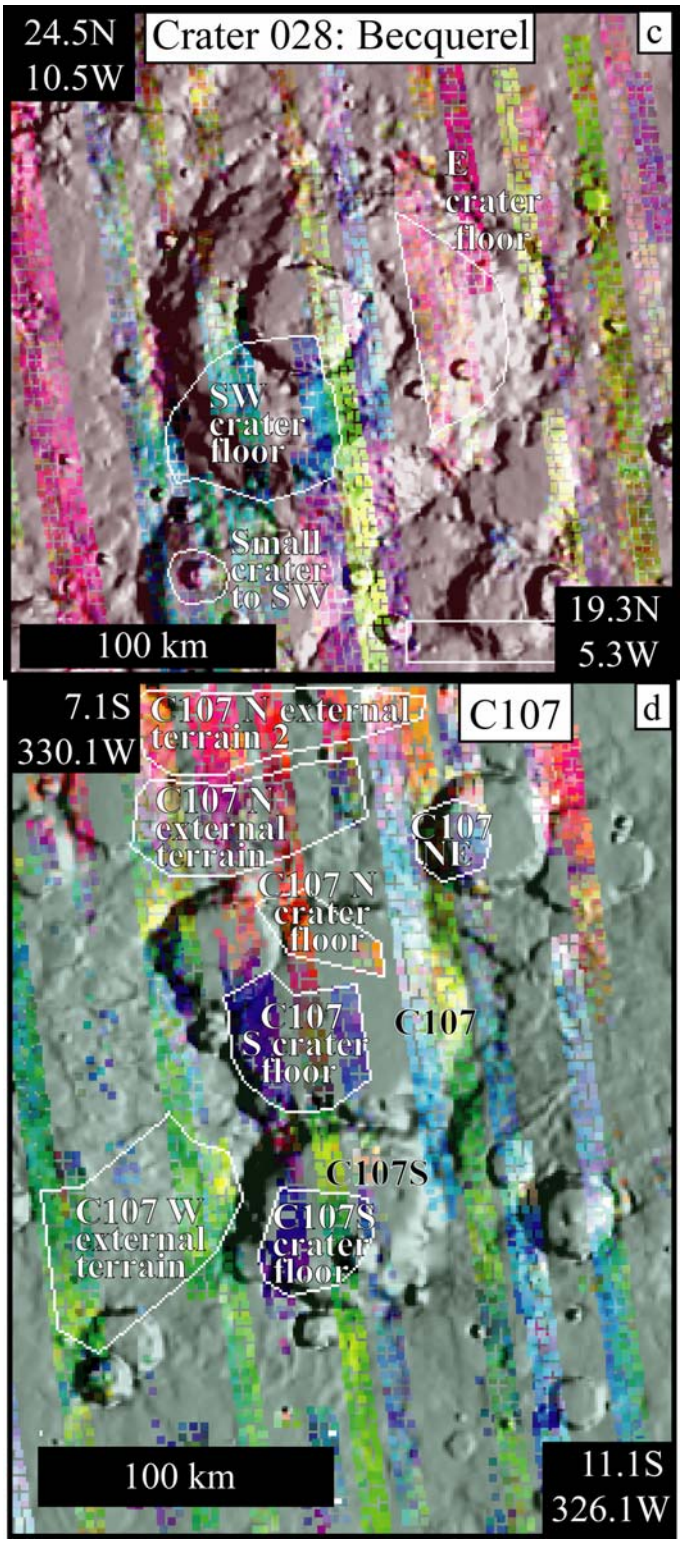

Figure 1 (con't): (c) Becquerel Crater and (d) crater C107.

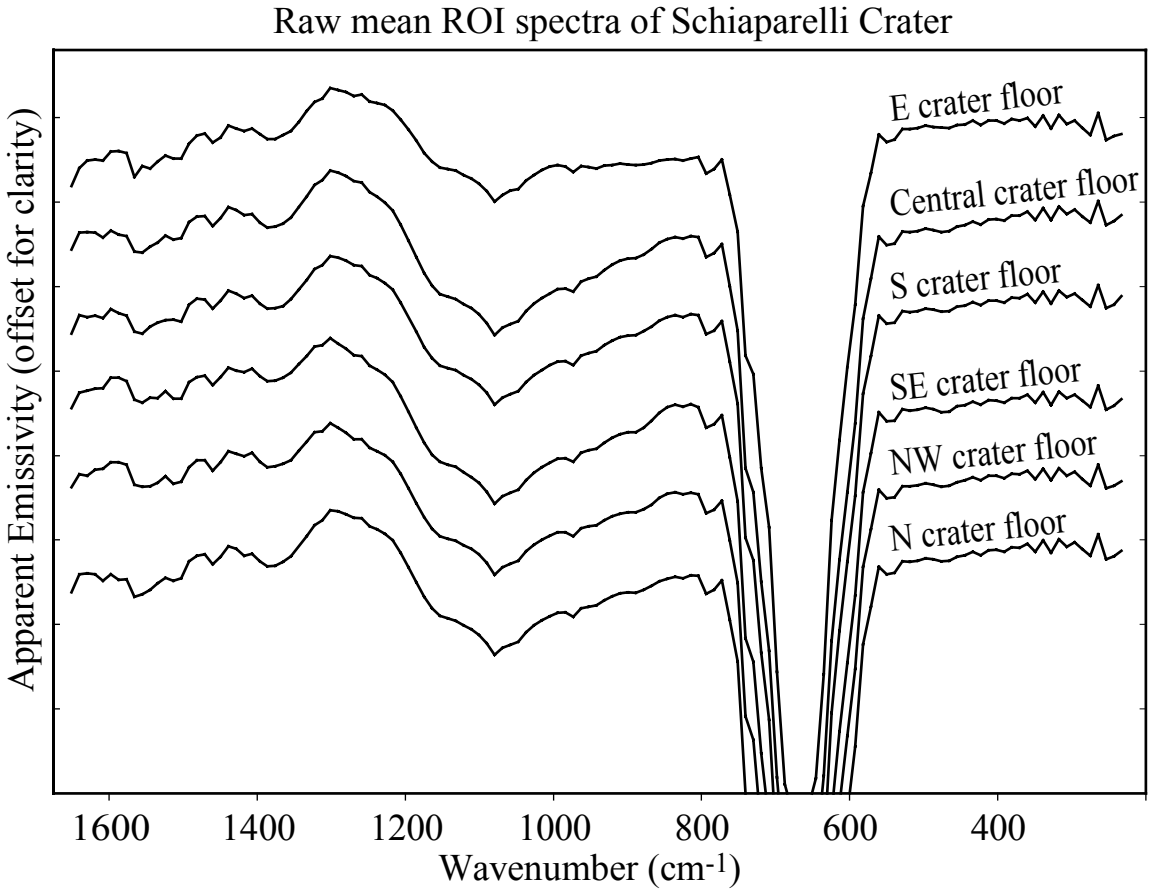

Figure 2: Spectra and spectral ratios for Schiaparelli Crater. (a) Raw mean ROI spectra from Schiaparelli Crater input into linear deconvolution routine, including the deep CO_2 feature near 670-cm^{-1}. Spectra have been offset for clarity.

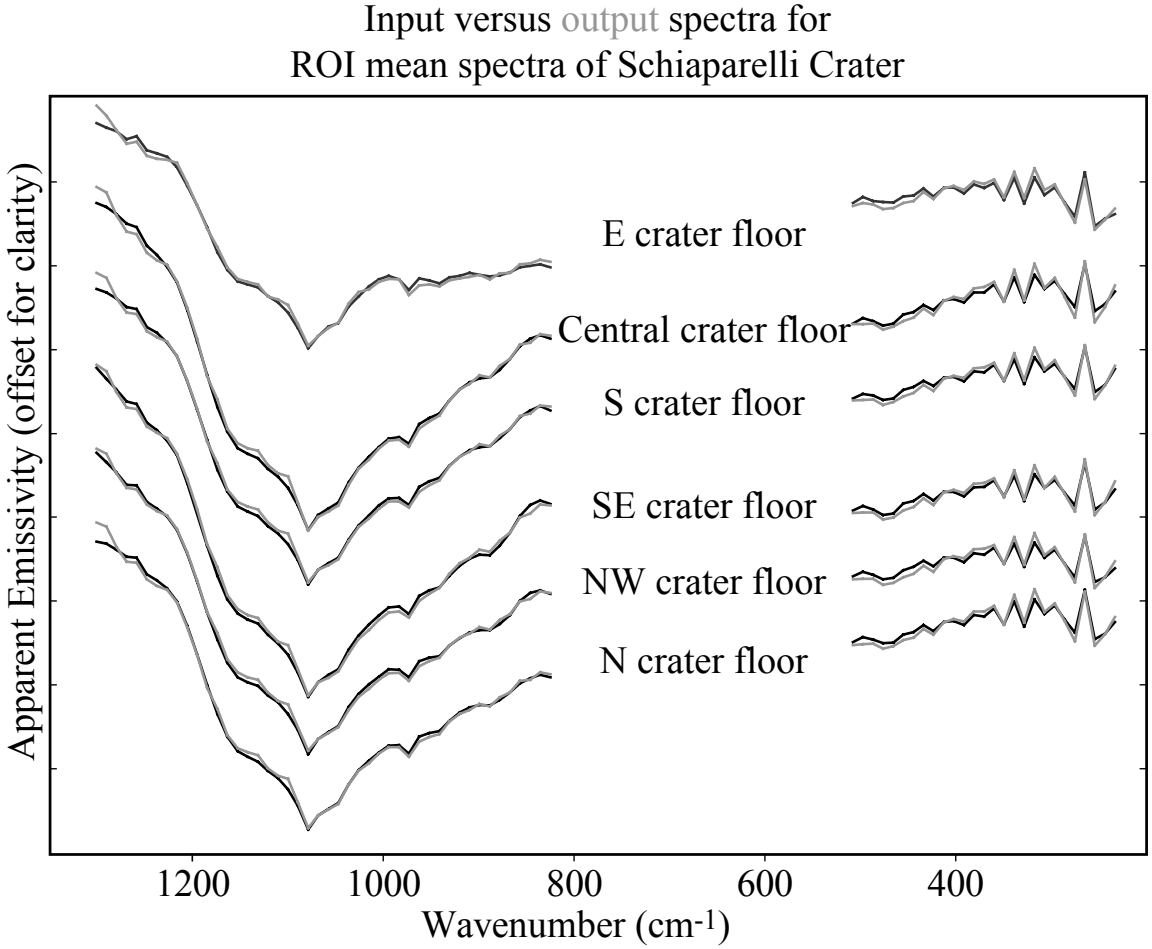

Figure 2 (con't): (b) Measured mean ROI spectra (black) and modeled spectra (gray) produced by linear deconvolution for Schiaparelli Crater. Spectra of have been offset for clarity and do not include the deep CO_2 feature.

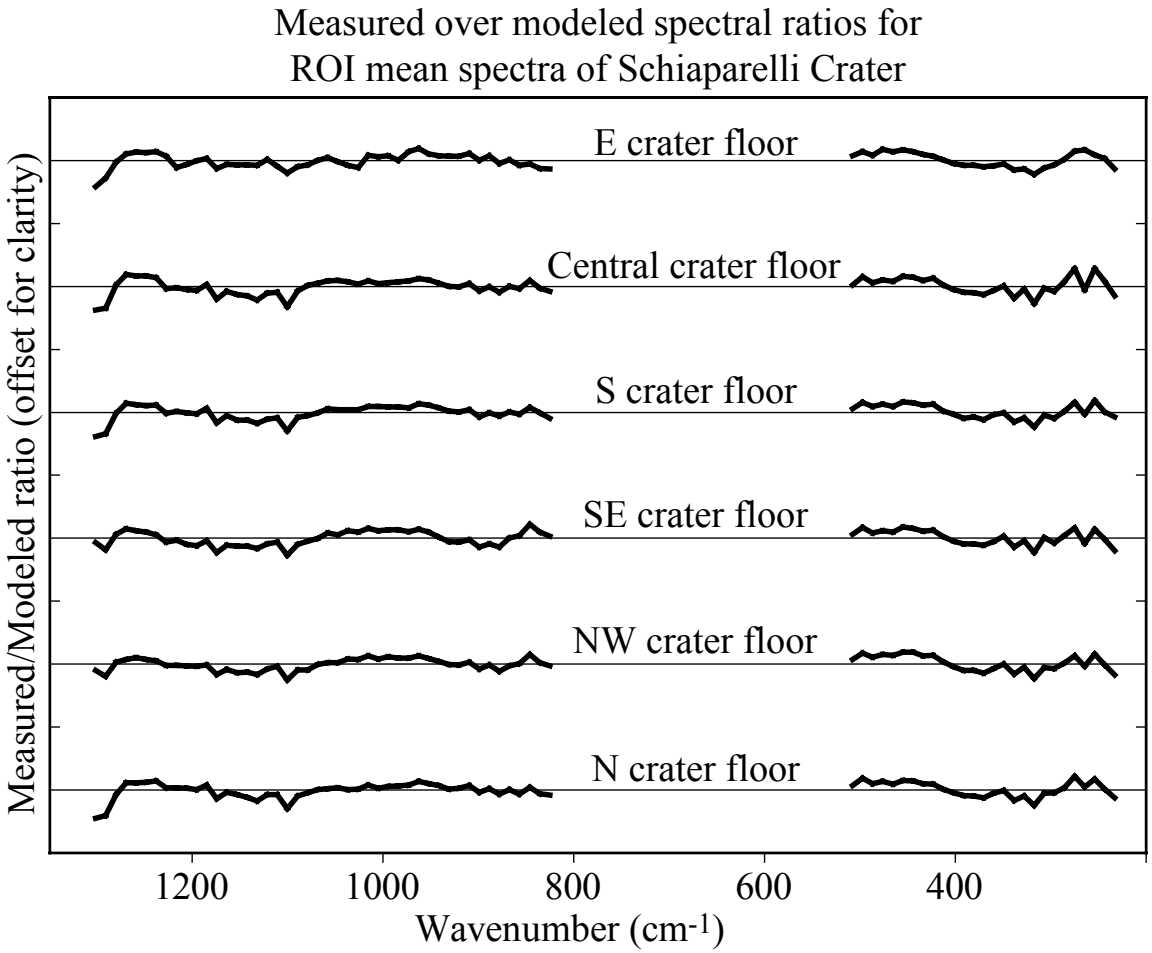

Figure 2 (con't): (c) Measured-to-modeled spectral ratios for Schiaparelli Crater ROIs, offset for clarity.

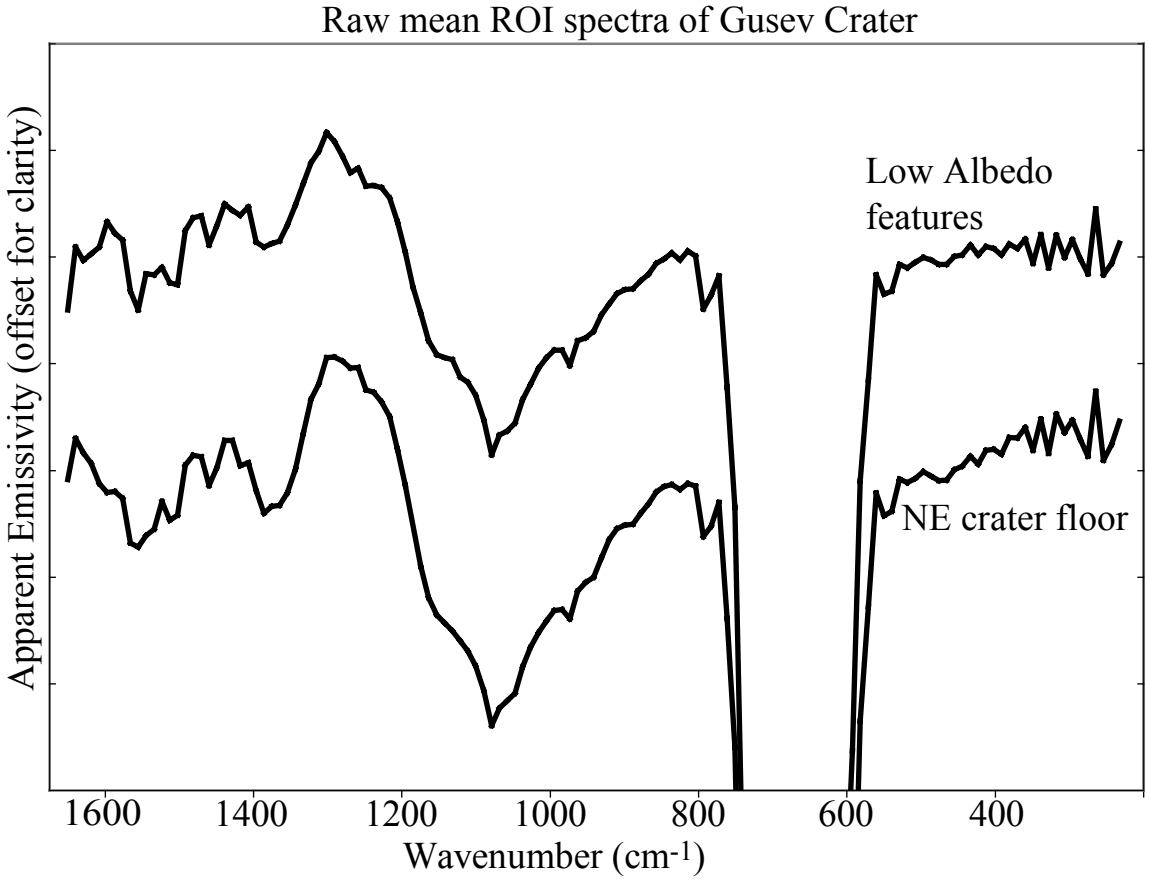

Figure 3: Spectra and spectral ratios for Gusev Crater. (a) Raw mean ROI spectra from Gusev Crater input into linear deconvolution routine, including the deep CO_2 feature near 670-cm^{-1}. Spectra have been offset for clarity.

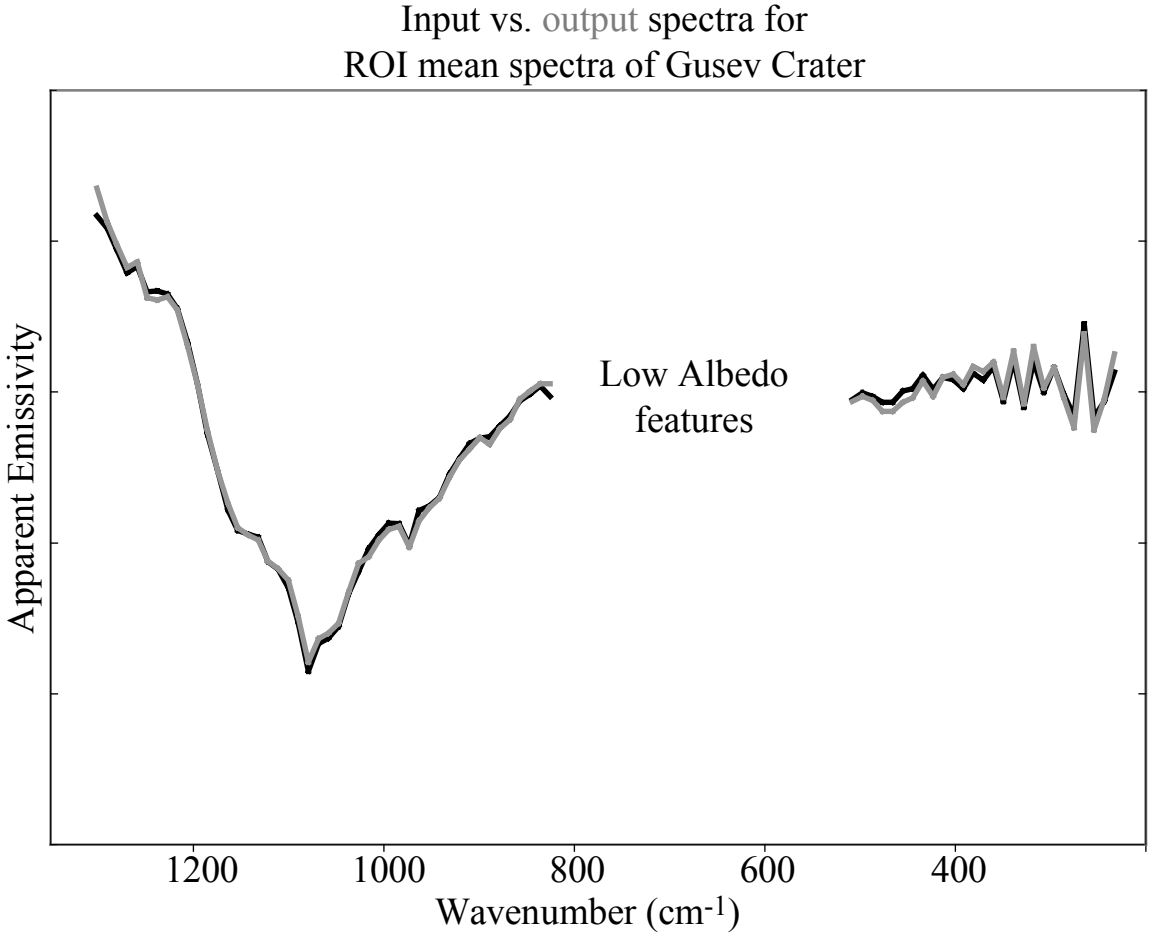

Figure 3 (con't): (b) Measured mean ROI spectra (black) and model spectra (gray) produced by linear deconvolution for Gusev Crater. Spectra of have been offset for clarity and do not include the deep CO_2 feature.

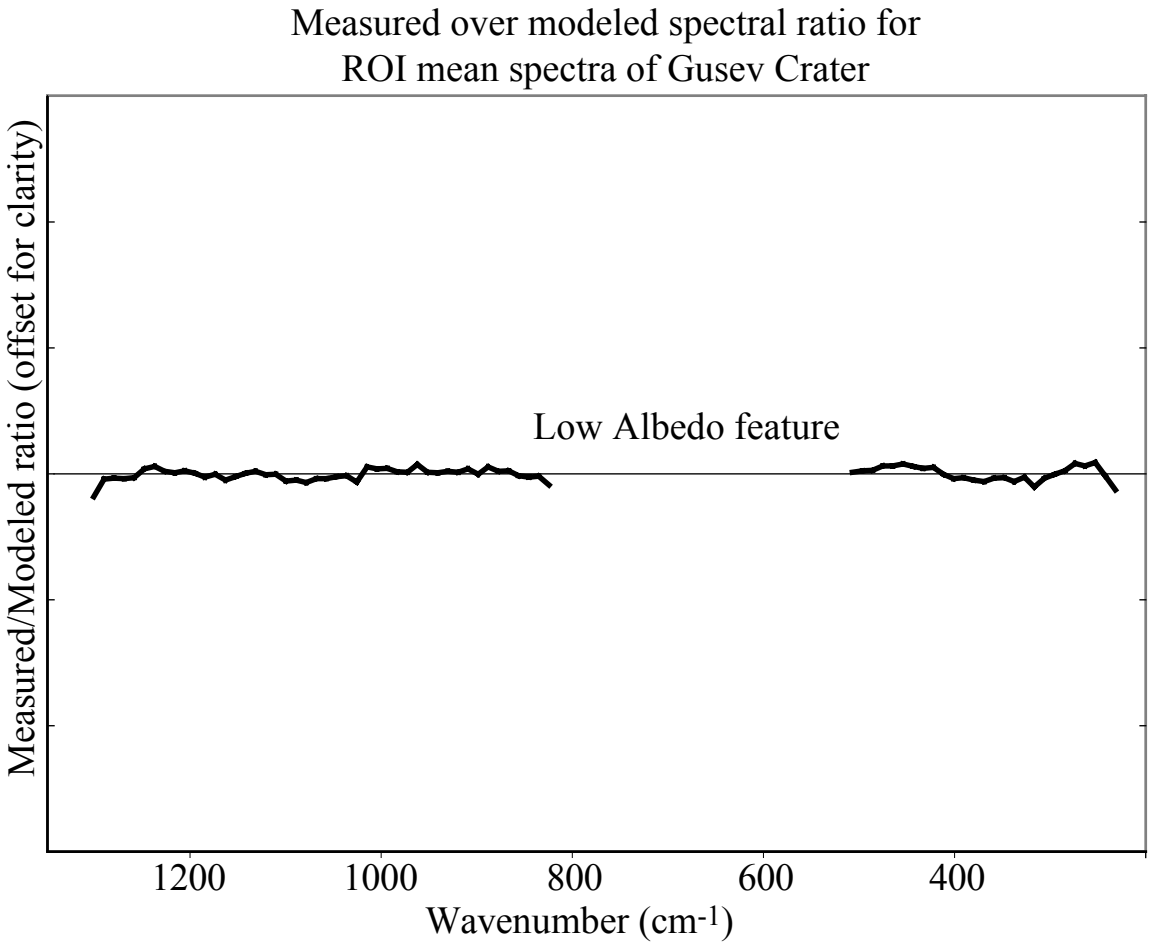

Figure 3 (con't): (c) Measured-to-modeled spectral ratios for Gusev Crater ROIs, offset for clarity.

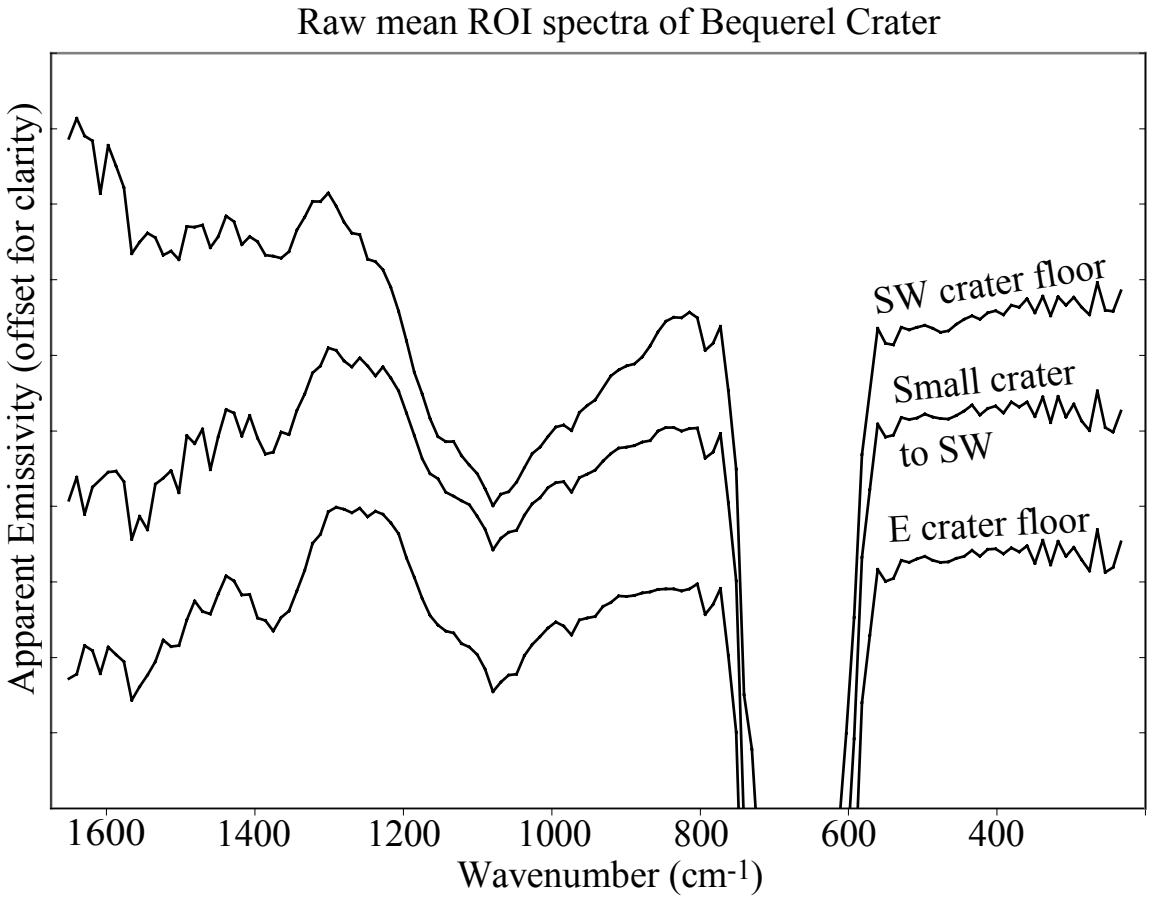

Figure 4: Spectra and spectral ratios for Becquerel Crater. (a) Raw mean ROI spectra from Becquerel Crater input into linear deconvolution routine, including the deep CO_2 feature near 670-cm^{-1}. Spectra have been offset for clarity.

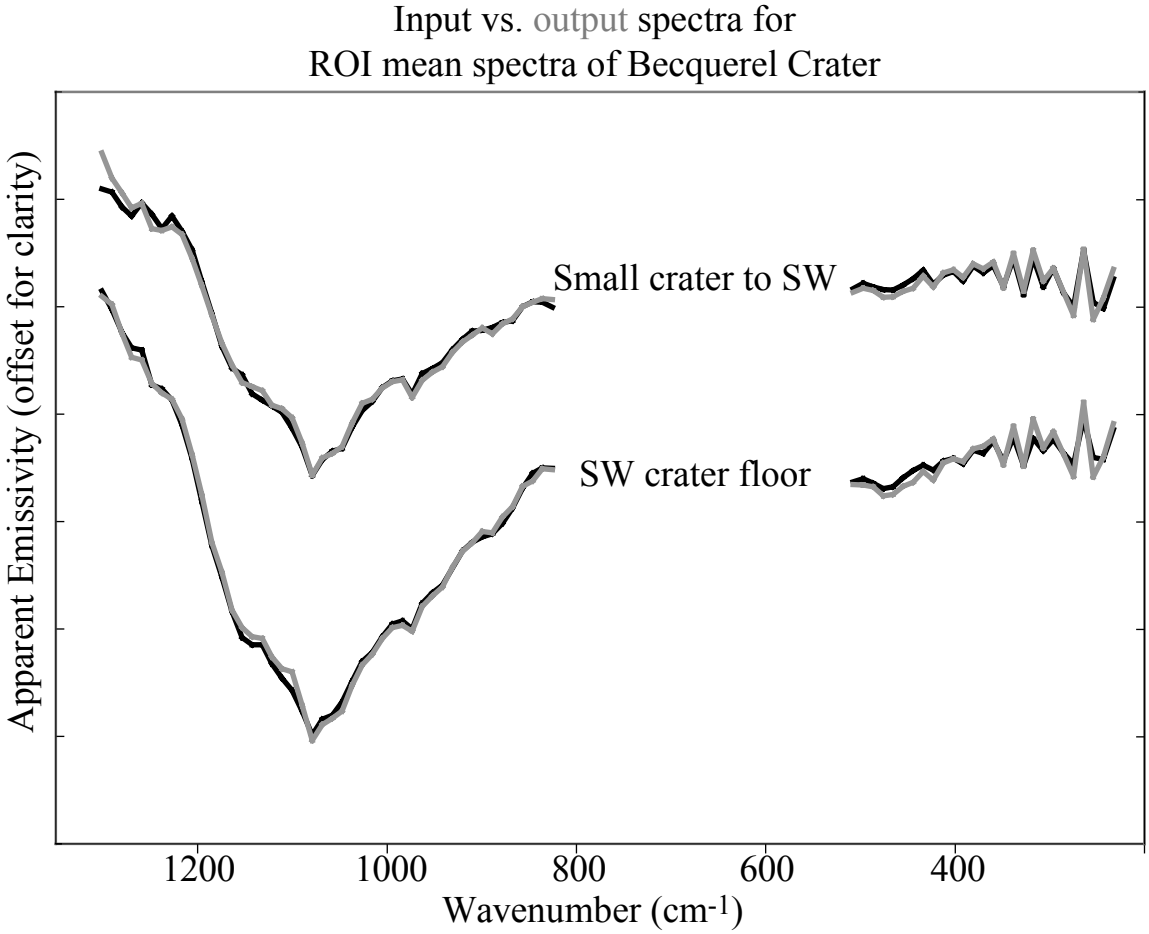

Figure 4 (con't): (b) Measured mean ROI spectra (black) and modeled spectra (gray) produced by linear deconvolution for Becquerel Crater. Spectra of have been offset for clarity and do not include the deep CO_2 feature.

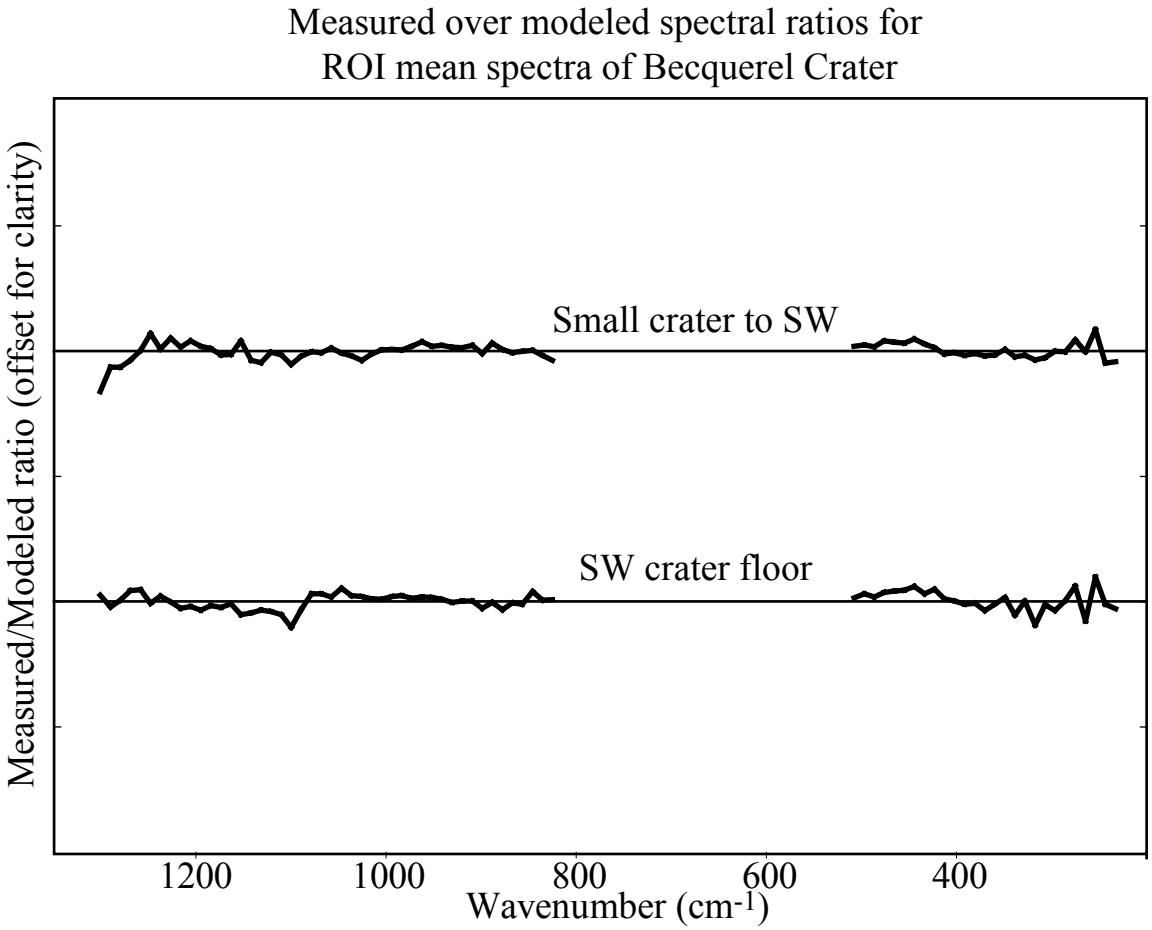

Figure 4 (con't): (c) Measured-to-modeled spectral ratios for Becquerel Crater ROIs, offset for clarity.

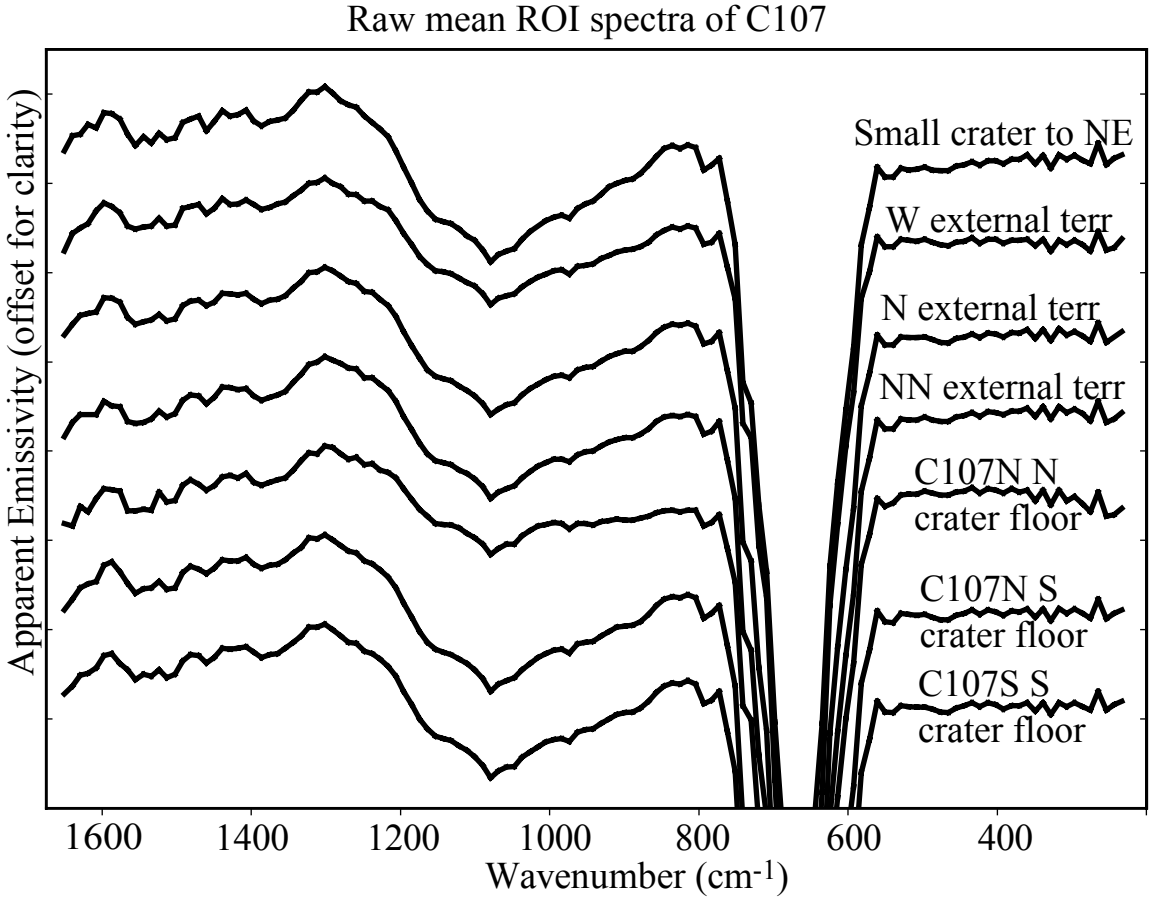

Figure 5: Spectra and spectral ratios for crater C107. (a) Raw mean ROI spectra from crater C107 input into linear deconvolution routine, including the deep CO_2 feature near 670-cm^{-1}. Spectra have been offset for clarity.

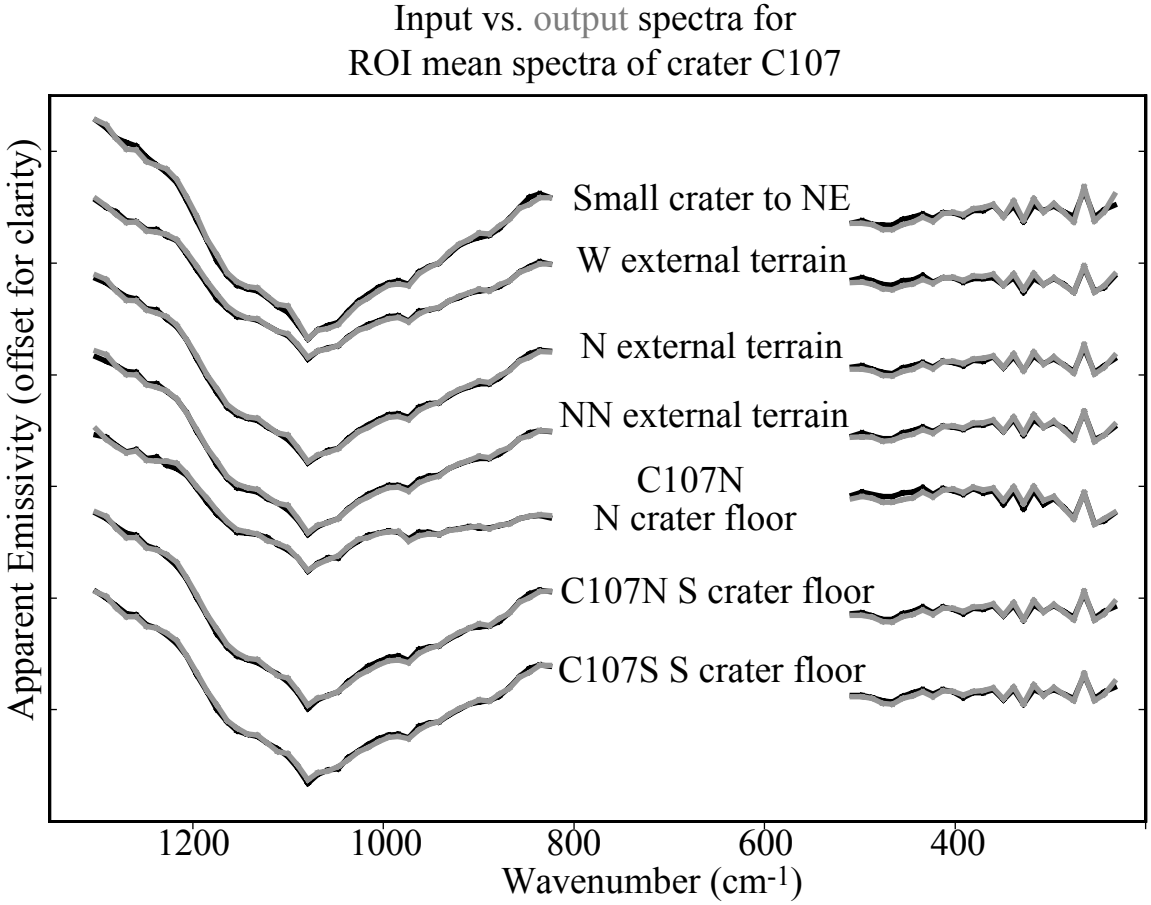

Figure 5 (con't): (b) Measured mean ROI spectra (black) and modeled spectra (gray) produced by linear deconvolution for crater C107. Spectra of have been offset for clarity and do not include the deep CO_2 feature.

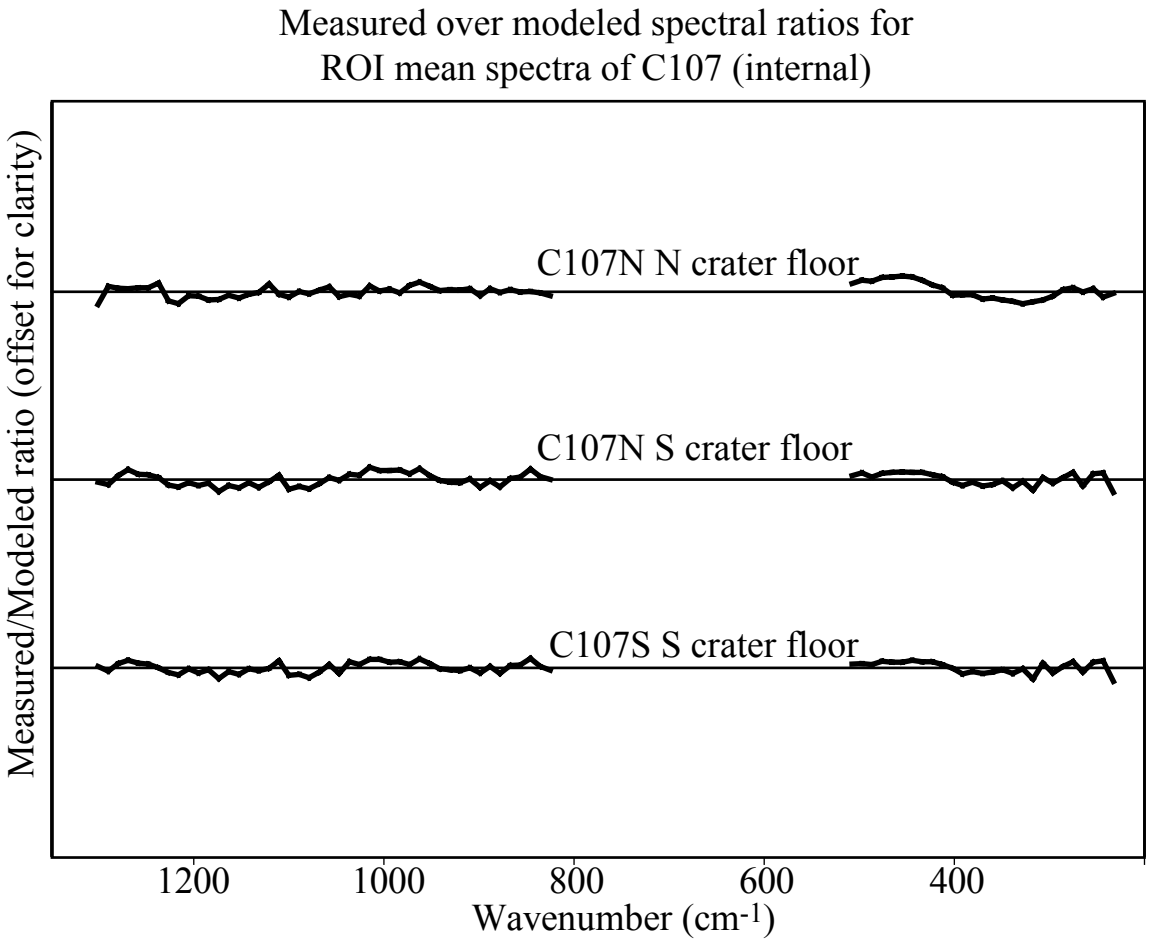

Figure 5 (con't): (c) Measured-to-modeled spectral ratios for crater C107 internal ROIs, offset for clarity.

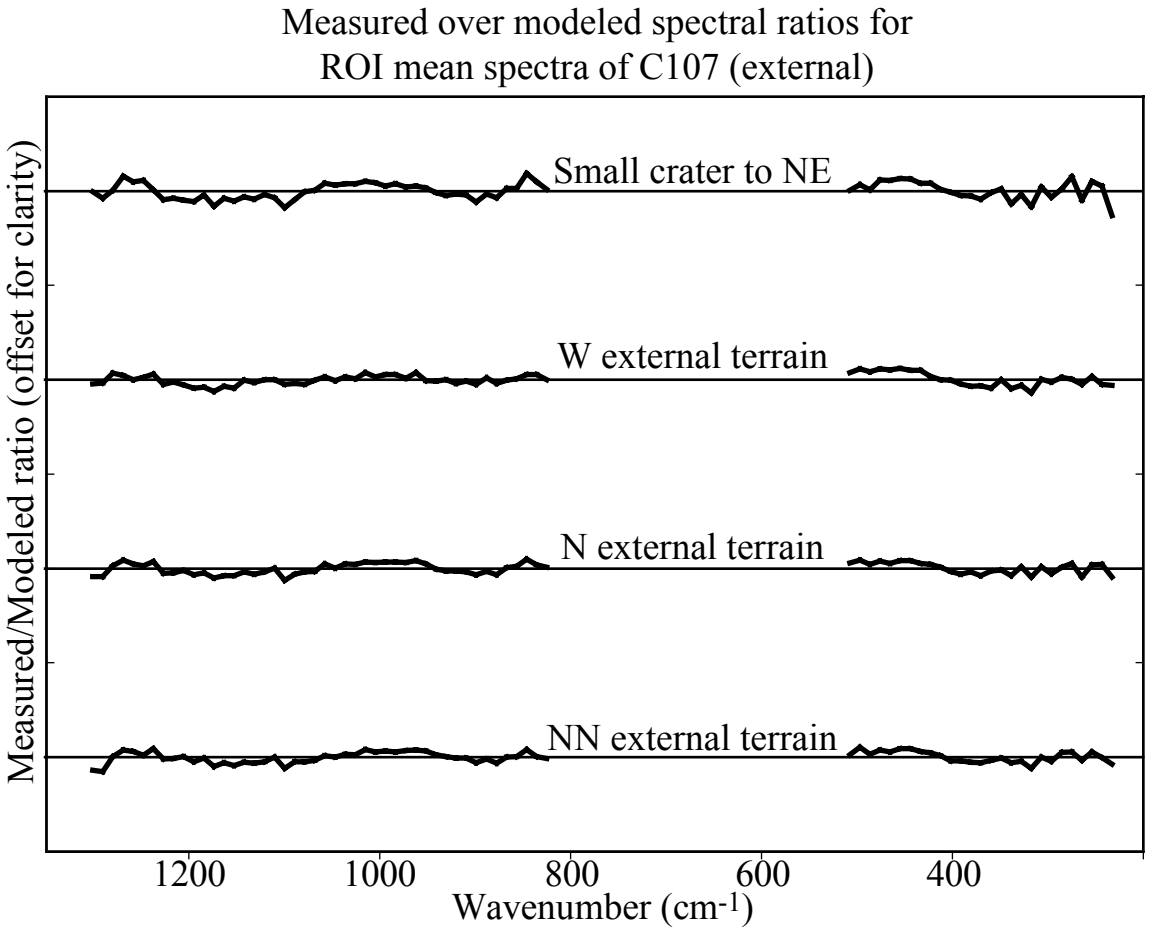

Figure 5 (con't): (d) Measured-to-modeled spectral ratios for crater C107 external ROIs, offset for clarity.

Part 5

THEMIS study of Proposed Paleolake Basins within the Aeolis Quadrangle of Mars

This chapter is a reformatted version of a paper by the same name submitted to the Journal of Geophysical Research - Planets in 2005 by Karen Renée Stockstill, Jeffrey E. Moersch, Harry Y. McSween, Jr., Jennifer Piatek and Phillip R. Christensen

Stockstill, K.R., Moersch, J.E., McSween, Jr., H.Y., Piatek, J. and Christensen, P.R., THEMIS study of Proposed Paleolake Basins within the Aeolis Quadrangle of Mars, JGR-Planets, *submitted*, 2005.

Abstract

Several studies have described photogeologic evidence for paleolacustrine basins on Mars, mostly within impact craters. If these basins contained persistent standing water subsequently lost through evaporation, they would likely have formed deposits of evaporite minerals. Such deposits, if exposed to a sufficient extent, would be detectable in orbital thermal infrared spectra. Using data from the Mars Odyssey Thermal Emission Imaging System (THEMIS) and the Mars Global Surveyor Thermal Emission Spectrometer (TES), we have conducted a study of proposed paleolake basins within the Aeolis quadrangle, which contains 35 such basins including, Gusev and Gale Craters. Gusev Crater is dominated by units which have a spectrally-intermediate to -thick layer of dust mantling the surface, obscuring most spectral units. However, the low albedo features appear to have a thinner mantling of dust, revealing THEMIS surface emissivity spectra that are consistent with Syrtis-type basalt. Gale Crater is relatively dust-free, except for a mound which is covered in a spectrally-intermediate to -thick layer of dust. Materials on the crater floor have THEMIS surface emissivity spectra that are consistent with a mix of Syrtis- and Acidalia-type materials, while the spectrum of the mound layers is consistent with Acidalia-type materials and dust. Additional craters within the Aeolis region were also studied, revealing that surface dust is relatively ubiquitous throughout

this quadrangle and that dust-free surfaces in Gusev and Gale Craters may be fairly unique for this area. Finally, we find no spectral evidence for evaporite deposits that would substantiate paleolakes in these craters.

1. Introduction and background

1.1. Water on Mars

Under current temperature and pressure conditions at the surface of Mars, liquid water is not stable and will rapidly evaporate or freeze. However, a number of geomorphic features suggest that the climatic conditions of early Mars may have been quite different, allowing abundant and persistent liquid water to have existed [e.g., *Carr*, 1996*a*]. For example, the high degree of erosion of large impact craters and dissection of the oldest terrain by large channels and smaller "valley networks" provide compelling evidence that early Mars was indeed warmer and wetter than at present. Many authors suggest that the channels on Mars were formed by catastrophic floods, whereas the valley networks were formed by surface runoff or groundwater sapping [e.g., *Masursky*, 1973; *Milton*, 1973; *Sagan et al.*, 1973; *Baker and Milton*, 1974; *Sharp and Malin*, 1975]. Other studies have argued for the existence of paleolake basins based on photogeologic evidence [*Forsythe and Zimbelman*, 1995; *Cabrol and Grin*, 1999; *Malin and Edgett*, 2000]. In fact, the sedimentary layers described by *Malin and Edgett* [2000] are found within some of the proposed paleolake basins studied in the present work.

The climatic conditions necessary to produce these features remain a matter of debate. Initially, researchers were reluctant to accept that past climatic conditions would have allowed water to exist in any other form besides permafrost or groundwater and in

the ice caps [*Carr*, 1996*b*]. In this scenario, outflow channels were formed by a medium other than liquid water, such as liquid hydrocarbons [*Yung and Pinto*, 1978], lavas [*Carr*, 1974], glaciers or ice streams [*Lucchitta et al.*, 1981; *Lucchitta*, 1982], aeolian erosion [*Cutts and Blasius*, 1981], and debris flows [*Nummedal and Prior*, 1981]. Likewise, the valley networks would have been formed by groundwater sapping in ice-rich terrains [*Brakenridge*, 1990; *Baker et al.*, 1992].

More recently, some researchers have argued that Mars was warmer and wetter in the past, but underwent drastic climate change to produce the climatic conditions observed today [*Pollack et al.*, 1987; *Schneeberger*, 1989; *Forsythe and Zimbelman*, 1995; *Cabrol and Grin*, 1997; *Baker*, 2001]. In this scenario, pressure and temperature conditions would have allowed liquid water to carve the valley networks and to pond as lakes within craters [*Pollack et al.*, 1987; *Schneeberger*, 1989; *Cabrol et al.*, 1998]. The outflow channels would have been carved by large floods produced by massive release of groundwater or drainage of surface lakes [*Baker and Milton*, 1974; *Baker*, 1978; *McCauley*, 1978; *Carr*, 1979].

The Opportunity and Spirit rover sites appear to support this scenario [*Golombek et al.*, 2005]. Meridiani Planum appears to be Noachian in age and contains abundant "dirty" evaporites, suggesting an aqueous environment at the time of formation [*Squyres et al.*, 2004*a*]. In contrast, the dry, desiccated plains of Gusev near the Spirit landing site appears to be Late Hesperian/Early Amazonian in age and show only limited evidence of aqueous alteration [*Gellert et al.*, 2004; *McSween et al.*, 2004; *Morris et al.*, 2004]. A comparison of erosion rates for Noachian terrains to erosion rates estimated for Gusev plains [*Golombek et al.*, 2005] suggests a drastic climate change between Noachian and

Hesperian time periods. If the atmosphere was warm enough and the atmospheric pressure high enough during the Noachian, standing water could have persisted at the surface of Mars. The stability of standing water at the surface is directly relevant to the question of whether life could have arisen and persisted on early Mars [e.g., *Farmer and Des Marais*, 1999].

Even more recently, researchers have proposed an intermediate view of the climatic history, in which Mars has always been cold but had (and continues to have) transient episodes of H_2O cycling [*Baker*, 2001; *Haberle et al.*, 2001; *Christensen*, 2003; *Lee and McKay*, 2003]. *Haberle et al.* [2001] identified five favorable regions that, for at least a portion of a Martian year, meet the minimum surface pressure and temperature requirements for the existence of liquid water in the present climate system. Moreover, *Christensen* [2003] proposed that gullies found within craters at mid-latitudes formed by recent melting of water-rich snow that had been transported from the poles to mid-latitudes during past periods of high obliquity. In addition, some researchers suggested that transient episodes of H_2O cycling could explain the degree of erosion of Martian craters, based on erosion rates calculated for the terrestrial Haughton Crater [*Lee and McKay*, 2003; *Lee et al.*, 2005]. Furthermore, researchers suggested that channel networks in the Arctic and Antarctica, formed by glacial melt water, may be a good analog for the Martian valley networks [*Rice et al.*, 1997; *Lee and McKay*, 2003].

1.2. Aeolis quadrangle

Cabrol and Grin [1999] presented a survey of 179 possible paleolake basins in Martian impact craters. These basins were classified according to their relationship to neighboring basins and the types of associated channels. For each basin, the survey

identified specific lines of geomorphic and photogeologic evidence used to support a paleolake hypothesis. The evidence cited included putative lacustrine deltas, sedimentary terraces, layering, shorelines, and mounds. In addition, some basins contained bands of alternating light and dark albedo material conformable with the basin's margin or bright materials exposed in the central portion of the basin [*Cabrol and Grin*, 1999]. *Cabrol and Grin* [1999] interpreted these materials as possible evaporite deposits. On Earth, playa basin evaporites often display a characteristic (bulls-eye) spatial pattern resulting from their order of deposition [*Jones*, 1965; *Eugster and Hardie*, 1978; *Eugster*, 1980].

Thirty-five basins from the *Cabrol and Grin* [1999] list are within the Aeolis quadrangle, making it the most populated quadrangle of those represented on the list. In addition, this quadrangle contains both Gusev and Gale craters. Both craters were well-studied as potential landing sites for the MER missions; Gale Crater was excluded because the landing ellipse exceeded the size of the crater [*Golombek et al.*, 2002] and Gusev Crater was chosen as the landing site of Spirit rover [*Squyres et al.*, 2004*b*]. For these reasons, we chose to use thermal infrared data of the basins within the Aeolis quadrangle to search for spectral evidence that they were once paleolakes.

The Aeolis quadrangle encompasses a portion of the dichotomy boundary between the heavily cratered and dissected highlands and the relatively smooth lowlands of Mars (Figure 1). The heavily cratered highlands have been dated as Noachian [*Greeley and Guest*, 1987] and are dissected by Ma'adim and Al-qahira Valles as well as numerous smaller valleys [*Brakenridge*, 1990]. The northern lowlands are considered to be post-heavy bombardment and may consist of lava or sedimentary deposits [*Brakenridge*, 1990].

Brakenridge [1990] noted a similar orientation between thrust faults and small valley networks and suggested that valley locations are partly controlled by preexisting thrust faults and related fractures. He proposed that the valley networks developed due to volcanism in interstratified, ice-rich terrains, which caused subsidence and faulting and produced scarps that intersected local aquifers. Water discharged at these scarps may have carved the network valleys through both down-valley erosion by water/ice/debris and headward erosion by groundwater sapping.

Development of the valley network systems has been estimated to be Upper Noachian to Lower Hesperian in age [*Brakenridge*, 1990]. However, the surface deposits within Gusev and Gale Craters have been dated as Early Amazonian [*Cabrol et al.*, 1998; *Cabrol et al.*, 1999]. If these basins were lakes in the early Amazonian, this suggests that water was stable at the surface of Mars, at least episodically, for most of Martian history and was stable relatively recently. If lakes existed within craters as recently as the Early Amazonian, deposits of evaporite minerals may still be present. The two largest craters within the Aeolis quadrangle, Gusev and Gale Craters, have been well studied; background information for these two craters follows.

1.2.1. Gusev Crater

Gusev Crater is a 160 km-diameter basin located at the end of the 900 km-long Ma'adim Vallis. Several researchers have proposed that Gusev was a lacustrine depocenter for the Ma'adim drainage system [*Schneeberger*, 1989; *Cabrol et al.*, 1998]. *Cabrol and Grin* [1999] classified Gusev as a lake chain basin with a fluvial valley network. Proposed sedimentary structures associated with Gusev include delta deposits, sedimentary terraces, shorelines, mounds and possible indicators of evaporite deposits

[*Cabrol and Grin*, 1999]. *Farmer and DesMarais* (1999) classify Gusev as the terminal basin for the Ma'adim Vallis. Similar terminal lake basin settings on Earth typically have high rates of chemical sedimentation and high biological productivity and are very favorable for the preservation of biomarkers [*Farmer and Des Marais*, 1999]; if life existed on Mars in the past, Martian fluvio-lacustrine environments would be a favored setting for exploring for evidence of past Martian life. The sediments filling Gusev Crater have been estimated to be 500-m thick, giving a volume of 7,300 km^3 [*Cabrol et al.*, 1998], or up to 3200-m thick, with a volume of 15,100 km^3 [*Carter et al.*, 2001].

Recent investigations using TES, THEMIS and MOC data have yielded detailed maps of surface units within Gusev [*Milam et al.*, 2003; *Martínez-Alonso et al.*, 2005]. The *Milam et al.* [2003] study distinguished nine surface units within Gusev crater that were consistent with either fluvio-lacustrine, aeolian and/or volcanic deposition. However, the spatial resolution of the data did not allow for the distinction of textures diagnostic of any one type of deposition, nor did it provide unambiguous evidence for a fluvio-lacustrine depocenter. The study by *Martínez-Alonso et al.* [2005] concluded that the current surface in Gusev Crater is consistent with volcanic (basaltic) and aeolian deposits, although fluvio-lacustrine deposits may be present beneath these deposits and may be exposed in impact craters.

The Mars Exploration Rover Spirit landed in Gusev Crater in early January of 2004 and continues to explore its surface. During the primary mission, rocks examined on the floor of Gusev Crater we found to be pristine basalts containing olivine, lacking phyllosilicates or other aqueous weathering products, but sometimes exhibiting minor surface coatings [*Christensen et al.*, 2004*b*; *Gellert et al.*, 2004; *McSween et al.*, 2004;

Morris et al., 2004]. The presence of olivine suggests that physical weathering, rather than chemical, currently dominates the weathering processes at Gusev Crater [*Morris et al.*, 2004]. More recently, the Spirit rover has encountered rocks on and around Columbia Hills that are highly altered, with decreased olivine contents and variations in the Fe oxide component consistent with the presence of water [*Klingelhöfer et al.*, 2005; *Morris et al.*, 2005; *Schröder et al.*, 2005]. Additional evidence for alteration exists within the walls of trenches dug by Spirit rover, which displayed a 10% decrease in olivine relative to the undisturbed surface at the top of the trench, but no appreciable decrease in Ca-feldspar and Ca-pyroxene, suggesting only minor alteration [*Wang et al.*, 2005]. However, the trench also contained sulfates, silica and Fe-oxides not found at the surface, suggesting a higher degree of alteration [*Wang et al.*, 2005]. *Wang et al.* [2005] suggested that salty materials were formed at some distant location and were redistributed to this location by impact processes. It is important to note that mini-TES aboard the Spirit rover has not detected sulfates at the surface in Gusev Crater [*Christensen et al.*, 2004*b*], although they have been detected using APXS and Mössbauer [e.g., *Gellert et al.*, 2004; *Morris et al.*, 2005].

1.2.2. Gale Crater

Gale Crater is a 142 km diameter crater located near the boundary of cratered uplands and lowlands in Elysium Planitia. Gale appears to post date the elevation difference between the uplands and lowlands, which occurred in the mid- to late-Noachian [*Frey et al.*, 1998]. The northern rim of Gale Crater is 2 km lower than its southern rim due to this regional slope [*Frey et al.*, 1998].

Cabrol and Grin [1997] proposed that the source of water for Gale Crater was floods from the Elysium Basin overflowing the northern rim of the crater. They identified 21 layers on the 1000-m tall central mound in Gale, terracing, and drainage systems that they interpreted as evidence for a pre-existing ice-covered lake [*Cabrol and Grin*, 1997]. Crater age dating for proposed lacustrine deposits suggested an early Amazonian age [*Cabrol*, 1997]. *Cabrol and Grin* [1999] classified Gale as an open basin with an associated outflow channel showing evidence for sedimentary layering, sedimentary deposits, shoreline terraces and a central mound.

Pelkey and Jakosky [2002] studied Gale Crater using MOLA, TES, and MOC data and found that the crater floor is generally dust-free relative to the central mound. The central mound was found to have a thermally thick layer of dust near its top, but the dust layer thins with decreasing elevation. The lower portions of the mound appear to represent either a surface with a thermally-thin dust layer atop an intermediate-thermal-inertia material or thermally-intermediate dust layer atop (or spatially mixing with) a higher-thermal-inertia surface. The northern crater floor has a smooth floor interpreted to be a cemented mantle with a thermally thin layer of dust that decreases to the east and west. The crater floor to the east, west and south of the central mound has a smooth floor and crater ejecta material, with the southern floor likely being dust-free. Their observations require multiple formation mechanisms to explain the various surface layers within Gale Crater, including sedimentary deposition, erosion and weathering, and aeolian processes [*Pelkey and Jakosky*, 2002].

A more recent study of Gale using the THEMIS data set [*Pelkey et al.*, 2004] confirmed previous observations regarding the particle sizes present in and around Gale

Crater; however, the data provided more complete and detailed information. At the higher spatial resolution of THEMIS, abundant small channels were discernable supporting an aqueous history for Gale. In addition, more detailed structures of sand dunes were discernable, revealing that the wind direction is probably controlled by the local topography within Gale Crater. *Pelkey et al.* [2004] identified channels on the crater walls and central mound that reach the crater floor, indicating that they post-date the existence of any paleolakes within Gale Crater. Their results indicated that aeolian processes have played a major role in shaping much of the present surface layer within Gale.

1.3. Thermal infrared spectral data

Minerals, including evaporites, have diagnostic absorption features that result from vibrational modes within the crystal in the thermal infrared spectral region (1670-200 cm^{-1} or 6-50 μm) [e.g., *Lyon*, 1965; *Lyon and Lee*, 1970; *Christensen et al.*, 1992; *Salisbury et al.*, 1994]. Carbonates have absorption features centered near 1540, 890, 730 and 330 cm^{-1} (6.5, 11.2, 13.7 and 30.3 μm, respectively) as a result of vibrations within the CO_3 structure [e.g., *Keller et al.*, 1952; *Huang and Kerr*, 1960; *Adler and Kerr*, 1962; *Adler and Kerr*, 1963*a*; *Adler and Kerr*, 1963*b*; *Lane and Christensen*, 1997]. Sulfate minerals have absorption features centered near 1160, 680, and 600 cm^{-1} (8.6, 14.7, and 16.7 μm, respectively) corresponding to vibrations in the sulfate anion [*Adler and Kerr*, 1965; *Lane and Christensen*, 1998]. The strong ionic bonding of chlorides prevents individual bond vibrations; instead, the entire crystal lattice vibrates, resulting in a broad absorption (low emissivity at frequencies >600 cm^{-1} for halite and >400 cm^{-1} for sylvite) rather than discrete bands that exist for other evaporite minerals [e.g., *Lane and*

Christensen, 1998]. Unfortunately, this feature is too subtle and broad to be readily detected, so the thermal infrared is not particularly well-suited for mapping chlorides.

Previous global-scale studies using data from the Mars Global Surveyor Thermal Emission Spectrometer (TES) have only revealed two mineral signatures with possible aqueous origins: coarse-grained crystalline hematite [*Christensen et al.*, 2000] and a minor (~2 to 5 weight %) component of carbonate in globally-distributed fine-grained surface dust deposits [*Bandfield et al.*, 2003]. Although carbonates may be a minor component of the surface dust deposits, a global search of TES data binned to 1 pixel per degree by *Bandfield* [2002] did not reveal any large-scale occurrences of evaporite minerals on Mars. Even an intensive study of "White Rock", a feature suggested as a candidate evaporite deposit since the days of the Mariner 9 mission [*McCauley*, 1974; *Ward*, 1979; *Zimbleman and Kieffer*, 1979; *Williams and Zimbelman*, 1994], has not revealed the spectral signatures of evaporite minerals [*Ruff et al.*, 2001].

Stockstill et al. [*in press*] conducted a TES study at the spatial resolution limit of the dataset (3x5 km) to search for in-situ evaporite deposits within the 80 largest basins from the *Cabrol and Grin* [1999] list. However, surface exposures of evaporite deposits were not detected in amounts exceeding the lower detection limits for the methods used. This study could not confirm a paleolacustrine origin for deposits within these basins [*Stockstill et al.*, *in press*]. Nevertheless, with a spatial resolution nearly 2000 times better (by area) than TES data, THEMIS allows us to search for potential evaporite deposits of a smaller scale than was previously discernible.

THEMIS, aboard the Odyssey spacecraft, is acquiring infrared images at 100 m/pixel resolution, 320 pixels across, in nine spectral bands between 6.6 μm and 15.0 μm

with near-global coverage [*Christensen et al.*, 2004*a*]. Due to its higher spatial resolution, THEMIS is best utilized as a spectral unit mapper whereas TES, due to its higher spectral resolution, is better at mineral identification [e.g., *Christensen et al.*, 2003]. If potential small-scale outcrops are detected within a THEMIS image, a spectrum from the TES pixel (or pixels) covering the outcrop region can be analyzed to determine the mineralogy. By localizing a potential carbonate outcrop to a single TES observation, the spectral contribution from the carbonate would be increased, perhaps above the lower detection limits of previous techniques [*Stockstill et al.*, *in press*].

Baldridge et al. [2004] produced a spectral map of the Badwater Basin (in Death Valley, California) using high-resolution MODIS/ASTER Airborne Simulator (MASTER) data. At MASTER spatial resolution (5-15 m/pixel), spectral signatures of evaporite minerals could be identified within the thermal infrared spectra (~7.9-12.75 μm). MASTER data were also degraded to TES and THEMIS spatial resolutions to better understand the capabilities of TES and THEMIS in detecting evaporite minerals. That study revealed that the spatial resolution of THEMIS (100 x 100 m/pixel) should be sufficient to detect evaporite sequences at the scale observed at Badwater Basin (500 km^2). However, the spatial resolution of TES (3 x 5 km/pixel) would not be sufficient to detect evaporites at this scale, although basins on Mars may have developed evaporite deposits of a larger scale than terrestrial analogs [*Baldridge et al.*, 2004].

2. Methods

2.1. THEMIS data compilation

THEMIS infrared data consists of 10 bands within the thermal infrared at 100m/pixel spatial resolution. The bands are centered at 9 different wavelengths ranging from ~1472 cm^{-1} to ~670 cm^{-1} (~6.8-14.9 μm) [*Christensen et al.*, 2004*a*]. Bands 1 and 2 have identical filters centered at ~1472 cm^{-1} (~6.8 μm) in order to boost the signal-to-noise ratio in this spectral region [*Christensen et al.*, 2004*a*]. These are also the bands where carbonates have their deepest, broadest absorption feature centered ~1530 cm^{-1} (~6.5μm) [*Lane and Christensen*, 1997].

THEMIS data for each basin were collected for images acquired prior to 1600 local solar time (LST). Scenes acquired later in the day were not used because of the inferior signal-to-noise ratios associated with cooler surface temperatures. Geo-referenced and projected THEMIS multispectral radiance data were read into ITT Industries' ENVI remote sensing package using custom software. A data mask band was created to filter pixels with incomplete data around the border of each scene. A maximum brightness temperature image was calculated using a one-sided fit to the Planck function convolved to the THEMIS bandpasses. The brightness temperature image was then evaluated to ensure that sufficient surface temperatures were present. THEMIS emissivity data are not considered trustworthy for surfaces below ~240K (J. Bandfield, *pers. comm. 2004*); therefore, if most pixels in the brightness temperature image were below 240K, the radiance data were not processed further. This filtering step is diagramed in Figure 2, Step 1.

2.2. THEMIS radiance offset (additive) correction and conversion to emissivity

Before THEMIS radiance data could be converted into emissivity data, a correction was applied to account for several sources of systematic radiance errors described by *Christensen et al.* [2004] and *Bandfield et al.* [2004]. Methods for correcting for the noise and errors are described in detail by *Bandfield et al.* [2004] and *Piatek et al.* [2004] and are diagrammed in Figure 2, Step 2.

This technique, called a radiance offset correction, required identifying a geologic feature that can be assumed (through photogeologic arguments) to have fairly homogeneous emissivity spectrum but a wide range of temperatures (e.g., an impact crater that has both sunlit and shadowed crater walls). A region of interest (ROI) was defined to cover this training area. The radiance offset algorithm collected radiance spectra from this training area and iteratively calculated offsets required for each band to produce a single emissivity spectrum. The calculated radiance offsets were applied to all pixels within the image. The corrected radiance data were then converted to emissivity by finding the highest brightness temperature from bands 3 to 9 (~1265 – 670 cm^{-1} or 7.9 – 12.6μm) and dividing by the Planck function that corresponds to that brightness temperature, convolved to the THEMIS bandpasses. The emissivity image was then evaluated to determine how well the temperature-slope effects have been removed and this process was repeated, if necessary. As a final step in creating the multispectral emissivity cube, bands 1 and 2 were co-added to enhance the signal at their shared wavelength.

2.3. MNF rotation and identification of surface spectral units

At this point, the emissivity data were evaluated to determine if sufficient spectral variation was present to warrant further analysis. To distill the enormous amount of data contained within a single THEMIS multispectral emissivity image, a type of principal component analysis (PCA) was used. Each spectrum in the cube can be treated as a point in n-dimensional space, where n is the number of spectral bands. Spectral data plotted in this space forms a cloud of points. The original coordinate system can be translated and rotated to maximize the variance of the data cloud along a new set of orthogonal axes, and then the data cloud is rescaled to fit the full available dynamic range along each of the new axes. The axes in the new coordinate system are the principal components of the data. PCA axes are ordered according to the eigenvalues of the transform, which express the degree of variance of the data cloud along each axis. Principal component bands with the highest eigenvalues are usually associated with true spectral end members. This step is diagramed in Figure 2, Step 3.

The PCA application used for this study was the Minimum Noise Fraction (MNF) in ENVI [*Green et al.*, 1988]. A forward MNF rotation was performed, estimating the noise statistics from the data. The data mask was applied so that areas lacking data from any band were not included in the MNF statistics. The MNF used 8 THEMIS emissivity bands between ~670- and 1472 cm^{-1}. This rotation produced an 8-band MNF image cube, which could then be displayed as single band images or as three band RGB-composite images. The result of the MNF rotation was evaluated to determine the amount of spectral variability present a number of ways.

First, we examined the eigenvalues produced for each MNF band. ENVI's MNF routine produces a plot of eigenvalues versus MNF band numbers, with the highest eigenvalues in the lowest MNF band numbers representing "real" spectral variation. With increasing MNF band number, the eigenvalues typically decrease in an exponential manner; where the eigenvalues level off, the spectral variation represented is dominated by noise. We examined this plot to determine how many MNF bands contained real spectral variation. Second, we evaluated the 8-band MNF image cube by viewing each of the bands as a grayscale image. This technique allowed us to identify which bands contained real spectral variation related to surface features and which bands appeared to contain noise. Third, we evaluated the 8-band MNF image file as 3-band color images in multiple MNF band combinations. This allowed us to evaluate the variability in the scene based on how many colors were present in the 3-band image. If insufficient spectral variation was present within the scene, no further analysis of that THEMIS image was pursued.

In some cases, we used an additional type of PCA, called a decorrelation stretch (DCS), to enhance the spectral variation within a chosen subset of three spectral emissivity bands [*Gillespie et al.*, 1986]. The DCS of emissivity bands 5, 8 and 7 was used to enhance the spectral variation related to the previously-defined TES surface end members [*Bandfield et al.*, 2000*a*; *Christensen et al.*, 2003]. When these contrast-enhanced bands are displayed as an RGB color composite, red pixels are associated with Acidalia-type (weathered basalt or andesite), green pixels are associated with Syrtis-type (basalt), and blue pixels are associated with surface dust [*Christensen et al.*, 2003].

In THEMIS images where sufficient spectral variation existed, ROIs were defined to sample each of the surface units. These regions were identified using a combination of the corrected brightness temperature (T_b) image, a DCS image, and a color composite image resulting from the MNF rotation of the emissivity data. Each image type was found to have assets that, when combined, allowed for identification of more surface units within craters. The ROIs defined using the DCS or MNF image are surface units that vary spectrally, whereas the ROIs defined using the T_b image are surface units that may have variable thermophysical characteristics (e.g., grain size or degree of induration).

2.4 Removal of atmospheric absorptions from spectra (multiplicative correction)

THEMIS radiance and derived emissivity data contain spectral contributions from both the atmosphere and the surface. To determine the surface emissivity, atmospheric contributions (atmospheric dust and ice) to the measured radiance must be removed. These contributions can be additive (e.g., reflection of downwelling radiance) or multiplicative (e.g., absorption by aerosols between the surface and the detector). Additive atmospheric contributions were removed by the radiance offset correction described in Section 2.2. A method for removing the multiplicative atmospheric contribution to the emissivity spectrum is described in detail in *Bandfield et al.* [2004]. This method uses a TES atmospherically-corrected surface emissivity spectrum of the same area on the surface to "bootstrap" multiplicative correction values for each THEMIS band. The method is based on the fact that a more robust atmospheric removal is possible with TES data because of the instrument's superior spectral resolution. This step is diagrammed in Figure 2, Step 4.

To derive the multiplicative atmospheric correction factors, a large (at least comparable to a single TES footprint), spectrally homogeneous area was identified in the THEMIS emissivity image as a training area. The training area was defined as an ROI on the THEMIS emissivity image and this ROI is overlain onto TES emissivity data. A mean TES spectrum was collected for the ROI and deconvolved using the techniques of *Ramsey and Christensen* [1998] and *Smith et al.* [2000*a*] to produce a removed atmosphere (surface) spectrum. The TES surface spectrum was then convolved to THEMIS spectral bandpasses to produce a known surface spectrum for bands 3-9 (~1265–670 cm^{-1} or ~7.9–12.6μm).

The surface emissivity for bands 1 and 2 (~1472 cm^{-1} or ~6.8 μm) cannot be derived by this same technique because the TES atmospheric and surface end members used in deconvolution do not extend beyond 1301 cm^{-1} (~7.7 μm), as shown in Figure 3a. Data at higher wavelengths is excluded due to increased noise and contributions from CO_2 and water vapor at wavelengths >1350 cm^{-1} [*Bandfield et al.*, 2000*a*; *Smith et al.*, 2000*b*]. As a proxy for true atmospheric removal, we chose to divide each pixel by an average THEMIS emissivity value of bands 1 and 2 for the entire scene. This technique is beneficial to this study because 1) atmospheric dust and water ice have very little influence on the effective emissivity at high wavenumbers (>1300 cm^{-1}) [*Bandfield and Smith*, 2003], 2) most rock-forming minerals do not have strong absorptions in bands 1 and 2 (Figure 3a-b), 3) carbonates do have a strong absorption at these high wavenumbers [*Lane and Christensen*, 1997] (Figure 3b), and 3) carbonates are not present on the scale of an entire THEMIS image [*Stockstill et al.*, *in press*]. Therefore, by dividing each pixel by a scene average for bands 1 and 2, a pixel that does not contain

carbonate absorption would produce a ratio near 1. However, pixels that do contain an absorption due to carbonates would have lower ratio values.

The TES-derived removed atmosphere spectrum for THEMIS bands 3-9 was combined with the ratio value from bands 1 and 2 to produce the best approximation for a corrected (atmospherically-removed) emissivity spectrum. The uncorrected THEMIS mean spectrum for the training area was then divided by the corrected spectrum to calculate a multiplicative correction that, when applied to all pixels in the image, yields a THEMIS surface emissivity image.

2.5 Collection and evaluation of mean THEMIS spectra of surface spectral units

Next, the ROIs defined using the MNF and DCS images were overlain on the THEMIS surface emissivity image and mean THEMIS ROI spectra collected. This step yielded 8-band emissivity spectra for each region of interest. These spectra were compared to the previously defined TES surface spectral end members (Acidalia-type, Syrtis-type, hematite and surface dust) convolved to THEMIS bandpasses (Figure 2, Step 5). However, because THEMIS emissivity is limited to 8 bands, its utility as a mineral/rock identifier is limited. Therefore, evaluation of THEMIS spectra were used in concert with TES spectra of the same ROIs, where TES data coverage was available.

2.6 Collection and evaluation of mean TES spectra of the same surface spectral units

The THEMIS-derived ROIs were overlain on the TES emissivity data and mean TES emissivity spectra for each region were collected (Figure 2, Step 6). As in our previous TES study [*Stockstill et al.*, *in press*], the TES data we used were from individual TES spectra (not averaged into latitude/longitude bins *a priori*). A mean ROI

spectrum was collected from the individual TES pixel or pixels covered by each THEMIS-derived ROI. This method of spectral averaging provides the same type of SNR-enhancing benefit that simple geographic binning [e.g., *Bandfield*, 2002] affords, but avoids the problem of spatially "diluting" minor spectral components because only pixels of similar spectral nature are averaged together in custom-tailored regions of interest [*Stockstill et al.*, *in press*]. Mean TES ROI spectra were then evaluated using the dust cover index (DCI) of *Ruff and Christensen* [2002], using linear deconvolution technique of *Smith et al.* [2000*a*] and *Bandfield et al.* [2000*a*] , as well as the spectral ratio technique and carbonate indices developed in previous work [*Stockstill et al.*, *in press*].

According to the study of *Ruff and Christensen* [2002], spectra that have a DCI value ≤0.940 are considered dust covered, meaning that the spectrum of any underlying material is completely obscured by the surface dust component. DCI values between 0.940 and 0.962 are intermediate, meaning the underlying material is only partially obscured by the surface dust component [*Ruff and Christensen*, 2002]. Spectra that have DCI values ≥0.962 are considered dust free, meaning that the spectrum of the surface is not obscured by dust [*Ruff and Christensen*, 2002]. When possible, the ROI or ROIs with the lowest amount of dust cover were used when evaluating the deconvolution results for a collection of ROIs of the same surface feature. The deconvolution technique fits the measured TES apparent emissivity spectrum in a linear least squares sense using both atmospheric spectral shapes and surface spectral shapes simultaneously. This strategy is based on the empirical finding that atmospheric spectral components may be treated as

linearly-mixed end members in emissivity-space [*Gillespie*, 1992; *Thomson and Salisbury*, 1993; *Ramsey and Christensen*, 1998; *Feely and Christensen*, 1999].

The spectral ratio technique uses the ratio of the measured TES ROI spectrum to the deconvolution modeled spectrum. This ratio uses the modeled spectrum produced by linear deconvolution using the previously-known TES end members to test how well the measured spectra were modeled using only the TES end members. This technique relies on the fact that the eight TES end members are dominated by relatively broad and deep features that would not mask the narrower features of minerals. This technique is useful for emphasizing any residual surface spectral features that are not well modeled by the eight TES end member spectra [e.g., *Stockstill et al.*, *in press*].

In addition, the carbonate indices of *Stockstill et al.* [*in press*] were used to look for the presence of carbonates. These indices are conceptually similar to the hematite index of *Christensen et al.* [2000], the dust cover index of *Ruff and Christensen* [2002] and the bound water index of *Ruff* [2004]. The carbonate indices were tuned to be sensitive to the carbonate absorption features near 890 cm^{-1} and 350 cm^{-1}; the exact position of these absorptions vary with composition so that different varieties of carbonates can be distinguished at TES spectral resolution [*Lane and Christensen*, 1997]. In addition, carbonates are unique from other minerals (e.g., silicates) in that the relative depth of the 350 cm^{-1} feature is between 1.75 and 2.63 times deeper than the 890 cm^{-1} absorption feature, a relationship that persists in mineral mixtures as well as for grain sizes down to ~125 μm [*Stockstill et al.*, *in press*].

3. Results

The Aeolis quadrangle includes 35 craters from the *Cabrol and Grin* [1999] list (Figure 1). Of those 35 craters, 15 craters did not have THEMIS data coverage obtained before 1600 LST and were excluded. Two craters were excluded because the associated THEMIS scene did not overlap the crater sufficiently (e.g., only showed the eastern rim), and three other craters were excluded due to a lack of overlapping TES data (precluding atmospheric removal and spectral mineral identification). An additional nine craters were excluded because their THEMIS data were too cold and/or did not display sufficient spectral variation when processed by the MNF transform. Results for the remaining six craters, including Gusev, Gale, and four unnamed craters, are presented here. The unnamed craters will be referred to by the letter "C" with their number from the *Cabrol and Grin* [1999] list. These remaining four craters studied include C133, C142 and 144 (paired), and C147. Table 1 displays geographic information for these six craters and lists the THEMIS scenes used in this study.

3.1 Gusev Crater (-14.5N, 175.5E)

The regions of interest for Gusev Crater are displayed on a radiance offset corrected THEMIS daytime T_b image in Figure 4a. The most distinct spectral unit in both images is that associated with the low albedo (LA) features. The LA features appear brighter (warmer) than the rest of the crater in the T_b image (Figure 4a), in green in the DCS image (Figure 4b), and in red tones in the MNF image (Figure 4c). A second unit is the crater floor, which appears dominantly blue in the DCS image and appears in blues and greens in the MNF image. In addition, there are several low T_b materials present in the crater floor that appear darker (cooler) in the T_b image as well as a intermediate T_b

unit that appears brighter (warmer) in the T_b image. However, these units are not distinguished in either the DCS or MNF images. (There also appears to be a low T_b unit within the western portion of the small crater on the NE rim of Gusev. This crater, C133 from the *Cabrol and Grin* [1999] list, will be evaluated separately.) The north external terrain appears in blues and greens in the DCS image, with hints of red near the rim of Gusev and nearby craters, whereas the south external terrain appears dominantly in reds in the DCS image. In the MNF image, the north external terrain appears in blues and is distinct from the south external terrain, which appears in greens.

The mean TES spectra of the THEMIS-determined ROIs in Gusev Crater were evaluated using the DCI of *Ruff and Christensen* [2002]. All regions were seen to exhibit some degree of surface dust cover (Table 2). The DCI values for the LA features ROI spectra, as well as the intermediate and low T_b materials ROI spectra, indicate only intermediate dust cover (Table 2). Conversely, the DCI values of the crater floor ROI spectra indicate that the crater floor has an intermediate to thick layer of dust. The DCI values for the external terrain spectra indicate that these surfaces are dust covered. The very low T_b material (south of the southern LA feature) and the floor of the small crater on the NE rim of Gusev do not have TES coverage, and therefore cannot be evaluated using the DCI and linear deconvolution methods.

Linear deconvolution results for Gusev Crater are also displayed in Table 2 and are relatively consistent with the DCI in regard to their use of the surface dust end member. Deconvolution models of both the south LA feature and the adjacent intermediate T_b material do not include any surface end members (Syrtis, Acidalia, Hematite or surface dust) in amounts exceeding the lower detection limits of 10-15% for

this method [*Bandfield et al.*, 2000*a*], but are dominated by low CO_2 atmospheric dust. However, the north LA feature is well modeled by a combination of Acidalia-type materials and surface dust in significant amounts (>10-15%). Deconvolution of the crater floor ROI spectra included surface dust and Acidalia-type materials; however, the only spectrum not considered dust-covered did not use any surface end members. The low T_b materials appear to be well modeled by Syrtis-type material. The north external terrain is well modeled by Acidalia-type material and surface dust, while the south external terrain is well modeled by the surface dust end member alone.

The variation displayed by the measured-to-modeled spectral ratios for these ROIs appears to be related to the dusty nature of these spectra (Figure 5). Specifically, the concave-down shape of ratio values at the highest wavenumbers is typically observed in spectra that have a thermally thick layer of surface dust [*Stockstill et al.*, *in press*]. In addition, spectra that have linear deconvolution results dominated by atmospheric end members, such as Crater floor unit 1 (Table 2 and Figure 5), display this same behavior at high wavenumbers as well as erratic and divergent ratio values at the lowest wavenumbers. Therefore, the spectral ratio plots for the Gusev ROIs do not contain remnant absorptions not modeled by linear deconvolution using the eight TES end members. Furthermore, application of the carbonate indices method did not detect the signature of carbonates for any region defined for this basin.

Mean THEMIS surface emissivity spectra for the Gusev ROIs are displayed in Figure 6. Note that for all ROIs, the scene-relative emissivity value for bands 1 and 2 are close to one (Figure 6 and Table 2), indicating no carbonate absorptions are present in any mean ROI spectra. The emissivity spectra of the LA features display the most

spectral contrast of any ROI spectra from this crater (Figure 6), although they still show less contrast than pure Acidalia- and Syrtis-type materials (Figure 3a). These emissivity spectra are consistent with a mix of Syrtis-type material with surface dust. Note that this is inconsistent with the deconvolution results for the LA features (Table 2). The intermediate T_b material shows less spectral contrast than its adjacent LA feature, suggesting even more surface dust. Finally, the very low T_b materials south of the LA feature matches well to the surface dust spectrum. Spectra of the external terrain are all relatively flat (Figure 6), consistent with the dust-covered surfaces indicated by the DCI and linear deconvolution results for these surfaces.

3.2 Gale Crater (-5.5N, 137.8E)

The regions of interest for Gale Crater are displayed on a corrected THEMIS T_b image in Figure 7a. THEMIS provided a much more complete, detailed view of Gale Crater compared to TES. Specifically, TES lacked coverage of portions of the central mound that have been imaged by THEMIS [*Stockstill et al.*, *in press*]. In addition, at the higher spatial resolution of THEMIS, we were able to identify more individual spectral units within the crater than was possible using TES data [*Stockstill et al.*, *in press*]. Higher spectral resolution allows more effective isolation of individual units, which in turn allows more accurate selection of spectrally-pure TES pixels. *Pelkey et al.* [2004] also noted that the higher spatial resolution of THEMIS allowed for identification of units and small scale channels within Gale that were not discernable at TES spatial resolution.

In the T_b image (Figure 7a), numerous units appear within the floor of Gale Crater. There are several areas with high T_b materials, which appear brighter than the rest of the crater floor on the T_b image. These materials wrap around the NW and SE

sides of the mound and have patches in the south crater floor (two of which are outlined by an ROI in Figure 7a). However, these materials do not appear distinct in the DCS or MNF images. In fact, both the bright materials that wrap around the crater's central mound and the crater floor south of the mound appear in greens (Syrtis basalt) in the DCS image (Figure 7b) and appear in greens in the MNF image (Figure 7c). In THEMIS visible images, these high T_b materials have low albedo relative to the surrounding crater floor [*Pelkey et al.*, 2004]. In addition, a "smooth" unit (in the T_b image) and lower T_b crater floor unit have been defined just southeast of the mound. These units also do not appear to be distinct in the DCS or MNF images. Furthermore, the mound appears in hues grading from reds (Acidalia-type) to blues (dust) in both the DCS and MNF images. Finally, the south external terrain appears in red hues in the both the DCS and MNF images, while the north external terrain appears in blue hues in the DCS image and in yellows in the MNF image.

When the mean ROI TES spectra of Gale Crater were evaluated using the DCI [*Ruff and Christensen*, 2002], the ROI spectra varied from dust covered (the western portion of the mound) to dust-free (the crater floor), as shown in Table 3. The dustiest regions are the top surface of the mound and the northern external terrain. The crater floor, including the high T_b material, and the southern external terrain appear to be relatively dust-free.

Linear deconvolution results for Gale Crater, also displayed in Table 3, are relatively consistent with the DCI in regards to their use of the surface dust end member. The crater floor and the high T_b materials in the crater floor are well modeled by a combination of Syrtis- and Acidalia-type materials. The deconvolution results for the

western mound unit only include surface dust component in significant amounts, using the most amount of surface dust of any ROI, which is consistent with it also having the lowest (dustiest) DCI value. The other two mound units have intermediate DCI values. Deconvolution of the central mound unit included a mix of Syrtis-type basalt and Acidalia-type material, whereas the mound layers unit only included Acidalia-type material. The north external terrain is well modeled by surface dust and Acidalia-type, while the south external terrain is well modeled by Syrtis-type and Acidalia-type materials.

The measured-to-modeled spectral ratios for these ROIs do not display large variations from unity (Figure 8). Again, the mound units and the north external terrain display variations in spectral ratio values at high wavenumber typical of a dusty surface. Therefore, the spectral ratio plots for the Gale ROIs do not contain remnant absorptions that were not modeled by linear deconvolution using the eight TES end members. In addition, application of the carbonate indices method did not detect the signature of carbonates for any region defined for this basin.

Mean THEMIS surface emissivity spectra for the Gale ROIs are displayed in Figure 9. Note that for most ROIs, the scene-relative emissivity value for bands 1 and 2 are close to one (Figure 6 and Table 2), indicating no carbonate absorption are present in these mean ROI spectra. However, the scene-relative emissivity value of the north external terrain is 0.94; this is the only ROI in this study that has scene-relative emissivity value <0.98. The spectra of the crater floor materials and the high T_b materials on the crater floor are consistent with a dust-free surface that is a mix of Syrtis-type and Acidalia-type materials (Figure 3a). The spectra of the mound show less spectral

contrast, consistent with a dustier surface, with the eastern mound spectrum most resembling the surface dust end member spectrum (Figure 3a). In addition, the spectrum of the north external terrain also appears fairly dusty, while the spectrum of the south external terrain matches to a mix of Syrtis- and Acidalia-type materials.

3.3 Smaller basins within Aeolis quadrangle

The small craters that display non-negligible spectral variation and could be atmospherically corrected using corresponding TES data are C133, a paired set of craters called C142 and 144, and C147. Craters C133 and C142 and 144 are located on the rim of Gusev Crater, while C147 is just south of Gusev on Ma'adim Vallis (Figure 1). The T_b images for these basins, with associated ROIs, are displayed in Figure 10a-b, while the DCS and MNF images are displayed in Figures 11a-f.

Crater C133 (13.3S, 176.6E) C133 is a 30 km crater located on the NE rim of Gusev Crater (Figure 1). Cabrol and Grin [1999] classified this as a closed lake basin with a fluvial valley network. Proposed sedimentary structures associated with C133 include a delta deposit, sedimentary terraces, possible layering, sedimentary deposits, evaporites, shorelines and a mound [*Cabrol and Grin*, 1999]. The low T_b materials in western floor of this crater were previously defined as an ROI for Gusev Crater.

The ROIs for C133 are displayed on a corrected (for radiance offset) THEMIS T_b image in Figure 10a. These regions were identified mainly using the color composite image resulting from the MNF rotation of the emissivity data (Figure 11b), although these same units can be identified in the T_b image (Figure 10a) and/or the DCS image (Figure 11a).

A distinct unit in the western portion of C133 appears darker (cooler) the T_b image and in red tones in both the DCS and MNF images. This unit is distinct from the rest of the crater floor, which appears in blues in the DCS image and in greens in the MNF image. The channel that cuts into the NW rim of C133 appears quite distinct in green in the MNF image, but is less apparent in the DCS and T_b images. Likewise, a unit in the SW rim of C133 appears in a distinct red tone in the MNF image, but is not as obvious in the DCS and T_b image. Finally, an ROI was defined for the north external terrain, which appears in greens in the DCS image and blues in the MNF image.

For the three ROIs within C133 that had TES coverage, the DCI values indicated that they are dust covered surfaces. The linear deconvolution of these spectra also indicated that these surfaces are relatively dusty, using between 29 and 42% surface dust component (Table 4). Furthermore, the linear deconvolution models did not use significant amounts of any other surface end member to model these spectra. The measured-over-modeled spectral ratios for all three ROIs do not vary greatly from unity (Figure 12), so it does not appear that the measured spectra contain residual absorptions not being modeled by the linear deconvolution. Finally, the carbonate indices did not detect any spectral signatures of carbonates in the ROI spectra.

Mean THEMIS surface emissivity spectra for the C133 ROIs are displayed in Figure 13. Note that for all ROIs, the scene-relative emissivity value for bands 1 and 2 are close to one (Figure 13 and Table 4), indicating no carbonate absorption is present in any mean ROI spectra. In addition, all THEMIS spectra for this crater are relatively featureless, varying slightly from unity, consistent with the dusty nature of this region.

Craters C142 and 144 (15.9S, 175.8E and 16.0S, 175.8E) C142 is a 30 km crater located on the SSW rim of Gusev, intersecting the mouth of Ma'adim Vallis. C144 is a 24 km crater that sits just south of C142, and also overlaps the rim of Gusev and Ma'adim Vallis. *Cabrol and Grin* [1999] classified these craters as lake chain basins associated with a fluvial valley network. Proposed sedimentary structures associated with both craters include sedimentary terraces, sedimentary deposits, possible shorelines and a mound [*Cabrol and Grin*, 1999].

The ROIs for C142 and C144 are displayed on a corrected (for radiance offset) THEMIS T_b image in Figure 10b. These regions were identified mainly using the color composite image resulting from the MNF rotation of the emissivity data (Figure 11d), although most of these same units can be identified in the DCS image (Figure 11c). The north external terrain appears in red in the MNF image and in greens and blues in the DCS image. The south external terrain varies from purplish tones to blue tones in the MNF, but only appears in red tones in the DCS image. The crater floor units appear in red tones in the MNF image, but are more mixed than the north external terrain. In the DCS image, the crater floor units appear in greens and blues, quite similar to the north external terrain. Since the original ROI for C142 did not have TES data coverage, an additional ROI was defined that did have TES coverage (Figure 10b). However, it should be noted that in the MNF image, this portion of the crater floor may be a distinct unit (blues) from the rest of the crater floor (reds).

For the ROIs within C142 and C144, the DCI values indicated that they are intermediate to dust covered surfaces [*Ruff and Christensen*, 2002], with the north external terrain being the only ROI with intermediate dust cover. The linear

deconvolution of these spectra also indicated that these surfaces are relatively dusty, using between 18 and 38% surface dust component (Table 4). The deconvolution model for the north external terrain includes both Acidalia-type materials and surface dust. The measured-over-modeled spectral ratios for all ROIs for C142 and C144 do not vary greatly from unity (Figure 12). Therefore, it does not appear that the measured spectra contain residual absorptions not being modeled by the linear deconvolution. In addition, the carbonate indices did not detect any spectral signatures of carbonates in the ROI spectra.

Mean THEMIS surface emissivity spectra for the C142 and 144 ROIs are displayed in Figure 13. Note that for these ROIs, the scene-relative emissivity value for bands 1 and 2 are close to unity (Figure 13 and Table 4), indicating that no carbonate absorptions are present in any mean ROI spectra. Similar to the spectra from C133, these THEMIS spectra are relatively featureless, only varying slightly from unity, and are consistent with the dusty nature of this region.

Crater C147 (17.7S, 177.6E) C147 is a 32 km crater located at a bend in Ma'adim Vallis ~40 km SE of where it enters Gusev Crater. *Cabrol and Grin* [1999] classified this crater as lake chain basins associated with a fluvial valley network. Proposed sedimentary structures associated with C147 include sedimentary deposits, shorelines and a mound [*Cabrol and Grin*, 1999].

The ROIs for C147 are displayed on a corrected (for radiance offset) THEMIS T_b image in Figure 10c. These regions were identified using both the DCS image (Figure 11e) and MNF image (Figure 11f). The crater floor appears in blues in the MNF image and in greens and blues in the DCS image (as does much of the image). The rim of the

crater, the west and the north, appears in reds in the MNF, but does not vary from the surroundings in the DCS image. Finally, a small unit on the crater floor appears in cyan in the MNF image and in red in the DCS image.

The DCI values for C147 ROIs indicate that these surfaces have an intermediate dust cover. The linear deconvolution of these spectra also indicates that these surfaces are relatively dusty, using between 13 and 33% surface dust component (Table 4). However, the linear deconvolution models did not use any other surface end members to model these spectra. The measured-over-modeled spectral ratios for all ROIs for C142 and 144 do not vary greatly from unity and the variation present is typical of a dusty spectrum (Figure 12). Therefore, it does not appear that the measured spectra contain residual absorptions not being modeled by the linear deconvolution. Finally, the carbonate indices did not detect any spectral signatures of carbonates in the ROI spectra.

Mean THEMIS surface emissivity spectra for the C147 ROIs are displayed in Figure 13. Note that for these ROIs, the scene-relative emissivity value for bands 1 and 2 are close to unity (Figure 13 and Table 4), indicating that no carbonate absorption are present in any mean ROI spectra. Again, these THEMIS spectra are resemble the TES surface dust spectrum (Figure 3a) and are consistent with the dusty nature of this region.

4. Discussion

4.1 Gusev Crater (-14.5N, 175.5E)

The DCI values of the LA features are consistent with either a surface with intermediate dust cover or a surface with more indurated particulate materials [*Ruff and Christensen*, 2002]. Fortunately, the Spirit Rover recently landed within one of the

regions of low albedo in Gusev Crater and these low albedo features are now believed to be zones that have had recent removal of some fine particulate material by dust devils [*Squyres et al.*, 2004*b*]. This would suggest that the intermediate DCI values for LA features are consistent with only partial dust cover and that spectral signature of the surface is only partially obscured by the dust.

In a recent thermal inertia study of Gusev Crater, *Martínez-Alonso et al.* [2005] identified the LA features as a surface that is a mixture of indurated material, coarse particles, and exposed rocks or bedrock that has a (Syrtis-type) basaltic composition. Many rocks within Gusev Crater appear to be pristine basalts containing olivine [*Christensen et al.*, 2004*b*; *McSween et al.*, 2004; *Morris et al.*, 2004] and even the regolith shows only a slight decrease in basaltic mineralogy in trenches relative to the undisturbed surface regolith [*Wang et al.*, 2005], suggesting relatively little alteration of the rocks and regolith in Gusev Crater.

In the DCS image of Gusev Crater, the LA features appear to be Syrtis-type basalt (Figure 4b). However, our deconvolution results for the low-albedo features for this study used Acidalia-type, not Syrtis-type materials. Acidalia-type has been interpreted as either an andesite [*Bandfield et al.*, 2000*a*; *Hamilton et al.*, 2001] or as partly weathered basalt [*Wyatt and McSween*, 2002; *Kraft et al.*, 2003; *Ruff*, 2004]. Neither interpretation is consistent with relatively unaltered basaltic terrain evidenced by Spirit Rover and the study of *Martínez-Alonso et al.* [2005]. However, the regolith of Gusev Crater has been found to contains up to 16% sulfates [*Wang et al.*, 2005], which may affect the deconvolution results. Specifically, a basaltic spectrum mixed with sulfates [e.g., *Lane*,

2005] may deconvolve using the Acidalia end member when sulfates are not provided as end members [*M. Lane, pers. comm*., 2005].

To test this idea, the spectra of the low-albedo features and associated intermediate low T_b material were deconvolved again, using the eight TES end members and spectra of two sulfates (bloedite and glauberite) that have been identified in spectra from northeast Meridiani [*Lane*, 2005]. When these sulfates were provided, they were used in small amounts by the models (Table 5), well below their lower detection limit of 15% [*Christensen et al.*, 2001]. Including sulfates as end members does not necessarily improve the spectral RMS (Table 5) or drastically change the measured-to-modeled spectral ratio (Figure 14). However, their inclusion did eliminate the use of the Acidalia-type end member from some models and increase the amount of Syrtis-type materials used to believable amounts for these models (e.g., the south LA feature and associated intermediate T_b unit, Table 5). This model provides a better match to the surfaces observed at Gusev by the Spirit rover. Note that the models for the north LA feature are fairly unaffected by the inclusion of sulfates for modeling; however, these units also appear to be dustier than the south LA feature, since they use up to 37% surface dust end member. Therefore, it is possible that the surface composition of this the north LA feature is obscured by more dust, at least at the time the TES data were acquired. The THEMIS spectra of the low-albedo units (Figure 6) have a spectral shape that resembles a THEMIS-resolution Syrtis spectrum (Figure 3a), with a low emissivity value at band 5 and generally concave-up shape in higher band numbers.

Two of the low T_b units (south of the northern LA feature and in the SW crater floor) have DCI values that indicate an intermediate dust cover. However, the model of

the low T_b unit in the SW part of Gusev Crater includes only the surface dust (no other surface end members). With a DCI value (0.942) approaching the threshold for a dust-covered surface (0.940) and the results of the deconvolution suggest that this surface has a large spectral contribution from surface dust. The final unit with an intermediate DCI value is the low T_b unit that lies south of the northern LA feature. This unit has the highest DCI value (0.958) of any ROIs in Gusev, which approaches the threshold for a dust-free surface (0.962). In addition, the linear deconvolution model included only Syrtis-type end member, suggesting that this material represents a relatively dust-free, basaltic surface. However, in the DCS image these units do not appear distinct from the crater floor, which appears as a mix of surface dust and Syrtis-type basalt (Figure 4b). In addition, all THEMIS spectra of the low T_b units are relatively flat (Figure 6), with a slightly concave-down spectrum similar to the surface dust spectrum (Figure 3a).

All remaining ROIs within Gusev Crater either have DCI values that indicate a dust-covered surface or have a DCI value that approaches the threshold for a dust-covered surface and uses only surface dust end member and/or atmospheric components (e.g., Crater floor 1 unit). These units have spectrally-thick dust mantling their surface, so the spectral signal from the surface units is obscured by the dust. The crater floor is dominantly blue in the DCS image, consistent with a dusty surface (Figure 4b). Furthermore, the THEMIS spectra for these units also appear relatively flat (Figure 6), resembling the spectrum for surface dust (Figure 3a).

The ROIs of the external terrain of Gusev have DCI values that indicate a dust covered surfaces and their deconvolution models included significant amounts of surface dust end member (Table 2). This suggests that these units have a spectrally-thick dust

mantling their surface, obscuring the spectral signature of the underlying material. THEMIS emissivity spectra of the external terrain are fairly flat with a slight concave-down shape (Figure 6), consistent with the dust spectrum (Figure 3a). However, the DCS image displays the north external terrain as a mix Syrtis-type basalt and dust, whereas the south external terrain appears to be Acidalia-type material (Figure 4b).

The external terrains are the only areas in Gusev where the DCS image conflicts with other lines of evidence (DCI, TES deconvolution, THEMIS surface emissivity spectrum). The decorrelation stretch was performed on emissivity data that has had the additive portion of the atmospheric contribution removed (i.e., the radiance offset). Because we are mainly interested in units within the crater, the ROI for this step (Figure 1, Step2) is defined within the crater. Therefore, the amount of atmosphere removed is based on the path length of the atmosphere at the crater floor. However, there is a 2 km increase in elevation from the crater floor of Gusev to the external terrain, so the path length through the atmosphere is significantly different for the external terrain. The mismatch between the DCS image and other lines of evidence probably results from incorrect amounts of atmospheric removal for that elevation. Furthermore, this suggests that the colors in the DCS image for the external terrain may not be correct and that the other lines of evidence are probably more reliable. Therefore, the external terrains of Gusev are interpreted to be dust-covered surfaces.

4.2 Gale Crater (-5.5N, 137.8E)

The surface deposits at Gale Crater have less dust cover than the surfaces at Gusev Crater. The crater floor units have DCI values that indicate they are relatively dust-free surfaces, in agreement with thermal inertia values for these units which suggest

they range from lightly to extensively indurated materials with small amounts of dust [*Pelkey et al.*, 2004]. The deconvolution results of the crater floor units suggest they are composed of Syrtis-type basalt mixed with some Acidalia-type material. Mean THEMIS emissivity spectra of the crater floor units (Figure 9) resemble the Syrtis-type basalt spectrum (Figure 3a). Furthermore, in the DCS image the crater floor appears to be Syrtis-type basalt (Figure 7b).

Likewise, the high T_b units within the floor of Gale Crater have DCI values that indicate relatively little dust cover, ranging from intermediate dust cover to dust-free. The high T_b units correspond to the sand sheets mapped in the floor of Gale Crater by *Pelkey et al*. [2004] and have relatively low albedo. Thermal inertia values from that study suggested that these materials consisted of coarse or lightly indurated sand that is at least a few cm in thickness [*Pelkey et al.*, 2004]. Like the rest of the crater floor, the deconvolution results for the high T_b units were consistent with a mix of Syrtis-type basalt and Acidalia-type materials. Furthermore, these units are not distinguishable from the crater floor within the DCS (i.e., Syrtis-type basalt) or MNF images (Figures 7b and c) of Gale Crater. Therefore, the high T_b units differ from the rest of the crater floor in their physical properties (i.e., degree of induration or grain size), but not in composition. THEMIS emissivity spectra for these units are consistent with Syrtis-type and Acidalia-type spectral shapes (Figure 9).

The mound units have DCI values that suggest a spectrally intermediate to thick layer of dust. Both the mound layers and the central mound unit have a DCI value that indicates only intermediate dust cover. The deconvolution results for these two units suggest that the mound is a mix of Syrtis-type basalt and Acidalia-type materials. (These

spectra were also deconvolved with the eight TES end members and two sulfate spectra; however, the availability of sulfates did not affect the inclusion of Acidalia-type materials in deconvolution models.) THEMIS emissivity spectra for the mound units are consistent with a fairly dusty surface for all units (Figure 9). Finally, in the DCS image, the mound appears to Acidalia-type material near the center, grading to surface dust on the flanks (Figure 7b).

The inclusion of Acidalia-type materials in deconvolution models for the mound layers is interesting in light of the various origins that have been proposed for this layering. Proposed origins for the mound layers include sedimentary rocks deposited in a standing lake [*Cabrol and Grin*, 1999; *Malin and Edgett*, 2000], sedimentary rocks deposited by aeolian or fluvial processes [*Greeley and Guest*, 1987; *Scott and Chapman*, 1995], interbedded lava flows [*Greeley and Guest*, 1987] and pyroclastic deposits [*Scott and Chapman*, 1995]. If these layers represent sedimentary rocks deposited by lacustrine, aeolian or fluvial processes, then a plausible interpretation of the Acidalia-type material included in the deconvolution results is that it is weathered basalt [*Wyatt and McSween*, 2002]. However, if these layered deposits were emplaced as lava flows or pyroclastic deposits, then the Acidalia-type spectral component could be andesite [*Bandfield et al.*, 2000*b*; *Hamilton et al.*, 2001].

According to DCI values, the terrain surrounding Gale Crater appears to be dust-covered surfaces to the north and dust-free basaltic materials (with some Acidalia-type material) to the south, consistent with the findings of *Pelkey et al.* [2004]. Deconvolution results indicate that the north external terrain is a mix of dust and Acidalia-type material, whereas the south external terrain is dominated by Syrtis-type basalt. THEMIS

emissivity spectrum of the north external terrain (Figure 9) closely resembles the surface dust spectrum, including low emissivity values in bands 1 and 2 with a maximum emissivity value in band 4 and concave-down shape. THEMIS emissivity spectrum of the south external terrain appears consistent with a somewhat dusty Syrtis-type basaltic surface. In the DCS image, the north external terrain appears to be a mix of dust and Acidalia-type, whereas the south external terrain appears to be dominated by Acidalia-type material.

As with the external terrain of Gusev, there is an apparent conflict between the DCS image and the other lines of evidence for the south external terrain of Gale Crater. Again, the south external terrain of Gale lies ~2.2 km above the crater floor, so that the atmospheric path length for the external terrain is significantly different from the crater floor. Therefore, the mismatch between probably results from incorrect amounts of atmospheric removal for that elevated external terrain and the colors in the DCS image for the external terrain may not be correct. Therefore, the south external terrain of Gale is interpreted to be Syrtis-type basalt.

4.3 Smaller basins within Aeolis quadrangle

The ROIs defined in and around the smaller basins within the Aeolis quadrangle have low to intermediate DCI values, indicating that these surfaces are partly to completely obscured by dust. All regions within C133 have DCI values that indicate a dust-covered surface, and deconvolution models for these ROIs use large amounts of the surface dust component. The THEMIS emissivity spectra of these ROIs are consistent with a dusty surface as well.

For C142 and C144, all ROIs defined within the craters themselves also have DCI values indicating dust-covered surfaces. One ROI defined for these craters in the north external terrain has an intermediate DCI value, indicating that the surface spectral signal may not be completely obscured by the dust cover. The deconvolution model for this ROI includes both Acidalia-type and surface dust end members. The THEMIS emissivity spectra for these ROIs are consistent with a dusty surface.

Finally, the three ROIs defined for C147 have DCI values that indicate intermediate dust cover. However, the only surface end member included by the deconvolution models for these spectra is surface dust. In addition, the THEMIS emissivity spectra for C147 ROIs resemble the surface dust spectrum. Therefore, it appears that very little compositional information can be derived for these smaller basins within the Aeolis quadrangle.

The DCS and MNF images appear to show more spectral variation than is apparent from other lines of evidence. Specifically, the DCI values and linear deconvolution results derived from TES data as well as the mean THEMIS emissivity spectra indicate fairly dusty surfaces for these craters. One would then expect fairly featureless color composite images derived from PCA rotations (i.e., DCS and MNF). However, the MNF eigenvalues for the THEMIS scenes of the small craters are quite low (Table 1) and the images appear fairly noisy (Figure 11 a-f). Therefore, the spectral variation being enhanced by the PCA rotation probably lies at or just above the noise levels of this data.

5. Summary

Gusev Crater: Most of the surface of Gusev Crater is blanketed by a thermally thick layer of dust that obscures the spectral signal from the surface. However, the low-albedo features appear to only have intermediate dust cover, consistent with these areas having fine particulate materials removed by dust devils in the recent past [*Squyres et al.*, 2004*b*]. THEMIS emissivity spectral shapes resemble the Syrtis-type end member spectrum at THEMIS resolution, consistent with the findings of relatively unaltered basaltic materials for low-albedo features, rocks, and regolith of Gusev [*Christensen et al.*, 2004*b*; *Gellert et al.*, 2004; *McSween et al.*, 2004; *Morris et al.*, 2004; *Martínez-Alonso et al.*, 2005; *Wang et al.*, 2005]. However, deconvolution of TES spectra for the low-albedo features using the eight TES surface end members only included the Acidalia-type and surface dust end members in significant amounts; this deconvolution did not use any Syrtis-type materials.

New deconvolutions using the eight TES end members and two sulfate (bloedite and glauberite) spectral end members did result in models that no longer used the Acidalia-type end member and used the Syrtis-type basalt end member in significant amounts. These models also used sulfates in small (insignificant) amounts. Clearly, although the sulfates are not present in significant amounts, their presence for the deconvolution modeling process may affect which surface type is included and provide a better match to what is observed at the surface of Mars. However, when the sulfates are chosen in such low amounts, it is difficult to say with certainty which model is better without available ground-truth results.

Gale Crater: On a broad scale, our view of Gale Crater via THEMIS is quite similar to our view from TES: a fairly dust-free crater floor composed of a mix of Syrtis-type and Acidalia-type materials, a fairly dusty central mound composed of Acidalia-type materials, a dusty north external terrain and dust-free south external terrain composed of a mix of both Syrtis-type and Acidalia-type materials [*Stockstill et al.*, submitted]. However, THEMIS has provided a more detailed view of Gale that demonstrates thermophysical variations within the crater floor unit that are independent of composition. In addition, the dust mantling the central mound is variable in thickness, revealing some compositional information from some areas of the mound.

Specifically, the mound layers appear to have only an intermediate dust cover and deconvolution model only uses the Acidalia-type surface end member to model this spectrum. The presence of Acidalia-type materials in the mound layers is generally interesting due to the various ways this spectral end member is interpreted (i.e., andesite or weathered basalt) as well as the various origins proposed for the layered mound in Gale (sedimentary deposition vs. volcanic deposition). Acidalia-type material would be consistent with either 1) sedimentary deposition of weathered basalt by fluvio-lacustrine or aeolian processes or 2) volcanic deposition of an andesitic lava flow or pyroclastic deposit.

Smaller craters: The smaller craters within Aeolis quadrangle attest to the generally dusty nature of the Aeolis quadrangle. Data from many small craters were eliminated due to low spectral variation revealed by the MNF rotation. One possible explanation is that the surfaces within these images were mantled by a spectrally-thick layer of dust, so that any spectral variation present on the surface is obscured by the dust

cover. If this were the case, then the only spectral contributions would be from the surface dust and the atmosphere, where the atmosphere should have a fairly homogeneous contribution within a THEMIS image (excluding large variations in elevation).

In addition, the few small craters that do display some spectral variation were surfaces that ranged from intermediate to dust-covered. Likewise, the THEMIS emissivity spectra for these surfaces were relatively featureless and, in some cases, resembled the spectrum of the TES surface dust end member. Therefore, the dust-free surfaces observed within Gale and the surfaces within Gusev with only intermediate dust cover may be unique among basin surfaces within Aeolis quadrangle.

Proposed paleolake basin origin: We have not found any unambiguous spectroscopic evidence supporting a paleolacustrine origin for the surficial deposits in Gusev, Gale or other craters in the Aeolis quadrangle. In THEMIS emissivity spectra, bands 1 and 2 (6.79 μm or ~1470-cm^{-1}) are relatively unaffected by atmospheric end members and most rock-forming minerals. However, carbonates have their deepest absorption in these bands. We did not observe any absorption in these bands that was strong enough to be attributed to carbonates. We also did not find absorptions in the THEMIS emissivity spectra that might be related to other evaporites, such as sulfates.

TES spectra corresponding to the THEMIS-defined regions of interest also fail to confirm a paleolake origin for any surface deposits. Deconvolution using the eight TES end members models the measured spectra well. In fact, spectral ratios of the measured over modeled spectra revealed no significant remnant absorptions, suggesting that the end members used were sufficient to explain the observed spectral variation. In addition,

application of the carbonate indices to the TES spectra did not find any spectral signature of carbonates in these spectra.

At the spatial resolution of THEMIS data, the layers within the mound of Gale Crater are discernable near the limits of the data. We attempted to delineate any spectral patterns associated with these layers; however no appreciable spectral differences could be detected. Perhaps moving the orbit of Odyssey to an earlier local solar time in the future will improve the signal-to-noise ratio of THEMIS sufficiently to make subtle spectral differences discernable.

The mound seems to be a good spectral match to a combination of Acidalia-type materials and surface dust. This is pertinent to the discussion of possible paleolake origin for the mound layers because Acidalia-type spectrum has been interpreted as either andesite or weathered basalt. Indeed, a single interpretation may not be appropriate for the whole of Mars. If interpreted as weathered basalt, these layers may represent a sedimentary rock composed of weathered basalt or interbedded basaltic rocks that have undergone weathering. Either of these interpretations could support a lacustrine history for Gale Crater. However, the interpretation that the mound is composed of andesite cannot be discounted. Therefore, although this evidence does not disprove a possible paleolake origin, it does not exclusively support a paleolacustrine period for Gale Crater.

Acknowledgements. This work benefited from discussions with Vicky Hamilton, Deanne Rogers, and Will Koeppen. This study was supported by Arizona State University THEMIS subcontract 01-082 (HYM) and by the THEMIS Participating Scientist Program JPL contract 1241129 (JEM).

References cited

Adler, H.H., and P.F. Kerr, Infrared study of aragonite and calcite, *American Mineralogist*, *47*, 700-717, 1962.

Adler, H.H., and P.F. Kerr, Infrared absorption frequency trends for anhydrous normal carbonates, *American Mineralogist*, *48*, 124-137, 1963*a*.

Adler, H.H., and P.F. Kerr, Infrared spectra, symmetry and structure relations of some carbonate minerals, *American Mineralogist*, *48*, 839-853, 1963*b*.

Adler, H.H., and P.F. Kerr, Variations in infrared spectra, molecular symmetry and site symmetry of sulfate minerals, *American Mineralogist*, *50*, 132-147, 1965.

Baker, V.R., The Spokane flood controversy and the Martian outflow channels, *Science*, *202*, 1249-1256, 1978.

Baker, V.R., Water and the Martian landscape, *Nature*, *412* (6843), 228-236, 2001.

Baker, V.R., and D.J. Milton, Erosion by catastrophic floods on Mars and Earth, *Icarus*, *23*, 27-41, 1974.

Baker, V.R., M.H. Carr, V.C. Gulick, C.R. Williams, and M.S. Marley, Channels and Valley Networks, in *Mars*, edited by H.H. Kieffer, B.M. Jakosky, C.W. Snyder, and M.S. Matthews, pp. 493-522, The University of Arizona Press, Tucson, 1992.

Baldridge, A.M., J.D. Farmer, and J.E. Moersch, Mars remote-sensing analogy studies in the Badwater Basin, Death Valley, California, *Journal of Geophysical Research*, *109* (E12), doi:10.1029/2004JE002315, 2004.

Bandfield, J.C., D. Rogers, M.D. Smith, and P.R. Christensen, Atmospheric and surface spectral units mapping using Thermal Emission Imaging System data, *Journal of Geophysical Research*, *109* (E10), 10.1029/2004JE002289, 2004.

Bandfield, J.L., Global mineral distributions on Mars, *Journal of Geophysical Research*, *107* (6), 5042, 10.1029/2001JE001510, 2002.

Bandfield, J.L., and M.D. Smith, Multiple emission angle surface-atmosphere separations of Thermal Emission Spectrometer data, *Icarus*, *161*, 47-65, 2003.

Bandfield, J.L., P.R. Christensen, and M.D. Smith, Spectral data set factor analysis and end-member recovery: Application to analysis of Martian atmospheric particulates, *Journal of Geophysical Research*, *105* (E4), 9573-9587, 2000*a*.

Bandfield, J.L., V.E. Hamilton, and P.R. Christensen, A global view of Martian surface compositions from MGS-TES, *Science*, *287* (5458), 1626-1630, 2000*b*.

Bandfield, J.L., T.D. Glotch, and P.R. Christensen, Spectroscopic Identification of Carbonate Mineral in the Martian Dust, *Science*, *301*, 1084-1087, 2003.

Brakenridge, G.R., The Origin of Fluvial Valleys and Early Geologic History, Aeolis Quadrangle, Mars, *Journal of Geophysical Research*, *95* (B11), 17289-17308, 1990.

Cabrol, N.A., Early Amazonian lake in Gale Crater, Mars, in *Lunar and Planetary Science Conference XXVIII*, edited by D. Black, pp. 191-192, Lunar and Planetary Institute, Houston, TX, 1997.

Cabrol, N.A., and E.A. Grin, Hydrogeology and exobiology significance of Martian large crater lakes, in *Conference on early Mars; geologic and hydrologic evolution,*

physical and chemical environments, and the implications for life, edited by S.M. Clifford, A.H. Treiman, H.E. Newsom, and J.D. Farmer, pp. 14-15, Lunar and Planetary Institute, Houston, TX, 1997.

Cabrol, N.A., and E.A. Grin, Distribution, Classification, and Ages of Martian Impact Crater Lakes, *Icarus*, *142*, 160-172, 1999.

Cabrol, N.A., E.A. Grin, R. Landheim, R.O. Kuzmin, and R. Greeley, Duration of the Ma'adim Vallis/Gusev Crater hydrogeologic system, *Icarus*, *133* (1), 98-108, 1998.

Cabrol, N.A., E.A. Grin, H.E. Newsom, R. Landheim, and C.P. McKay, Hydrogeologic evolution of Gale crater and its relevance to the exobiological exploration of Mars, *Icarus*, *139* (235-245), 1999.

Carr, M.H., The role of lava erosion in the formation of lunar rilles and Martian channels, *Icarus*, *22*, 1-23, 1974.

Carr, M.H., Formation of Martian flood features by release of water from confined aquifers, *Journal of Geophysical Research*, *84* (B6), 2995-3007, 1979.

Carr, M.H., Formation of the Martian drainage system; redistribution of groundwater in response to global topography and cold climates, in *Workshop on Evolution of Martian volatiles LPI Technical report*, edited by B.M. Jakosky, and A. Treiman, pp. 7-9, Lunar and Planetary Institute, Houston, TX, 1996*a*.

Carr, M.H., *Water on Mars*, 229 pp., Oxford University Press, New York, 1996*b*.

Carter, B.L., H.V. Frey, S.E.H. Sakimoto, and J.H. Roark, Constraints on Gusev Basin Infill from the Mars Orbiter Laser Altimeter (MOLA) Topography, in *Lunar and Planetary Science Conference*, pp. 2042, Lunar and Planetary Institute, Houston, TX, 2001.

Christensen, P.R., Formation of recent Martian gullies through melting of extensive water-rich snow deposits, *Nature*, *422* (6927), 45-48, 2003.

Christensen, P.R., D.L. Anderson, S.C. Chase, R.N. Clark, H.H. Kieffer, M.C. Malin, J.C. Pearl, J. Carpenter, N. Bandiera, F.G. Brown, and S. Silverman, Thermal Emission Spectrometer Experiment - Mars-Observer Mission, *Journal of Geophysical Research*, *97* (E5), 7719-7734, 1992.

Christensen, P.R., B.M. Jakosky, H.H. Kieffer, M.C. Malin, H.Y. McSween, Jr., K.H. Nealson, G.L. Mehall, S. Silverman, S. Ferry, M. Caplinger, and M. Ravine, The Thermal Emission Imaging System (THEMIS) for the Mars 2001 Odyssey Mission, *Space Science Reviews*, *110* (1-2), 85-130, 2004*a*.

Christensen, P.R., J.L. Bandfield, R.N. Clark, K.S. Edgett, V.E. Hamilton, T. Hoefen, H.H. Kieffer, R.O. Kuzmin, M.D. Lane, M.C. Malin, R.V. Morris, J.C. Pearl, R. Pearson, T.L. Roush, S.W. Ruff, and M.D. Smith, Detection of crystalline hematite mineralization on Mars by the Thermal Emission Spectrometer: Evidence for near-surface water, *Journal of Geophysical Research*, *105* (E4), 9623-9642, 2000.

Christensen, P.R., J.L. Bandfield, J.F. Bell, III, N. Gorelick, V.E. Hamilton, A. Ivanov, B.M. Jakosky, H.H. Kieffer, M.D. Lane, M.C. Malin, T. McConnochie, A.S. McEwan, H.Y. McSween, Jr., G.L. Mehall, J.E. Moersch, K.H. Nealson, J. Rice, W., Jr., M.I. Richardson, S.W. Ruff, M.D. Smith, T.N. Titus, and M.B. Wyatt,

Morphology and Composition of the Surface of Mars: Mars Odyssey THEMIS Results, *Science*, *300* (5628), 2056-2061, 2003.

Christensen, P.R., J.L. Bandfield, V.E. Hamilton, S.W. Ruff, H.H. Kieffer, T.N. Titus, M.C. Malin, R.V. Morris, M.D. Lane, R.L. Clark, B.M. Jakosky, M.T. Mellon, J.C. Pearl, B.J. Conrath, M.D. Smith, R.T. Clancy, R.O. Kuzmin, T.L. Roush, G.L. Mehall, N. Gorelick, K. Bender, K. Murray, S. Dason, E. Greene, S. Silverman, and M. Greenfield, Mars Global Surveyor Thermal Emission Spectrometer experiment: Investigation description and surface science results, *Journal of Geophysical Research*, *106* (E10), 23823–23871, 2001.

Christensen, P.R., S.W. Ruff, R.L. Fergason, A.T. Knudson, S. Anwar, R.E. Arvidson, J.L. Bandfield, D.L. Blaney, C. Budney, W.M. Calvin, T.D. Glotch, M.P. Golombek, N. Gorelick, T.G. Graff, V.E. Hamilton, A. Hayes, J.R. Johnson, H.Y. McSween, Jr., G.L. Mehall, L. Mehall, J.E. Moersch, R.V. Morris, A.D. Rogers, M.D. Smith, S.W. Squyres, M.J. Wolff, and M.B. Wyatt, Initial Results from the Min-TES Experiment at the Spirit Landing Site in Gusev Crater, *Science*, *305* (5685), 837-841, 2004*b*.

Cutts, J.A., and K.R. Blasius, Origin of Martian outflow channels: The eolian hypothesis, *Journal of Geophysical Research*, *86*, 5075-5102, 1981.

Eugster, H.P., Geochemistry of Evaporitic Lacustrine Deposits, *Annual Reviews of Earth and Planetary Science*, *8*, 35-63, 1980.

Eugster, H.P., and L.A. Hardie, Saline lakes, in *Lakes; chemistry, geology, physics*, edited by A. Lernam, pp. 237-293, Springer-Verlag, New York, 1978.

Farmer, J.D., and D.J. Des Marais, Exploring for a record of ancient Martian life, *Journal of Geophysical Research*, *104* (E11), 26977-26995, 1999.

Feely, K.C., and P.R. Christensen, Quantitative compositional analysis using thermal emission spectroscopy: Application to igneous and metamorphic rocks, *Journal of Geophysical Research*, *104* (E10), 24195-24210, 1999.

Forsythe, R.D., and J.R. Zimbelman, A case for ancient evaporite basins on Mars, *Journal of Geophysical Research*, *100* (E3), 5553-5563, 1995.

Frey, H.V., S.E.H. Sakimoto, and J.H. Roark, MOLA topography of the crustal dichotomy boundary zone, Mars, *Abstracts with Programs - Geological Society of America*, *30* (7), 404, 1998.

Gellert, R., R. Rieder, R.C. Anderson, J. Brückner, B.C. Clark, G. Dreibus, T. Economou, G. Klingelhöfer, G.W. Lugmair, D.W. Ming, S.W. Squyres, C. d'Uston, H. Wänke, A. Yen, and J. Zipfel, Chemistry of Rocks and Soils in Gusev Crater from the Alpha Particle X-ray Spectrometer, *Science*, *305* (5685), 829-832, 2004.

Gillespie, A.R., Spectral mixture analysis of multispectral thermal infrared images, *Remote Sensing of Environment*, *42* (2), 137-145, 1992.

Gillespie, A.R., A.B. Kahle, and R.E. Walker, Color enhancement of highly correlated images. 1. Decorrelation and HSI contrast stretches, *Remote Sensing of Environment*, *20* (3), 209-235, 1986.

Golombek, M., J.A. Grant, L.S. Crumpler, R. Greeley, R.E. Arvidson, and T.A.S. Team, Climatic change from the Mars Exploration Rover Landing Sites: From wet in the Noachian to dry and desiccating since the Hesperian, in *Lunar and Planetary*

Science Conference XXXVI, pp. Abstract #1539, Lunar and Planetary Institute, Houston, TX, 2005.

Golombek, M., J.A. Grant, T. Parker, T. Scholfied, D. Kass, P. Knocke, R. Roncoli, N. Bridges, F.S. Anderson, J. Crisp, A. Haldemann, M. Adler, W. Lee, S.W. Squyres, R.E. Arvidson, M.H. Carr, and C. Weitz, Downselecting of Landing Sites for the Mars Exploration Rovers, in *Lunar and Planetary Science Conference XXXIII*, pp. Abstract #1245, Lunar and Planetary Science Conference, Houston, TX, 2002.

Greeley, R., and J.E. Guest, Geologic map of the eastern equatorial region, Mars, in *U.S. Geological Survey Miscellaneous Investigations Series Map*, pp. I-1802-B, U.S. Geologic Survey, 1987.

Green, A.A., M. Berman, P. Switzer, and M.D. Craig, A transformation for ordering multispectral data in terms of image quality with implications for noise removal, *IEEE Transactions on Geosciences and Remote Sensing*, *26* (1), 65-74, 1988.

Haberle, R.M., C.P. McKay, J. Schaeffer, N.A. Cabrol, E.A. Grin, A.P. Zent, and R. Quinn, On the possibility of liquid water on present-day Mars, *Journal of Geophysical Research*, *106* (E10), 23317-23326, 2001.

Hamilton, V.E., M.B. Wyatt, H.Y. McSween, Jr., and P.R. Christensen, Analysis of terrestrial and Martian volcanic compositions using thermal emission spectroscopy, *Journal of Geophysical Research*, *106*, 14733-14746, 2001.

Huang, C.K., and P.F. Kerr, Infrared study of the carbonate minerals, *American Mineralogist*, *45* (3-4), 311-324, 1960.

Jones, B.F., The hydrology and mineralogy of Deep Springs Lake, Inyo County, California, pp. 56, USGS Professional Paper 502-A, in *USGS Professional Paper 502-A*, pp. A1-A56, U. S. Geological Survey, Reston, VA, United States, 1965.

Keller, W.D., J.H. Spotts, and D.L. Biggs, Infrared spectra of some rock forming minerals, *American Journal of Sciences*, *250* (6), 453-471, 1952.

Klingelhöfer, G., D.S. Rodionov, R.V. Morris, C. Schröder, P.A. de Souza, Jr., D.W. Ming, A.S. Yen, B. Bernhardt, F. Renz, I. Fleischer, T. Wdowiak, S.W. Squyres, and T.A. Team, MIMOS II on MER - One year of Mössbauer spectroscopy on the surface of Mars: from Jarosite at Meridiani Planum to Geothite at Gusev Crater, in *Lunar and Planetary Science Conference XXXVI*, pp. Abstract #2349, Lunar and Planetary Science Conference, Houston, TX, 2005.

Kraft, M.D., J.R. Michalski, and T.G. Sharp, Effects of pure silica coatings on thermal emission spectra of basaltic rocks: Considerations for Martian surface mineralogy, *Geophysical Research Letters*, *30* (24), 2288, doi: 10.1029/ 2003GL018848., 2003.

Lane, M.D., Evidence for aqueously precipitated sulfates in Northeast Meridiani using THMEIS and TES data, in *Lunar and Planetary Science Conference XXXVI*, pp. Abstract #2180, Lunar and Planetary Institute, Houston, TX, 2005.

Lane, M.D., and P.R. Christensen, Thermal infrared emission spectroscopy of anhydrous carbonates, *Journal of Geophysical Research*, *102* (E11), 25581-25592, 1997.

Lane, M.D., and P.R. Christensen, Salt Minerals Predicted for Mars and Their Thermal Infrared Emission Spectra, in *Lunar and Planetary Science XXIX*, pp. Abstract #1102, Lunar and Planetary Institute, Houston, TX (CD-ROM), 1998.

Lee, P., and C.P. McKay, Mars: Always Cold, Sometimes Wet?, in *Lunar and Planetary Science XXXIV*, pp. Abstract #2127, Lunar and Planetary Institute, Houston, TX (CD-ROM), 2003.

Lee, P., M. Boucher, C. Desportes, B.J. Glass, D. Lim, C.P. McKay, G.R. Osinski, J. Parnell, and J.W. Schutt, Mars, Always Cold, Sometimes Wet: New constraints on Mars denudation rates and climate evolution from analogs studies at Haughton Crater, Devon, Island, High Arctic, in *Lunar and Planetary Science Conference*, pp. Abstract #2270, Lunar and Planetary Science Institute, Houston, TX, 2005.

Lucchitta, B.K., Ice sculpture in the Martian outflow channels, *Journal of Geophysical Research*, *87*, 9951-9973, 1982.

Lucchitta, B.K., D.M. Anderson, and H. Shoji, Did ice streams carve Martian outflow channels?, *Nature*, *290*, 759-763, 1981.

Lyon, R.J.P., Analysis of rocks by spectral infrared emission (8-25 μm), *Economic Geology*, *60* (4), 715-736, 1965.

Lyon, R.J.P., and K. Lee, Remote sensing in exploration for mineral deposits, *Economic Geology*, *65* (7), 785-800, 1970.

Malin, M.C., and K.S. Edgett, Sedimentary rocks of early Mars, *Science*, *290* (5498), 1927-1937, 2000.

Martínez-Alonso, S., B.M. Jakosky, M.T. Mellon, and N.E. Putzig, A volcanic interpretation of Gusev Crater surface materials from thermophysical, spectral, and morphological evidence, *Journal of Geophysical Research*, *110*, doi:10.1029/2004JE002327, 2005.

Masursky, H., An overview of geological results from Mariner 9, *Journal of Geophysical Research*, *78*, 4009-4049, 1973.

McCauley, J.F., White Rock: A Martian enigma, *NASA Special Publication*, *329*, 170-171, 1974.

McCauley, J.F., Geologic map of the Coprates quadrangle on Mars, in *U. S. Geologic Survey Miscellaneous Investigations Series*, U. S. Geologic Survey, 1978.

McSween, H.Y., Jr., R.E. Arvidson, J.F. Bell, III, D.L. Blaney, N.A. Cabrol, P.R. Christensen, B.C. Clark, J. Crisp, L.S. Crumpler, D.J. Des Marais, J.D. Farmer, R. Gellert, A. Ghosh, S. Gorevan, T.G. Graff, J.A. Grant, L.A. Haskin, K.E. Herkenhoff, J.R. Johnson, B.L. Jolliff, G. Klingelhöffer, A.T. Knudson, S. McLennan, K.A. Milam, J.E. Moersch, R.V. Morris, R. Rieder, S.W. Ruff, P.A. de Souza, Jr., S.W. Squyres, H. Wänke, A. Wang, M.B. Wyatt, A. Yen, and J. Zipfel, Basaltic Rocks Analyzed by the Spirit Rover in Gusev Crater, *Science*, *305* (5685), 842-845, 2004.

Milam, K.A., K.R. Stockstill, J.E. Moersch, H.Y. McSween, Jr., L.L. Tornabene, A. Ghosh, M.B. Wyatt, and P.R. Christensen, THEMIS Characterization of the MER Gusev Crater Landing Site, *Journal of Geophysical Research*, *108* (E12), 19-1-19-24, 2003.

Milton, D.J., Water and processes of degradation on Martian landscape, *Journal of Geophysical Research*, *78* (29), 4037-4047, 1973.

Morris, R.V., D.W. Ming, B.C. Clark, G. Klingelhöfer, R. Gellert, D.S. Rodionov, C. Schröder, P.A. de Souza, Jr., A. Yen, and T.A. Team, Abundance and speciation of water and sulfate at Gusev Crater and Meridiani Planum, in *Lunar and*

Planetary Science Conference XXXVI, pp. Abstract #2239, Lunar and Planetary Science Institute, Houston, TX, 2005.

Morris, R.V., G. Klingelhöfer, B. Bernhardt, C. Schröder, D.S. Rodionov, P.A. de Souza, Jr., A. Yen, R. Gellert, E.N. Evlanov, J. Foh, E. Kankeleit, P. Gütlich, D.W. Ming, F. Renz, T. Wdowiak, S.W. Squyres, and R.E. Arvidson, Mineralogy at Gusev Crater from the Mössbauer Spectrometer on the Spirit Rover, *Science*, *305* (5685), 833-836, 2004.

Nummedal, D., and D. Prior, Generations of Martian chaos and channels by debris flows, *Icarus*, *45*, 77-86, 1981.

Pelkey, S.M., and B.M. Jakosky, Surficial geologic surveys of Gale Crater and Melas Chasma, Mars: Integration of remote-sensing data, *Icarus*, *160* (2), 228-257, 2002.

Pelkey, S.M., B.M. Jakosky, and P.R. Christensen, Surficial properties in Gale Crater, Mars, from Mars Odyssey THEMIS data, *Icarus*, *167*, 244-270, 2004.

Piatek, J.L., K.R. Stockstill, and J.E. Moersch, A strategy for atmospheric correction of THEMIS IR data, in *Division for Planetary Sciences of the American Astronomical Society*, Division for Planetary Sciences of the American Astronomical Society, Louisville, Kentucky, 2004.

Pollack, J.B., J.F. Kasting, S.M. Richardson, and K. Poliakoff, The case for a wet, warm climate on Mars, *Icarus*, *71* (2), 203-224, 1987.

Ramsey, M.S., and P.R. Christensen, Mineral abundance determination: Quantitative deconvolution of thermal emission spectra, *Journal of Geophysical Research*, *103* (B1), 577-596, 1998.

Rice, J., W., Jr., P. Lee, J.W. Schutt, and A.P. Zent, Periglacial geomorphic investigations; Devon Island, Northwest Territories, Canada, in *AGU 1997 Fall Meeting*, pp. 274, American Geophysical Union, San Francisco, CA, 1997.

Ruff, S.W., Spectral evidence for zeolites in the dust on Mars, *Icarus*, *168*, 131-143, 2004.

Ruff, S.W., and P.R. Christensen, Bright and dark regions on Mars: Particle size and mineralogical characteristics based on Thermal Emission Spectrometer data, *Journal of Geophysical Research*, *107* (E12), 5127-5148, 2002.

Ruff, S.W., P.R. Christensen, R.N. Clark, H.H. Kieffer, M.C. Malin, J.L. Bandfield, B.M. Jakosky, M.D. Lane, M.T. Mellon, and M.A. Presley, Mars' "White Rock" feature lacks evidence of an aqueous origin: Result from Mars Global Surveyor, *Journal of Geophysical Research*, *106* (E10), 23921-23927, 2001.

Sagan, C., O.B. Toon, and P.J. Gierasch, Climatic change on Mars, *Science*, *181* (4104), 1045-1049, 1973.

Salisbury, J.W., A. Wald, and D.D. Aria, Thermal-infrared remote sensing and Kirchhoff's law; 1, Laboratory measurements, *Journal of Geophysical Research*, *99* (6), 11897-11911, 1994.

Schneeberger, D.M., Episodic channel activity at Ma'adim Vallis, Mars, in *Lunar and Planetary Science XX*, pp. 964-965, Lunar and Planetary Institute, Houston, TX, 1989.

Schröder, C., G. Klingelhöfer, R.V. Morris, D.S. Rodionov, P.A. de Souza, Jr., D.W. Ming, A.S. Yen, R. Gellert, J.F. Bell, III, and T.A. Team, Weathering of basaltic

rocks from the Gusev Plains up into the Columbia Hills from the perspective of the MER Mössbauer Spectrometer, in *Lunar and Planetary Science Concerence XXXVI*, pp. Abstract #2309, Lunar and Planetary Institute, Houston, TX, 2005.

Scott, D.H., and M.G. Chapman, Geologic and topographic maps of the Elysium Paleolake basin, Mars, in *Miscellaneous Investigations Series*, pp. 1:500,000-scale, U.S. Geological Survey, 1995.

Sharp, R.P., and M.C. Malin, Channels on Mars, *Geological Society of America Bulletin*, *86*, 593-609, 1975.

Smith, M.D., J.L. Bandfield, and P.R. Christensen, Separation of atmospheric and surface spectral features in Mars Global Surveyor Thermal Emission Spectrometer (TES) spectra, *Journal of Geophysical Research*, *105* (E4), 9589-9607, 2000*a*.

Smith, M.D., J.C. Pearl, B.J. Conrath, and P.R. Christensen, Mars Global Surveyor Thermal Emission Spectrometer (TES) observations of dust opacity during aerobraking and science phasing, *Journal of Geophysical Research*, *105* (E4), 9539-9552, 2000*b*.

Squyres, S.W., J.P. Grotzinger, R.E. Arvidson, J.F. Bell, III, W.M. Calvin, P.R. Christensen, B.C. Clark, J.A. Crisp, W.H. Farrand, K.E. Herkenhoff, J.R. Johnson, G. Klingelhöfer, A.H. Knoll, S.M. McLennan, H.Y. McSween, Jr., R.V. Morris, J. Rice, W., Jr., R. Rieder, and L.A. Soderblom, In Situ Evidence for an Ancient Aqueous Environment at Meridiani Planum, Mars, *Science*, *306* (5702), 1709-1714, 2004*a*.

Squyres, S.W., R.E. Arvidson, J.F. Bell, III, J. Brückner, N.A. Cabrol, W.M. Calvin, M.H. Carr, P.R. Christensen, B.C. Clark, L. Crumpler, D.J. Des Marais, C. d'Uston, T. Economou, J.D. Farmer, W. Farrand, W. Folkner, M. Golombek, S. Gorevan, J.A. Grant, R. Greeley, J. Grotzinger, L. Haskin, K.E. Herkenhoff, S. Hviid, J.R. Johnson, G. Klingelhöffer, A. Knoll, G. Landis, M. Lemmon, R. Li, M.B. Madsen, M.C. Malin, S. McLennan, H.Y. McSween, Jr., D.W. Ming, J.E. Moersch, R.V. Morris, T. Parker, J. Rice, W., Jr., L. Richter, R. Rieder, M. Sims, M.D. Smith, P. Smith, L.A. Soderblom, R. Sullivan, A. Wald, H. Wänke, T. Wdowiak, M.J. Wolff, and A. Yen, The Spirit Rover's Athena Science Investigation at Gusev crater, Mars,, *Science*, *305* (5685), 794-799, 2004*b*.

Stockstill, K.R., J.E. Moersch, S.W. Ruff, A.M. Baldridge, and J.D. Farmer, TES Hyperspectral Analyses of Proposed Paleolake Basins on Mars: No Evidence for In-Place Carbonates, *Journal of Geophysical Research*, *in press*.

Thomson, J.L., and J.W. Salisbury, The mid-infrared reflectance of mineral mixtures (7–14 μm), *Remote Sensing of Environment*, *45* (1), 1-13, 1993.

Wang, A., L.A. Haskin, S.W. Squyres, R.E. Arvidson, L. Crumpler, R. Gellert, J. Hurowitz, C. Schröder, N. Tosca, K.E. Herkenhoff, B.L. Jolliff, and T.A. Team, Sulfate deposition in regolith exposed in trenches on the plains between the Spirit landing site and Columbia Hills in Gusev Crater, Mars, in *Lunar and Planetary Science Conference XXXVI*, pp. Abstract #2236, Lunar and Planetary Science Institute, Houston, TX, 2005.

Ward, A.W., Yardangs on Mars: Evidence of Recent Wind Erosion, *Journal of Geophysical Research*, *84* (B14), 8147-8166, 1979.

Williams, S.H., and J.R. Zimbelman, "White Rock": An eroded Martian lacustrine deposit(?), *Geology*, *22* (2), 107-110, 1994.

Wyatt, M.B., and H.Y. McSween, Jr., Spectral evidence for weathered basalt as an alternative to andesite in the northern lowlands of Mars, *Nature*, *417* (6886), 263-266, 2002.

Yung, Y.L., and J.P. Pinto, Primitive atmosphere and implications for the formation of channels on Mars, *Nature*, *288*, 735-738, 1978.

Zimbleman, J.R., and H.H. Kieffer, Thermal Mapping of the Northern Equatorial and Temperate Latitudes of Mars, *Journal of Geophysical Research*, 84 (B14), 8239-8251, 1979.

Appendix

Table 1: Geographic information and THEMIS scene numbers for basins presented in this paper.

C & G (1999)[1] list number	Crater name[2]	Crater center		Rim diam. (km)	Depth (km)	THEMIS scene(s) number used	Eigenvalues for the three most significant MNF bands		
		Lat (˚S)	Lon (˚E)						
135	**Gusev**	14.5	175.5	160	2.0	I01605002	14.035	7.781	6.323
						I01243001	19.690	7.270	7.015
						I00881002	34.848	10.648	9.557
						I00856001	23.330	11.367	10.677
85	**Gale**	5.4	137.8	142	2.2	I01131009	69.167	20.485	8.611
						I01469001	75.047	36.240	7.423
						I01855008	110.823	34.075	9.113
						I01494001	95.665	43.138	10.169
133	**C133**	13.3	176.6	30	0.7	I00856001	9.478	5.112	4.619
142	**C142**	15.9	175.8	30	0.7	I01580002	5.714	3.908	2.999
144	**C144**	16.0	175.8	24	0.7				
147	**C147**	17.7	177.6	32	0.7	I01530002	5.479	4.648	4.111

[1]C & G (1999)* referes to the Cabrol and Grin (1999) paper.

[2]Official name or, for unnamed craters, name used in this paper.

Table 2: Results from deconvolution of TES emissivity data for Gusev Crater. Deconvolution of TES data (where available) used only the TES end members. Percentages in bold indicate end members used in significant amounts (>10-15%, see text).

	Gusev crater floor 1	Gusev crater floor 2	Gusev crater floor 3	South low albedo feature	Very low T_b mat (S of S LA feat)	Int T_b mat (N of S LA feat)	North low albedo feature 1	North low albedo feature 2
Acidalia-type	0.0	0.0	**13.8**	9.2	-	4.0	**25.1**	0.0
Syrtis-type	0.0	0.0	0.0	5.8	-	8.8	0.0	0.0
Hematite	0.0	0.0	0.0	0.0	-	0.0	0.0	0.0
Dust Low-CO_2	**96.9**	**62.4**	**27.3**	**82.2**	NO	**84.1**	**18.3**	**63.4**
Dust High-CO_2	0.0	4.6	**20.1**	0.0	TES	0.0	**29.1**	0.0
H_2O Ice $Cloud_1$	2.8	0.0	0.0	0.0	coverage	0.0	0.0	0.0
H_2O Ice $Cloud_2$	0.0	2.9	3.0	2.6	-	2.6	6.4	1.6
Surface dust	0.0	**30.3**	**36.7**	0.0	-	0.0	**22.2**	**35.3**
Blackbody	-	-	-	-	-	-	-	-
Sum	99.8	100.3	101.0	99.7	-	99.5	101.1	100.2
Spectral RMS	0.01027	0.00294	0.00292	0.00449	-	0.00429	0.00325	0.00470
DCI value	0.943	0.937	0.935	0.943	-	0.946	0.941	0.943
Interpretation	inter-mediate	dust covered	dust covered	inter-mediate	-	inter-mediate	inter-mediate	inter-mediate
B1/2 relative ϵ	1.00	1.00	1.00	1.03	0.99	1.03	1.03	1.03

Table 2 (con't):

	Low T_b materials			N external terrain	S external terrain
	South of N LA feat	**North**	**South**		
Acidalia-type	0.0	0.0	0.0	**23.2**	0.1
Syrtis-type	**25.6**	0.2	0.0	0.0	3.3
Hematite	0.0	0.0	0.0	0.4	3.7
Dust Low-CO_2	**67.0**	**39.9**	**43.5**	**42.3**	**42.8**
Dust High-CO_2	0.0	**11.3**	9.3	7.8	**10.1**
H_2O Ice Cloud$_1$	0.0	0.0	0.0	0.0	5.2
H_2O Ice Cloud$_2$	6.7	4.9	6.6	7.6	3.1
Surface dust	0.0	**44.6**	**41.4**	**19.6**	**32.2**
Blackbody	-	-	-	-	-
Sum	99.3	100.9	100.8	100.9	100.6
Spectral RMS	0.00396	0.00272	0.00272	0.00336	0.00411
DCI value	0.958	0.940	0.942	0.935	0.939
Interpretation	intermediate	dust covered	intermediate	dust covered	dust covered
B1/2 relative ϵ	0.99	1.00	1.00	0.99	0.99

Table 3: Results from deconvolution of TES emissivity data for Gale Crater. Deconvolution of TES data (where available) used only the TES end members. Percentages in bold indicate end members used in significant amounts (>10-15%, see text).

	Crater floor (SSW of md)	Crater floor (Low T_b)	South crater floor	Western mound	Mound layers	Central mound	Eastern mound	Crater floor (SSW of md)
Acidalia-type	0.0	**13.6**	**26.1**	7.7	**11.5**	**15.0**	-	0.0
Syrtis-type	**33.6**	**41.3**	**31.1**	0.0	5.3	**12.2**	-	**33.6**
Hematite	0.4	0.0	0.0	0.0	0.0	1.7	-	0.4
Dust Low-CO_2	**63.0**	**31.2**	**28.0**	**30.6**	**73.3**	**28.8**	NO	**63.0**
Dust High-CO_2	0.0	7.9	**11.7**	**21.7**	4.0	**28.7**	TES	0.0
H_2O Ice $Cloud_1$	1.8	0.5	0.0	8.4	2.0	1.6	coverage	1.8
H_2O Ice $Cloud_2$	0.0	5.3	2.7	8.0	3.6	7.5	-	0.0
Surface dust	0.0	0.0	0.0	**25.1**	0.0	5.2	-	0.0
Blackbody	-	-	-	-	-	-	-	-
Sum	98.8	99.8	99.7	101.6	101.4	100.6	-	98.8
Spectral RMS	0.00462	0.00299	0.00330	0.00317	0.00470	0.00297	-	0.00462
DCI value	0.963	0.967	0.966	0.929	0.944	0.954	-	0.963
Interpretation	dust free	dust free	dust free	dust covered	inter-mediate	inter-mediate	-	dust free
B1/2 relative ϵ	1.03	1.05	1.02	1.03	1.01	0.99	0.98	1.03

Table 3 (con't):

	High T_b material (W of mound)	**High T_b material** (S of md)	**North ext terr**	**South ext terr**
Acidalia-type	**13.6**	**24.2**	**18.0**	**10.1**
Syrtis-type	**11.3**	**35.5**	0.0	**37.0**
Hematite	0.0	0.0	0.0	0.0
Dust Low-CO_2	**68.7**	**26.5**	**24.5**	**44.7**
Dust High-CO_2	0.0	**10.8**	**19.2**	3.8
H_2O Ice Cloud$_1$	0.0	0.0	0.0	0.0
H_2O Ice Cloud$_2$	5.9	2.6	**12.9**	3.8
Surface dust	0.0	0.0	**27.3**	0.0
Blackbody	-	-	-	-
Sum	99.5	99.6	101.8	99.4
Spectral RMS	0.00323	0.00366	0.00338	0.00161
DCI value	0.960	0.967	0.934	0.968
Interpretation	intermediate	dust free	dust covered	dust free
B1/2 relative ϵ	1.05	1.03	0.94	1.02

Table 4: Results from deconvolution of TES emissivity data for small craters in the Aeolis quadrangle. Deconvolution of TES data (where available) used only the TES end members. Percentages in bold indicate end members used in significant amounts (>10-15%, see text).

	C133 channel to NW	C133 SW crater rim	C133 low Tb unit	C133 SE crater floor	C133 N ext terr	C142 floor	C144 floor	C142 floor (TES)
Acidalia-type	0.0	0.0	0.0	-	-	-	**20.5**	**25.7**
Syrtis-type	1.3	0.0	2.5	-	-	-	0.0	0.0
Hematite	0.0	0.0	0.0	-	-	-	0.0	0.0
Dust Low-CO_2	**54.5**	**59.0**	**59.5**	NO	NO	NO	**16.2**	**15.1**
Dust High-CO_2	7.4	0.0	7.5	TES	TES	TES	**35.0**	**35.7**
H_2O Ice Cloud$_1$	0.0	0.0	0.0	coverage	coverage	coverage	0.0	0.0
H_2O Ice Cloud$_2$	1.8	0.0	2.0	-	-	-	3.7	5.8
Surface dust	**35.5**	**41.9**	**29.1**	-	-	-	**25.4**	**18.7**
Blackbody	-	-	-	-	-	-	-	-
Sum	100.6	100.9	100.6	-	-	-	100.8	101.1
Spectral RMS	0.00335	0.00551	0.00366	-	-	-	0.00261	0.00343
DCI value	0.928	0.933	0.934	-	-	-	0.939	0.937
Interpretation	dust covered	dust covered	dust covered	-	-	-	dust covered	dust covered
B1/2 relative ϵ	1.00	1.00	0.99	1.01	1.00	1.00	1.00	1.00

Table 4 (con't):

	C142&144			C147 crater floor dep	C147 W rim dep	C147 N rim dep	C147 crater floor
	S ext terr1	**S ext terr2**	**N ext terr**				
Acidalia-type	**18.4**	**22.6**	**23.0**	0.0	0.0	-	0.0
Syrtis-type	0.0	0.0	0.0	0.0	0.0	-	0.0
Hematite	0.0	0.0	2.9	0.0	0.0	-	0.0
Dust Low-CO_2	6.1	6.8	**12.0**	**67.3**	**84.3**	NO	**72.3**
Dust High-CO_2	**37.1**	**34.0**	**37.7**	0.0	0.0	TES	0.0
H_2O Ice Cloud$_1$	2.0	0.0	0.0	0.0	0.0	coverage	0.0
H_2O Ice Cloud$_2$	0.0	4.0	4.8	0.0	2.1	-	0.0
Surface dust	**37.5**	**33.7**	**21.0**	**33.0**	**13.6**	-	**27.8**
Blackbody	-	-	-	-	-	-	-
Sum	101.0	101.1	101.4	100.3	99.9	-	100.1
Spectral RMS	0.00307	0.00304	0.00483	0.00771	0.00495	-	0.00370
DCI value	0.940	0.936	0.950	0.943	0.949	-	0.949
Interpretation	dust covered	dust covered	intermediate	intermediate	intermediate	-	intermediate
B1/2 relative ϵ	0.99	0.99	1.01	1.02	1.00	0.98	1.00

Table 5: Results from deconvolution of TES emissivity data for the LA feature ROI in Gusev Crater, using TES spectral end members and two sulfates. Numbers in bold indicate end members used in significant amounts (>10-15%, see text).

	S low albedo feature		**Int T_b mat** (N of S LA feat)		**N low albedo feature 1**		**N low albedo feature 2**	
	8 TES only	**8 TES + 2 sulf**	**8 TES only**	**8 TES + 2 sulf**	**8 TES only**	**8 TES + 2 sulf**	**8 TES only**	**8 TES + 2 sulf**
Acidalia-type	9.2	0.0	4.0	0.0	**25.1**	**20.5**	0.0	0.0
Syrtis-type	5.8	**12.1**	8.8	**11.4**	0.0	0.0	0.0	0.0
Hematite	0.0	0.0	0.0	0.0	0.0	0.0	0.0	0.0
Dust Low-CO_2	**82.2**	**80.6**	**84.1**	**80.8**	**18.3**	**13.7**	**63.4**	**61.9**
Dust High-CO_2	0.0	0.0	0.0	0.0	**29.1**	**29.2**	0.0	0.0
H_2O Ice $Cloud_1$	0.0	0.0	0.0	0.0	0.0	0.0	0.0	0.0
H_2O Ice $Cloud_2$	2.6	3.4	2.6	3.6	6.4	5.5	1.6	1.4
Surface dust	0.0	0.0	0.0	0.0	**22.2**	**30.3**	**35.3**	**36.5**
Bloedite	-	3.3	-	3.4	-	2.0	-	0.0
Glauberite	-	0.4	-	0.4	-	0.0	-	0.3
Blackbody	-	-	-	-	-	-	-	-
Sum	99.7	99.9	99.5	99.7	101.1	101.2	100.2	100.2
Spectral RMS	0.00449	0.00386	0.00429	0.00359	0.00325	0.00309	0.00470	0.00470
DCI value	0.943		0.946		0.941		0.943	
Interpretation	intermediate		intermediate		intermediate		intermediate	

Figure 1: MOLA-derived shaded relief map of the Aeolis Quadrangle of Mars. The 35 craters from the *Cabrol and Grin* [1999] list of putative paleolake basins are outlined by colored squares, which are proportional to the size. The red squares enclose craters studied in this paper. The green squares enclose craters that display insufficient spectral variation or contained surfaces that were too cold to afford useful signal-to-noise ratios. The blue squares enclose craters that had no THEMIS data coverage prior to 1600 LST or craters that had THEMIS stamps with insufficient overlap to merit additional processing.

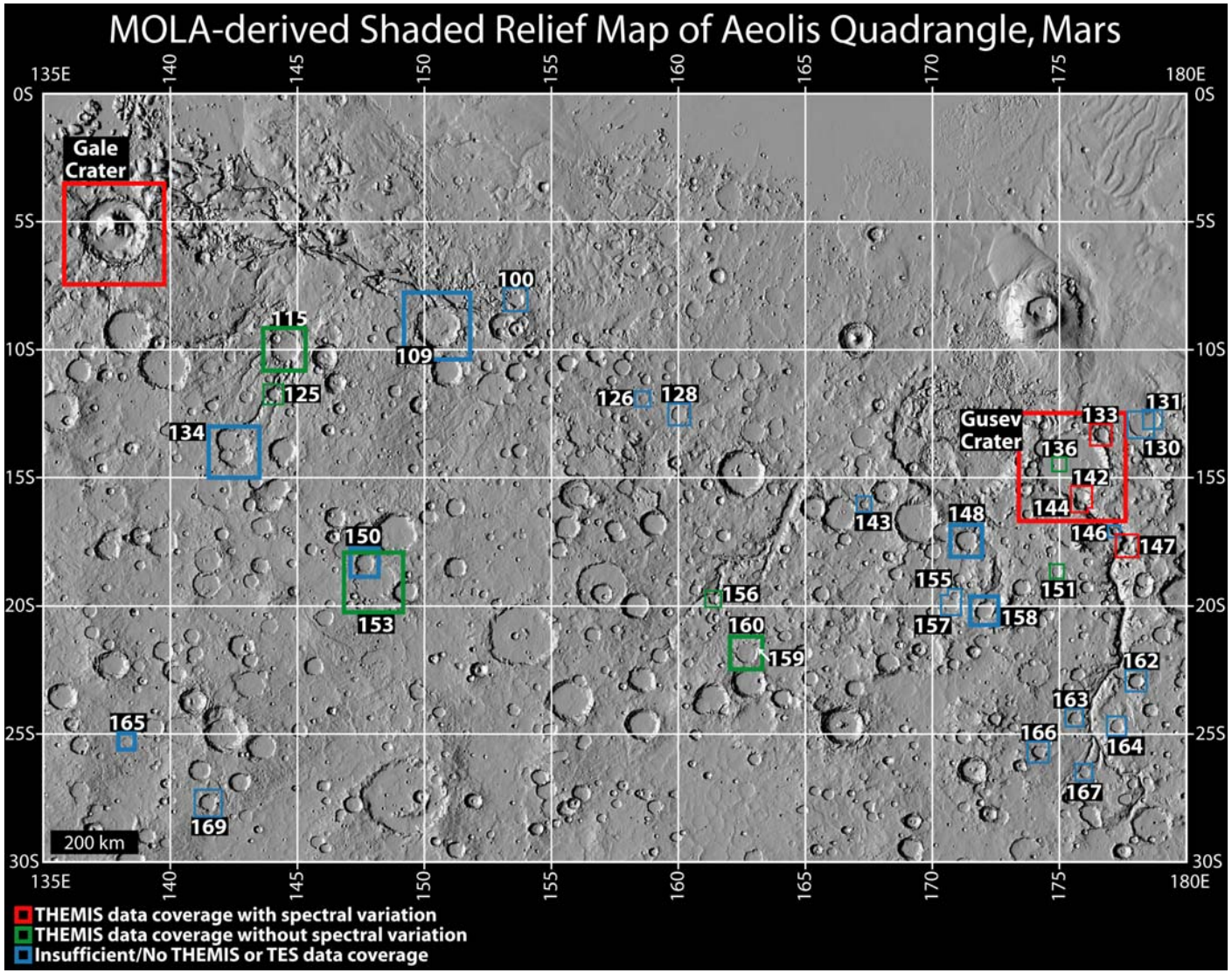
MOLA-derived Shaded Relief Map of Aeolis Quadrangle, Mars
135E
140
145
150
155
160
165
170
175
180E
0S
5S
10S
15S
20S
25S
30S
Gale Crater
Gusev Crater
100
109
115
125
126
128
131
133
130
136
142
144
134
143
148
146
147
150
155
151
156
153
157
158
160
159
162
163
165
166
164
167
169
200 km
THEMIS data coverage with spectral variation
THEMIS data coverage without spectral variation
Insufficient/No THEMIS or TES data coverage

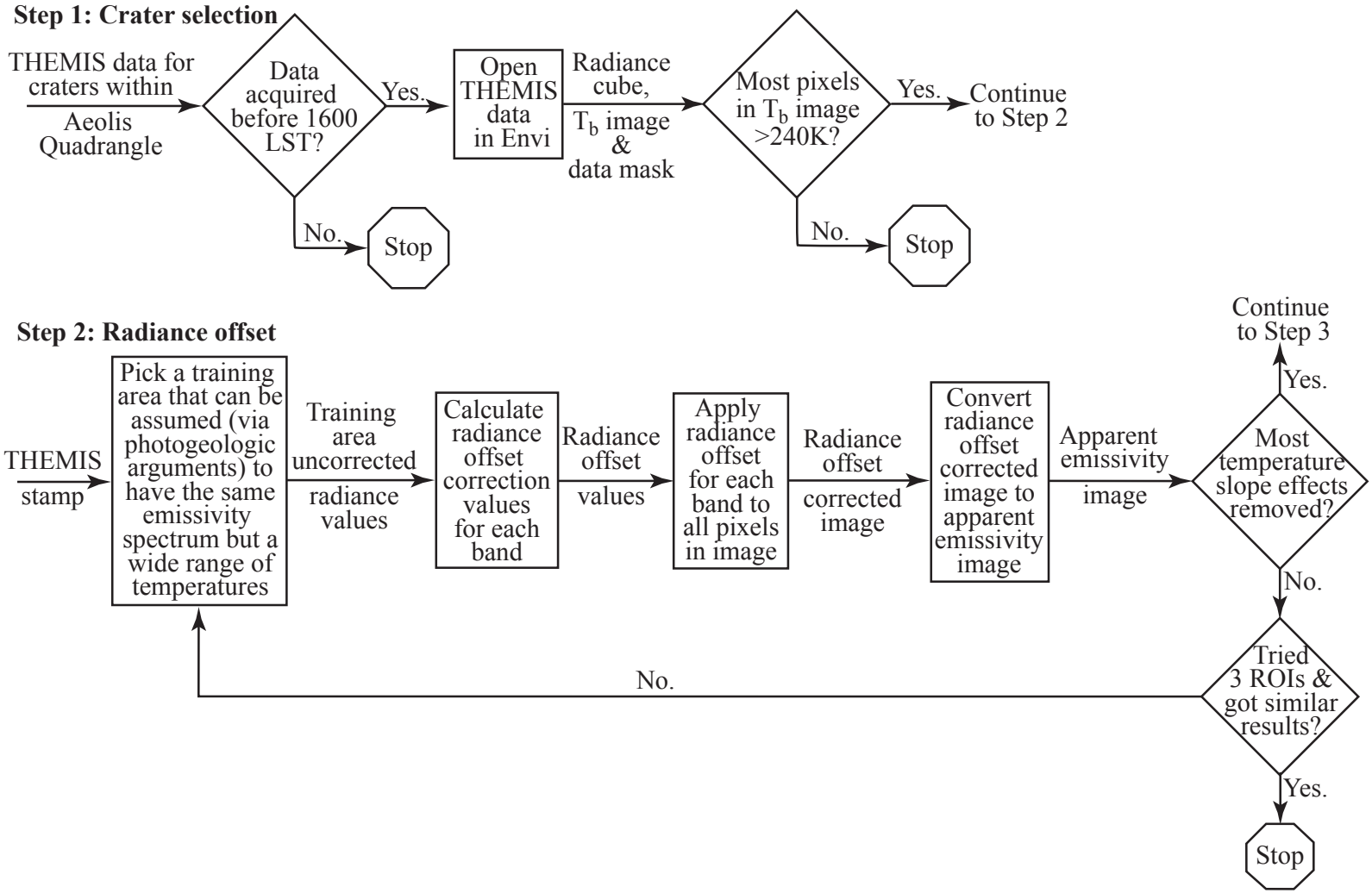

Figure 2: Flowchart of THEMIS processing steps. Step 1: Diagram of the THEMIS data selection and filtering done to preclude data with cold, low signal-to-noise ratio pixels. Step 2: Diagram of the radiance offset applied to THEMIS data.

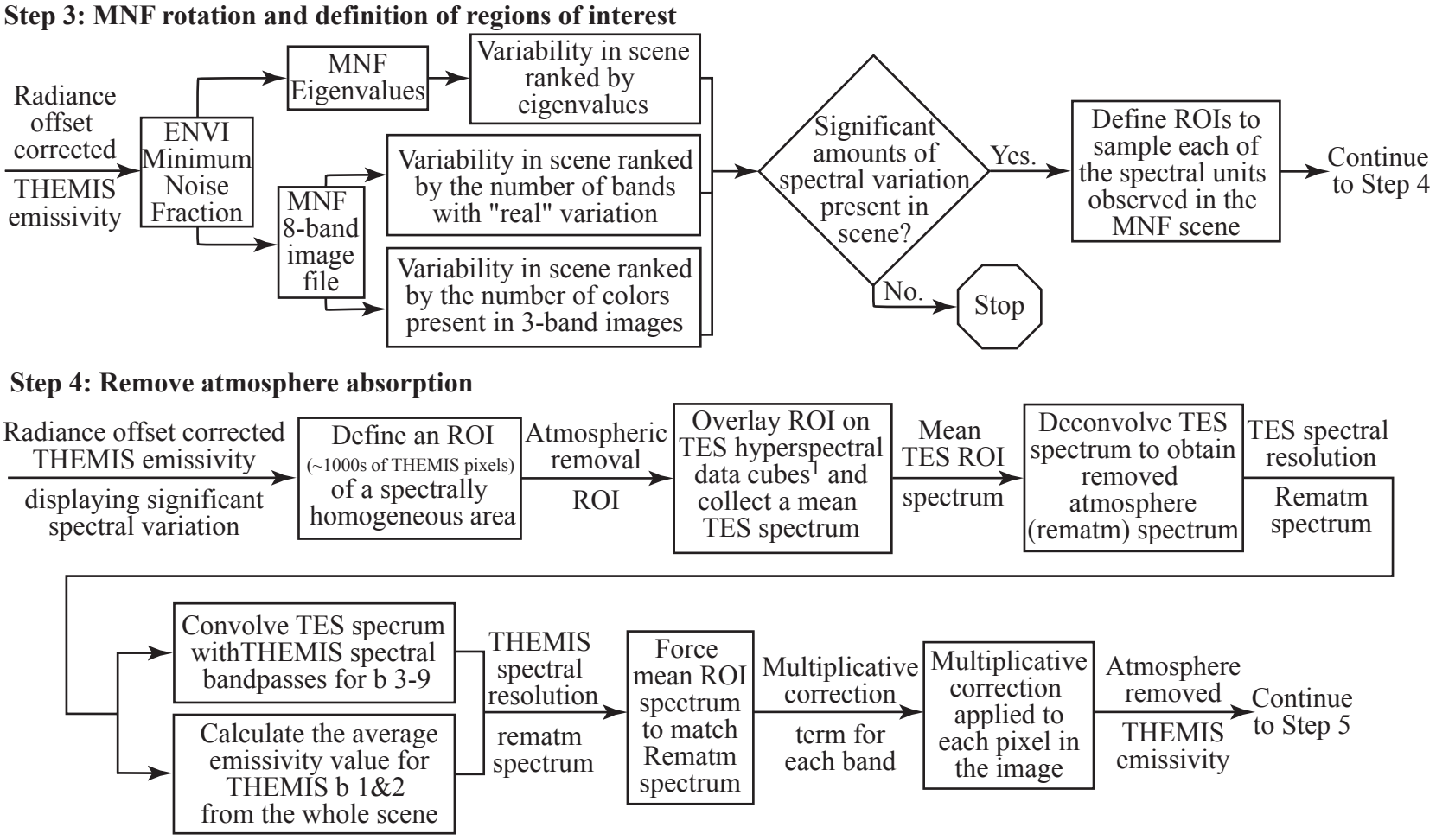

Figure 2 (con't): Step 3: Diagram showing how data are analyzed to ascertain if they contain enough spectral variation present and definition of ROIs. Step 4: Diagram of the atmospheric removal technique used in this study.

Step 5: Collect mean THEMIS spectra for regions of interest and evaluate the THEMIS spectra

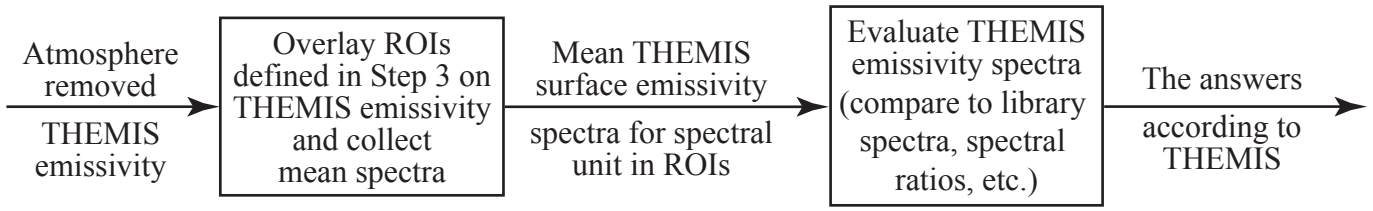

Step 6: For ROIs of sufficient size, collect mean TES spectra for regions of interest and evaluate the TES spectra

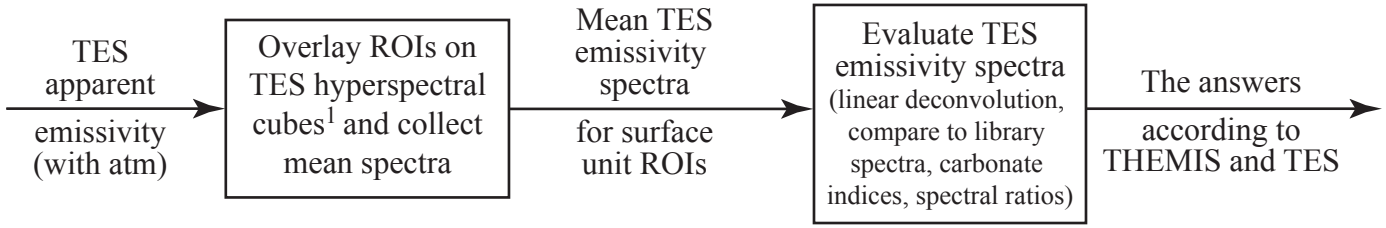

Figure 2 (con't): Step 5: Diagram of spectral analysis of THEMIS surface spectra for ROIs defined in Step 3. Step 6: Diagram of the spectral analysis of TES surface spectra for the same ROIs

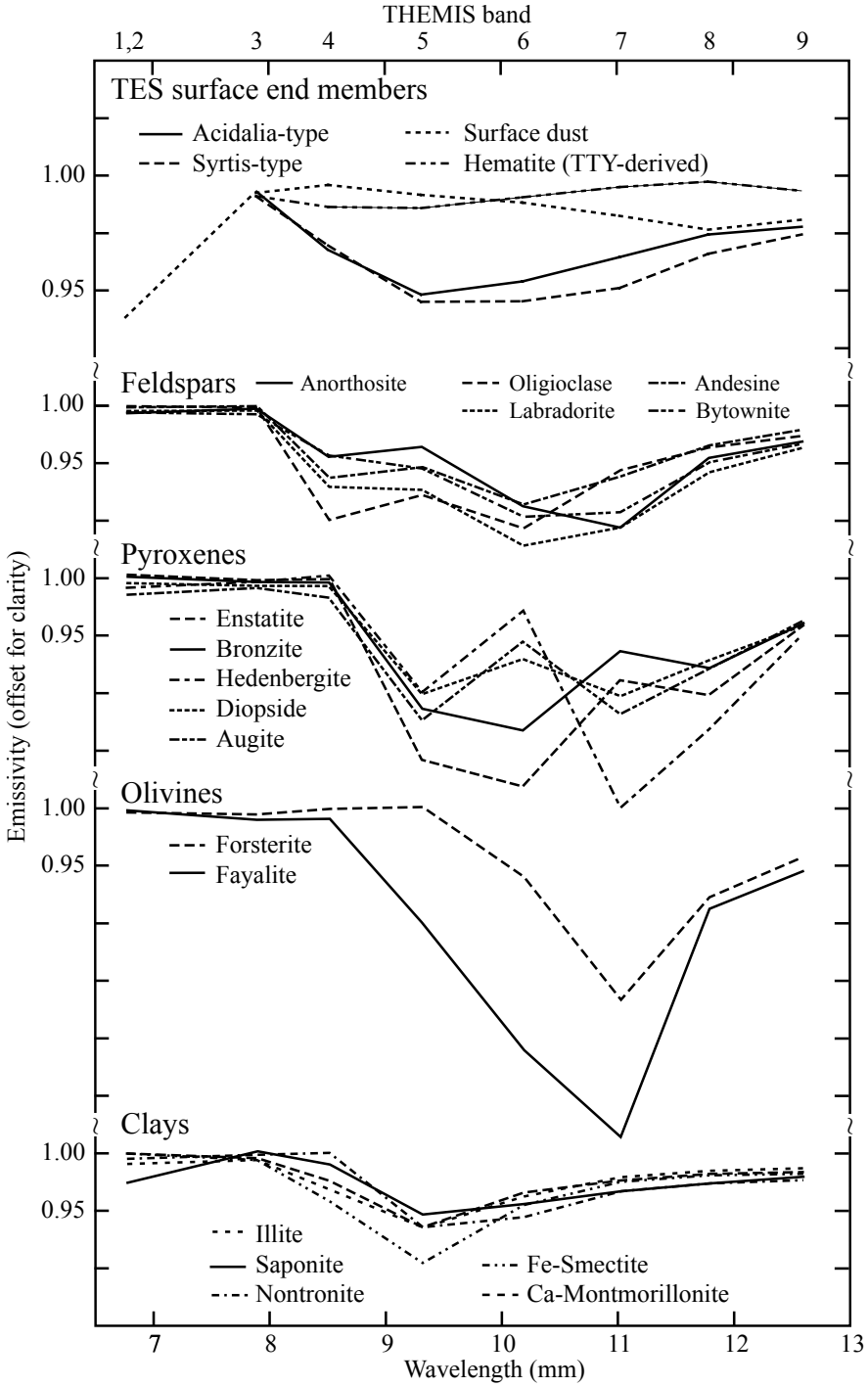

Figure 3: THEMIS resolution emissivity spectra for TES surface end members, various rock-forming igneous minerals, weathering products and evaporite minerals. (a) TES surface end members and various rock-forming igneous minerals and associated weathering products. Note that the TES surface end members do not have emissivity values for bands 1 and 2, as discussed in the text. *Bandfield et al.* [2003] derived the emissivity spectrum for surface dust using multiple emission angle TES data, resulting in a TES emissivity spectrum that extended to ~6.0 μm.

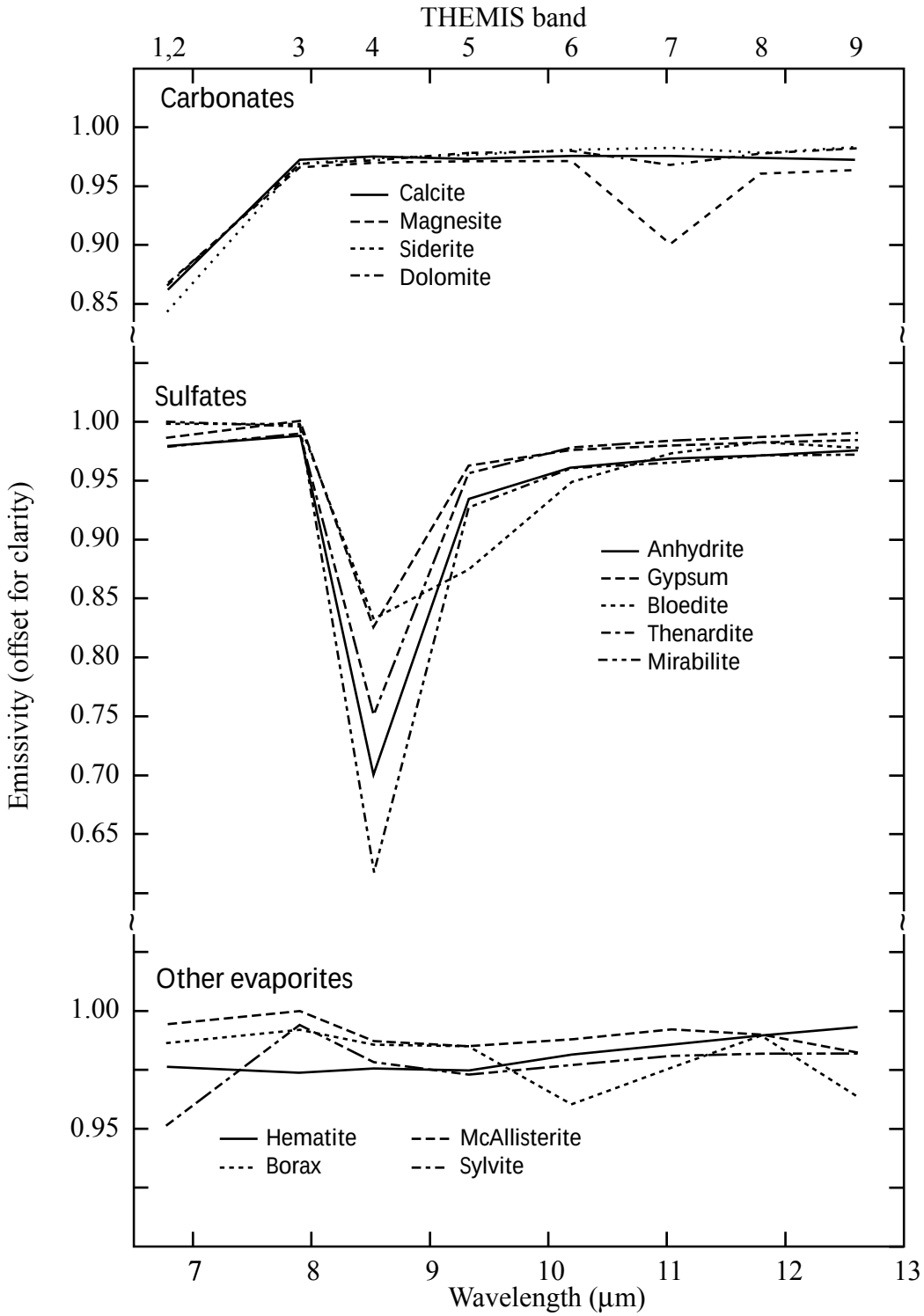

Figure 3 (con't): (b) THEMIS resolution emissivity spectra for TES surface end members and various rock-forming evaporite minerals. Note that the y-axis scale for the "Other evaporite" emissivity spectra differs from the y-axis scale used for the other mineral emissivity spectra.

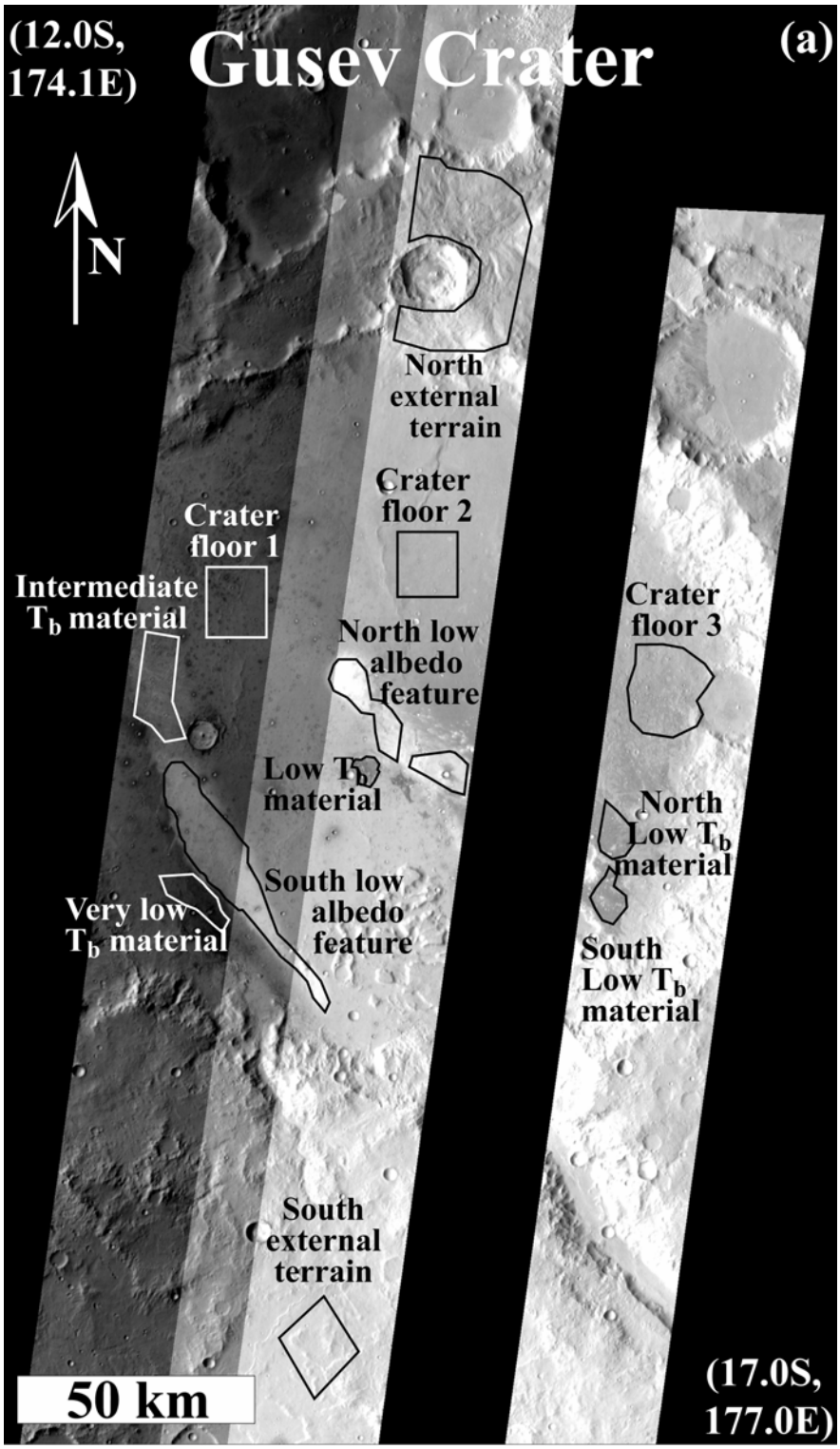

Figure 4: Mosaic of four THEMIS corrected T_b images, decorrelation stretch image and MNF image of Gusev crater (a) Radiance-corrected T_b images of Gusev crater showing the location of regions of interested discussed in the text. From left to right, THEMIS stamps are I01605002, I01243001, I00881002 and I00856001.

Figure 4 (con't): (b) Mosaic of decorrelation stretched images for the four THEMIS stamps covering Gusev Crater, overlain on a MOLA-derived shaded relief map. The decorrelation stretch used bands 5, 8, 7 respectively. The canonical interpretation of colors in this type of image is that greens are consistent with Syrtis-type basalts, reds are consistent with the Acidalia-type TES spectral endmember, and blues are consistent with surface dust [*Christensen et al.*, 2003]. (c) Mosaic of MNF images for the four THEMIS scenes covering Gusev Crater, overlain on a MOLA-derived shaded relief map. Each individual MNF image contains some combination of the first three MNF bands, but the order in which they are displayed into RGB varies. This was done in order to display similar units in similar colors (e.g., the low albedo deposits in red), providing a more contiguous image. From left to right, the MNF band orders are as follows: 312, 123, 213, 123.

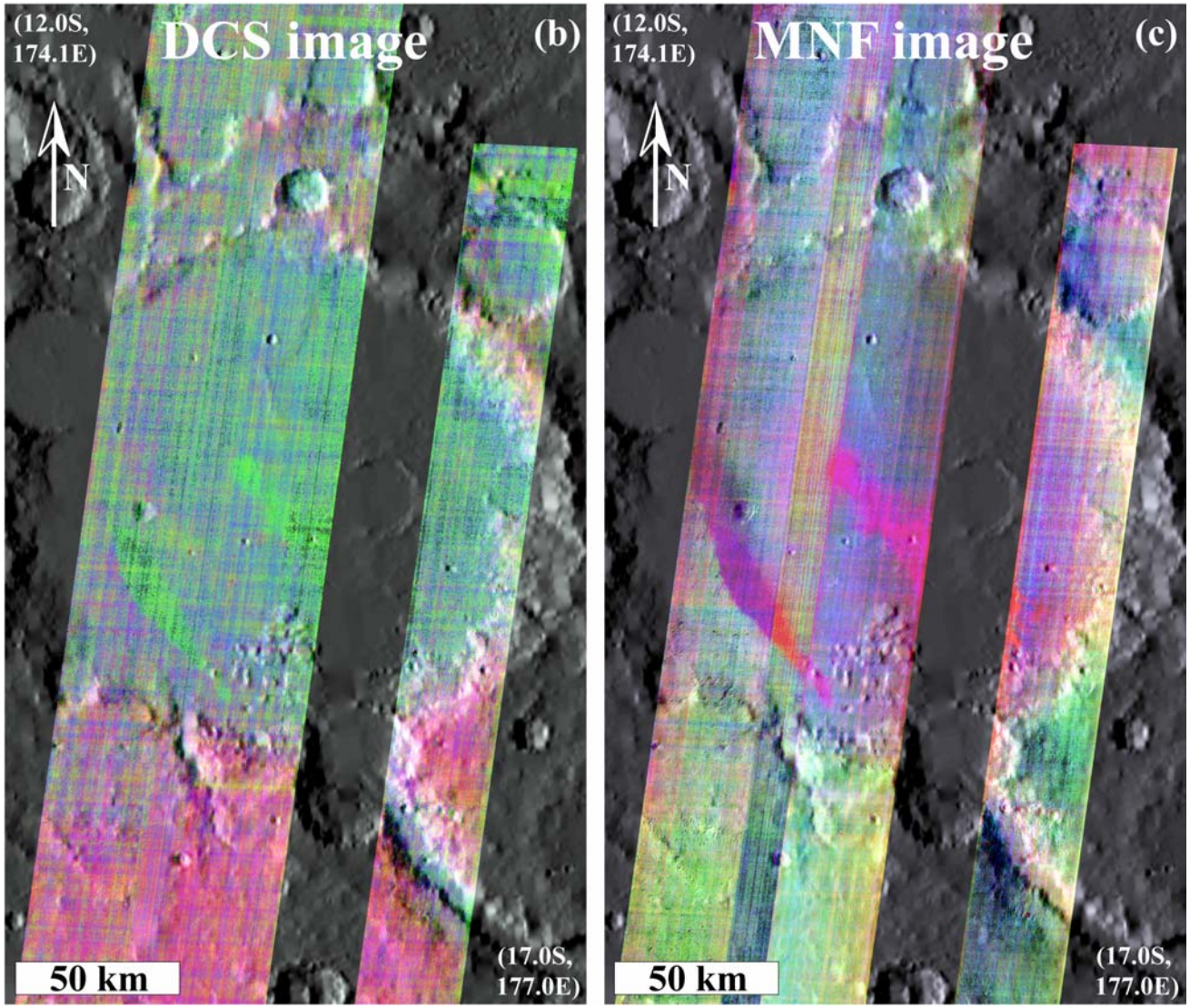
(12.0S,
174.1E)
DCS image
(b)
N
50 km
(17.0S,
177.0E)
(12.0S,
174.1E)
MNF image
(c)
N
50 km
(17.0S,
177.0E)

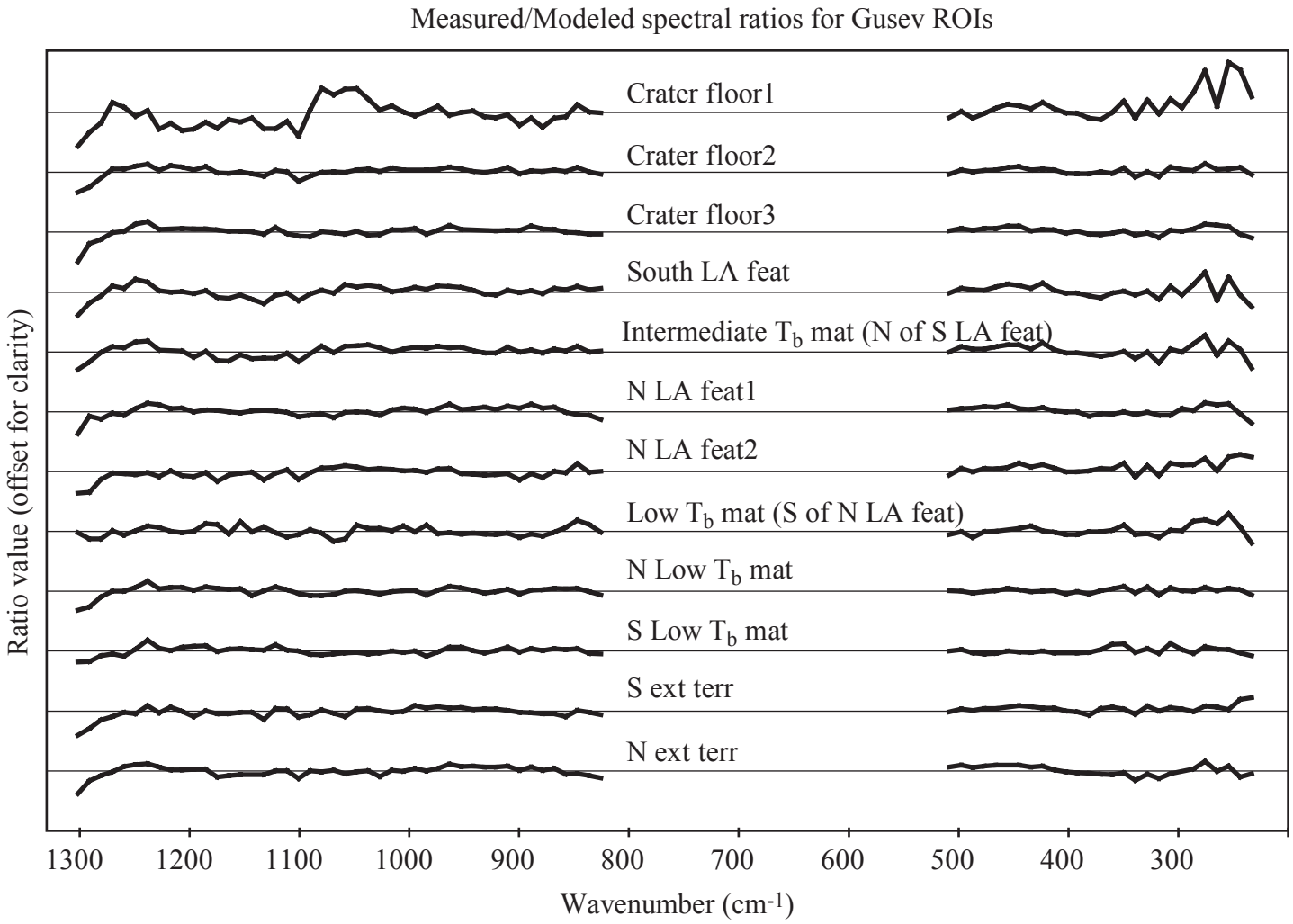

Figure 5: Measured-over-modeled spectral ratios for the Gusev ROIs. (Spectra offset 0.05 for clarity.)

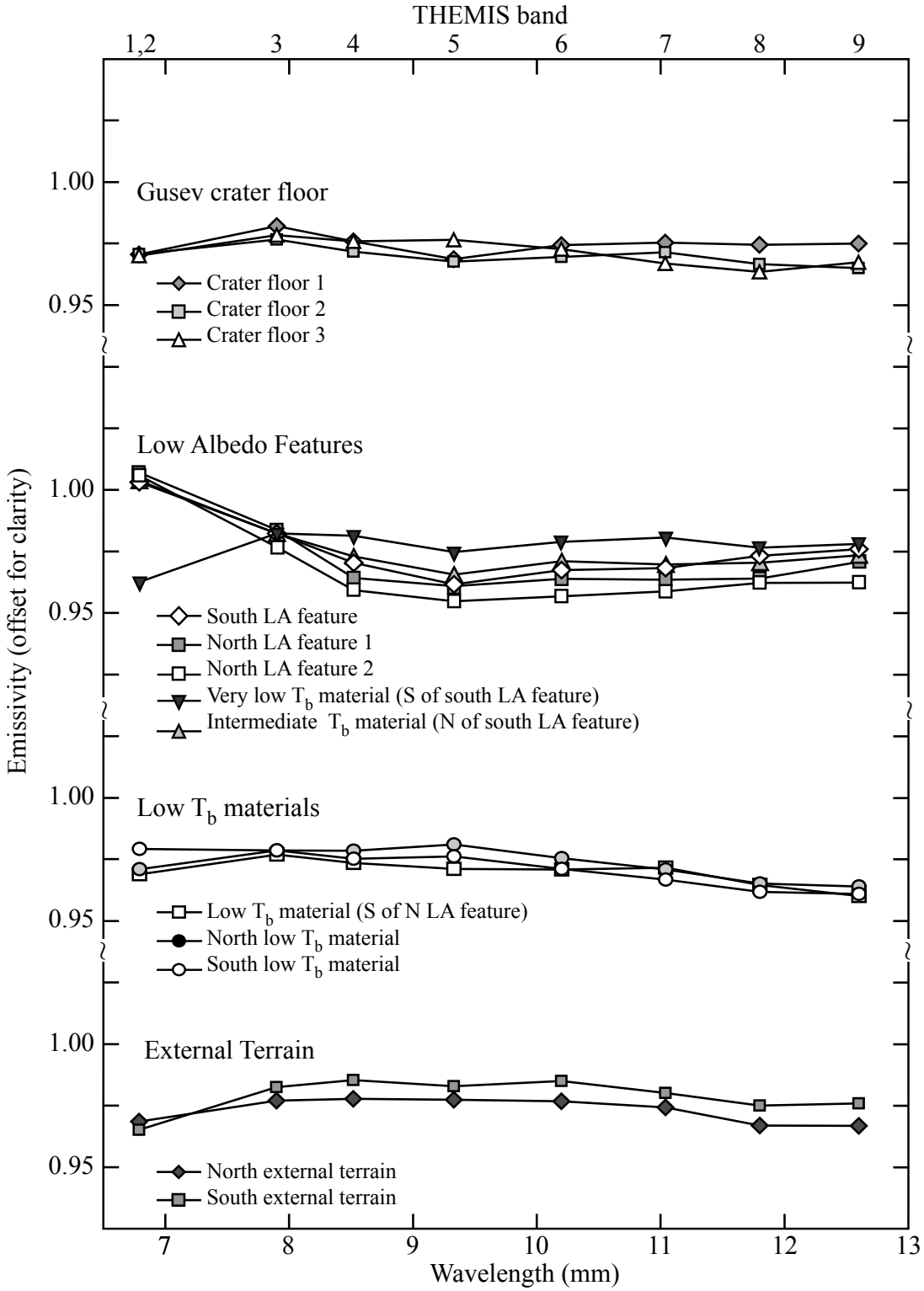

Figure 6: Mean THEMIS emissivity spectra for Gusev Crater. Note that the emissivity displayed for bands 1 and 2 are actually scene-relative emissivity values, not true emissivity. It is important to note that all band 1 and 2 relative emissivity values are close to unity for all ROIs.

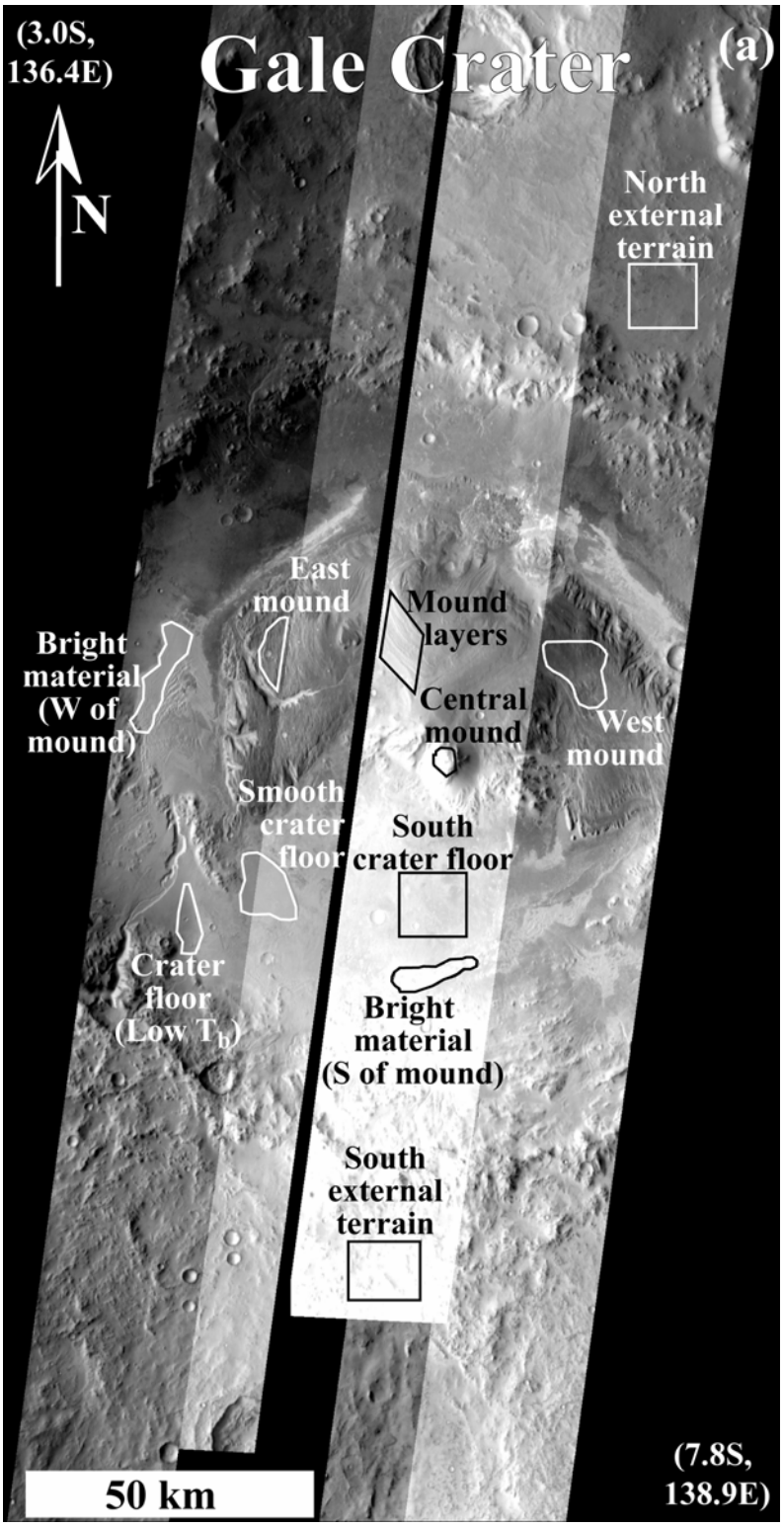

Figure 7: Mosaic of four THEMIS corrected T_b images, decorrelation stretch image and MNF image of Gale Crater (a) Radiance-corrected T_b images of Gale crater showing the location of regions of interested discussed in the text. From left to right, THEMIS stamps are I018550008, I01494001, I01131009 and I01469001.

Figure 7 (con't): (b) Mosaic of decorrelation stretched images for the four THEMIS stamps covering Gale Crater, overlain on a MOLA-derived shaded relief map. The decorrelation stretch used bands 5, 8, 7 respectively. Color-composition relationships are the same as in Figure 4b. (c) Mosaic of MNF images for the four THEMIS stamps covering Gale Crater, overlain on a MOLA-derived shaded relief map. Each individual MNF image contains some combination of the first three MNF bands, but the order in which they are displayed into RGB varies. This was done in order to display similar units in similar colors (e.g., the low albedo deposits in red), providing a more contiguous image. From left to right, the MNF band orders are as follows: 132, 123, 123, 213.

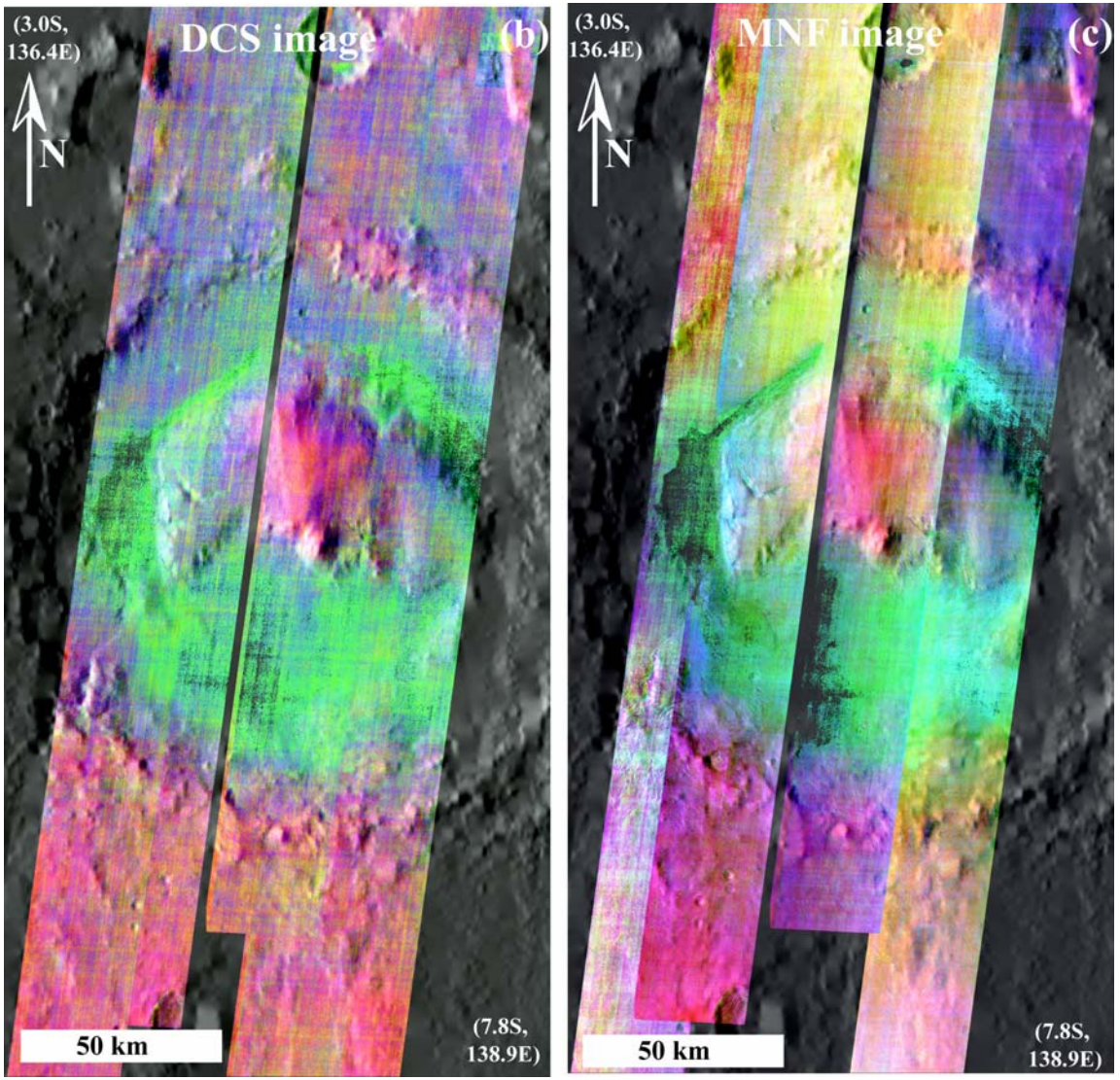
(3.0S,
136.4E)
DCS image
(b)
N
50 km
(7.8S,
138.9E)
(3.0S,
136.4E)
MNF image
(c)
N
50 km
(7.8S,
138.9E)

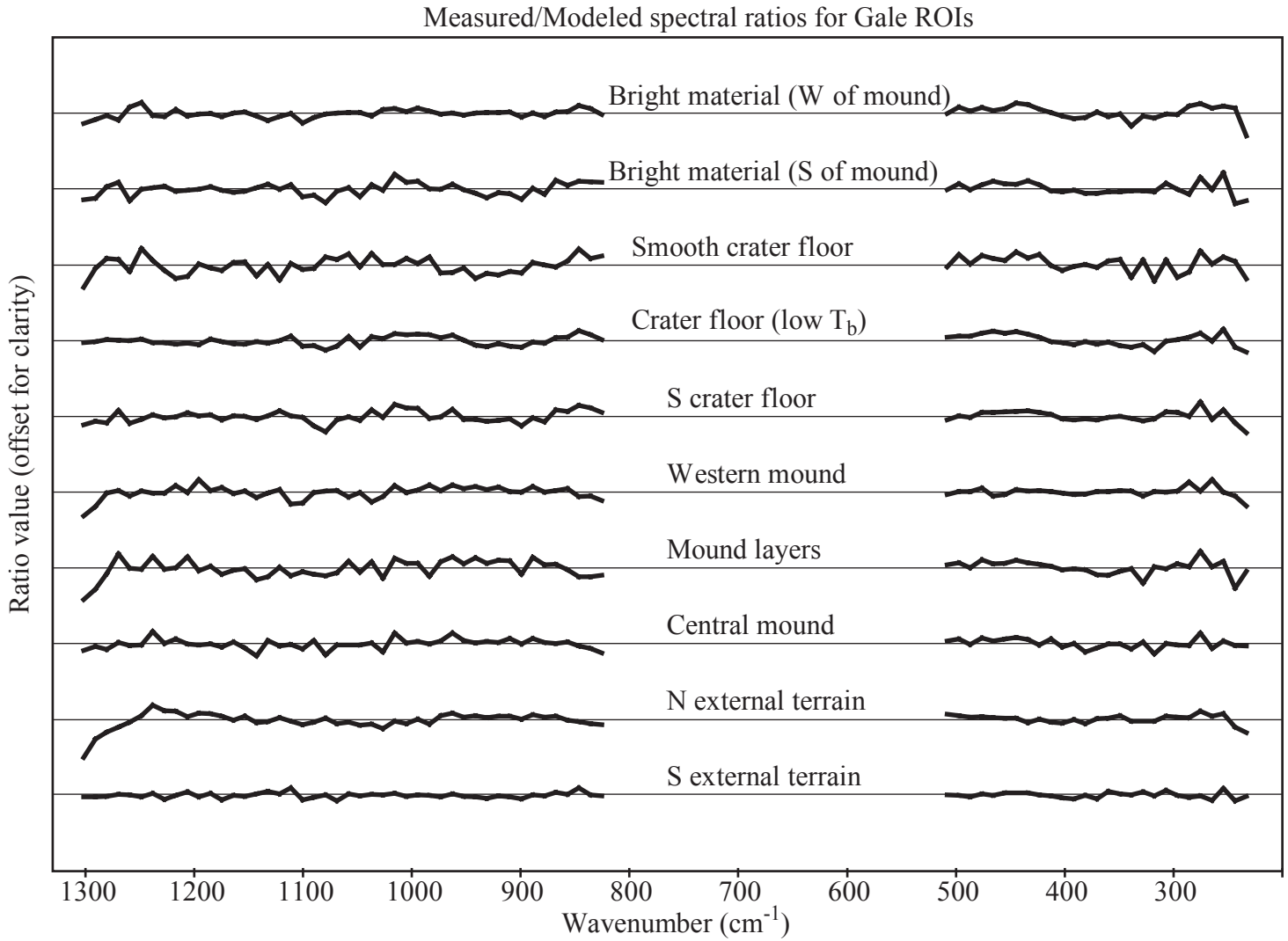

Figure 8: Measured-over-modeled spectral ratios for the Gale Crater ROIs. (Spectra offset 0.05 for clarity.)

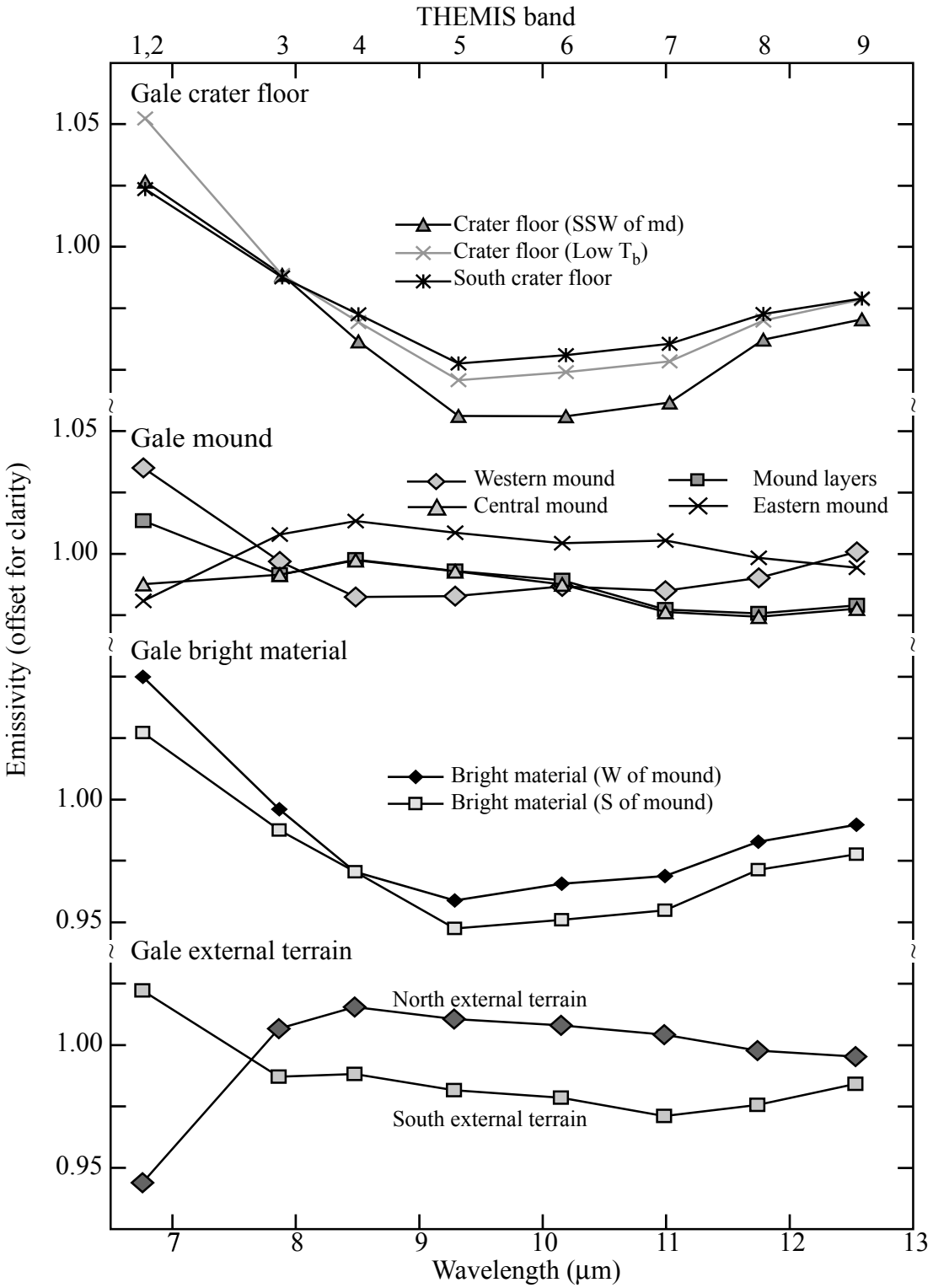

Figure 9: Mean THEMIS emissivity spectra for Gale Crater. Note that the emissivity displayed for bands 1 and 2 are actually scene-relative emissivity values, not true emissivity. It is important to note that all band 1 and 2 relative emissivity values are close to unity for all ROIs.

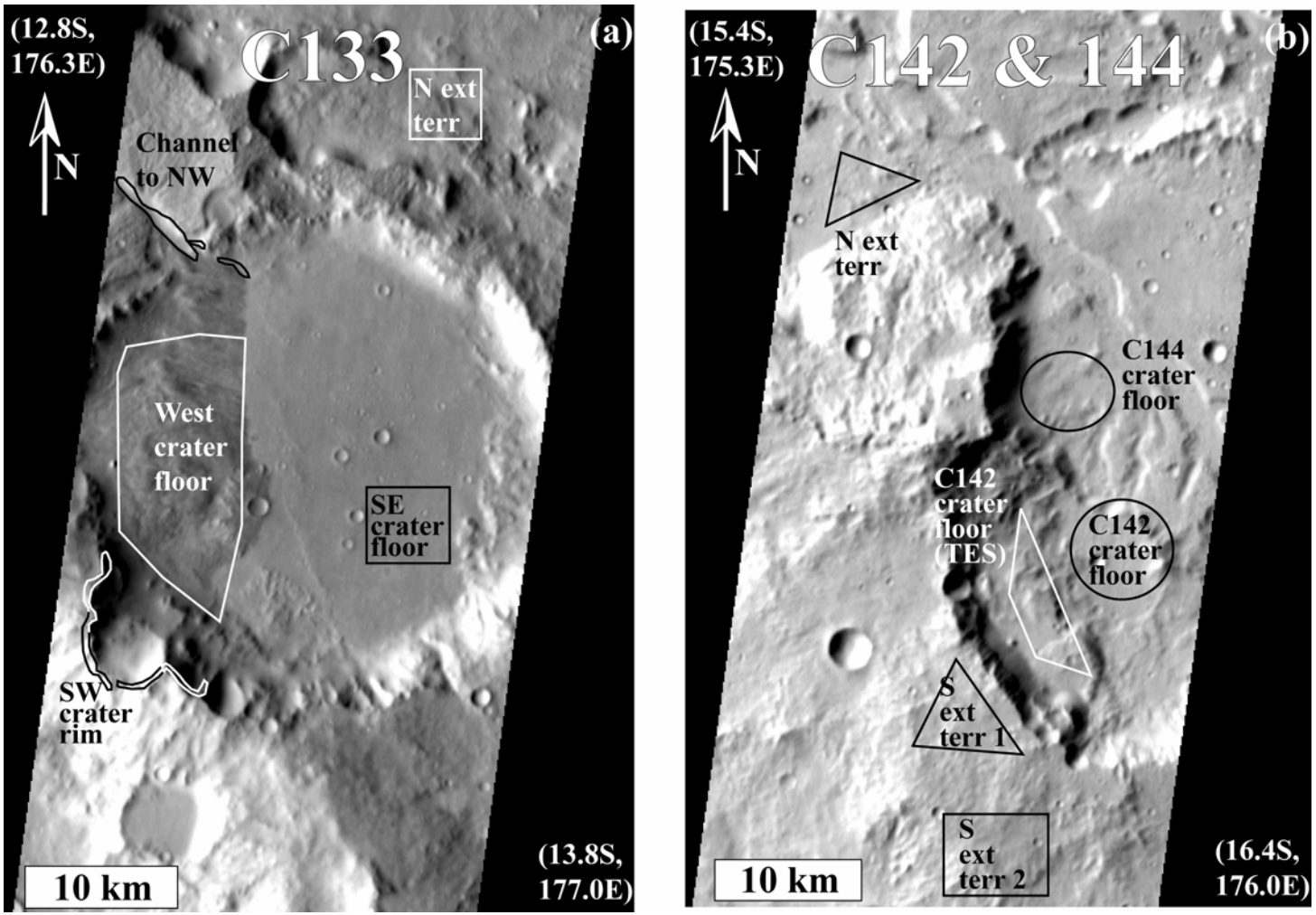

Figure 10: THEMIS corrected T_b image of craters C133, C142, C144 and C147 . (a) THEMIS corrected T_b image (I00856001) of crater C133 showing the location of regions of interested discussed in the text. (b) THEMIS corrected T_b image (I01580002) of craters C142 and C144 showing the location of regions of interested discussed in the text.

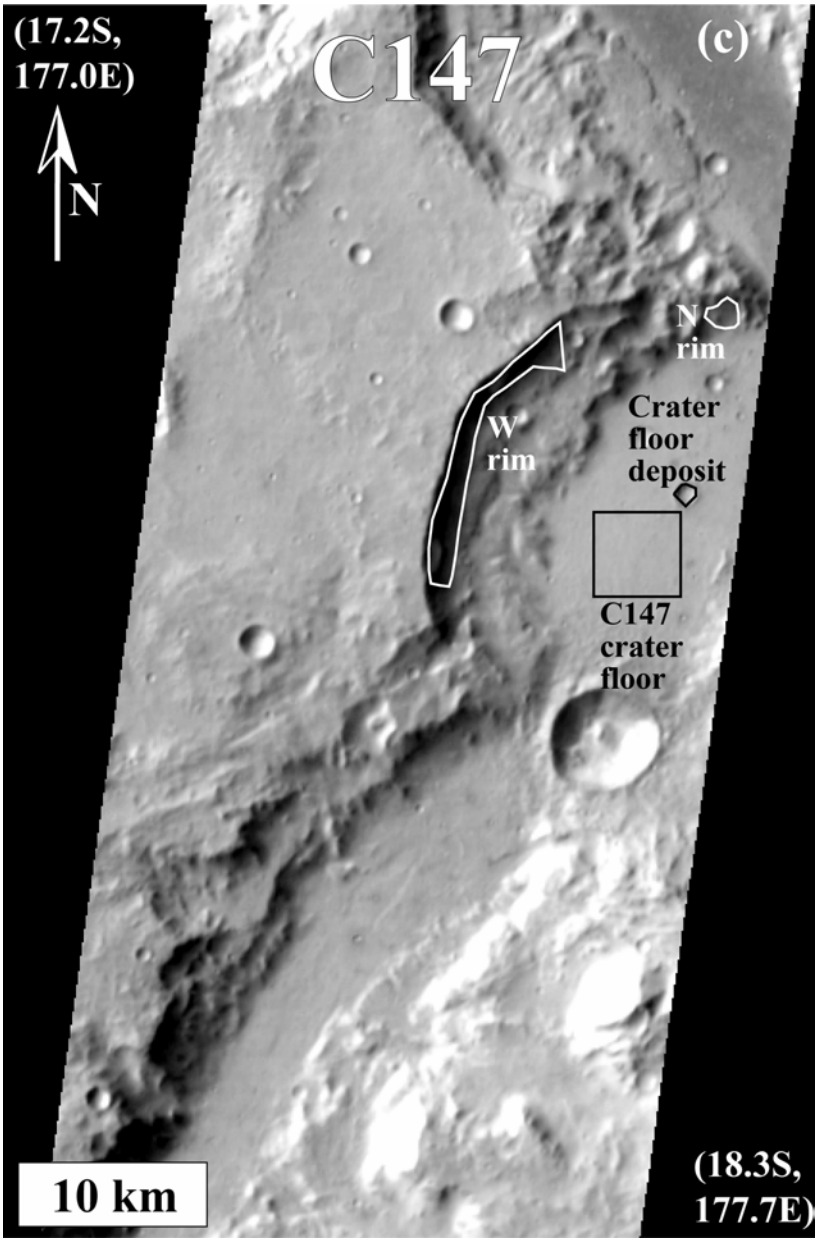

Figure 10 (con't): (c) THEMIS corrected T_b image (I01530002) of crater C147 showing the location of regions of interested discussed in the text.

Figure 11: Decorrelation stretched and MNF images for craters C133, C142, C144 and C147. (a) Decorrelation stretched image for crater C133, overlain on a MOLA-derived shaded relief map. The decorrelation stretch used bands 5, 8, 7 respectively (b) MNF color composite image for crater C133, overlain on a MOLA-derived shaded relief map. (c) Decorrelation stretched image for craters C142 and C144, overlain on a MOLA-derived shaded relief map. The decorrelation stretch used bands 5, 8, 7 respectively (d) MNF color composite image for craters C142 and C144, overlain on a MOLA-derived shaded relief map.

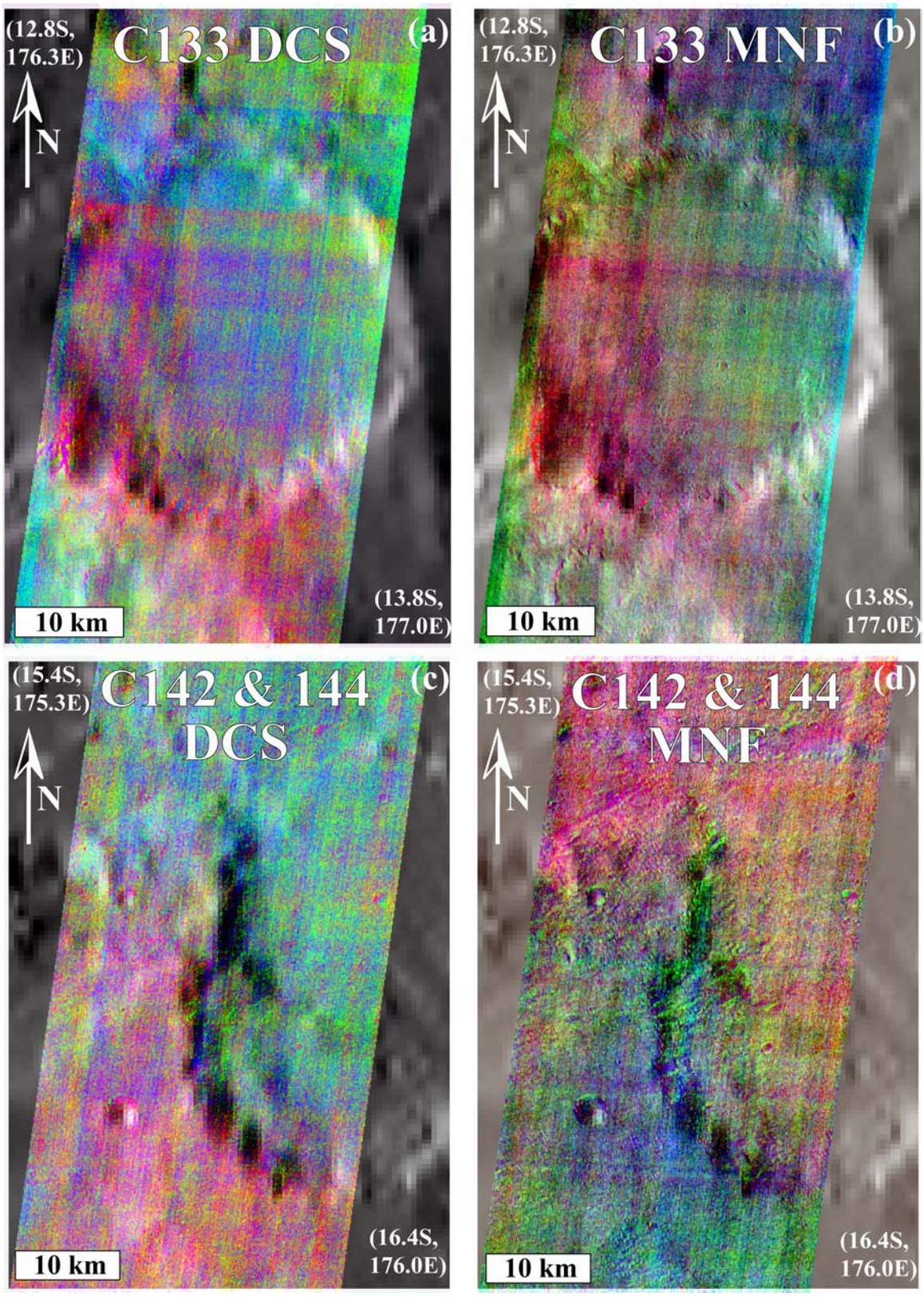
(12.8S, 176.3E)
C133 DCS
(a)
N
10 km
(13.8S, 177.0E)
(12.8S, 176.3E)
C133 MNF
(b)
N
10 km
(13.8S, 177.0E)
(15.4S, 175.3E)
C142 & 144 DCS
(c)
N
10 km
(16.4S, 176.0E)
(15.4S, 175.3E)
C142 & 144 MNF
(d)
N
10 km
(16.4S, 176.0E)

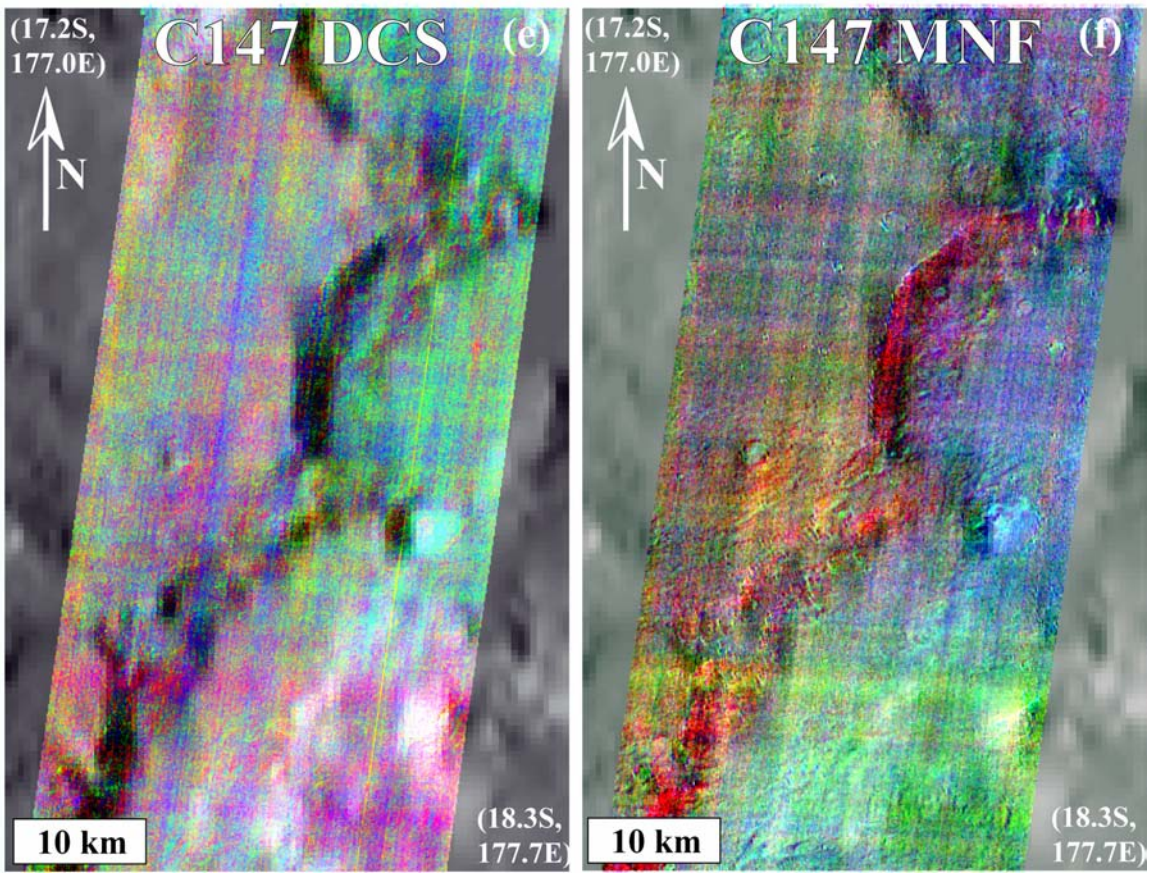

Figure 11 (con't): (e) Decorrelation stretched image for crater C147, overlain on a MOLA-derived shaded relief map. The decorrelation stretch used bands 5, 8, 7 respectively (b) MNF color composite image for crater C147, overlain on a MOLA-derived shaded relief map.

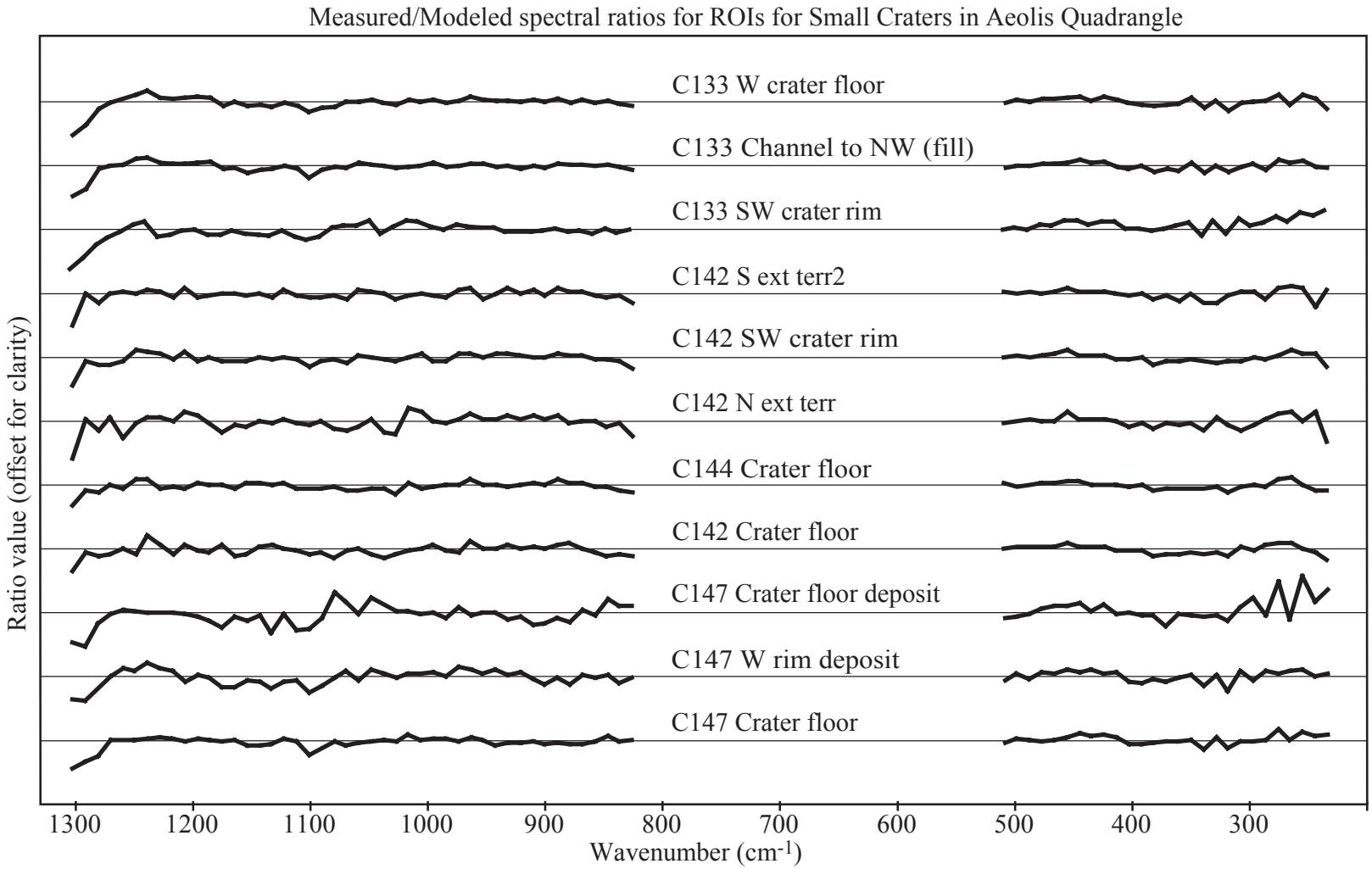

Figure 12: Measured-over-modeled spectral ratios for of small craters within Aeolis Quadrangle. (Spectra offset 0.05 for clarity.).

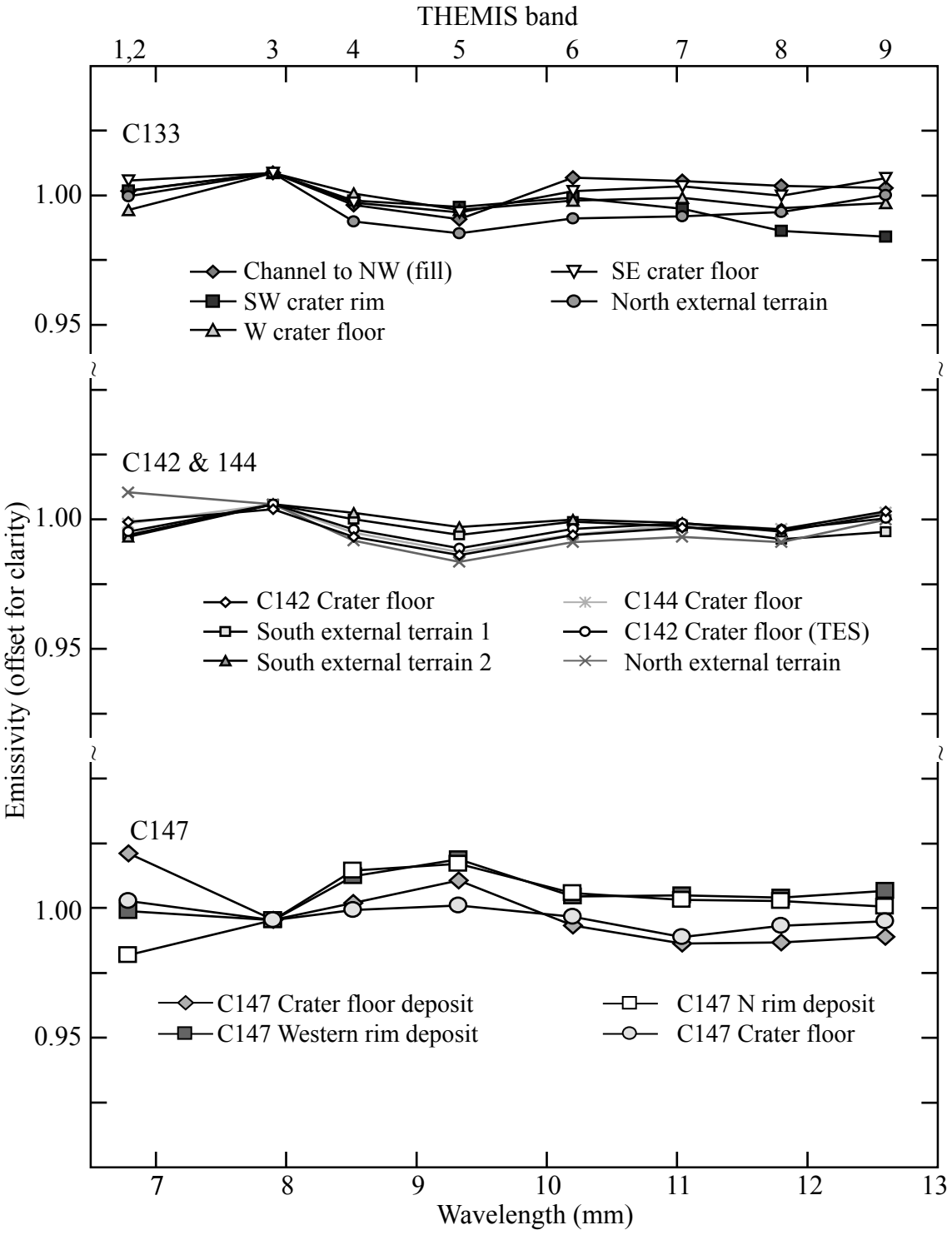

Figure 13: Mean THEMIS emissivity spectra for small craters in Aeolis Quadrangle. Note that the emissivity displayed for bands 1 and 2 are actually scene-relative emissivity values, not true emissivity. It is important to note that all band 1 and 2 relative emissivity values are close to unity for all ROIs.

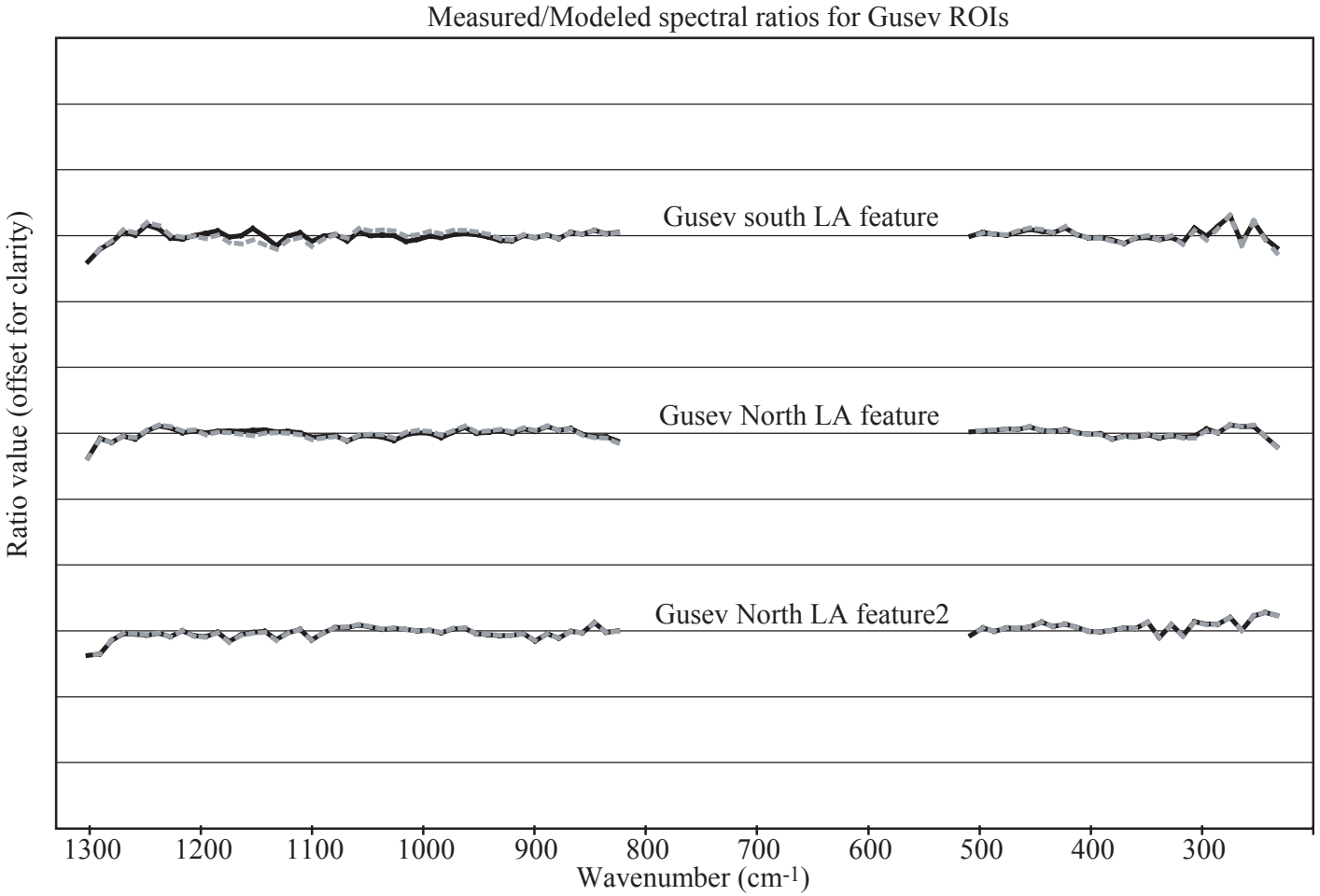

Figure 14: Measured-over-modeled spectral ratios for the low albedo features in Gusev Crater. Spectra offset for clarity. The solid black lines are the measured-over-modeled ratios from deconvolution using the eight TES end members only. The dashed gray lines are the measured-over-modeled ratios from deconvolution using the eight TES end members plus two sulfate (Bloedite and Glauberite) spectra.

Vita

Karen Renée Stockstill was born on the 25th of June, 1972 in Sidney, Ohio. She spent the first year of her life in Milwaukee, Wisconsin and was raised for her remaining childhood years in Sidney by Ray Lee and Karen Rose Stockstill. In Sidney, she attended Holy Angles Grade School and Lehman High School, graduating in May of 1990. She then attended Ohio Wesleyan University in Delaware, Ohio, receiving a B.A. in Physics in 1994. Following her undergraduate degree, she worked at the Lunar and Planetary Institute in Houston, Texas, first as a summer intern during the summer of 1994 and then as a Visiting Graduate Fellow from August 1994 through August 1996. In 1996, she returned to school at Michigan State University in East Lansing, Michigan, studying the Burroughs Mountain lava flow on Mt. Rainier, Washington. She successfully defended her thesis on the 25th of June, 1999 and received a M.S. in Geology in August of 1999. She then attended the University of Tennessee, Knoxville to pursue her doctorate degree in Planetary Geology, which she completed successfully on the 3rd of June, 2005.

Karen is currently working as a post-doctoral fellow at the University of Hawaii-Manoa, Honolulu, Hawai'i.